HIGH TEMPERATURE DEFORMATION MECHANISMS OF CEMENTED CARBIDES AND CERMETS

THÈSE N^{O} 3095 (2004)

PRÉSENTÉE À LA FACULTÉ SCIENCES DE BASE

Institut de physique de la matière complexe

SECTION DE PHYSIQUE

ÉCOLE POLYTECHNIQUE FÉDÉRALE DE LAUSANNE

POUR L'OBTENTION DU GRADE DE DOCTEUR ÈS SCIENCES

PAR

Katharina BUSS

Dipl.-Ing. (FH), Fachhochschule Jena, Allemagne
et de nationalité allemande

acceptée sur proposition du jury:

Prof. W. Benoit directeur de thèse
Prof. H.-O. Andren, rapporteur
Dr D. Mari, rapporteur
Dr I. Reineck, rapporteur
Prof. P. Stadelmann, rapporteur

Lausanne, EPFL
2004

Abstract

The motivation of this work derives from the need of the cutting tool industry to improve its products in order to support harder and harder working conditions, namely increasing cutting speeds and working on stronger modern materials. The lifetime of the tools is limited by plastic deformation that occurs at the cutting edge under working conditions, which involve high temperatures and stresses.

The high temperature deformation of the materials that are used for the production of cutting tools is studied. Two base materials are chosen, a WC-Co cemented carbide and a TiWCN-Co cermet, with the same amount and composition of the cobalt binder. The experimental strategy combines macroscopic deformation tests by three-point bending with microscopical observation and mechanical spectroscopy. We also analyze residual stresses and crystal structure as a function of temperature by neutron and X-ray diffraction.

By three-point bending, the transition temperature at which, macroscopically, grain boundary sliding (GBS) of the ceramic phase becomes the dominant deformation mechanism is determined to be 1100 K for the cemented carbide and 1350 K for the cermet.

Measurements of residual stresses show that high compressive stresses are present in the hard phase at room temperature and that they relax as the temperature increases. These stresses are much higher in WC-Co, 800 MPa at room temperature, and do not relax completely before 1500 K. In the cermet, they are around 200 MPa at room temperature and relax at 1200 K. Moreover, important changes in the chemical composition of binder and hard phase are observed. In WC-Co, a strong increase of the tungsten content in the cobalt binder is observed above 1100 K. In the cermet, the cobalt composition does not substantially change, but the hard phase exhibits a change in the C/N ratio above 1350 K.

Mechanical spectroscopy evidences a number of relaxation phenomena in both materials. At high temperature, three peaks in WC-Co and two peaks in the cermet have been related to grain boundary sliding. A model is proposed that involves two regimes: *limited GBS* due to cobalt segregation at grain boundaries, and *extensive GBS* due to fully infiltrated grain boundaries. The latter behavior is similar in WC-Co and cermets and it is associated with a high and very broad relaxation peak. On the other hand, the mechanisms for the limited GBS are different in WC-Co and in cermets. In cermets, cobalt segregation increases continuously with temperature, starting at about 1350 K. In WC-Co, the segregation of cobalt depends on the type of WC/WC grain boundaries: different relaxation mechanisms can be attributed to general grain boundaries and special grain boundaries, where the special grain boundaries are stabilized by a half-monolayer of segregated cobalt.

The effect of tantalum on the plastic deformation behavior is furthermore investigated. Tantalum leads to a beneficial effect in WC-Co below 1273 K, by rejecting cobalt from the grain boundaries and therefore suppressing GBS. At higher temperatures, it leads to an increasing instability of the grain boundary structure both in cermets and cemented carbides, which goes

along with a decrease of the tool performance. In different cermet grades, the performance of the tools seems strongly correlated with the stability of the structure of the grain boundaries at high temperatures evidenced by mechanical spectroscopy. Moreover, the impact of tantalum on the deformation behavior of the cermet grades depends strongly on the carbon content.

Finally, both the cemented carbide with tantalum and the cermet with tantalum show a phase transformation of the grain boundaries from a crystalline to an amorphous viscous state.

Generally, the two basic cutting tool materials, WC-Co cemented carbide and TiWCN-Co cermet, show differences regarding the onset temperature and the low-temperature mechanisms of GBS. However, the GBS of fully infiltrated grain boundaries at high temperature seems to be quite comparable in both materials.

Version abrégée

Ce travail est motivé par le besoin d'améliorer les outils de coupe, de façon à supporter des conditions de travail de plus en plus dures, en particulier des vitesses de coupe toujours plus grandes sur des matériaux modernes très résistants. La durée de vie de l'outil est limitée par la déformation plastique qui a lieu sur l'arête de coupe pendant l'usinage, qui fait intervenir des températures et des contraintes élevées.

La déformation à haute température des matériaux utilisés pour la production d'outils de coupe est étudiée dans ce travail. On a choisi deux matériaux de base : un carbure cémenté de type WC-Co et un cermet de type TiWCN-Co avec la même teneur en cobalt et une composition du cobalt comparable. La stratégie expérimentale de ce travail combine des essais macroscopiques par flexion trois-points avec l'observation de la microstructure et la spectroscopie mécanique. On analyse également les contraintes résiduelles ainsi que la structure cristalline en fonction de la température, par diffraction de neutrons et rayons X.

Les essais de flexion trois-points permettent de déterminer la température de transition à partir de laquelle le glissement aux joints de grains de la phase céramique devient le mécanisme dominant. Cette transition a lieu à 1100 K pour le carbure cémenté et à 1350 K pour le cermet.

La mesure des contraintes résiduelles montre que, à température ambiante, des contraintes de compression élevées sont présentes dans la phase dure, et que celles-ci sont relaxées lorsque la température augmente. Ces contraintes sont beaucoup plus grandes dans le WC-Co (800 MPa à température ambiante) et ne relaxent pas totalement avant 1500 K. Dans le cermet, elles se situent autour de 200 MPa à température ambiante et sont relaxées autour de 1200 K. On observe de plus des changements importants dans la composition chimique du liant métallique et de la phase dure : dans le WC-Co, la teneur en tungstène dans le cobalt augmente fortement au-dessus de 1100 K, tandis que dans le cermet, la composition du cobalt ne change pratiquement pas, mais la phase dure montre un changement du rapport C/N au-dessus de 1350 K.

La spectroscopie mécanique a permis de mettre en évidence de nombreux phénomènes de relaxation dans les deux matériaux. A haute température, trois pics dans le WC-Co et deux pics dans le cermet ont été attribués au glissement aux joints de grains. Nous proposons un modèle qui implique deux régimes: glissement *limité,* dû à la ségrégation du cobalt aux joints de grains, et glissement *étendu*, dû à la présence de joints infiltrés par le cobalt. Ce dernier comportement est similaire dans le WC-Co et dans les cermets, et est associé à un pic de relaxation très haut et très large. En revanche, les mécanismes responsables du glissement limité sont différents. Dans les cermets, la ségrégation du cobalt change de manière continue en fonction de la température, et ceci dès 1350 K. Dans le WC-Co, par contre, la ségrégation du cobalt dépend du type de joint de grains WC/WC : différents mécanismes de relaxation sont attribués aux joints d'orientation quelconque et à ceux ayant une orientation particulière rendus stables par la présence d'une demi couche atomique de cobalt ségrégé.

L'effet de l'ajout de tantale sur la déformation plastique est aussi étudié. Le tantale a une influence bénéfique dans le WC-Co au-dessous de 1273 K en rejetant le cobalt des joints et en supprimant ainsi le glissement aux joints de grains. A des températures plus élevées, le tantale crée une instabilité accrue de la structure des joints dans le WC-Co ainsi que dans le cermet. Dans ces derniers, la performance des outils semble liée à la stabilité de la structure des joints de grains à haute température, mise en évidence par la spectroscopie mécanique. L'impact du tantale sur la déformation dépend fortement de la teneur en carbone.

Finalement, les carbures cémentés et les cermets contenant du tantale présentent tous deux une transformation de phase aux joints de grains, d'un état cristallin à un état amorphe visqueux.

Kurzfassung

Schneidwerkzeuge sind immer härter werdenden Arbeitsbedingungen, wie steigender Schnittgeschwindigkeit, Verzicht auf Kühlschmiermittel und anspruchsvolleren zu bearbeitenden Materialien, ausgesetzt. Die Lebensdauer der Werkzeuge wird durch plastische Verformung begrenzt, die unter diesen Arbeitsbedingungen, d.h. hohen Temperaturen und angreifenden Kräften, an der Schneidkante auftreten.

Die Hochtemperatur-Verformung der Materialien, die bei der Herstellung von Schneidwerkzeugen (speziell Wendeschneidplatten) Verwendung finden, ist untersucht worden. Zwei Grundwerkstoffe wurden ausgewählt: Wolframkarbid-Kobalt und Titankarbonitrid-Kobalt mit gleichem Volumenanteil und gleicher chemischer Zusammensetzung der Kobalt-Bindephase. Das experimentelle Konzept dieser Arbeit beruht auf der Kombination von makroskopischen mechanischen Testverfahren wie Drei-Punkt-Biegung mit Mikroskopie und Mechanischer Spektroskopie. Darüberhinaus wurden die Eigenspannungen und Veränderungen der kristallinen Phasen mittels Neutronen- und Röntgenbeugung in Abhängigkeit von der Temperatur ermittelt.

Mit Hilfe der Drei-Punkt-Biegung wurde die Temperatur bestimmt, bei der der Übergang zum Korngrenzengleiten der Karbidphase als Hauptverformungsmechanismus erfolgt. Diese Übergangstemperatur beträgt 1100 K für WC-Co und 1350 K für TiWCN-Co.

Die Messungen der Eigenspannungen zeigen, dass bei Raumtemperatur hohe Druckspannungen in der Hartphase vorhanden sind, welche mit steigender Temperatur geringer werden. Diese Druckeigenspannungen sind in WC-Co mit 800 MPa in der WC-Phase bei Raumtemperatur vergleichsweise hoch und werden erst bei Temperaturen oberhalb 1500 K vollständig abgebaut. Die bei ca. 1200 K vollständig abgebauten Druckspannungen in der Karbonitridphase des TiWCN-Co betragen bei Raumtemperatur nur ungefähr 200 MPa. Darüberhinaus konnten interessante Veränderungen der chemischen Zusammensetzung von Hart- und Bindephase festgestellt werden. In WC-Co steigt die Wolframkonzentration in der Kobaltphase beginnend bei 1100 K stark an. In TiWCN-Co verändert sich die Kobaltphase dahingegen nicht wesentlich. Jedoch zeigt die Karbonitridphase oberhalb 1350 K Veränderungen, welche wahrscheinlich auf eine Änderung des Kohlenstoff-Stickstoff-Verhältnisses zurückzuführen sind.

Eine Reihe von Relaxationsvorgängen konnte in beiden Werkstoffen mittels der Mechanischen Spektroskopie festgestellt werden. Drei der Relaxationsmaxima in WC-Co und zwei in TiWCN-Co werden mit Korngrenzengleiten (KGG) in Verbindung gebracht. Ein Modell mit zwei verschiedenen Domänen wird aufgestellt: *eingeschränktes KGG* aufgrund von Kobaltausscheidungen in den Korngrenzen der Hartphase und *ausgedehntes KGG* aufgrund vollständig vom Bindemetall infiltrierter Korngrenzen. Das KGG der vollständig infiltrierten Korngrenzen in WC-Co und TiWCN-Co verhält sich sehr ähnlich. Es wird in beiden Fällen durch ein hohes und stark verbreitertes Relaxationsmaximum charakterisiert. Die dem eingeschränkten KGG unterliegenden Mechanismen sind jedoch in beiden Werkstoffen verschieden. Im TiWCN-Co

nimmt die Kobaltausscheidung in den Korngrenzen beginnend bei ca. 1350 K mit steigender Temperatur zu. In WC-Co hängt die Kobaltausscheidung jedoch von der Art der WC/WC-Korngrenzen ab. Den allgemeinen Korngrenzen wird ein anderer Relaxationsmechanismus zugeordnet als den speziellen Korngrenzen, welche durch Einlagerung einer halben Atomschicht Kobalt stabilisiert werden.

Der Einfluss Tantals auf das Verformungsverhalten ist ebenfalls untersucht worden. Tantal hat einen positiven Einfluss auf WC-Co unter 1273 K, indem es das Kobalt aus den Korngrenzen verdrängt und somit das Korngrenzengleiten unterbindet. Bei höheren Temperaturen führt es jedoch sowohl in WC-Co als auch in TiWCN-Co zu einer instabileren Struktur der Korngrenzen und somit zu einer schlechteren Zerspanleistung. Eine direkter Zusammenhang konnte für die TiWCN-Co-Cermets zwischen der Verformung beim Zerspanen und der durch die Mechanische Spektroskopie nachgewiesenen Hochtemperaturstabilität hergestellt werden. Bei diesen Materialien hängt der Einfluss des Tantals zudem stark vom Kohlenstoffgehalt ab.

Beide Hartmetallsorten, WC-Co und TiWCN-Co, zeigen bei Zusatz von Tantal und bei hohen Temperaturen eine Phasenumwandlung der Korngrenzen von einem kristallinen hin zu einem amorphen, viskosen Zustand.

Zusammenfassend lässt sich feststellen, dass beide Hartmetalle gewisse Unterschiede zeigen, vor allem für die Temperatur bei der das Korngrenzengleiten beginnt sowie den Mechanismen die dabei auftreten. Das Korngrenzengleiten vollständig infiltrierter Korngrenzen bei höheren Temperaturen scheint hingegen in beiden Materialien recht ähnlich abzulaufen.

Content

Chapter 1

Introduction

Metals, especially steels, are still important technical and design materials in the industry today. Functional metal parts can be produced in many ways as for example by casting, sintering, metal forming and machining. Each of these processes has its advantages, but also limits. Machining such as drilling, milling and turning are processes that a manufacturer would actually try to avoid. They are time consuming, lubricants and cooling aids pose environmental problems and moreover a not negligible amount of (precious) material is wasted in form of small chips. However, it is the most widely used process in the metal working industry, due to its high precision and the almost unlimited possibilities regarding forms and design of the work piece. The therefore necessary cutting tools can be made of diamond, ceramics, hardmetals, high speed steels and tool steels. They are often produced in small pieces of the size of a thumbnail, called inserts, which are fixed to a long-lasting tool holder that is mounted on the lathe, mill or drill (Fig. 1.1 and Fig. 1.2). These inserts are manufactured in geometrical forms of triangles, squares or rhombs, the edges of which are the active cutting parts. The longer the time a cutting edge can be used, the higher is the efficiency of the tool or in other words, the better is its performance. However, while the wear of the cutting edge gradually increases, the

Figure 1.1: Examples of different types of cutting tools

Figure 1.2: Cutting insert during turning application

precision and the quality of the surface finish of the work piece decreases. Sooner or later, the insert has to be changed or turned so that a fresh edge can be used.

The insert may be cheap, but to turn it means to interrupt the machining process, which costs time and therefore money. The lifetime of a cutting tool is consequently an important economic factor, creating huge competition among cutting tool producers. The tools have to withstand high temperature and stress during turning, they have to be shock resistant during milling, corrosion resistant and chemically inert towards the work piece material. Moreover, the metal working industry demands not only a long tool life, but it is trying to push the limits of the tools still further, as higher and higher cutting speeds are required possibly even without lubrication and cooling liquids, which produces even more severe cutting conditions.

From the material science point of view, the tool material must combine properties typical for ceramics such as high hardness, temperature resistance and chemical stability with typical metal properties as for example high toughness and good thermal conductivity. Hardmetals, which are composite materials with a dominant ceramic phase bonded by a metal binder, fulfill these requirements. However, the perfect tool material does not exist. Different applications demand different tool properties. A great variety of cutting tool materials was therefore developed during the past hundred years, mostly by empirically changing the composition or microstructure. Only in recent times, the microscopy has developed to the point, where the microstructure can be studied down to the atomic scale, computational methods are available to study the distribution of temperature and stresses inside a material and macroscopic material properties can be related with calculated electron structures and the strength of atomic bonds.

With these new possibilities and because of the strong competition, the cutting tool industry is highly interested in fundamental research about the wear of these materials in order to gain a better understanding of the mechanisms leading to the destruction of the cutting edge and to find ways to prolong the life-time of the tools. A big step in that direction was the development of special coatings that help to prevent the tools from oxidation and abrasion. Today, almost all inserts have very efficient coatings. The life-time limiting factor therefore is no longer the wear at the contact zone of the tool with the work piece, but the plastic deformation that occurs in the underlying bulk of the insert material.

The plastic deformation of inserts upon machining has been already observed. The base materials for cutting tools are hardmetals consisting mainly of ceramic phase with small additions of metal as binder. As the main phase is a hard ceramic that show little or no bulk deformation, the main deformation mechanism could be, as in ceramics, the rearrangement of the hard phase grains by grain boundary sliding (GBS). This sliding is probably helped by small layers of the soft binder metal that has been observed at the grain boundaries. A joint project has been established to study the “Fundamental deformation mechanisms of cermets and cemented carbides” between our laboratory (IPMC), AB Sandvik Coromant, Stockholm, and Chalmers University of Technology, Göteborg. In this project, model materials are produced and their wear behavior is tested by turning. The deformed as well as undeformed reference material is investigated by electron microscopy and atom probe by a specialized group at Chalmers University in order to analyse the compositional and microstructural changes of the different phases and especially of the interfaces during deformation. Another group, specialized in ab initio calculations, studies the strength of interfacial configurations and how it is affected by impurities.

The aim of this work is to study the deformation behavior at high temperature of the cutting tool material. By combining the results of macroscopic deformation tests with the measurement of the microstructural defect mobility and the analysis of internal stresses, the deformation mechanism or mechanisms are determined. Moreover, we investigate how the high–

temperature mechanical properties are affected and possibly improved by structural modifications. The deterioration of the mechanical properties at high temperature is shown to be closely correlated with the onset of ceramic grain boundary sliding. The effect of tantalum addition to prevent GBS is studied and discussed in comparison with the results of the turning tests.

In this thesis, **Chapter 2** will be dedicated to a presentation of the knowledge about hardmetals, and especially of their high-temperature properties, summarized from former works of our laboratory and from literature.

Chapter 3 introduces the investigated materials. In the second part of the chapter, the principles and experimental setups of the techniques used in this work are described.

The experimental results together with partial conclusions are presented in the following chapters. The macroscopic mechanical behavior is studied by three-point bending in **Chapter 4**. Internal stresses, always present in composite materials, are measured by diffraction and presented in **Chapter 5**. And the defect mobility, in particular that of grain boundaries, is studied by mechanical spectroscopy, the so-called internal friction (IF), in **Chapter 6**.

The effect of tantalum, which is capable of enhancing the tool performance as shown by machining tests, is studied in **Chapter 7**. The “laboratory results” are compared with the wear measured after standard turning tests. The combination of “field test” and mechanical properties is unique. The high-temperature deformation mechanisms are discussed here in the light of the industrial application.

Chapter 8, finally, presents the main results and conclusions in a condensed form.

Chapter 2

High-temperature mechanical properties of cutting tool materials

This chapter provides a bibliographic background for the present work. First, the historical development of the materials used for the production of cutting tools, the general production process and their typical structure are described. The second part illustrates the mechanical properties of these materials and, in particular, the deformation that occurs at high temperatures limiting their use. In the third part, mechanical spectroscopy is introduced as a tool to study deformation mechanisms. Typical phenomena and observations are shown and their interpretation is discussed. Finally, this knowledge background leads to the formulation of the aim of this thesis.

1 Hardmetals

1.1 Nomenclature

The classification of typical cutting tool materials described below is basically adapted from Mari [1].

The term "hardmetal", introduced in 1953 by Schwarzkopf and Kieffer [2], was actually attributed to carbides, nitrides, borides and silicides of metals of the fourth to sixth group of the table of elements. These materials show mechanical properties typical for ceramics such as high hardness and brittleness. Other features are unusual for ceramics such as a relatively high electrical and thermal conductivity, which are due to the metallic character of the atomic bonds. For structural applications, these materials are much too brittle. Therefore, a small amount of metal is added to bind the ceramic phase. The result is a composite material made of a ceramic matrix and a metallic binder, better described by the term "cer–met". Today the word "hardmetal" is generally used for cermets based on hardmetal ceramics.

The largest commercial success has to be attributed to a small group of hardmetals that was used for the production of cutting tools. They consist mainly of one or several of the following compounds: tungsten carbide (WC), titanium carbide (TiC) and titanium carbonitride (TiCN) and are bound by one of the metals of the iron-group or by an alloy of these elements. Their success is mostly due to their unique thermodynamic properties that allow to produce them by liquid phase sintering, which creates a dense composite without altering the nature of each

phase. The favorable ceramic and metallic properties are therefore combined in a very beneficial way.

Traditionally, the materials used for the production of cutting tools are divided into two large families. Those with a majority of WC phase are generally named “cemented carbides”, while the term “cermet” is reserved for TiC-based cutting tool materials. Often authors include cermets in the cemented carbide family [3,4], while others rather talk of cemented carbides being part of cermets is general [1]. The first justify it by saying cermets are produced by the cemented carbide industry, while the latter rather refer to the ceramic-metal composite character of both families. One could use the term hardmetals to include both types of materials [4].

In this work, one member of each family is studied, the cemented carbide WC-Co and the cermet TiCN-Co.

1.2 Manufacturing

The mechanical properties of hardmetals are closely related to their complex structure. Many factors determine the final morphology of the material, such as the choice of the raw material, the pre-sintering production steps and finally the careful control of the thermodynamic parameters such as temperature, pressure and time during the sintering process. A lot of research during the last 20 years has been dedicated to the improvement of the processing in order to reach a better control and predictability of the microstructure and morphology and consequently of the material properties [4]. The general production process is briefly described here.

The raw material is constituted of pure or pre-alloyed powders of hard metal carbides, the binder metal and sometimes carbon black. A polymeric binder is added to obtain a more stable body after pressing. All ingredients are mixed in ball mills with alcohol (or another solvent) to facilitate the homogenization of the powders. The grain size of the carbides is reduced during milling to 1–3 μm, that of the cobalt even down to nanometer size. The alcohol is removed during spray drying, when the powder forms granules. The obtained powder mixture is pressed to the desired shape, the so-called green body. The porous green bodies are placed on graphite plates and sintered in special furnaces with a well-defined temperature-time program in order to achieve full densification. The sintering atmosphere and pressure is changed during the sintering process, a flow of gases like N_2 or CO, for example, can prevent from denitrification or decarburisation.

A typical sintering cycle is shown in Fig. 2.1. The first part of the sintering is a slow heating with several dwells, where the polymeric binder is removed and the outgassing of adsorbed gases and gaseous reduction products takes place, while the material still presents open porosity. Solid state sintering occurs below the eutectic temperature. Some amount of the hard phase is dissolved in the still solid binder, new phases may be formed and material transport through surface and bulk diffusion leads to decreasing porosity. The next sintering stage, the liquid phase sintering, starts when the temperature raises above the ceramic-metal eutectic melting point. An extensive dissolution-precipitation process takes place, where bigger grains grow on expense of small ones. The grain growth continues even during the final solid state sintering until the temperature becomes too low and the structure is frozen in. The sintering time at high temperature must be long enough to reach full densification of the structure, but it should be as short as possible to limit grain growth, which is detrimental for the mechanical properties.

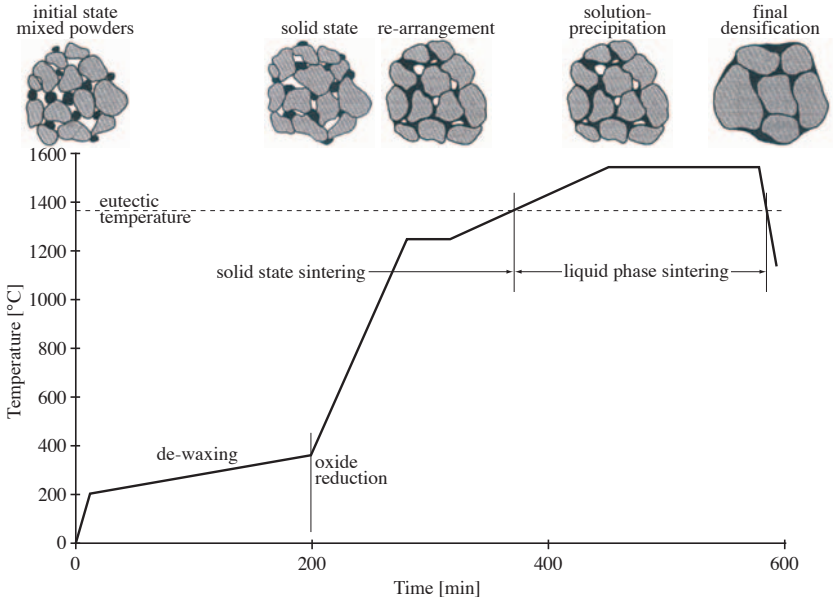

Figure 2.1: General sintering cycle showing the important sintering stages and the corresponding changes in the microstructure (adopted from [4] and [5])

1.3 Structure and microstructure

Hardmetals used for the production of cutting tools consist of a majority of ceramic hard phase and a small amount of metallic binder. A typical structure of a cemented carbide and a cermet, each with 10 vol.% cobalt binder, is shown in Fig. 2.2. Depending on the volume fraction (usually 80 vol.% or higher), the hard phase forms a continuous structure throughout the sample, called the ceramic skeleton. For lower volume fractions, the hard phase is present in form of single grains or clusters of grains entirely surrounded by the metal phase, which leads to mechanical properties dominated by the metal phase. In general, also the binder phase forms a continuous network structure. Only for very small fractions of metal, isolated cobalt pools may be present at triple points. A schematic representation of the two interconnected phases is shown in Fig. 2.3. The degree of connectivity is quantitatively described by the contiguity, the ratio of the length of hard phase grain boundaries and the total length of all grain boundaries. The microstructure of the different phases and of the grain boundaries is described below.

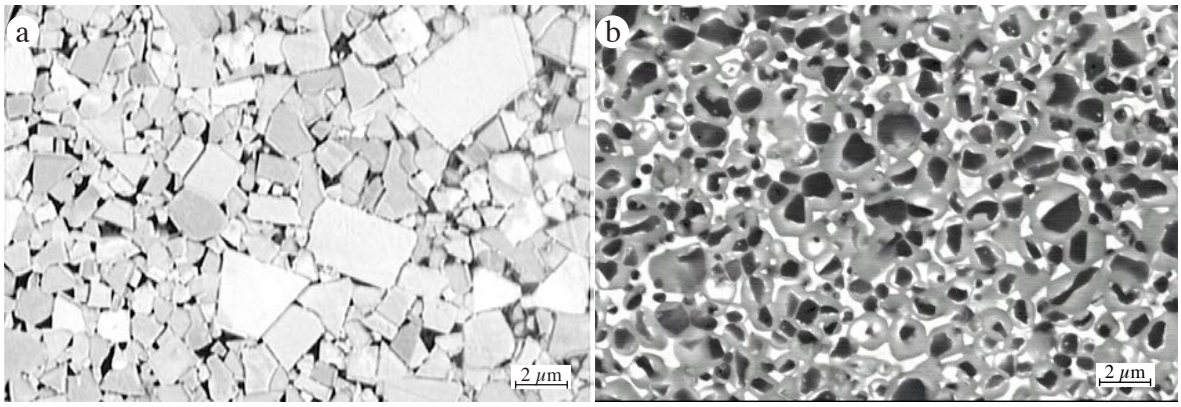

Figure 2.2: SEM micrographs using back-scattered electrons of a) cemented carbide and b) cermet, each with 10 vol.% cobalt binder. The cobalt appears dark in WC-Co and light in TiCN-Co.

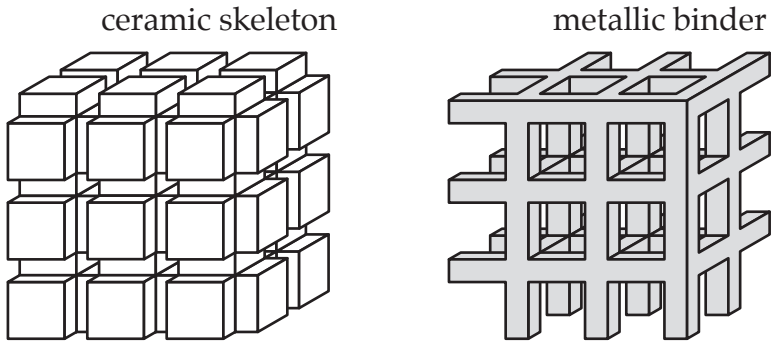

Figure 2.3: Cermets and cemented carbides are formed of a main ceramic phase bond by a metal binder. Both metal and ceramic phase form continuous interpenetrated skeletons.

1.3.1 Cobalt binder phase

Cobalt is, since its introduction as binder metal of WC by Schröter in 1922 [6], the traditional and most widely used binder metal in the cutting tool industry. Some attempts have been made to find alternatives [7,8], but even if nickel was quite successfully applied as binder for cubic carbides, it is rather an interesting variation for niche applications than an equivalent substitute for cobalt. All materials studied in this work have a cobalt binder.

Pure cobalt is hexagonal at room temperature and undergoes a first order phase transition from close packed hexagonal to face centered cubic at 690 K. However, in hard materials, cobalt is generally present in its high-temperature fcc configuration. Whether the fcc structure is stabilized by the presence of tungsten and carbon atoms or by the internal stresses resulting from the differential thermal contraction of hard phase and binder during cooling, has been an unsolved question for decades [9]. The tendency of cobalt to be hexagonal at low temperature is manifested by the presence of many stacking faults in the structure [10].

The binder is the transport medium for the hard phase atoms during solid and liquid phase sintering. It forms from the liquid during the solidification process. It is well-known that the grain size of the cobalt can reach up to 1 mm, so that one single cobalt grain builds the matrix for many micron-size hard phase grains. An important parameter for the mechanical properties is therefore the mean free path of the binder, which is the average distance between two Co/carbide interfaces within the binder [9]. This parameter constitutes the maximum free path for dislocations and it is therefore related to the hardness of the binder. However, hardening also occurs by the solid solution of tungsten in the cobalt phase [4]. WC dissolves into the liquid binder during the sintering and W and C re-precipitate in equal amounts. As carbon may be lost during the sintering process, additional carbon black is added to the raw powders and the total carbon content in the material can be controlled. This influences the amount of tungsten that remains in the binder, which influences the hardness and toughness of the binder. In contrast, the amount of soluted titanium and tantalum in cobalt is very small.

1.3.2 WC hard phase

WC is a very stable and absolutely stoichiometric phase. The crystal structure of WC is simple hexagonal with one tungsten and one carbon atom per unit cell and an a/c ratio very close to unity. However, the equilibrium shape of the crystals (Fig. 2.4), established only with high binder content and a sufficient carbon activity, is that of a triangular prism [11,12]. In fact, the preferential growth of three of the six prismatic WC $\{10\bar{1}0\}$ planes has been already observed

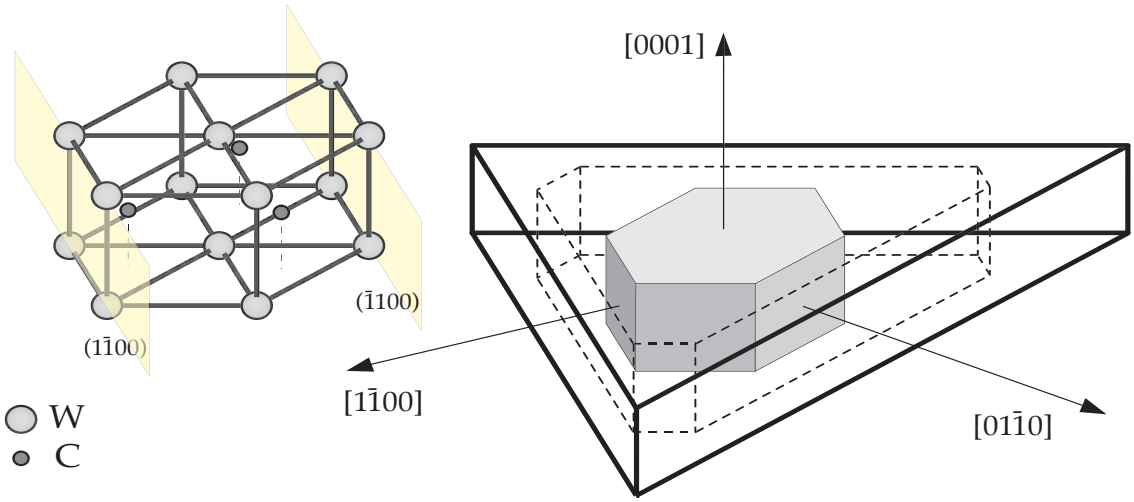

Figure 2.4: The hexagonal WC cell and the WC grain shape resulting from preferential growth along one type of prismatic planes.

by [3] and explained by the difference in lattice spacings of tungsten and carbon planes in these directions (Fig. 2.4). Recent studies showed that this preferential growth is reversely dependent on the carbon content [11]. The equilibrium triangular shape of the prism becomes therefore truncated with decreasing carbon content. On the other hand, ab initio calculations of the Co/WC interface energies of the prismatic WC$\{10\bar{1}0\}$ surfaces show an increasing anisotropy between the two types of surfaces with increasing carbon potential [12]. However, in common WC-Co grades (Fig. 2.2a), the equilibrium shape is usually not fully developed because of impingement with other grains [9]. Moreover, unusually large grains of a more rectangular shape are often found in the structure. This so-called discontinuous grain growth has been related with dissolution-reprecipitation, coalescence and recarburisation of eta carbide [9]. Still, a satisfactory explanation for this undesired phenomenon has not been given. In [12], two populations of grains are found, which supports the solution-precipitation idea, where larger grains grow on the expense of small ones. But it is also reported that the large grains are mostly found close to eta phase.

The development of the WC-Co structure is influenced by the carbon content, or better, by the carbon activity during sintering. However, it should be remarked that the amount of carbon necessary to form WC has to be rather precise, as can be seen in the phase diagram of WC in Fig. 2.5 and especailly for the composition used in this work in a section of the ternary W-C-Co phase diagram in Fig. 2.6. Too little carbon leads to the formation of eta phase and too much carbon leads to the presence of graphite. Both, graphite and eta phase, are detrimental for the mechanical properties of WC-Co.

1.3.3 TiCN hard phase

The typical cermet hard phase always contains titanium, carbon and nitrogen forming titanium carbonitride (TiCN). The TiCN crystal has an fcc structure, where the titanium atoms occupy one fcc sublattice and carbon and nitrogen occupy another fcc sublattice. Contrary to WC, the TiCN is always slightly substoichiometric in carbon and nitrogen. Often, other carbides are added in order to control the grain growth or modify the mechanical or thermal properties. The carbonitride grains of general cermets show a core-rim structure, as seen in Fig. 2.2b. Its development during sintering has been investigated quite extensively and can be summarized as follows.

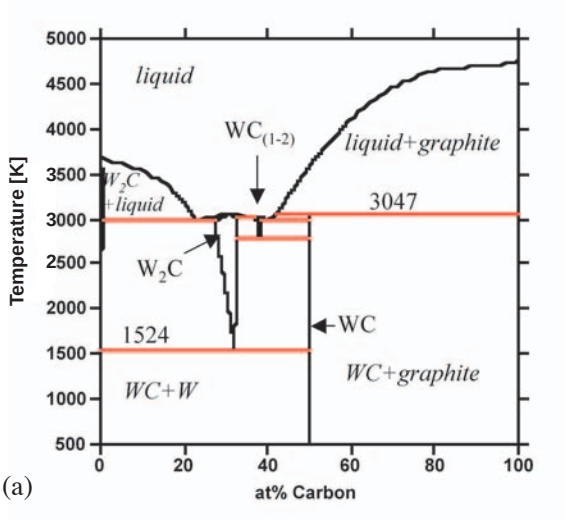

Figure 2.5: W-C binary phase diagram calculated from [13] using the Thermo-Calc software [14] (courtesy of Susanne Norgren, AB Sandvik Coromant)

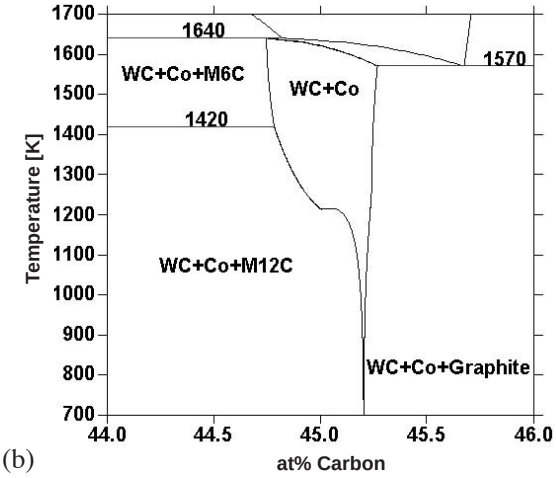

Figure 2.6: WC-Co ternary phase diagram for 6 wt.% Co calculated from [15] using the Thermo-Calc software [14] (courtesy of Susanne Norgren, AB Sandvik Coromant)

Heavy atom carbides such as Mo_2C or WC already dissolve into the binder before it becomes liquid, i.e. during solid state sintering [4,16]. Both, heavy atoms and carbon, move inside the binder and precipitate on the undissolved TiCN particles (the cores) forming the inner rim. This inner rim is usually irregularly distributed, which is related to a lack of nucleation sites on the cores [16]. The TiCN further dissolves during liquid state sintering, in particular TiN, until the saturation of the binder is reached. The outer rim forms entirely during the liquid sintering stage and continues to grow during cooling by precipitation from the binder and further dissolution of smaller carbonitride grains. The outer rim composition is that of a mixed carbonitride with mainly titanium and a smaller amount of heavy atoms. The system reaches equilibrium of carbon and nitrogen, because these elements diffuse during the sintering process. On the other hand, the metal atoms hardly move and they are therefore far from thermodynamic equilibrium. Cobalt as a binder usually contains tungsten and molybdenum (if present in the material), but only very limited amounts of titanium and tantalum and no carbon or nitrogen. The composition of the binder is determined by the freezing temperature. As in WC-Co, the content of heavy atoms and therefore possible solution hardening of the binder can be controlled by the carbon activity during sintering [4].

The cermet in this work has been designed to have a cobalt binder, which matches in composition that of the WC-Co with the same binder volume fraction at sintering temperature. Therefore, it has a higher total carbon content than usual cermet grades in order to reach the same level of soluted tungsten.

Opposite to tungsten carbide, the titanium carbonitride grains are generally more rounded in shape. This is often observed for substoichiometric cubic carbides and TiC is particularly sensitive to stoichiometry. TaC grains, for example, often have a cubic shape, but they also become more rounded for substoichiometric compositions [3].

1.3.4 Grain boundaries and interfaces

Cemented carbides and cermets that consist of a single hard phase present basically three types of interfaces: grain boundaries between hard phase grains, grain boundaries between binder grains and interfaces between hard phase and binder.

In the binder phase of hardmetals, where one cobalt grain envelopes many hard phase grains, the role of the mean free path (or better the mean free intercept [3]) of the binder is much more important for the mechanical properties than the cobalt grain size. Therefore, the Co/Co grain boundaries have only little influence on the overall mechanical properties.

The relative amount of Co/hard phase grain boundaries and hard phase/hard phase grain boundaries is described by the contiguity. An important difference in contiguity between cemented carbides and cermets has been pointed out by Exner [3]. The contiguity in cubic carbides depends linearly on the dihedral angle between cobalt and the cubic grains. Therefore, it depends on the type of carbide, on the amount of binder phase and the size of the carbide grains. Instead, in WC-Co, the contiguity does not fit this scheme. It is independent of crystal size or binder content, so that all WC-Co alloys show a similar microstructure. Exner concludes that the contiguity in WC-Co is, in contrast to cubic carbide hardmetals, governed by geometrical conditions rather than by interfacial energy equilibrium. This is related to the fact that the wetting angle between WC and cobalt, and thus the dihedral angle, is practically 0°.

The strength of Co/WC, Co/TiC and Co/TiN interfaces has been studied by ab initio calculations [17,18]. It is shown that strong covalent bonds between cobalt atoms and the carbon or nitrogen atoms of the hard phase are formed at all three interfaces. The strength of these bonds is even higher than the metal/C bonds in the bulk and leads to a strong adhesion of the two phases. Moreover, strong metallic bonds are created between cobalt and tungsten. This gives additional strength to the Co/WC interface and explains the better wetting of cobalt on WC surfaces.

The largest proportion of WC/WC grain boundaries are perfectly straight. Faceted grain boundaries are often found between larger grains and curved and irregular grain boundaries are rare. Still, it seems that longer sintering or annealing times and even the cobalt volume fraction do not influence the occurrence of different types of interfaces [3]. The interlocking of grains may prevent them from preferred arrangement during sintering, so that interfaces are formed where they meet during crystal growth [19]. The orientation relation of neighboring grains can be described by the coincidence site lattice (CSL). The lattices of two grains that meet are virtually extended through the three-dimensional space. The CSL is then formed by the points in space, where atoms of both lattices meet. The value Σ is defined as the ratio of the volume of a unit cell of the CSL to the volume of a unit cell of one of the lattices of the neighboring grains. This concept has been used to study WC/WC grain boundaries. The $\Sigma 2$ 90° twist boundary has been found to be particularly strong. It is probably already present after powder production and does not break during sintering nor during high-temperature deformation [12]. The $\Sigma 2$ 90° asymmetric tilt boundary is less strong, but intergranular segregation of cobalt in submonolayer quantities is shown to enhance the cohesion of this grain boundary and to prevent further cobalt infiltration [20]. Kim and Rohrer analyzed ca. 15600 WC/WC grain boundaries, showing that three types of grain boundaries appear more frequently than others, i.e. the 90° $[10\bar{1}0]$ twist boundary, the 30° [0001] twist boundary and the 30° [0001] asymmetric tilt boundary [21]. They consider structural rearrangements to establish these preferred boundaries as improbable because of the high constraints by the surrounding grains, and relate the occurrence of these grain boundaries to a special stability against wetting by cobalt.

The TiCN/TiCN grain boundaries are less well studied. The rounded grains form general grain boundaries where they meet during sintering. The presence of cobalt in segregated form or as a layer is reported quite frequently [10].

2 Mechanical properties

The separation of the deformation behavior of WC-Co into different temperature domains dates back to 1977 [22]. This description has been revived in the beginning of the ‘90s [6], in the following years it was more and more refined and also applied to cermet materials with cobalt binder [10,23-28]. A representation of these temperature domains for hardmetals with cobalt binder is given in Fig. 2.7. In the first domain, up to temperatures between 800 and 900 K, the materials deform elastically and show brittle fracture. The second domain is characterized by the plastic deformation of the binder (IIa) and the carbonitride grains (IIb). Even if dislocations have been observed in WC grains, no considerable plastic deformation of WC grains has been found. Domain III is characterized by extended creep at temperatures above 1200 - 1300 K and has been attributed to grain boundary sliding. There is a noticeable difference in transition temperatures between the domains describing the behavior of WC-Co and TiCN-Co. The transition temperatures furthermore depend on the cobalt content. With increasing cobalt content the transition between the different domains is shifted towards lower temperatures. Fig. 2.8 presents an example of deformation tests of a cermet at different temperature, showing the behavior in the different domains.

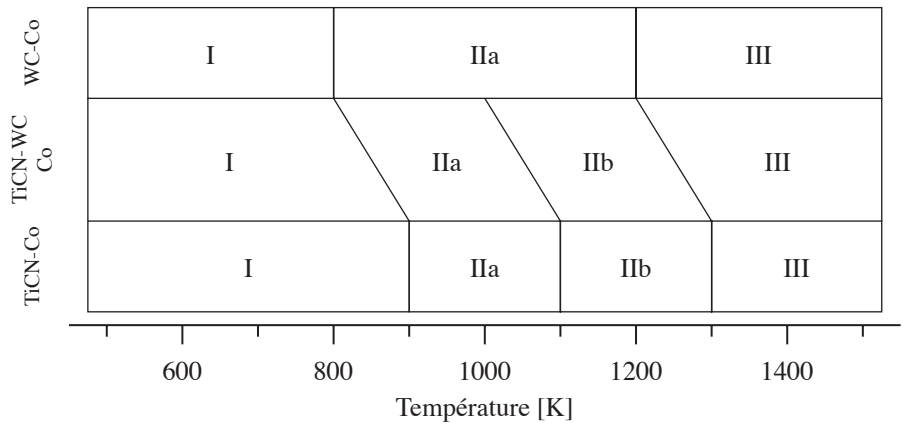

Figure 2.7: Three temperature domains characterize the deformation behavior of cemented carbides and cermets with cobalt binder. I - brittle, II - plastic deformation of the bulk (a - binder, b - hard phase) and III - grain boundary sliding [25]

2.1 Domain I

The mechanical properties in domain I are dominated by the cobalt binder. The cobalt is very brittle. Dislocations that are present are entirely blocked by a dense network of stacking faults, high tensile stresses are present in the binder and soluted atoms like tungsten lead to additional hardening. Fracture can occur, starting at WC/WC grain boundaries, then the crack travels through the binder and grain boundaries by so-called multi-ligament cracking [29-31]. The cobalt forming the ligaments is free from constraints, it can deform and is responsible for the toughness of the material in this state. A certain toughness may also result from the absorption

of the energy of propagating cracks by local fcc to hcp phase transformation, i.e. the formation of stacking faults.

2.2 Domain II

The domain II is characterized by a limited plasticity, i.e. deformation in the bulk of the binder (IIa) and/or hard phase (IIb) by dislocation movement.

This domain has first been characterized in WC-Co by Ammann and Mari [6,32]. The region from 900 to 1100 K between brittle behavior and creep shows some plasticity in three-point bending. Together with the microscopic observation of the microstructure, the observed deformation is explained by dislocation movement in cobalt. Dislocations become mobile at these temperatures because the number of stacking faults decreases. The plasticity remains limited because of the rigid ceramic skeleton. No deformation of the WC grains is reported by these authors and therefore the deformation in domain II is entirely related to the deformation of the cobalt phase [6,32].

However, dislocations in WC are observed sometimes. Upon heavy compression, the dislocation density in the WC phase of WC-Co increases and a dislocation deformation mechanism is reported [33]. Also the analysis of WC grain boundary orientation after deformation by heavy turning studied by electron backscattered diffraction (EBSD) shows that dislocations are created and that they are mobile. The dislocations pile up at grain boundaries, which creates lattice distortions and makes the indexing by EBSD impossible [12]. The authors also show that special grain boundaries such as Σ2 are easily indexed. The explanation is that dislocations may travel through Σ2 grain boundaries because of their high symmetry.

In cermet materials, deformation of the cobalt (IIa) as well as deformation of the hard phase (IIb) is observed [10,25]. The deformation is however quite limited and plastic deformation tests in this temperature domain show a rather high fracture stress and small deformation at fracture (Fig. 2.8) [26,28]. As in WC-Co, the deformation of the cobalt starts, when stacking faults disappear. The deformation of the cobalt transfers stresses onto the TiCN grains that are then accommodated by dislocation motion, involving plastic deformation of the hard phase.

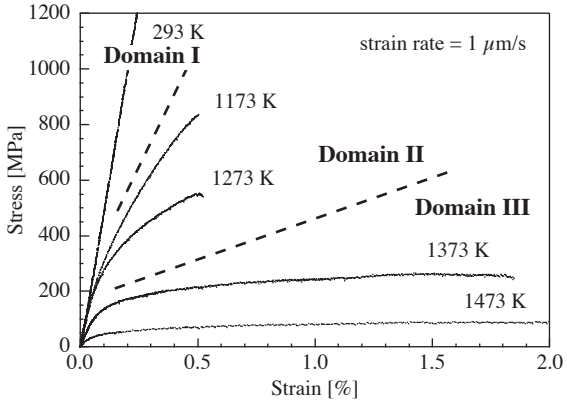

Figure 2.8: Stress-strain curves of cermet with 18 vol.% Co showing the different domains [23]

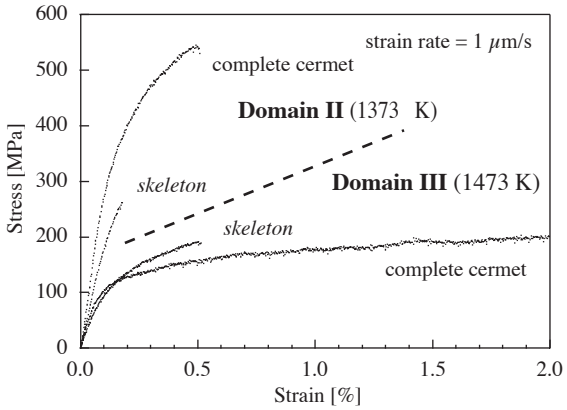

Figure 2.9: Transition between domains II and III shown by the comparison of complete and skeleton samples [23]

2.3 Domain III

The high temperature domain is marked by low flow stresses and high deformation at fracture in macroscopic bending tests of cemented carbides and cermets [10,23-28,34]. Grain-boundary sliding is proposed as the main deformation mechanism. This is supported not only by the low flow stresses and high strain rates, and by high strain before fracture, but also by a decrease of the flow stress (or yield stress [27]) with decreasing grain size [28]. Creep activation energies measured at different temperatures show a transition between a high activation energy level at high temperatures (creep) to a lower level at low temperatures (bulk deformation) in WC-Co and cermets [6,10,25,28].

The strong influence of the presence of cobalt on the high temperature deformation is shown by comparative deformation tests on hardmetals and their extracted ceramic skeleton. Skeleton samples are produced by removing the cobalt by chemical etching. The stress-strain curves of these skeletons show lower apparent flow stresses than the complete material in domain II, but the skeletons are more deformation resistant than the complete hardmetals in domain III (Fig. 2.9) [23,24,28,35].

A strong dependence of the deformation on the applied stress is furthermore observed [10,24,25,28]. It is shown that cermets with a higher cobalt content are more deformation resistant during creep at 1473 K when a low stress is applied. Moreover, high cobalt cermets are less deformation resistant when a high stress is applied (Fig. 2.10). This observation is not yet sufficiently explained. It may be due to internal stresses that are overcome at a certain threshold stress [10] or a change in the grain-boundary sliding controlling mechanism (dislocation glide and climb versus diffusion) [25]. A dependence of applied stress and strain-rate on the deformation mechanism is also observed by compression of WC-Co [33,36]. Three different regions are observed in the high temperature domain related with different strain rate sensitivities (Fig. 2.11) and different activation energies: I) diffusional flow of WC or a solution-precipitation process accompanying interface reaction at low stress and strain-rate, II) grain boundary sliding at medium stresses and strain-rates and III) dislocation climb in WC at high stresses

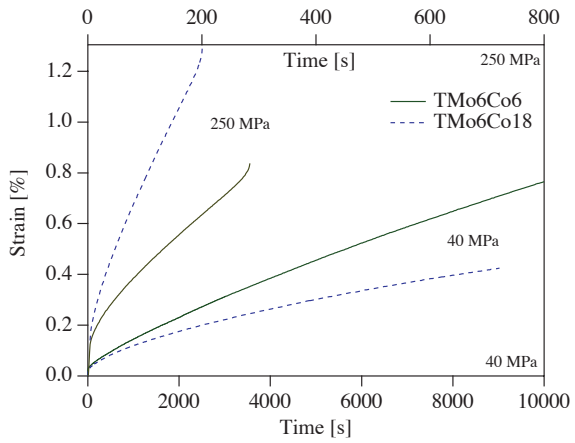

Figure 2.10: Creep curves of cermet at 1473 K at different stress levels and with different Co content [24]

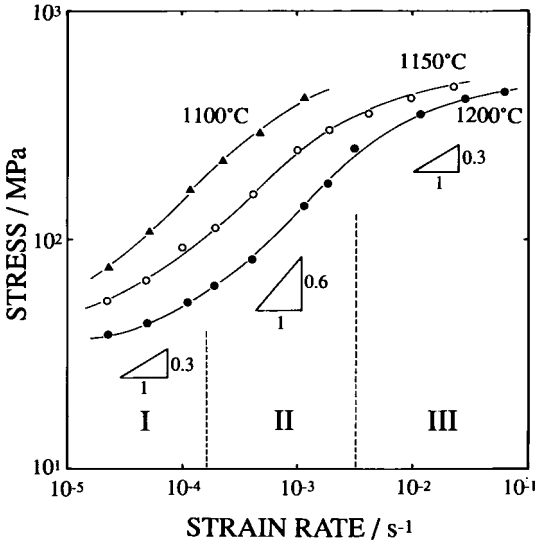

Figure 2.11: Log-log plot of 30% flow stress vs. strain rate showing three deformation regions in WC-Co [33]

and strain-rates. (Notice that these regions I to III are not related to the temperature domain I, II and III defined in this paragraph.)

Observations by microscopy techniques support the idea that grain boundary sliding is the main high temperature deformation mechanism. WC grains appear undeformable, even if dislocations are observed inside the grains and an increase of their number is observed after heavy deformation [33]. WC grains are shown to re-arrange and rotate during large high temperature compression of WC-Co [33,36,37]. Decohesion and lateral displacement of WC grains has been shown by grid markers [38] deposited on the polished surface of a WC-Co sample.

TiCN grains show some bulk deformation, but this bulk deformation cannot account for all the plastic deformation of cermets at high temperature so that grain boundary sliding is assumed to play the major role [28]. Grain boundary infiltration and TiCN grain decohesion after deformation has been observed [10,23,25,28].

A large number of publications propose grain boundary sliding with infiltration of cobalt as high-temperature deformation mechanism for cobalt hardmetals. However, clear proofs by microscopy are rare. Cobalt is often found between hard phase grains, sometimes as nanometer thick layers, sometimes in sub-monolayer quantities. However, grain boundaries often appear clean, even if clear signs of sliding are observed, as for example by the grid technique [38]. This may be related with a wetting/de-wetting process, i.e. the cobalt enters and leaves the grain boundaries depending on temperature and stress. As microscopy is mostly done at room temperature, no signs of cobalt infiltration are observed, even if cobalt layers may have been present during high temperature deformation.

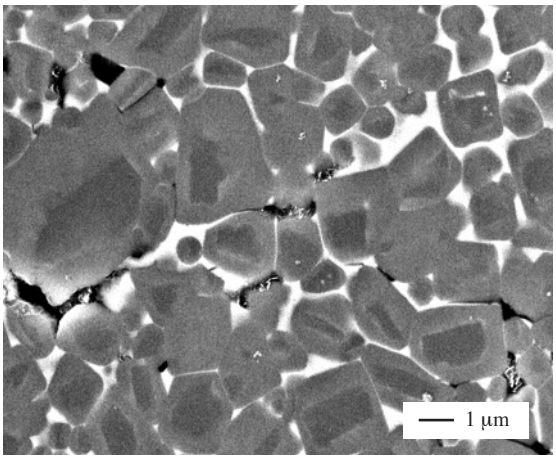

Figure 2.12: Decohesion of TiCN grains of a TiCN-3vol.%Mo2C-6vol.%Co after 2.2% deformation by three-point bending at 1473 K [28]

3 Internal friction in hardmetals

The clear separation of domains by macroscopic deformation techniques is in fact rather difficult. In the early 90's, [6,32,39], mechanical spectroscopy was used to link macroscopic deformation behavior and microscopic observation. Mechanical spectroscopy is a method to measure the damping (energy dissipation) inside a material due to the movement of structural

defects as a function of temperature or frequency. The anelastic movement of defects, for example dislocations, gives rise to characteristic internal friction peaks. Qualitatively one could say, that at temperatures below the peak (or frequencies above the peak) the defect cannot move, at the peak the defect moves reversibly around its equilibrium like a swinging chord, and at temperatures higher (or frequencies lower) than the peak maximum the defect moves in phase with the applied stress. Therefore, internal friction is a useful complementary tool to study deformation mechanisms. Moreover the activation energy related with a relaxation process can be assessed.

Cemented carbides and cermets have been studied with this technique [6,10,23-26,32,40-45]. Typical internal friction versus temperature spectra for a cemented carbide and a cermet are shown in Fig. 2.13 and Fig. 2.14. The interpretation of significant features is found below.

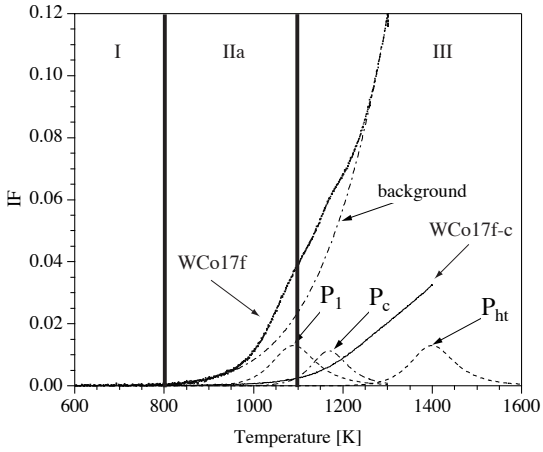

Figure 2.13: IF vs. temperature spectrum of WC-17vol%Co with spectrum deconvolution into background and three peaks and the indication of the temperature domains [24]

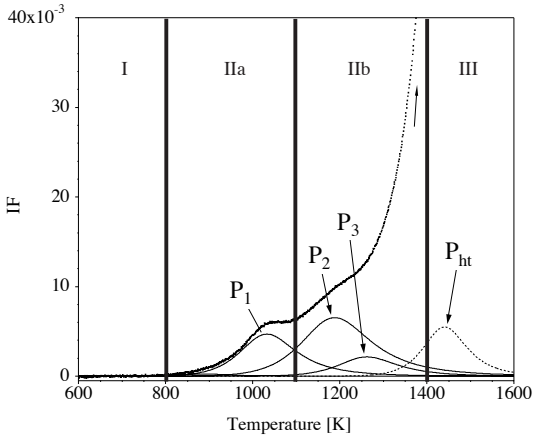

Figure 2.14: IF vs. temperature spectrum of TiCN-Mo-Co with spectrum deconvolution into background and four peaks and the indication of the temperature domains [24]

3.1 Domain I

Up to 800 K, the internal friction is very low, showing that at the low stress level of internal friction measurements defects dissipate little energy. This is characteristic for a brittle behavior. From 800 K on, internal friction slowly increases, giving rise to a first peak P_1. Therefore, a brittle to ductile transition can be assumed around this temperature.

3.2 Domain IIa

The domain IIa is related with IF peak P_1, which is found in nearly all hardmetals. However, peak P_1 is not observed in ceramic skeleton samples, where the cobalt has been removed, which means that the mechanism is located in the cobalt phase [24].

In WC-Co, the reduction of stacking faults by movement of partial dislocations has been observed in the temperature range of P_1 [40]. The activation energy of this peak measured in WC-Co corresponds well with the diffusion coefficient of tungsten in cobalt (2.5 eV). The peak has therefore been related to the movement of partial dislocations in cobalt controlled by the diffusion of tungsten atoms that are dragged by the dislocation [40].

In-situ observations of the microstructure of cermets has shown that partial dislocations become mobile in this temperature range [10]. In cermets, the temperature of the peak is higher, but the activation energy of this peak is much lower (1.6 eV) and does not correspond well with the diffusion coefficients of soluted atoms like molybdenum or titanium [10,24,25]. Nonetheless, the peak has been related with the movement of partial dislocations controlled by diffusion of soluted atoms. Pipe-diffusion might occur, which should account for lower activation energies [10].

3.3 Domain IIb

Domain IIb is related with the deformation of the hard phase and exists only in cermets, because deformation of the WC grains is only observed upon heavy deformation (high stresses).

In cermets, when the temperature is raised above the cobalt peak (P_1), the dislocations in the cobalt move freely and the cobalt deforms plastically. The stresses are then transferred to the hard phase, where dislocations start to move. Effectively, two internal friction peaks, P_2-P_3, are present in this domain (Fig. 2.14), which have been related to the movement of dislocations in the carbonitride grains by a Peierls mechanism [25]. The threshold stress necessary for the dislocations to overcome Peierls barriers is locally given by internal stresses.

The peak P_c, shown in WC-Co in Fig. 2.13, is not a relaxation peak as it is not present in frequency spectra. The peak has been found to be related with the magnetic transition of cobalt. Upon high-temperature annealing or thermal cycling the peak decreases and finally disappears. In fact, ferromagnetism in cobalt decreases with increasing solutes concentration and therefore the peak disappears after some time at high temperature, when more atoms get dissolved in the cobalt. The peak is not clearly seen in the cermet, probably because it is superimposed to P_2-P_3.

3.4 Domain III

The internal friction measured in domain III shows a steep increase accompanied by a strong decrease of the modulus. The cemented carbides show a much higher IF than cermets and the steep increase of IF is found at lower temperature. This behavior compares well with macroscopic observations by bending tests, where, at the same temperature, cemented carbides appear much more plastic than cermets.

An internal friction peak, P_{ht}, is found in cermets as well as in WC-Co between 1400 and 1480 K at 1 Hz [10,24,25]. This peak has not been studied extensively, but it occurs in the temperature range, where grain boundary sliding is observed. It is therefore attributed to the sliding of WC or TiCN grains. The activation energy of this peak, above 4 eV, corresponds to the high, apparent values that are measured in creep experiments. Its attempt frequency is much higher than the theoretical limit, the Debye frequency of about 10^{13} Hz. Moreover, the peak is much larger than a normal Debye peak. The measured activation energy of the peak in cermets increases with increasing cobalt content [10]. P_{ht} appears at lower temperature with increasing WC character of the hard phase [25].

The peak P_{ht} is also found in hard phase skeleton samples. Here, the measured activation energy for P_{ht} is found between 2.3 and 3.8 eV [25].

4 Characteristic parameters influencing the mechanical properties at high temperatures

4.1 Grain size

The influence of the grain size on the deformation resistance follows a Hall-Petch relation at low temperatures, i.e. the yield stress is inversely proportional to the square root of the grain size [28]. At high temperature, finer-grained materials show a lower resistance to deformation than coarse grained materials. This effect is well known in superplastic fine-grained ceramics, where the deformation occurs as grain boundary sliding of the undeformable grains.

According to Mari et al. [44], the transition temperature between domain II and domain III in WC-Co with micron-size WC is around 1100 K. Other authors report the transition to the grain boundary sliding domain at 1273 K for micron-size WC-Co and at 1073 K for WC-Co with submicron grain size [27]. An increase of the high temperature internal friction background (sign of microcreep) with decreasing WC grain size is reported by Ammann [32].

The dependence of creep rate on grain size in WC-Co is opposite between high stress (or relatively low temperature < 900°C) and low stress (or high temperature) [33,46]. At high stress levels, the creep rate increases with increasing grain size, and at low stress levels, the creep rate decreases with increasing grain size. These observations indicate that two different mechanisms are rate controlling during the deformation of WC-Co [46].

In cermets, the effect of grain size is less clear [10]. Macroscopic deformation by three-point bending at 1473 K shows lower deformation resistance with smaller grain size. In internal friction measurements, the background is much higher with larger carbonitride grain size, which is contrary to what one may expect. Here, obviously the stress applied during the experiment plays an important role.

4.2 Role of cobalt

The role played by cobalt in plastic deformation is proven for all hardmetals by a comparison of the deformation curves of the composite materials with their hard-phase skeletons, which are obtained by selective, chemical etching of the cobalt (Fig. 2.9). At low temperatures, the apparent flow-stress of cobalt-free samples is lower, because of their smaller cross section, but above a certain critical temperature the skeletons become (despite their lower cross-section) more resistant to deformation than the composite materials. This can only be interpreted by a mechanism where cobalt enhances the deformation of the carbide skeleton as for example by wetting the hard phase grain boundaries [6,10,23-25]. This behavior has never been observed in hard materials with nickel binder [10].

The question whether the deformation in domain III could simply be attributed to the deformation of the cobalt binder has been answered by investigating the effect of solution hardening of the binder on high-temperature deformation of WC-Co [6]. If the cobalt deformation would control the deformation at high temperature, then the hardening of the binder should have an influence. A strong dependence of the deformation on solutes has been shown at low temperature, where the deformation of the cobalt is predominant. Instead at high temperatures, the amount of soluted atoms in the binder does not affect the deformation behavior [6].

The volume fraction of the cobalt binder is also shown to influence the deformation resistance. A decrease of the flow stress with increasing cobalt content is observed in WC-Co by three-point bending [6]. Bending tests and hardness measurements in WC-Co show increasing plasticity with increasing cobalt content [27].

In cermets as well, the flow stress measured in stress-strain curves is lowered by an increase of cobalt content [10,25,28]. However, creep tests show that the effect of the cobalt content changes with the applied stress (Fig. 2.10). Under high stress, an increase of cobalt content leads to an increase of strain rate, while at low applied stress, an increase of cobalt content leads to lower strain rates [24]. The internal friction background (microcreep) increases with decreasing cobalt content [10]. So, logically, the effect of cobalt content on internal friction is in agreement with the effect on creep at low stress.

It should be noted here that the cobalt fraction does not only change the amounts of soft and hard phase of the composite, but that it also influences the internal stress state of the phases. Residual stresses are always present in these materials, because of the different thermal expansion of the constituents. The cobalt is generally under tension, while the hard phase is in compression [47-49]. With increasing cobalt content, the residual stresses in the cobalt decrease, whereas the hard phase becomes even more compressive. Another aspect to keep in mind is that the stresses in both phases tend to cancel upon heating. No residual stresses should be present at the liquid sintering temperature.

4.3 Applied stress

As mentioned before, the stress plays an important role in the deformation process. The strain rates during compression creep experiments at constant temperature in WC-Co depend on the applied stress, represented by three different stages with different activation energies (Fig. 2.11) [33,36]. The low stress/low strain-rate region was related with diffusional flow of WC or a solution-precipitation process accompanying interface reactions, the intermediate region was related to grain boundary sliding and the high stress/high strain-rate region was attributed to dislocation climb [33].

A dependence of the high temperature creep on stress is also observed in three-point bending experiments. A decrease of the creep activation energy is found in WC-Co, when decreasing the temperature at constant applied load [24].

High stress and low stress modes have been also observed in cermets [10,24,25,28]. The transition between these modes has been explained in different ways. Feusier suggests that different internal stresses are present at different temperatures (internal stresses decrease upon heating), which have to be overcome [10]. Bolognini differentiates between different grain boundary sliding controlling mechanisms depending on the applied stress: at low stress, diffusion of tungsten in cobalt and at high stress, dislocation motion in cobalt, pile-up at triple points and dislocation climb [25].

4.4 Hard phase character

A study of TiCN-Co, WC-Co and mixed cermets with different WC/TiCN ratio shows that an increase of the WC content leads to a decrease of the deformation resistance at high temperature [25]. The outstanding wetting capability of cobalt on WC is an experimental fact and has recently been related with the stronger bonding of a Co/WC interface and its more metallic character compared with Co/TiCN (see 1.3.4).

4.5 Overview

A summary of the materials parameters and their influence on creep resistance and residual stresses is given in Fig. 2.15.

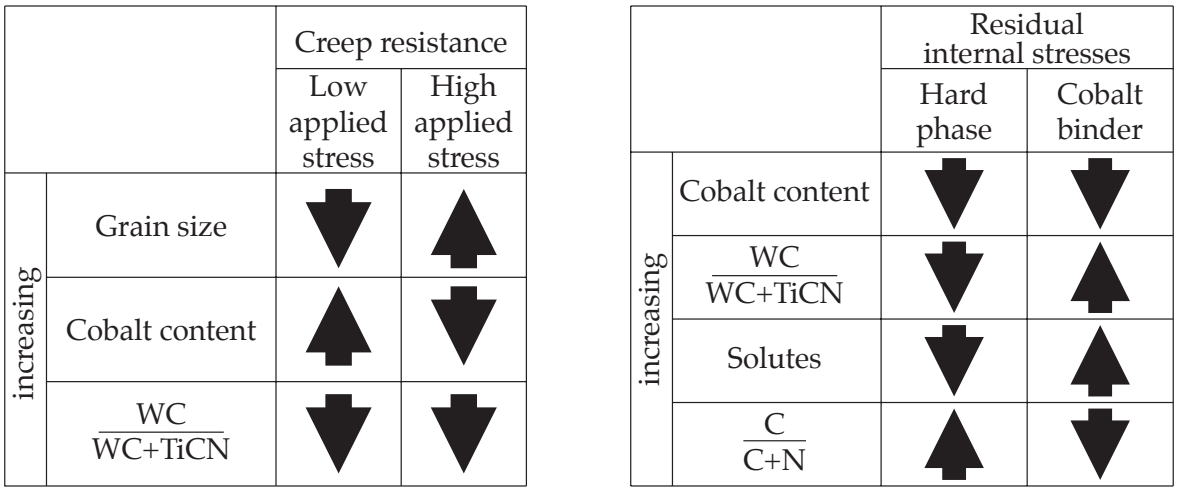

Figure 2.15: Schematic representation of the influence of different material parameters on creep resistance and residual stresses

5 Aim of the present work

The motivation of this work derives from the need of the cutting tool industry to improve their products in order to support harder and harder working conditions, namely increasing cutting speed and working on stronger modern materials. It is observed that, with increasing cutting speed, a limiting factor of tool life is the plastic deformation. This phenomenon occurs essentially because of the high temperature attained by the cutting tool tip. Many observations let us suppose that the mechanism controlling the high-temperature deformation of cemented carbides and cermets is grain boundary sliding of the hard phase. Fig. 2.16 for example, shows a cermet and a cemented carbide structure, taken at the tip of the cutting tool after heavy deformation. Layers of cobalt are found between hard phase grains, showing that deformation involves the infiltration of grain boundaries by cobalt. However, no detailed description of the grain boundary sliding mechanism in hardmetals has been given so far.

The aim of this work is to investigate the mechanical properties of tool materials at relatively high temperature i.e. as high and over 1000°C. We will base our study on two model hardmetals, WC-Co and TiCN-Co with the same amount and composition of the cobalt binder.

Combining macroscopic deformation testing by three-point bending, with microscopical observation and mechanical spectroscopy has proven to be a powerful strategy to investigate the fundamental mechanisms of materials deformation. This strategy will be used in this work with an additional analysis of residual stresses, which should play a fundamental role in the deformation mechanisms.

The high-temperature deformation of the base materials will be studied, especially pointing out the similarities and the differences in the deformation behavior.

Our attention will be focussed on grain boundary sliding as the controlling mechanisms for high temperature deformation. The arguments supporting this hypothesis will consider not

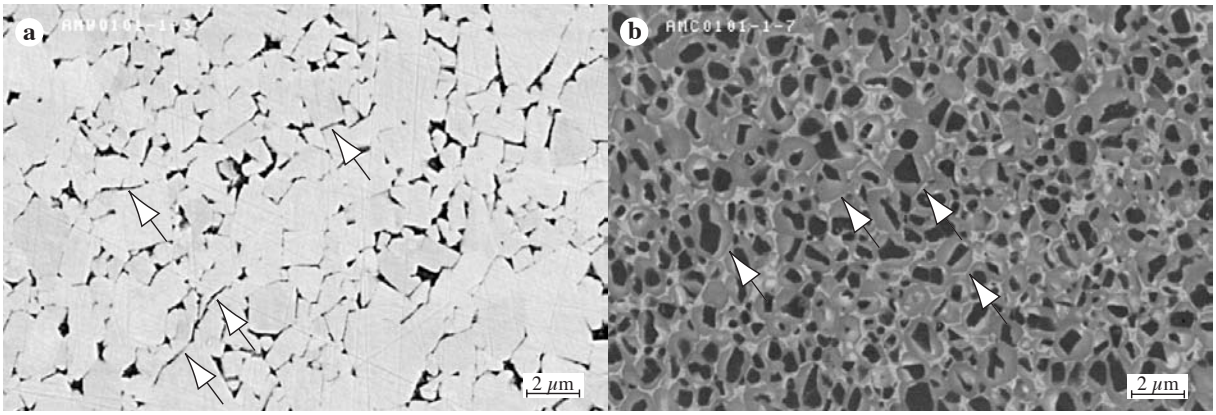

Figure 2.16: Structure of (a) cemented carbide and (b) cermet each with 10 vol.% cobalt binder. Images show regions close to the cutting edge after deformation by turning. Arrows indicate broken hard phase grain boundaries with cobalt layers. (images taken by G. Östberg, Chalmers University, Göteborg, Sweden)

only mechanical properties (microscopic or macroscopic), but also microscopical observations and theoretical simulations of the interfaces present in the investigated materials.

The mechanical spectroscopy will be used to locate in the different phases of the materials the mobility of defects such as dislocations and grain boundaries and to evidence the possible mechanisms of microplasticity. We need then to evaluate, if internal friction measurements are representative of high-temperature deformation.

Finally, some new technological solutions to improve the wear resistance of cutting tools will be investigated. In particular, on the basis of recent studies, the base materials are modified by the addition of tantalum. The influence of this element on the mechanical properties and on the carbide (or carbonitride) interfaces will be investigated.

Chapter 3

Materials and experimental techniques

1 Materials

The materials that have been chosen for this study are not industrial grades, but they are designed for the study of fundamental aspects. A very simple member of each of the families, cermets and cemented carbides, with the same volume fractions of hard phase and binder, similar grain size and similar binder composition are the base of this work. These materials were manufactured at AB Sandvik Coromant, Stockholm, Sweden.

The chemical composition of the two base materials after sintering are summarized in Table 3.1. It should be noted that the cobalt binder in WC-Co contains substantial amounts of tungsten. In order to have a similar binder composition in both materials carbon has been (apart from WC) especially added to the cermet. Therefore, the denomination TiWCN-Co is used instead of TiCN-Co. The tungsten is entirely dissolved in binder and cermet hard phase, i.e. no separate WC grains are found in the structure. SEM pictures of the morphology of the two materials have been presented in Fig. 2.2.

Table 3.2 shows some of the materials properties. The density, porosity, hardness, magnetic saturation and coercivity are determined at AB Sandvik Coromant after sintering. The magnetic saturation is directly proportional to the purity of the cobalt. The amount of soluted tungsten atoms in the binder can be determined empirically. The coercivity H_c is empirically related with the WC grain size d_{WC}. However, the grain size is determined by the mean linear intercept method (by Gustaf Östberg, Chalmers Technical University, Göteborg, Sweden).

Table 3.1 : Materials compositions determined by chemical analysis after sintering

	Chemical composition in wt.%					Chemical composition in at.%				
Material	Co	W	C	Ti	N	Co	W	C	Ti	N
WC-Co	6.04	88.3	5.68			9.71	45.49	44.80		
TiWCN-Co	14.00	19.5	8.89	52.4	5.98	9.13	3.92	28.46	42.08	16.41

Table 3.2 : Basic properties

Material	density [g/cm^3]	grain size (MLI) [µm]	HV_3 hardness	magnetic saturation B_S [µTm^3/kg]	$c_{W,sol}$ (calc) [wt.%]	coercivity H_c [kAm^{-1}]
WC-Co	14.97	2.10	1493	5.1	9.80	13.12
TiWCN-Co	6.34	2.05	1594	11.63	10.67	13.96

2 Three-point bending

The deformation of the cutting edge of an insert is very complex in nature and the local temperature and stress distribution during the cutting process is still little investigated. It has been shown that three-point bending is well suited to achieve similar deformation features, as for example cobalt-infiltrated grain boundaries, as during real cutting [6,10,25]. The advantage is that the deformation is achieved under controlled conditions of temperature, applied stress and deformation rate. Despite the disadvantage of the non-uniformly applied stress, this method is preferred over uniaxial tensile or compression tests, where the high stresses that are needed to deform the hard materials are very demanding for the test rig.

The method, the experimental setup and the measurements are described in the following sections. Two types of measurements are performed. Stress-strain curves, i.e. the measurement of the stress needed to deform a specimen at constant strain rate at a given constant temperature, give insight into the type of deformation that the specimen undergoes. The activation energy of the different deformation mechanisms is measured by creep tests under constant load by the temperature jump method.

2.1 Method

The applied stress is not distributed uniformly along the length and height of the specimen. The maximum stress is obtained at the upper and lower surface that are in compression and tension, respectively. The absolute value of this stress maximum is according to the theory of the deflection of a bar [6]:

$$\sigma_{max,el.} = \frac{3Pl}{2bh^2} \tag{3.1}$$

The used dimensional variables correspond to those in Fig. 3.1 and P is the applied force. For small deformations, as in the case of the here studied hard materials, the deformation ε is proportional to the deflection d of the specimen. According to the elastic theory, the maximum deformation can be calculated by:

$$\varepsilon_{max,el.} = \frac{6dh}{l^2} \tag{3.2}$$

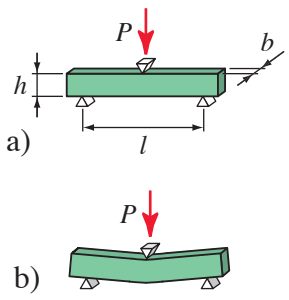

Figure 3.1: Three-point bending of a bar a) parameters and b) deformation

All values of the three-point bending deformation presented in this work are calculated with this formula. In fact, Eq. (3.2) is an approximation, considering the deformed specimen to be circular. For deformations larger than 2%, the deformed specimen is rather v-shaped because

only the region in the center of the specimen deforms. A correction might be applied according to Bolognini et al. [28], but the deformation remains a linear function of d.

2.2 Setup

The three-point bending installation used in this work was developed in our laboratory [6]. It is based on a *Schenck RMC 100-1* mechanical testing machine that can work in either load or position control. A general scheme of the installation is presented in Fig. 3.2. The load is transferred to the specimen via three alumina bearings. The deflection of the specimen is measured by an inductive extensometer of type *Tesa TTD 30* with a precision of 0.1 µm. The applied load is measured by an *Instron* load cell for tension and compression of 10 kN.

The samples are spark cut to a length of 35 mm, a thickness *b* of 7 mm and a height *h* of 3.5 mm and the sides are planed to be parallel. The distance between the lower alumina bearings, the effective length *l*, is 30 mm.

The specimen and the loading system are placed at the center of an induction furnace for measurements in a temperature range from 600 to 1550 K under a primary vacuum of $5*10^{-1}$ Torr at 1473 K. The temperature is measured with an IR pyrometer *Maurer QMPR 85*. The temperature is controlled by a *Eurotherm 2404* with auto-adaptive PID setting. The heating is done by a *KLN* high frequency generator that powers the induction furnace. Graphite susceptors inside the induction furnace additionally heat the sample at high temperatures by radiation. The temperature stability of the system and its high reactivity make it most suitable for temperature jump measurements used to measure activation parameters during creep.

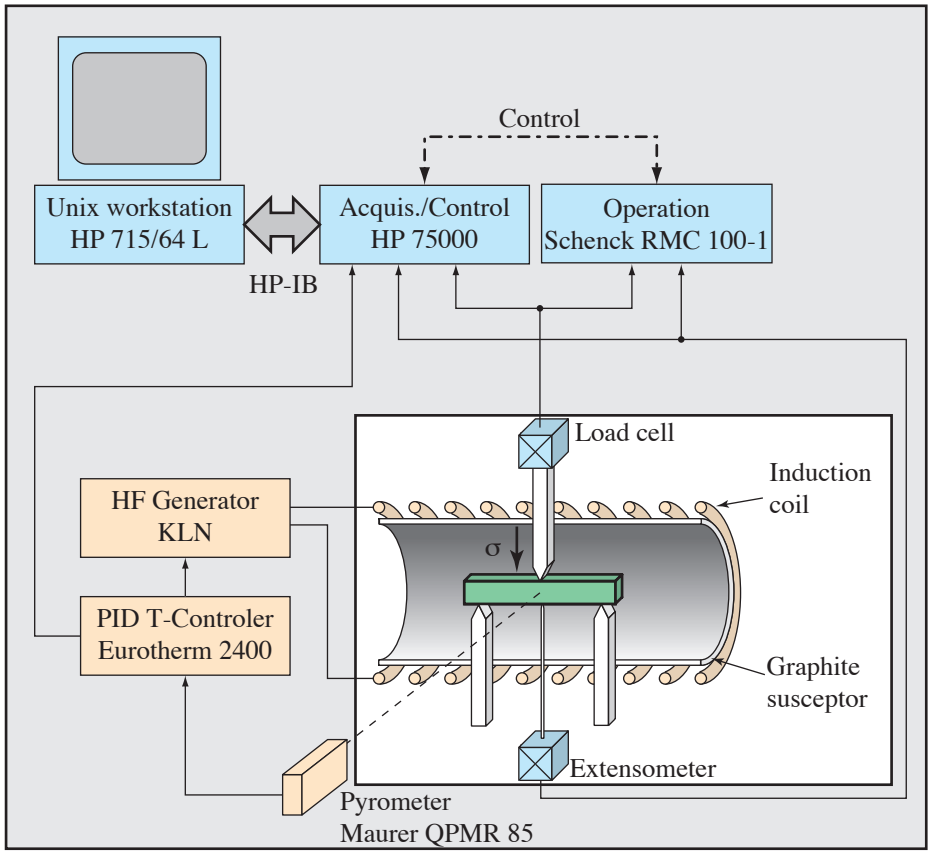

Figure 3.2: Scheme of the three-point bending installation

The operation, control and data acquisition of the measurement parameters such as load, deformation, temperature and time are performed by a *UNIX workstation* via an *HP* acquisition/control unit.

2.3 Measurements

2.3.1 Measurement at constant speed

The load necessary to deform a sample at a constant cross-head speed is measured as a function of the deflection of the sample. The load-deflection data is transformed into stress and strain. This type of experiments will be referred to as stress-strain experiments and the results as stress-strain curves. All experiments in this work are made at a cross-head speed of 1 μm/s, which corresponds to a deformation rate of $\dot{\varepsilon} = 1.5\times10^{-5}s^{-1}$ at the lower surface of the sample. The experiments are performed at constant temperature.

These measurements allow to compare the behavior of a material at different temperatures, or to compare the deformation behavior of different materials under the same conditions.

2.3.2 Measurement of the activation energy

The basis of this type of experiment is the creep test, where the deformation is measured as a function of time at constant load and temperature. A general creep curve shows three separate stages (see for example [50]). In stage I, the creep rate decreases, a constant creep rate related with the deformation mechanism is characteristic for stage II. Stage III is represented by an accelerated creep due to the formation of cracks and cavities, which finally leads to fracture. If the creep rate is constant (secondary creep), the activation enthalpy ΔH_{act} can be determined by

$$\Delta H_{act} \cong -k \left.\frac{\delta \ln \dot{\varepsilon}}{\delta(1/T)}\right|_{\sigma_a, A} \tag{3.3}$$

where k is Boltzmann's constant, σ_A is the applied stress and the constant microstructure is represented by the parameter A. As shown by Mari [6], steady-state creep is seldom observed in composite materials, due to the complexity of the mechanisms. With conventional creep experiments, it would be difficult to establish comparable conditions for different samples, because especially the thermal history of a material strongly influences its microstructure.

In this work, the temperature jump method is applied to measure the activation energy of the deformation mechanism. A sample is subjected to creep at a certain temperature and stress as described above, after some time (usually 1000 s) the temperature is abruptly lowered by 20 or 25 K and the creep test continues at the new temperature. A typical experiment with several temperature jumps is shown in Fig. 3.3a. Fig. 3.3b shows linear fits of the strain rates before and after the jump.

This method has been successfully applied for the study of creep of hardmetals in this laboratory [6,10,24,25,28,51]. With the temperature jump method, the microstructure is likely to be constant before and after the jump; a necessary condition for the determination of the activation energy.

The low inertia of the heating system on one hand and its high thermal stability on the other, allow precise temperature jumps between two levels. A jump of 20 K can therefore be performed in about 15 to 30 s depending on the temperature. The assumption of a constant micro-

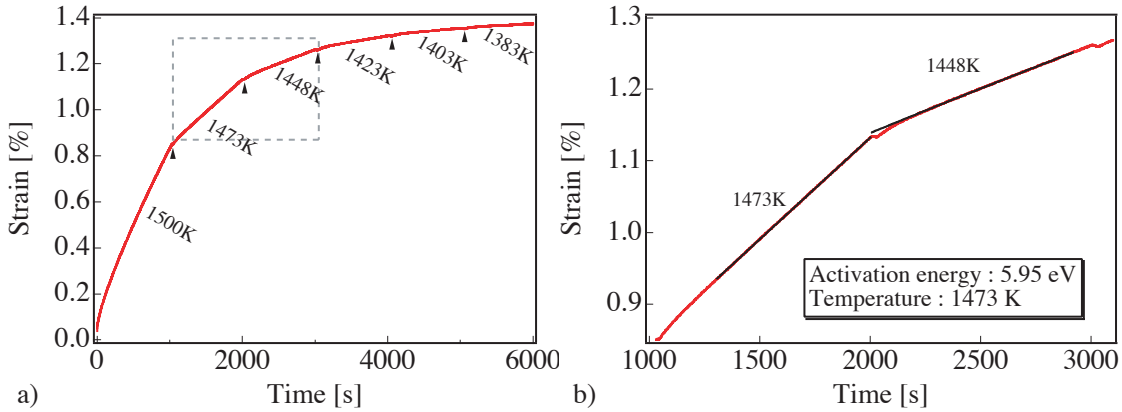

Figure 3.3: Temperature jump creep test of a cermet with several jumps starting from 1500 K (a), figure (b) shows that a constant strain rate is established after the jump (time between two jumps 1000 seconds.)

structure is generally difficult to verify, but only negative temperature jumps are performed in order to decelerate all microstructural evolution. Positive temperature jumps accelerate changes in the microstructure and thus lead to wrong activation energies as shown by Mari et al. [24].

Another critical parameter is the applied stress. To insure reasonable creep rates, a certain stress has to be applied, but by lowering the temperature, higher stresses are needed to remain in the creep regime. S. Bolognini [25] showed that the measured activation energies are rather independent of the applied stress for cermet materials. It seems that this may not always be the case in WC-Co [24].

3 Measurement of residual stresses by diffraction

3.1 Principle

The diffraction pattern of a crystalline material gives information about its structure and the d-spacings, i.e. the atomic layer distances in different crystallographic directions. Stresses acting on a crystalline material, no matter if externally applied or residual stresses, deform the crystal lattice. These stresses can be measured by comparing d-spacings or lattice parameters of the stressed sample with a stress-free reference sample of the same material. The lattice strains are simply obtained by the following equation:

$$\varepsilon_x = \frac{x - x_0}{x_0} \tag{3.4}$$

where x stands for any measured lattice parameter or d-spacing and x_0 is the same parameter, but measured in the reference material. To calculate the stresses, the elastic constants of the material are used together with Hooke's law.

Strains and stresses of the lattice are measured as a function of temperature and in the case of WC-Co also as a function of applied load.

3.2 Neutron diffraction of WC-Co at LANSCE

The Spectrometer for Materials Research at Temperature and Stress (SMARTS) at the Los Alamos Neutron Science Center at Los Alamos, USA, was used for the measurement of residual stresses of WC-Co. The instrument allows measurements as a function of temperature and, for the first time, as a function of applied tensile load. Note that only neutrons are appropriate for a bulk study of WC-Co due to the strong absorption of tungsten.

3.2.1 Material

A slightly different material is chosen for this study. Instead of the WC-10vol.%Co, a grade with 18 vol.% cobalt is used, in order to have enough intensity on the cobalt peaks to measure the peak shift and hence the residual stresses in the cobalt with a good accuracy. Bars of 89 x 19 x 4.5 mm^3 were produced in a usual sintering process and dog-bone shaped specimens were then spark cut leaving an effective gauge of 4.5 x 6.35 x 46 mm^3 (Fig. 3.4). For the in-situ sintering experiment, green bodies of the dimensions 5 x 5.5 x 53.3 mm^3 were produced. These samples were pre-sintered in order to debind the polymeric binder and give more strength to the specimens for better handling. During the sintering experiment, the sample underwent a shrinkage of 18%, as shown in Fig. 3.4. WC powder, the raw material for the sintering, was used as reference for the WC phase, as it is perfectly stoichiometric, homogeneous and stable. The green body and the powder are put in graphite containers, so that the material is surrounded by graphite during the measurements to prevent decarburisation. A stress-free reference for the cobalt cannot be produced, as the solution with tungsten and carbon varies with temperature.

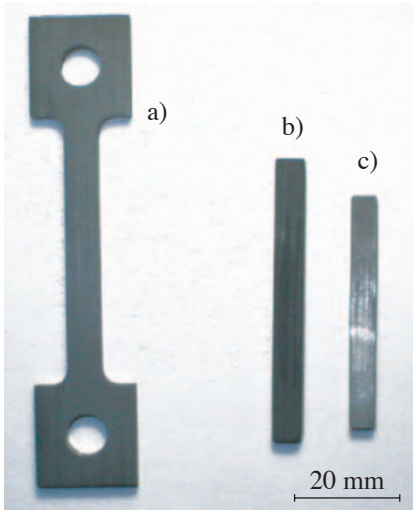

Figure 3.4: a) dog-bone sample in as-sintered state, b) green body for in-situ sintering, c) sample after in-situ sintering presenting ca. 18 % shrinkage

3.2.2 Experimental setup

The SMARTS uses a high energetic, bright neutron beam from a spallation source. Two diffraction patterns are collected by measuring the time-of-flight of the neutrons to two detector banks at +90 and -90 degrees to the incident beam. The detector banks are big arrays (about 1x2 m^2) of single detectors. The time of flight to each single detector is measured and the data from all detectors is then combined and gives, after geometrical correction, one spectrum for each bank. The specimen is positioned at 45° to the incident beam so that stresses longitudinally and transversely to the specimens main axis can be measured separately on the two banks. The time of flight of the neutrons is converted to d-spacing using Eq. (3.5), which is obtained considering the relations expressing the momentum of the neutrons $p_n = m_n v_n = h/\lambda_n$, their time-of-flight $tof = l/v_n$ and Bragg's law $\lambda = 2d\sin\theta_f$, where l and θ_f describe the position of a single detector.

$$d = \frac{tof \cdot h}{2lm_n \sin\theta_f} \tag{3.5}$$

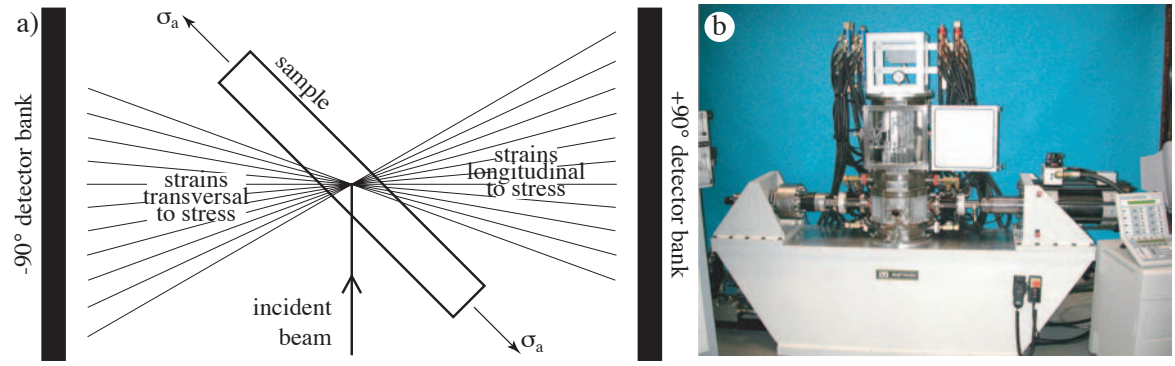

Figure 3.5: SMARTS setup, a) schematic representation of the diffraction, b) SMARTS load frame with furnace [52]

A load frame for uniaxial loading along the main axis of the specimen is placed between the detector banks, thus enabling the measurements of stresses parallel and perpendicular to the external load (Fig. 3.5). An additional extensometer measures the macroscopic deformation of the specimen. A furnace is mounted on the load frame and around the specimen and allows measurements under controlled atmosphere.

Two complete spectra are gathered simultaneously. The longer the time of data collection the higher is the intensity of the peaks. A data collection time of one hour has been found to be sufficient to have good statistics. Finally, the spectra are analyzed by the Rietveld refinement method and comparatively by single peak fitting with the help of the GSAS software [53]. Fig. 3.6 shows two spectra, taken at 1225 K in transverse (a) and longitudinal (b) direction, with Rietveld fitting. The different peaks are indicated in Fig. 3.6b.

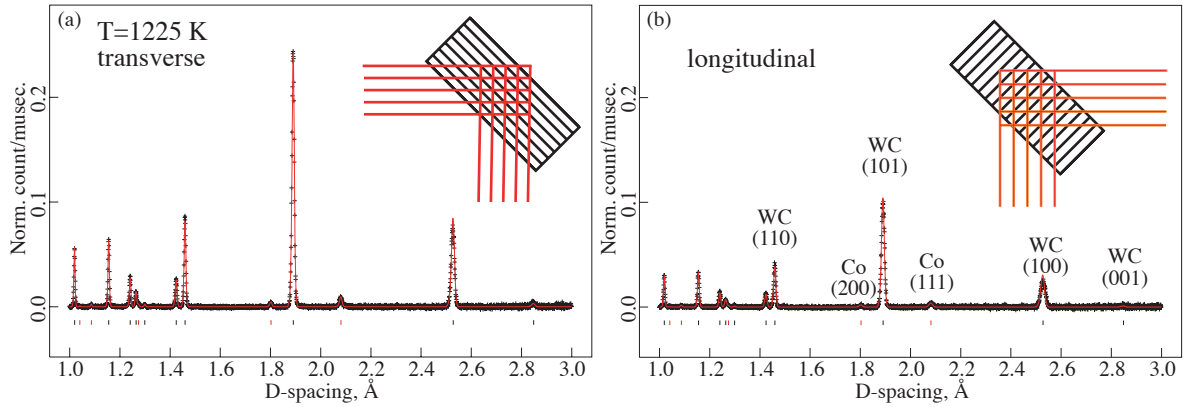

Figure 3.6: Diffraction pattern of WC-Co at 1225 K (a) transverse and (b) longitudinal, both with fitting by Rietveld refinement

3.3 X-ray diffraction of TiWCN-Co at SNBL

Residual stresses of the TiWCN-10vol.%Co cermet are measured at the Swiss-Norwegian Beam Line (SNBL) at the European Synchrotron Radiation Facility (ESRF) in Grenoble, France. Because of the low content of tungsten in this material, X-ray diffraction is appropriate for bulk measurements. The achieved penetration depth is of the order of 150 to 200 μm for cylindrical samples with 1 mm in diameter.

3.3.1 Material

The material is the same TiWCN-10vol.%Co cermet as described in chapter 2. Cylinders with a diameter of 1 mm and a length of 24.3 mm have been prepared by spark cutting from the bulk of sintered material.

The cobalt phase, as for WC-Co, contains tungsten, carbon and titanium. The concentration of these elements in cobalt may as well vary with temperature. Therefore, no stress-free reference for cobalt can be obtained.

The hard phase is rather complex. To produce a reference powder, a sintered cermet insert is crushed, the cobalt is removed by chemical etching and the powder is heat-treated for one hour at 1100°C under vacuum to release all internal stresses that have been produced by the crushing. A $TiC_{0.6}N_{0.4}$ powder is also measured for comparison.

3.3.2 Experimental setup

The X-ray beam is coming directly from a bending magnet source of the ESRF synchrotron. A Si (111) crystal is mounted inside the experimental hutch to monochromatize the beam. Two different wavelengths were used for the experiments, 0.33 Å and 0.37 Å. The beam cross-section is defined by a set of horizontal and vertical slits. A small furnace is installed in the beam to perform measurements up to 1210°C under Ar flow. The cermet samples are fixed to a support at one end and horizontally introduced into the furnace. The powder is filled in a quartz capillary, which is introduced in the furnace. Six detectors are mounted onto the diffractometer with an angular offset of 1.1°. The diffraction spectra, intensity vs. 2θ, are taken by sweeping the detectors around the sample. The six simultaneously taken diffraction patterns are combined. The angle is then converted to d-spacing using Bragg's law $d = \lambda_0/(2\sin\theta)$.

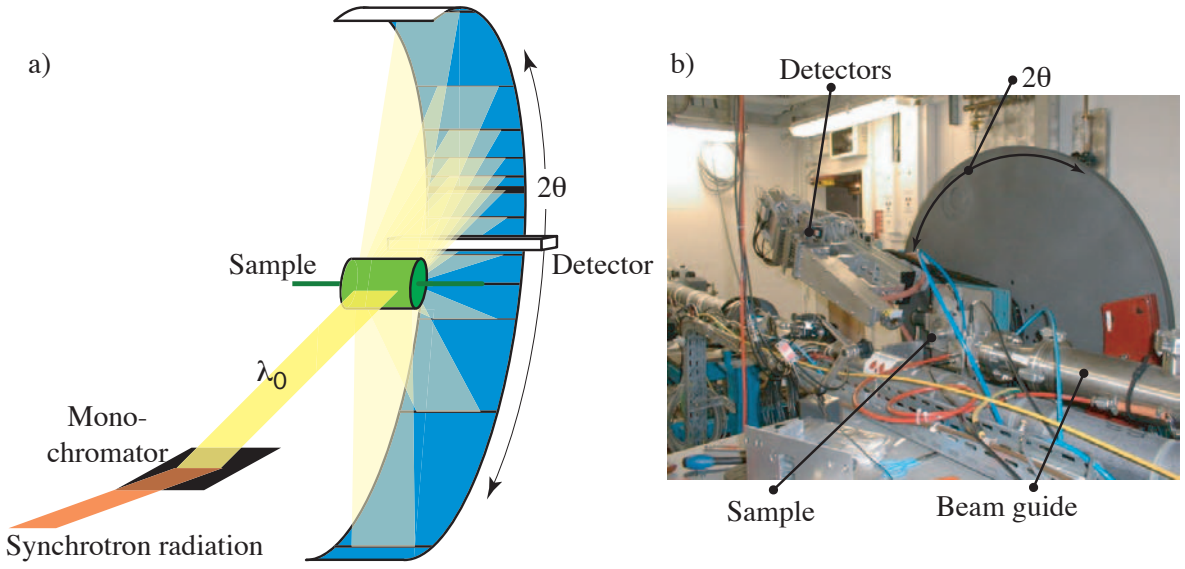

Figure 3.7: X-ray diffraction at SNBL a) schematic representation of the setup, b) photo of SNBL experimental hutch [54]

4 Mechanical spectroscopy

4.1 Anelasticity

When the stress applied to a material is smaller than the yield stress, no permanent plastic deformation occurs. The deformation is composed of an elastic, i.e. instantaneous, deformation and an anelastic or retarded deformation (Fig. 3.8). In both cases, the deformation recovers totally when the stress is removed. However, the time-dependent, anelastic deformation is related to the movement of defects and therefore mechanical energy is dissipated during the deformation.

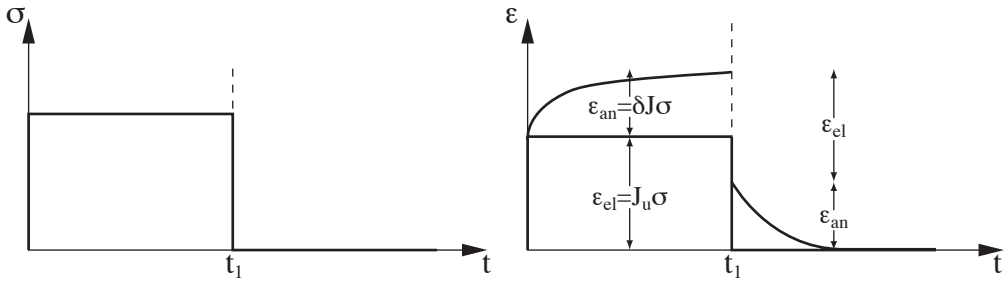

Figure 3.8: Strain response (right) to an instantaneously applied (at t=0) and released (at $t=t_1$) stress

The deformation of a material may be described by a constitutive equation relating the stress σ, the deformation ε and their time derivatives. This equation is best derived with the help of mechanical models that describe qualitatively the deformation behavior. The anelastic deformation can be modelled by a combination of two elements, the ideal-elastic Hooke solid represented by a spring and the ideal-viscous Newtonian liquid represented by a dashpot (Fig. 3.9 a+b). The stress-strain relation for the two elements are $\sigma = E\varepsilon$ and $\sigma = \eta\dot{\varepsilon}$, respectively, with Young's modulus E and the viscosity η. The combination of these elements, either in series or parallel (Fig. 3.9 c+d), represents viscoplastic and viscoelastic deformation, respectively [55]. The standard anelastic solid that describes anelastic behavior with instantaneous elasticity can be modelled either by combining the Maxwell model with a spring in parallel or by combining the Kelvin-Voigt model with a spring in series. The latter one (Fig. 3.9 e) will be further considered.

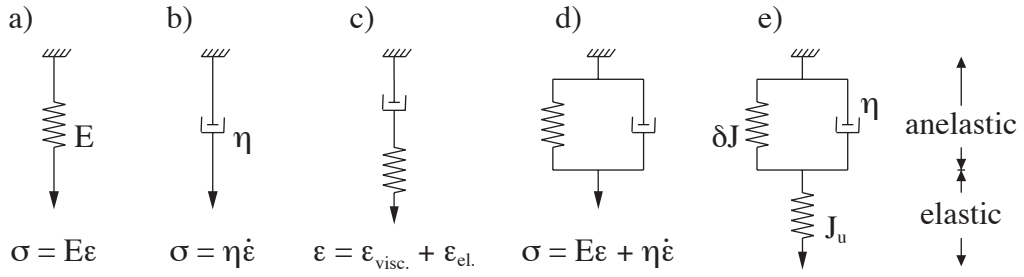

Figure 3.9: Mechanical models: a) elastic spring, b) viscous dashpot, c) Maxwell model, d) Kelvin-Voigt model and e) standard anelastic solid

The total strain ε is the sum of anelastic and elastic strain.

$$\varepsilon = \varepsilon_{el} + \varepsilon_{an} \tag{3.6}$$

The elastic strain is represented by Hooke's law with the unrelaxed compliance J_u ($J = 1/E$).

$$\varepsilon_{el} = J_u \sigma \tag{3.7}$$

The stress can be written as follows.

$$\sigma = \frac{\varepsilon_{an}}{\delta J} + \eta \dot{\varepsilon}_{an} = \frac{\varepsilon_{an}}{\delta J} + \frac{\tau}{\delta J} \dot{\varepsilon}_{an} \tag{3.8}$$

where the viscosity η is expressed as $\tau/\delta J$ (Eq. (3.6)). Eq. (3.7) and Eq. (3.8) together lead to the standard anelastic solid equation

$$\varepsilon + \tau \dot{\varepsilon} = (\delta J + J_u)\sigma + \tau J_u \dot{\sigma} \tag{3.9}$$

where $(\delta J + J_u) = J_r$ is the relaxed compliance.

4.2 Internal friction

Anelasticity is the time-dependent and reversible deformation caused by the movement of structural defects, thus causing the dissipation of energy. Internal friction IF (also called mechanical loss or damping) is a measure of this energy dissipation when a small cyclic stress is applied. It is defined as

$$IF = \frac{1}{2\pi} \frac{\Delta W}{W} \tag{3.10}$$

where ΔW is the dissipated energy and W is the maximum stored elastic energy during one cycle. If the sample is subjected to an alternating stress of the amplitude σ_0 with an angular frequency ω

$$\sigma = \sigma_0 e^{i\omega t} \tag{3.11}$$

then the strain response can be expressed as follows

$$\varepsilon = \varepsilon_0 e^{i(\omega t - \delta)} \tag{3.12}$$

where ε_0 is the strain amplitude and δ is the phase lag (or mechanical loss angle). The compliance J is therefore a complex quantity

$$J^*(\omega) = J' - iJ'' = \frac{\varepsilon}{\sigma} = \frac{\varepsilon_0}{\sigma_0} e^{-i\delta} \tag{3.13}$$

and the real and imaginary part of J are related with the loss angle δ

$$\tan\delta = \frac{J''}{J'} \tag{3.14}$$

If one now calculates the stored and dissipated energy per cycle, as for example in [55], it can be shown that tanδ is equal to the internal friction as defined in Eq. (3.10)

$$\tan\delta = IF \tag{3.15}$$

In order to calculate the IF due to a relaxation mechanism under a cyclic stress, Eq. (3.11) and Eq. (3.12) are introduced in Eq. (3.9)

$$\varepsilon + i\omega\tau\varepsilon = (J_u + \delta J)\sigma + i\omega\tau J_u \sigma \tag{3.16}$$

and this formula is rearranged in order to obtain the complex compliance J^*.

$$J^* = \frac{\varepsilon}{\sigma} = J_u + \frac{\delta J}{1+\omega^2\tau^2} - i\frac{\delta J\omega\tau}{1+\omega^2\tau^2} = J' - iJ'' \tag{3.17}$$

The IF is then calculated as the ratio between the imaginary and the real part of the complex compliance and simplified by assuming that

$$\delta J << J_u \tag{3.18}$$

and thus gives

$$\tan\delta = \frac{J''}{J'} = \frac{\delta J}{J_u}\frac{\omega\tau}{(1+\omega^2\tau^2)} \tag{3.19}$$

where $\delta J/J_u$ is called relaxation strength, generally denominated Δ. Eq. (3.19) describes the so-called Debye relaxation peak (Fig. 3.10). It can be easily seen that the IF for a single relaxation process has a maximum at $\omega\tau = 1$ with a peak height of $\Delta/2$. The modulus defect is described by the ratio of the real parts of the anelastic and elastic compliance $\delta J'/J_u$.

There are many cases where there is no single relaxation time associated with a physical process. It is often necessary to define a distribution of relaxation times. In that case, the IF can be described by the expression:

$$\tan\delta = \Delta\frac{(\omega\tau)^\alpha}{1+(\omega^2\tau^2)^\alpha}, \qquad 0 < \alpha \le 1 \tag{3.20}$$

where α is a broadening factor [56].

Most relaxation mechanisms are thermally activated and therefore the relaxation time is not constant but follows an Arrhenius law

$$\tau = \tau_0 e^{\frac{H}{kT}} \tag{3.21}$$

where τ_0 is the limit relaxation time or the inverse of the attempt frequency ν_0^{-1} related with the characteristic time between two jumps of a defect. The term $\exp(H/kT)$ represents the probability that the defect has enough thermal energy to overcome the barrier, with the activation enthalpy of the process H. k is Boltzmann's constant and T is the temperature.

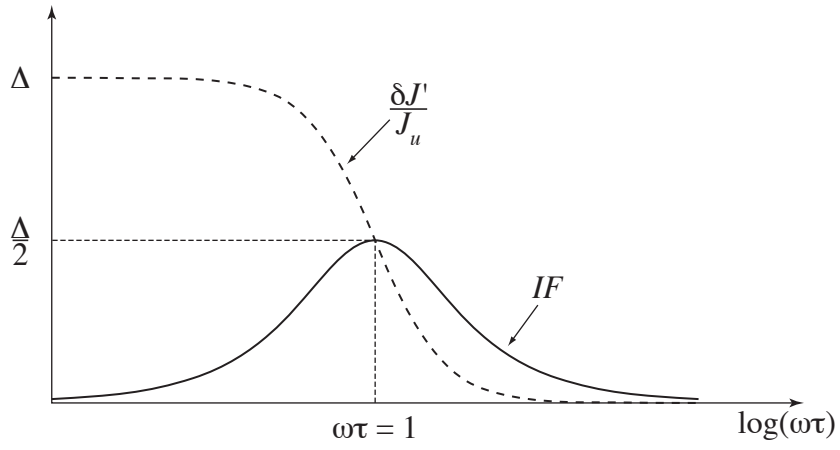

Figure 3.10: IF Debye peak and corresponding modulus defect

4.3 High-temperature relaxations

At high temperature, apart from intragranular creep by dislocation motion, which shall not be discussed here, the deformation often occurs by diffusion creep or grain boundary sliding. These two mechanisms are believed to be strongly coupled and mutually accommodating [50]. Diffusion creep occurs by transport of matter either by lattice diffusion (Nabarro-Herring creep), where the strain-rate varies as the square of the grain size d^2, or by grain–boundary diffusion (Coble creep), where the strain-rate varies with d^3. The two diffusion mechanism show a general difference in activation energy, i.e. $E_{Coble} \approx 0.6 \cdot E_{NH}$. Grain boundary sliding is the relative displacement of two neighboring grains parallel to their common interface. It is a complex phenomenon that may involve a variety of mechanisms. If these mechanisms produce an energy dissipation, they can be studied by mechanical spectroscopy.

4.3.1 High-temperature background

Anelasticity is related with the short range movement of structural defects confined by a restoring force. For example, the dislocation line tension limits the movement of a dislocation or the elastic stress concentration at triple points may limit the sliding of a grain boundary. Under these conditions, the defect motion gives rise to a relaxation peak. However, if this restoring force vanishes, the unlimited movement of these defects results in creep, which may lead to an exponential increase of the IF and simultaneously to a decrease of the modulus.

As mentioned before, high-temperature creep may be a coupled diffusion-grain boundary sliding mechanism. Either mechanism may be, depending on the case, rate-controlling.

Nabarro was the first to develop the idea of creep of a single crystal under stress by movement of matter [57]. A difference in vacancy concentration is created between the surface under tension and the surface under compression leading to a flux of vacancies towards the compressed surface and a flux of matter in the opposite direction. This process is then expected at high temperatures and for small grain sizes, as these are the ideal conditions for this type of creep with high vacancy mobility and short diffusion length through the grain. The strain-rate is expressed as follows

$$\dot{\varepsilon} = \alpha \frac{D_{sd} \sigma \Omega}{d^2 kT} \tag{3.22}$$

with the self-diffusion D_{sd}, the atomic volume $\Omega=b^3$, the grain size d and the numerical factor α, which depends on the grain shape and boundary conditions.

Herring formalized the lattice creep for polycrystals by assuming the driving force for transport of matter due to the difference in chemical potential of atoms and vacancies [58]. He arrived to the same formula as Nabarro and this type of creep is called Nabarro-Herring creep since then. Herring established values for α with and without grain boundary sliding accommodation, $\alpha=40$ and $\alpha=16$, respectively.

Coble investigated the creep of polycrystals in the same case as Nabarro, but considering that the transport of matter occurs along grain-boundaries and arrived to Eq. (3.23), assuming that GBS accommodation may take place [59].

$$\dot{\varepsilon} = 148\alpha \frac{D_{gb} \sigma \delta \Omega}{\pi d^3 kT} \tag{3.23}$$

where δ is the grain boundary width.

If diffusion occurs either in the lattice or through grain boundaries the strain-rate can be unified as [60]

$$\dot{\varepsilon} = \alpha \frac{D_{eff}\sigma\Omega}{d^2 kT} \qquad with \qquad D_{eff} = D_{sd} + \frac{\beta\delta}{d} D_{gb} \tag{3.24}$$

Generally, the Nabarro-Herring creep is active for high temperatures and larger grain sizes, whereas the Coble creep is active already at lower temperatures and for smaller grains. The important difference between the two types of diffusion creep is their dependence on the grain size. The strain-rate depends on the inverse of d^2 for lattice diffusion and on the inverse of d^3 for grain-boundary diffusion. Notice that dislocation creep is independent of grain size [50].

The internal friction for the diffusion process described above is given by [60]

$$\tan\delta = \frac{1}{J_u \omega} \frac{\alpha D_{eff}\Omega}{d^2 kT} \tag{3.25}$$

By expressing the diffusion coefficient as $D_{eff} = D_{eff,0}\exp(-H/kT)$ and reducing the other constants to the constant A, Eq. (3.25) can be simplified to

$$\tan\delta = \frac{A}{T\omega} e^{\left(\frac{-H_{act}}{kT}\right)} \tag{3.26}$$

Eq. (3.26) justifies an exponential background. However, Schoeck et al. [61] showed that this approach is too simplistic. In the case of dislocation related relaxations, Schoeck et al. consider a distribution of the dislocation lengths with the same activation energy. They obtain a new expression of the IF background

$$\tan\delta = \frac{C}{[\omega \exp(H/kT)]^n} = \frac{C}{\omega^n} e^{\left(\frac{-nH_{act,0}}{kt}\right)} \tag{3.27}$$

where C, n and the true activation energy $H_{act,0}$ are constant over a limited temperature range. Plotted in lnIF vs. lnω scale, Eq. (3.27) yields:

$$\ln IF = \left(\ln C - \frac{nH_{act,0}}{kT}\right) - n\ln\omega \tag{3.28}$$

The slope n can be derived from a linear fit as shown in Fig. 3.11. Knowing n, the true activation energy can then be evaluated from the intercept at different temperatures.

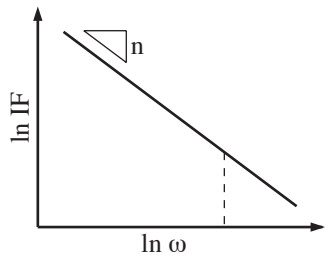

Figure 3.11: Slope of an IF frequency spectrum in log-log scale for determination of the true activation energy.

4.3.2 Grain boundary sliding in bicrystals

The simplest case of grain boundary sliding is represented in Fig. 3.12. A shear stress is applied parallel to the interface of a bicrystal causing instantaneous elastic deformation of the crystals and time-dependent sliding at the interface. After the shear stress is removed, the elastic deformation of the crystals is restored, but the viscous sliding at the interface is permanent. This behavior is represented by a Maxwell solid (Fig. 3.12b). The interface is characterized by

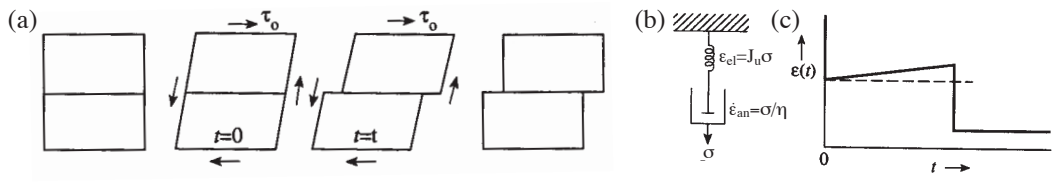

Figure 3.12: Viscous grain boundary sliding at an ideally planar bicrystal interface [62]

an intrinsic viscosity $\eta = \sigma/\dot{\varepsilon}$ [62]. The internal friction yields a background depending on the elastic constant the grain boundary intrinsic viscosity and the frequency of $IF=1/J_u\eta\omega$.

However, ideally flat grain boundaries are rarely found in real materials. Grain boundaries often present some curvature or stepping [63]. Assuming a shear stress applied parallel to a non-planar grain boundary (Fig. 3.13a), the resulting displacement remains rather limited due to the building-up of stresses at the irregularities of the grain boundary. If the applied stress is small, the accommodation of the sliding is purely elastic (Fig. 3.13b). However, accommodation can also take place by diffusion (Fig. 3.13c), especially at high temperatures, or by plastic flow due to lattice dislocation motion, if the applied stress is high (Fig. 3.13d). The different accommodation processes (for bicrystals) are discussed below.

Grain boundary sliding with elastic accommodation

Sliding of a non-planar grain boundary is anelastic. Elastic stresses are built up at the asperities of the grain boundary, which hinder further sliding and build the restoring force for the backward movement. The total sliding displacement, which is proportional to the grain size, is estimated to be up to 50 Å for 0.1 mm grain size [63]. The authors have calculated the deformation for a grain boundary with sinusoidal profile $y=a\cos(2\pi x/\lambda)$ and therefore the proportionality factor between applied stress and deformation is

$$K = \frac{\pi^3 E a^2}{(1-\nu^2)\lambda^3} \tag{3.29}$$

where ν is Poisson's ratio and E is Young's modulus. In contrast to planar interfaces that behave as Maxwell solids, the internal friction of non-planar grain boundaries is that of the standard anelastic solid (Eq. (3.19)). Using $\delta J=1/K$ and $\tau=\eta/K$, the IF can be expressed as

$$\tan\delta = \frac{1}{J_u K}\frac{\omega\eta}{1+\omega^2\eta^2} \tag{3.30}$$

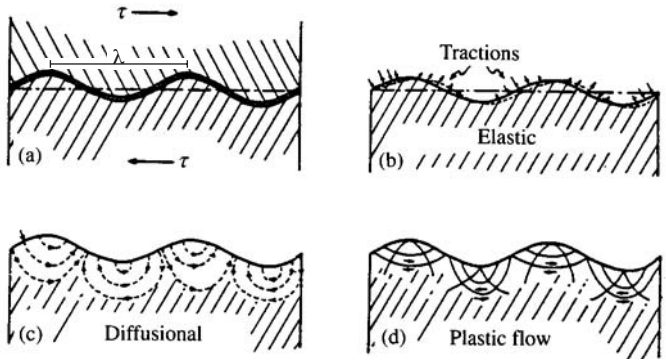

Figure 3.13: Accommodation mechanisms of sliding at non-planar grain boundary [64]

Grain boundary sliding with diffusional accommodation

Especially at high temperatures, grain boundary sliding at non-planar grain boundaries can be accommodated by diffusion of matter from the compressed faces to the faces under tension (Fig. 3.13b). Raj and Ashby [63] and Sutton and Balluffi [62] studied this problem and gave a linear relationship between applied stress and strain-rate, both for lattice and grain boundary diffusion. The grain boundary possesses an intrinsic Newtonian viscosity $\eta = \dot{\varepsilon}/\sigma$ that depends, among other parameters, on the lattice or grain-boundary diffusion D_B. The important difference between the two diffusion modes is that the viscosity depends on the boundary wavelength for lattice diffusion D_L, but it is independent of it in grain boundary diffusion. For short wave lengths and low temperature, D_B is larger than D_L and the grain boundary diffusion mechanism is favored [62].

Grain boundary sliding by plastic flow accommodation

To accommodate grain boundary sliding by plastic flow (Fig. 3.13), high stresses are necessary where deformation at the boundary occurs by the motion of lattice dislocations. The sliding rate depends on the plastic properties of the adjacent crystals and varies non-linearly with the applied stress. If dislocations can both glide and climb, the deformation obeys a power law creep relation of the form $\dot{\varepsilon} = A\sigma^n$, where A and n are constants. This type of accommodation, like the diffusional accommodation, leads to creep and does not show any anelasticity [62].

4.3.3 Grain boundary sliding in polycrystals

Elastic accommodation

Anelastic relaxation due to grain boundary sliding with elastic accommodation has been first described for polycrystals by Zener (Fig. 3.14) [66]. Grain 1 slides over grain 2 under an applied shear stress. Due to the displacement of grains 1 and 2, stresses are built up at grains 3 and 4 at the end of the grain boundary. The sliding continues until the shear stresses are completely relaxed. If the applied stress is small, the deformation at the triple points is purely elastic and the process is reversible upon removal of the stress. This behavior corresponds well to that of the standard anelastic solid, Eq. (3.9). Eq. (3.17) and Eq. (3.19) are therefore valid here with $\delta J = d/K$ and $\tau = \eta/K\delta$, where K represents the elastic constant of the grains, d is a factor related with the density of grain boundaries or the grain size and δ is a factor related with the thickness of the viscous grain boundaries. The resulting IF is:

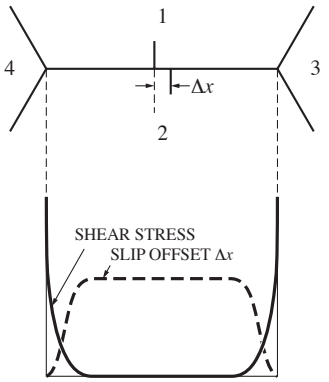

Figure 3.14: Grain boundary sliding relaxation with elastic restoration at triple points [65]

$$\tan\delta = \frac{\delta J}{J_u}\frac{\omega\tau}{1+\omega^2\tau^2} = \frac{d}{J_u K}\frac{\omega(\eta/(K\delta))}{1+\omega^2(\eta^2/(K^2\delta^2))} \qquad (3.31)$$

If the approximation Eq. (3.18) is omitted, which may be more correct at high temperatures, an additional term (highlighted) is found in Eq. (3.31) [67]

$$\tan\delta = \frac{\delta J}{J_u}\frac{\omega\tau}{1+\frac{\delta J}{J_u}+\omega^2\tau^2} = \frac{d}{J_u K}\frac{\omega\frac{\eta}{\delta}}{1+\frac{d}{J_u K}+\omega^2\frac{\eta^2}{K\delta^2}}. \tag{3.32}$$

The relaxation strength Δ depends on grain boundary density or grain size, whereas the relaxation time depends only on the grain boundary viscosity and its thickness.

Diffusional accommodation

If the grain size is rather large and the boundary is wavy but on a small scale, viscous grain boundary sliding may be accommodated by lattice diffusion. This will give rise to anelasticity, if the relaxation time of the sliding with diffusional accommodation is relatively short with respect to the elastic accommodation at triple junctions. If the grain size is much smaller and the boundaries are flat or present a waviness with a very short wavelength, the boundaries may be intrinsically viscous as in the Zener model (Fig. 3.14) or viscous via accommodation by localized grain boundary diffusion. Compared with diffusional accommodation by lattice diffusion (characteristic for large grain sizes), the IF grain boundary sliding peak appears at lower temperature and has a smaller activation energy [62].

The Kê peak is observed in pure metals with a very fine-grained structure with flat grain boundaries. The peak is not present in single crystal materials. Its relaxation behavior is that of the standard anelastic solid [68], Eq. (3.31) and Fig. 3.14. The viscosity is related to the grain boundary self-diffusion [60]

$$\eta = \frac{kT}{Da} \qquad with \qquad D = D_{GB} = \frac{1}{2}\nu a^2 = \frac{1}{2}\nu_D a^2 \exp\left(\frac{-E_{GB}}{kT}\right) \tag{3.33}$$

where D is the diffusion coefficient, a is the inter-atomic distance, ν_D is the Debye frequency and E_{GB} the activation energy of the diffusion process. As K is due to the elastic deformation of the grains at triple junctions, it is assumed that K and d in Eq. (3.31) are proportional and therefore the relaxation strength Δ is independent of the grain size [60].

For materials with a bamboo structure, where the grain size is as large as the specimen diameter, the sliding may either be accommodated elastically by the non-planarity of the grain boundary or it may be accommodated by lattice diffusion. In the first case, the deformation can be described by the standard anelastic solid as in Eq. (3.29) and Eq. (3.30). In the second case, the mechanical model presents the standard anelastic solid (Fig. 3.8e) with an additional dashpot in series with the spring δJ [68]. This model shows that at high temperature or low frequency, plastic deformation may occur.

Similar observations are made on grain boundary sliding with inert particles of diameter p and interparticle spacing λ present at the grain boundary. Diffusion accommodation can take place by lattice and/or boundary diffusion and the corresponding viscosity is according to Raj [63]

$$\eta = \frac{kTp^3}{1.6\Omega\lambda^2 D_{eff}} \qquad with \qquad D_{eff} = D_L + 5\frac{\delta}{p}D_{GB} \tag{3.34}$$

where δ is the grain boundary thickness, Ω the atomic volume of the adjacent grains and D_L, D_{GB} are the diffusion coefficients for lattice and boundary diffusion, respectively. Big particles do slow down the sliding rate more effectively than the same volume fraction of small particles [63]. Furthermore it is shown that the sliding rate is more sensitive to the grain size than the

particle diameter and spacing [63]. The expected relaxation peak should occur at higher temperatures than the pure metal peak, but with the same activation energy [60].

Accommodation by plastic flow

Grain boundaries can be described by a dense network of overlapping dislocations. These grain-boundary dislocations can only move inside the grain boundary plane, but as the glide plane of the dislocations must not necessarily coincide with the grain boundary plane, the motion generally involves two steps, glide and climb, the slower of which controls the dislocation motion. Assuming that grain boundary dislocation segments can vibrate around their equilibrium position under a small applied cyclic stress, this dissipation process can be measured by internal friction measurements [60].

In order to model the anelastic relaxation of grain boundary dislocation, the same model as for intragranular dislocations can be used (Fig. 3.15). For the mean displacement u of a dislocation with Burger's vector $\vec{b}$, the force necessary to bend the string is given by

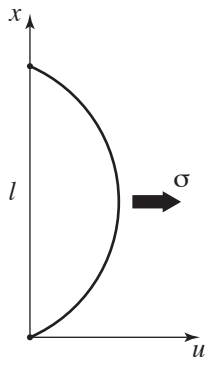

Figure 3.15: Dislocation string model

$$\sigma u = Ku + B\dot{u} \tag{3.35}$$

where K is the restoring force constant and B represents the viscous friction coefficient. The resulting deformation consists in an elastic and an anelastic part

$$\varepsilon = \varepsilon_{el} + \varepsilon_{an} = J_u\sigma + \lambda bu \tag{3.36}$$

where the dislocation density is given by $\lambda=\rho/d$, with ρ being the total dislocation length per unit grain boundary area. The IF is then given by

$$IF = \frac{\rho b^2}{J_u K d}\frac{\omega\tau}{1+\omega^2\tau^2} \qquad with \qquad \tau = \frac{B}{K} \tag{3.37}$$

The restoring force may have different origins [60]. If the dislocation is pinned at the ends, the restoring force constant is $K=12\gamma/l^2$ with the line tension $\gamma=0.5b^2/J_u$ and the segment length l. The relaxation strength than reduces to $\Delta=6b^2/l^2J_u$ and is therefore inversely proportional to the grain size d. The restoring character may also result from the presence of a grain boundary dislocation array. Then, the restoring force may be due to repulsion between vibrating dislocations for large grain sizes ($\Delta \approx 1/d$) or, in case of small grain size, the restoring force results from the elasticity of the grains at triple junctions (the elasticity itself varies with $1/d$ and Δ is therefore independent of d) [60].

The friction coefficient B is related with the climb of dislocations by jog formation and migration

$$B = \frac{kT}{b^2 D C_j} \tag{3.38}$$

where $D=D_0\exp(-E_{GB}/kT)$ is the grain boundary self-diffusion coefficient and $C_j=C_{j0}\exp(-E_{jogform}/kT)$ is the density of jogs. The resulting relaxation time therefore depends on temperature [60].

4.3.4 Experimental observations of grain boundary sliding

Pure metals [69]

A lot of peaks are described in the same temperature range and their relation with grain boundary sliding is widely discussed with contradictory interpretations. The Kê peak has only been observed in pure aluminium, but without a careful study of the grain boundary geometry. Studies in other pure metals, such as copper and iron, show that the situation is more complex than in the case of aluminium and that the observed peaks may as well be due to intragranular dislocation motion [69].

NiCr

An internal friction peak has been observed in Ni-20Cr [70]. The peak does, reproducibly, appear at about 1100 K, but only upon cooling after heating to 1200 K. The peak position is sensitive to the Cr content and also to frequency, which means that the corresponding dissipation process is thermally activated. However, the thermal hysteresis in IF (sharp increase upon heating and decrease upon cooling) is not sensitive to changes in the frequency, but the modulus is, which is characteristic for a structural evolution, e.g. phase transformation [69]. Both, peak and thermal hysteresis, are absent in single crystals with the same composition. However, the behavior of the polycrystal can be established in a single crystal material after cold-rolling at room temperature and recrystallization. Microscopic observations show that carbides are present at the grain boundaries at room temperature. These carbides get dissolved during heating leading to a sharp increase of IF and re-precipitate upon cooling. The peak observed during cooling is a grain boundary sliding peak at the clean grain boundaries. It has been shown that the microscopic mechanism of this peak is due to the reversible movement of grain boundary dislocation segments under the applied stress.

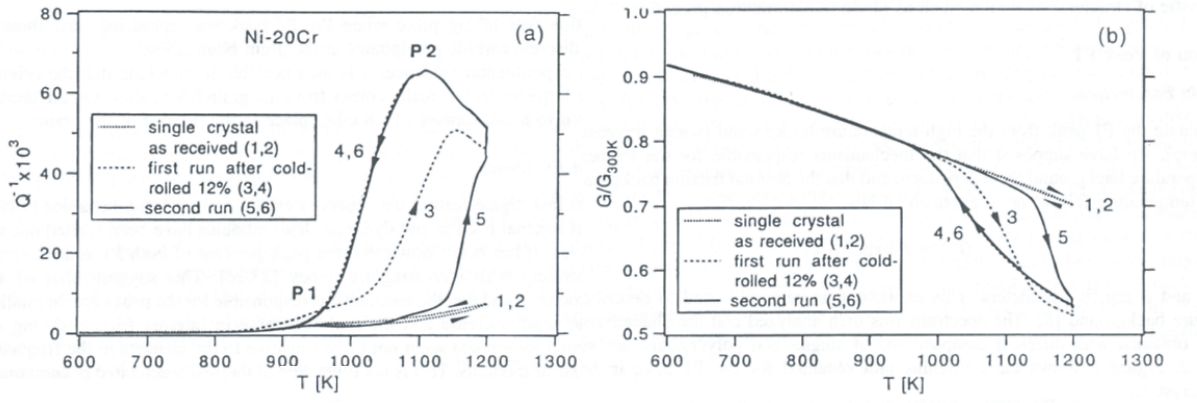

Figure 3.16: (a) IF and (b) dynamic modulus of Ni-20Cr polycrystal and single crystal

Ceramics [71]

The grain boundary sliding in alumina has been found to be accommodated by plastic flow and is therefore related with dislocation motion [71].

In zirconia, on the contrary, the grain boundary sliding is accommodated by diffusion mechanisms. The sliding is controlled by diffusion, which can moreover be slowed down by interface-reaction mechanisms. The internal friction is basically that described by Eq. (3.32), with

the viscosity being either the intrinsic viscosity of the grain boundary or that of an amorphous intergranular phase. Another representation of Eq. (3.32),

$$\tan\delta = \frac{G}{d}\frac{\omega\frac{\eta}{\delta}}{\left(\frac{KG}{d}+K^2\right)+\omega^2\frac{\eta^2}{\delta^2}}, \tag{3.39}$$

shows that if K is constant, tanδ has the form of a peak and if K vanishes (K=0), the same formula yield an IF background. The restoring force K in this model is assumed to be due to triple points and its evolution is related with the time-dependent modulus $G(t)$ during creep [71]

$$K = c_1\frac{\sigma}{\varepsilon_{el}+\varepsilon_{an}(t)} = c_1\frac{\sigma}{\frac{\sigma}{G}+A\frac{\sigma^2}{d}\exp\left(\frac{-E}{kT}\right)\cdot t} \tag{3.40}$$

where c_1 and A are constants.

4.4 Experimental methods

4.4.1 Inverted forced torsion pendulum

The inverted forced torsion pendulum works at sub-resonant mode, i.e. at frequencies below the resonant frequency of the pendulum-sample system. The plate shape sample has a cross-section of 4 x 1 mm^2 and a variable length between 35 and 60 mm. The shorter the sample the higher is the resonant frequency of the setup. A sketch of the pendulum is shown in Fig. 3.17. The sample is clamped on a rod, which is fixed to the bottom of the pendulum and

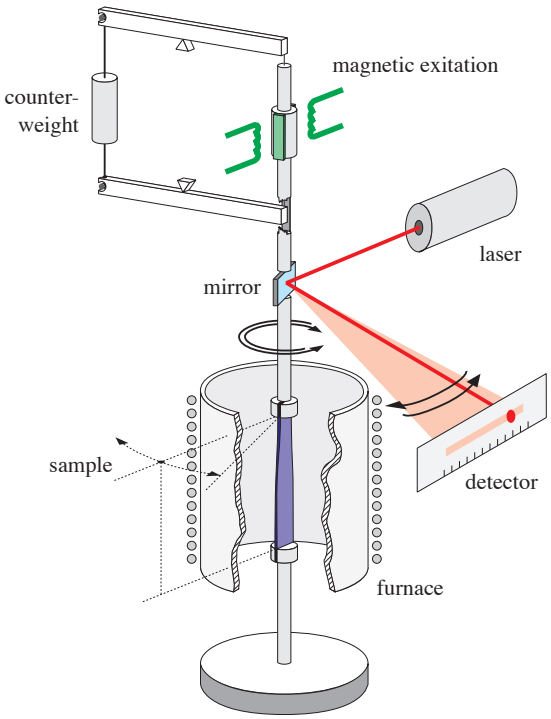

Figure 3.17: Principle of the inverted forced torsion pendulum

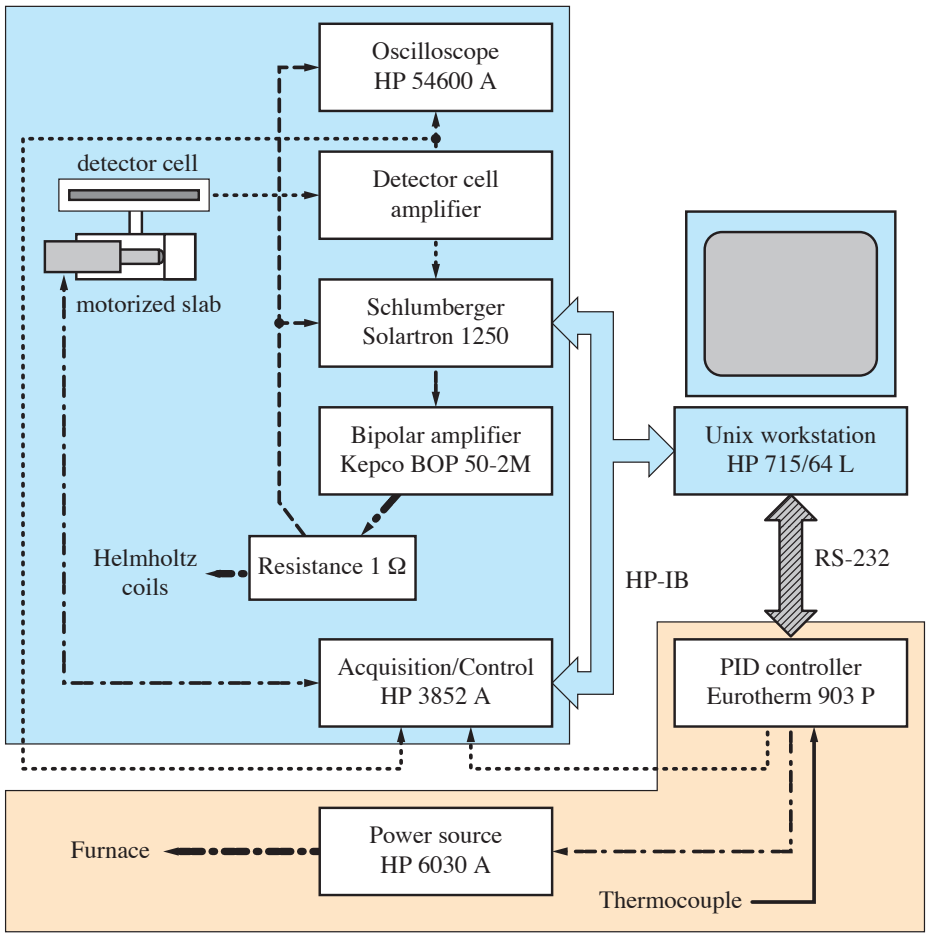

Figure 3.18: Electronic control of the pendulum

suspended at its top with thin tungsten wires. The wires are connected to a double balance system to accommodate the thermal expansion of the system. The weight of the rod and the sample is equilibrated by a counterweight. The torsional vibrations are driven by a set of Helmholtz coils acting on permanent magnets that are fixed to the rod. The deflection is measured optically by a laser-mirror-detector setup, with the mirror fixed to the vibrating rod. The sample is surrounded by a tubular BC_4 graphite resistivity furnace. The whole setup is set under vacuum of 10^{-5} mbar using a primary rotation pump and a secondary oil diffusion pump. Everything but the primary pump is mounted onto a concrete table on pneumatic vibration isolators with automatic levelling to prevent all influences from external noise.

The measurements are controlled by the setup shown in Fig. 3.18. The sinusoidal excitation signal is generated by a *Schlumberger Solartron 1250* and amplified. The response is detected by a detector cell, amplified and returned to the frequency generator, which serves also as signal analyzer for phase lag and ratio of the amplitudes of excitation and response. An oscilloscope is used for the visualization of the signals. The heating system comprises a *Eurotherm* PID controller, which regulates the power, sent to the furnace by a power source, and a type S thermocouple to read the temperature close to the specimen. All instruments are linked over an *HP* acquisition-control unit with an *HPVee* program to control the measurements and to collect the experimental data. An automated detector cell shifting makes sure that the response signal is centered, to prevent from angular deviations caused by internal stresses of the specimen.

Two types of measurements can generally be performed with the presented setup. Isothermal measurements are carried out at a fixed temperature by changing the frequency, usually from

10 Hz to 1 mHz as in Fig. 3.19. Isochronal measurements are carried out at 1 Hz by changing the temperature at a certain rate (1 K/min if not otherwise specified). The results are referred to as frequency or temperature spectra, respectively.

4.4.2 The resonance background

The measured phase lag φ is related to the specimen damping tan δ by

$$\tan\varphi = \frac{\omega_r^2}{\omega_r^2 - \omega^2}\tan\delta \tag{3.41}$$

where ω_r is the resonant frequency of the pendulum-specimen system. The measured phase lag ϕ therefore increases, when the resonant frequency is approached from the subresonant side of the spectrum. The chosen frequency range is 1 mHz to 10 Hz at a resonant frequency ω_r of 96 Hz for a specimen length of 50 mm (ω_r is higher for shorter samples, which are mostly used here). An additional parasitic background is observed at high frequencies resulting not only from approaching the resonance but also from the electronics of the installation. Assuming that those parasitic elements of internal friction and modulus stay the same in the whole temperature regime and knowing that the materials to be investigated have a very low internal friction at room temperature, the following procedure is used to treat the measured data for all results in this work. For each freshly mounted specimen, a frequency spectrum obtained at room temperature before the measurements is used as reference for the whole experiment. The frequency spectrum of internal friction at constant temperature is obtained by subtracting a polynomial fit of the room temperature internal friction curve from the 'raw' measurement (Eq. (3.42)) as shown in Fig. 3.19. The temperature spectrum at constant frequency is obtained by subtracting the fitted value of the room temperature internal friction curve for the corresponding frequency (Eq. (3.43)).

$$IF_T(f) = IF_{\mathrm{raw},T}(f) - IF_{\mathrm{fit,RT}}(f) \tag{3.42}$$

$$IF_f(T) = IF_{\mathrm{raw},f}(T) - IF_{\mathrm{fit,RT}}(f) \tag{3.43}$$

The absolute value of the shear modulus can not be measured with a forced pendulum. Therefore, the relative shear modulus $G(T,f)/G(\mathrm{RT},f)$, often simply called G/G_{300}, is presented.

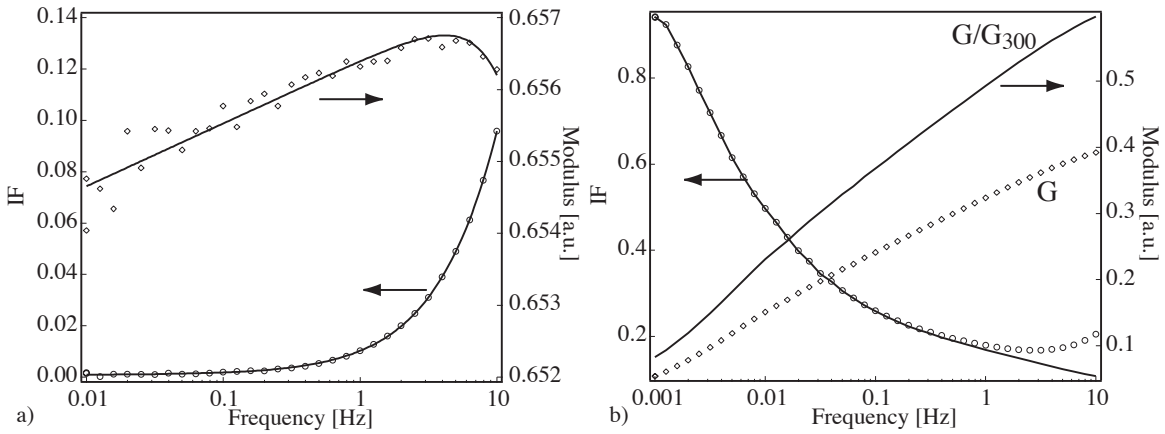

Figure 3.19: a) Room temperature spectrum (markers) with increasing IF and decreasing modulus at high frequencies (lines represent fittings). b) Frequency spectrum at fixed high temperature before (markers) and after correction (lines)

4.4.3 Numerical spectrum analysis

The internal friction spectra of the studied materials are often very complex comprising a superposition of several relaxation peaks and a background. The fitting of the spectra is performed with the commercial program *IgorPro*. The fitting procedures always comprise a background and one or more Debye shaped relaxation peaks with the parameters amplitude, position, broadening factor and in case of temperature spectra also the width of the peak, which is related with its activation energy. In temperature spectra, the background can be represented by

$$IF_{background} = A\exp\left(\frac{-B}{kT}\right) \tag{3.44}$$

which represents a line in a ln*(IF)* versus 1/*T* plot with the intercept ln*A* and a slope -*B*/*k*. The parameters *A* and *B* are empirical, but *B* can be attributed to the apparent activation energy of the mechanism responsible for the background (Eq. (3.27)). In frequency spectra, the background is a line in the ln*(IF)* versus ln*(ω)* plot, which can be expressed as

$$IF_{background} = A\omega^{-\alpha} \tag{3.45}$$

where the intercept *A* depends on the temperature, when the background is thermally activated, and α is the slope. If a single thermally activated mechanism is responsible for the background

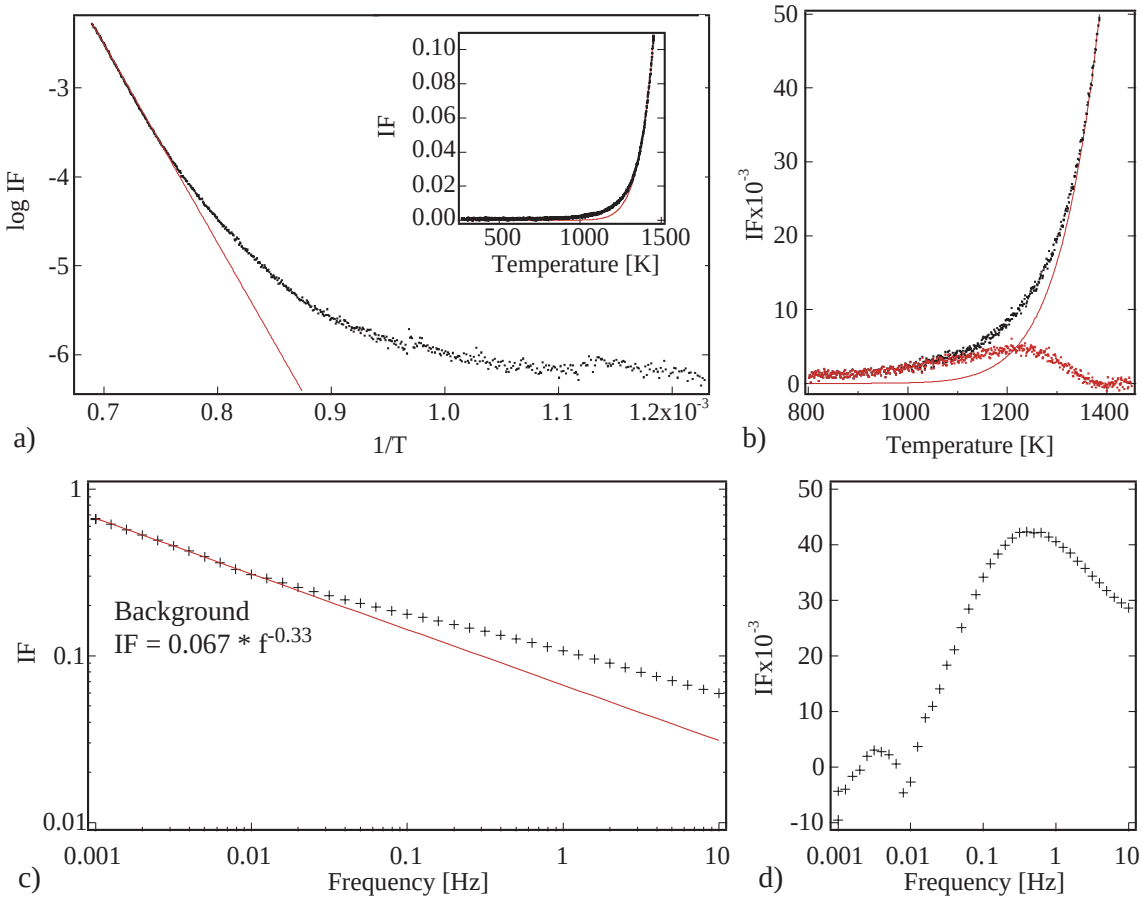

Figure 3.20: Background fitting on cermet: IF temperature spectrum at 1 Hz and 1 K/min (a) log IF vs. 1/T plot with line fit (inset shows exponential background) and (b) residual after background subtraction; IF frequency spectrum at 1450 K (c) prior to and (d) after subtraction

and the structure is stable, then α should be constant and the activation energy can be determined from the intercept A according to Eq. (3.27).

The deconvolution of the spectra can be done after subtraction of the background, if it can be well determined. Otherwise, the background can be part of the fitting procedure. Both ways have always been tried in this work, as either method can at times prove more useful than the other. Care should be taken about the origin of the background. Sometimes the background and a high temperature peak are due to the same mechanism and should than be fitted together.

4.4.4 Activation parameters

Thermally activated relaxation phenomena can be evidenced by internal friction measurements in several ways. First, the width at half maximum of a Debye relaxation peak measured as a function of temperature is related with the activation energy of the corresponding relaxation process [72]. The obtained value should be taken with caution, when the peak is very broad or when neighboring peaks are too close to separate them. Generally, the physical meaning of each peak should be clarified and spurious peaks should be avoided. Secondly, the shift of a peak, either in frequency spectra measured at different temperatures or in temperature spectra measured at different frequencies, can be used to determine the activation energy and the relaxation time (or attempt frequency). For the peak shift method, for example in frequency spectra, the frequency position of the peak is determined at different temperatures. Then the values are plotted in a $\log(IF)$ versus $1/T$ plot, the so-called Arrhenius plot. The points form a line if the activation energy and the relaxation time are independent of temperature [32,43]. With $\omega\tau = 1$ and $\tau = \tau_0 \exp(-E_{act}/kT)$ one can easily derive the following fitting function

$$\ln\omega = A + B\frac{1}{T} \tag{3.46}$$

with the activation energy E_{act} and the relaxation time τ_0 (in seconds) given as

$$\begin{aligned} E_{act} &= -Bk \\ \tau_0 &= \frac{1}{2\pi}e^{-A} \end{aligned} \tag{3.47}$$

It should be noted here that the activation energy is only physically meaningful if the attempt frequency $\nu_0 = 1/\tau_0$ is 10^{13} s^{-1} or smaller as it should not exceed the Debye frequency [65]. Often much higher attempt frequencies are measured and the corresponding activation energies are too high, then called “apparent” activation energies.

Chapter 4

Three-point bending results

In this chapter, the macroscopic properties of the materials are studied. The deformation behavior at different temperatures for both cermets and cemented carbides is presented. The materials can then be compared based on these results. A comparison with the ceramic skeletons shows the transition from bulk deformation to cobalt enhanced creep. The activation energy of creep is measured by the temperature jump method. Apart from the characterization of the deformation behavior of the base materials, the results will also serve as reference for possible improvements of the materials.

1 Brittle, ductile and plastic - the stress-strain curves

Stress-strain curves are measured with a constant cross-head speed of 1 µm/s (i.e. $\dot{\varepsilon} = 1.5 \cdot 10^{-5} s^{-1}$). The temperature of investigation ranges from 1023 K to 1473 K. In Fig. 4.1a, the deformation curves of WC-Co samples are presented. With increasing temperature the maximum flow stress attained decreases and, at the same time, the deformation at fracture increases. The softening behavior of the material with temperature appears regular and constant.

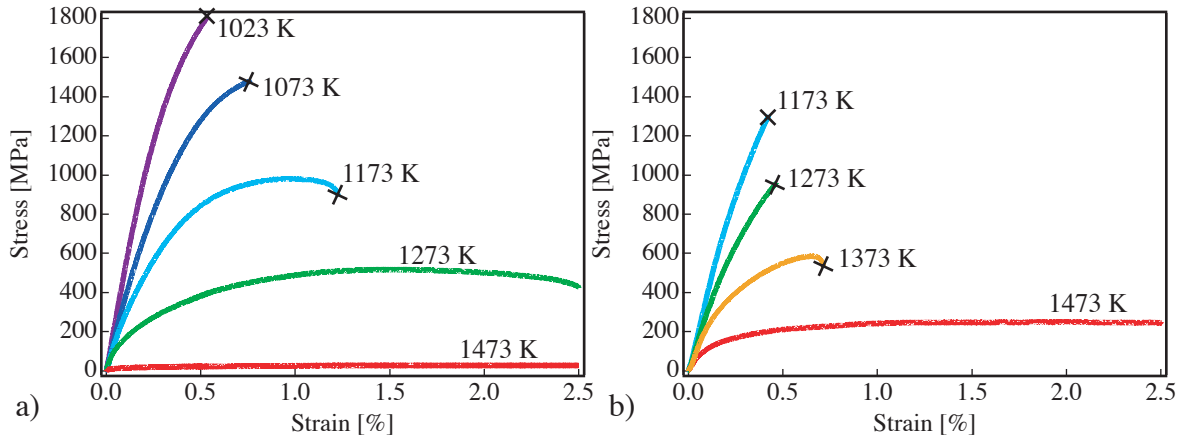

Figure 4.1: Measurements performed at different temperatures showing transitions from brittle to ductile and to highly plastic behavior. a) WC-Co and b) TiWCN-Co

A similar behavior is observed in TiWCN-Co (Fig. 4.1b). The flow stress decreases and the fracture strain increases with increasing temperature. The cermet is, in general, more refractory than the WC-Co. A comparison of the results at the same temperature shows that flow stresses of the cermet are higher and fracture strains lower than those of WC-Co.

2 The hard phase skeleton

In a certain range of binder volume fraction, between 5 and 20 vol.%, where the binder and the hard phase form continuously interconnected phases, the binder can be removed from the composite by chemical etching, leaving behind a rigid, purely ceramic, but very porous sample. These samples can be measured in the same way as the composites. Because of the reduced cross-section (no correction is applied here), the stress-strain curves of the skeletons should lie below the corresponding composite curve both in the elastic and plastic deformation regions. As shown in Fig. 4.2, this is true for temperatures below a certain threshold. At higher temperatures, the not-corrected skeleton curve lies above the composite curve. The skeleton appears to be stronger, even though more brittle, than the hard material composite. The temperature that marks the change from one to the other behavior, should be a transition temperature between two different deformation mechanisms. The high-temperature region shows higher plasticity, when cobalt is present, whereas the skeleton alone appears to be very brittle.

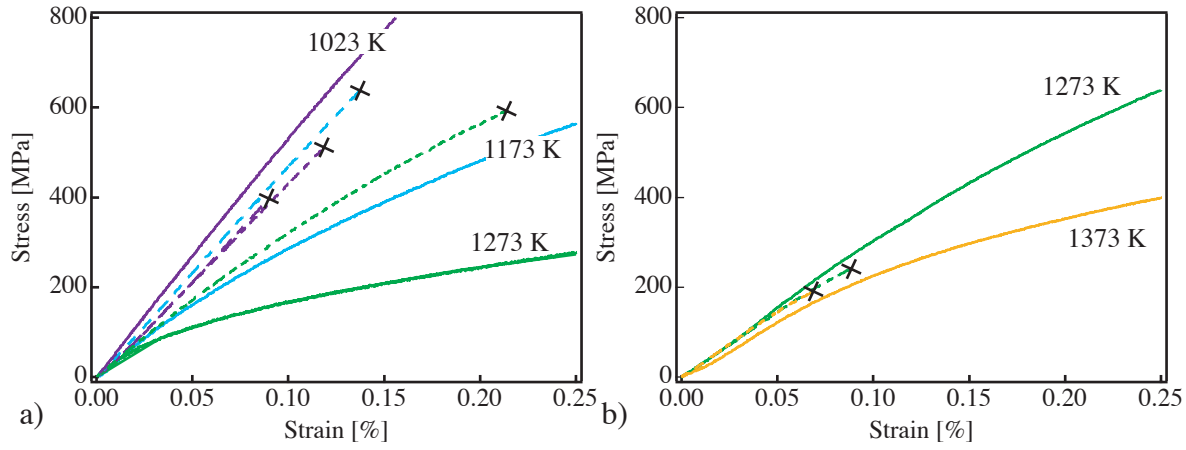

Figure 4.2: The transition between bulk deformation and cobalt enhanced creep is experimentally shown by comparing WC-Co (a) and TiWCN-Co (b) complete samples with their hard phase skeletons (dashed).

For WC-Co, this transition appears between 1023 and 1173 K. In the cermet, this transition temperature is much higher, between 1273 and 1373 K.

A comparison of the skeleton samples at two different temperatures is shown in Fig. 4.3. Some plastic deformation is seen in both materials, but the WC skeleton exhibits higher yield stresses and strain at fracture than the TiWCN skeleton. The stress at fracture of the WC skeleton is always higher than that of the TiWCN skeleton.

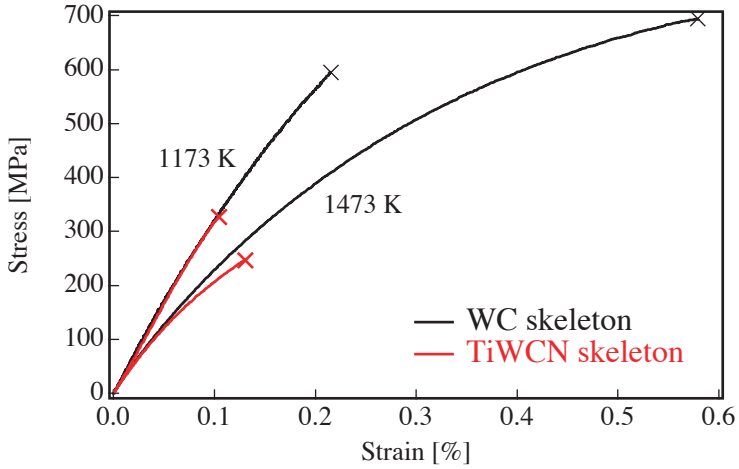

Figure 4.3: Stress-strain curves of WC and TiWCN skeletons showing the more refractory behavior of the cermet

3 Activation energy of creep

The activation energy of creep is determined by the temperature jump method (see Chapter 3 §2.3.2). Several temperature jumps can be performed on one specimen. Fig. 4.4 shows the activation energies measured at different temperatures. One point always stands for one discrete temperature jump, but the results of several samples, measured in overlapping temperature regimes, are shown together.

The WC-Co (Fig. 4.4 a) shows an activation energy of approximately (3.5±0.5) eV below 1200 K. Above 1200 K, the activation energy is around 6 eV with a trend towards even higher values with increasing temperature. The temperature of transition between the energy levels is not well defined.

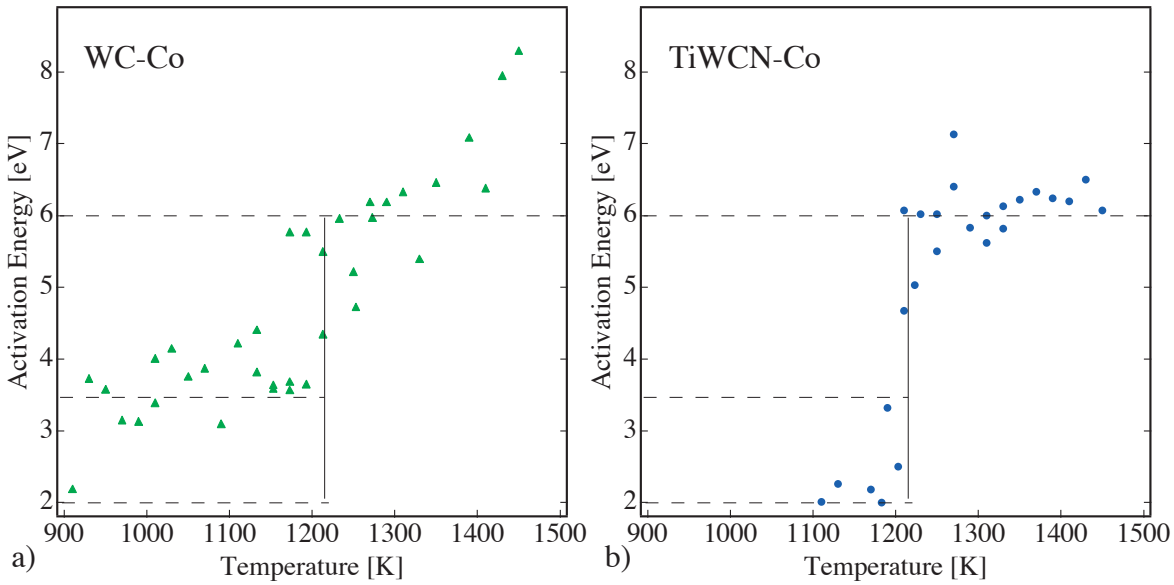

Figure 4.4: Activation energy of creep measured with the temperature jump method for (a) WC-Co and (b) TiWCN-Co

The cermet (Fig. 4.4 b) shows two well defined energy levels, i.e. 6 eV above 1200 K and ca. 2 eV between 1100 and 1200 K. At lower temperatures, the material is too brittle and breaks without creep. A transition temperature of 1200 K is evidenced in cermets experiments.

The transition in creep does not correspond exactly with the transitions defined in paragraph 2. In fact, the applied stress can influence the high temperature deformation behavior (Fig. 2.9 and Fig. 2.10). However, the stress applied during the temperature jump experiment has to be adapted to the temperature (the lower the temperature the higher the stress). If the stress is too high, then the strain rate becomes large, above 10^{-4} s^{-1}, and the creep does not reach a steady state. On the contrary, if the stress is too small and the strain rates drop below 10^{-8} s^{-1}, the instabilities of the setup become significant. The stress is therefore kept constant over a small number of jumps and it is changed from time to time to insure reasonable creep rates. Fig. 4.5 presents the stress applied during the creep experiments shown in Fig. 4.4 as a function of creep temperature. The stress decreases with increasing temperature. The relationship of σ versus $1/T$ can give an indication of the nature of the deformation process. Indeed, the slope of the curves change. The temperatures of the change correspond well to the temperatures of transition defined in paragraph 2.

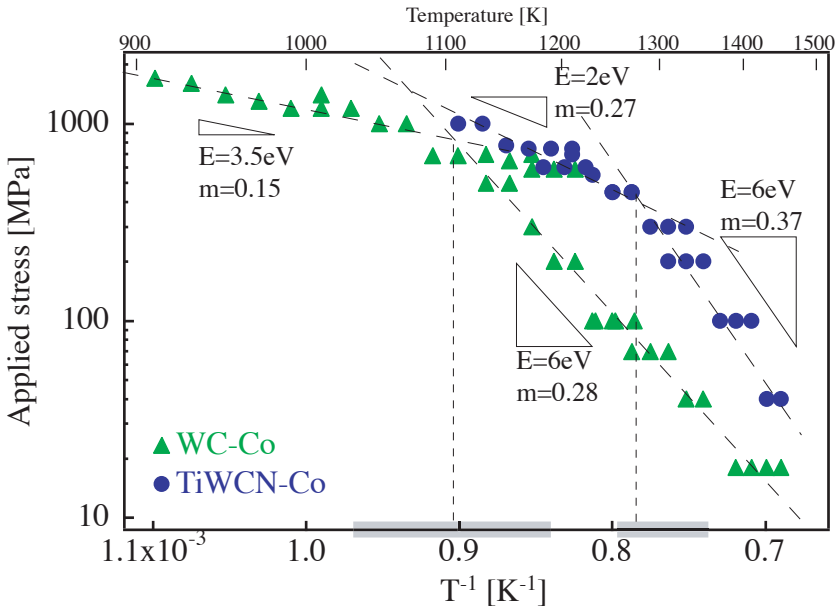

Figure 4.5: Applied stress versus temperature corresponding to the results of Fig. 4.4. The temperature ranges of transition found in comparative deformation test of complete hardmetals and skeletons are indicated on the axis.

The general power law equation for the intermediate (secondary) steady-state creep regime is given by [50]

$$\dot{\varepsilon} = A\sigma^{n}\exp(-E/kT) \tag{4.1}$$

where n is the stress exponent and A is a constant. This formula yields

$$\sigma = \left(A'\dot{\varepsilon}\exp\frac{E}{kT}\right)^{m} \tag{4.2}$$

where $m=1/n$ is the strain rate sensitivity. Using the activation energies for the different regions shown in Fig. 4.4 and an average strain rate of $\dot{\varepsilon} = 10^{-7} s^{-1}$, the slope m and the constant A can be determined. The values for m are shown in Fig. 4.5. High values for the stress exponent are observed by many authors [73-75]. Roebuck et al. [76,77] point out, that Eq. (4.1) is basically valid for secondary creep by diffusion controlled dislocation climb, associated with a stress exponent of n=2. The high values for the stress exponent $n>5$ do not have a clear physical meaning. Therefore Eq. (4.1) should not be appropriate in that case. Moreover, at lower temperatures, the fit according to Eq. (4.1) is not satisfactory. For the high stress creep regime, Roebuck et al. propose the following expression

$$\dot{\varepsilon} = B e^{\beta\sigma} e^{\frac{-E}{kT}} \tag{4.3}$$

where B and β are constants [76,77]. The authors state that the activation energies obtained with Eq. (4.3) are not really meaningful. Fig. 4.6 shows the fitting of the high stress regions with Eq. (4.3). The temperatures marking the transition between the power law creep and the high stress creep are close to the ones found in §2.

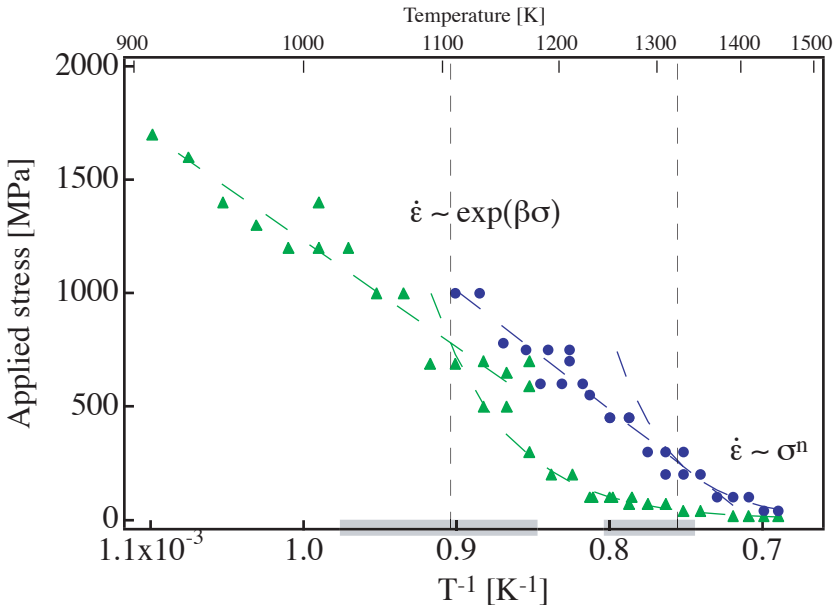

Figure 4.6: Same as Fig. 4.5, but the low temperature (high stress) regime is fitted with Eq. (4.3)

4 Main conclusions

Three main conclusions can be formulated at this point:

1. The transition between domain II and domain III as defined in Chapter 2 is observed in stress-strain experiments and in creep tests.

WC-Co shows the transition at lower temperature than the cermet. It is situated at 1100±75 K in WC-Co and at 1325±50 K in the cermet. The transition is evidenced in two different experiments. On one hand, the transition is shown by the comparison of the deformation behavior of composites and skeletons. On the other hand, it is shown in creep experiments. Different activation energies can be attributed to domain II and III. A high value of 6 eV is found for domain

III and lower values, 2 eV for TiWCN-Co and 3.5 eV for WC-Co, are measured in domain II. The transition between the activation energy levels is located around 1200 K, but it is not very sharp in particular for WC-Co. However, the transition temperatures are clearly marked by the change of slope in the $\sigma(1/T)$ plot (Fig. 4.5) and the above defined transition temperatures are confirmed.

The measurement of the activation energy by the temperature jump experiment is, in general, not very sensitive to the applied stress. However, two regimes appear from applicable stress conditions (Fig. 4.5). This leads to the definition of a transition temperature between the regimes. In the temperature range of the transition, a stress sensitivity is probably present. Similar observations have been made by Mari et al. [24].

2. Typical signs for grain boundary sliding in temperature domain III are found in both materials.

Extensive deformation with strains up to 5 % is observed at 1473 K with very low flow stresses. The creep activation energy is 6 eV for both cermets and cemented carbides in this domain. The important role of cobalt for the high temperature deformation is demonstrated with the measurements of the skeletons. Cobalt clearly enhances the creep deformation in domain III.

3. TiWCN-Co is more refractory than WC-Co.

The cermet is clearly more refractory at all temperatures. At 1473 K, the cermet shows a flow stress that is ten times higher than that of WC-Co. The transition temperatures between domains II and III differ by 200 K. The WC skeleton is much tougher than the TiWCN skeleton (Fig. 4.3). Already at 1173 K, the WC shows a two times higher yield stress and strain at fracture than the cermet skeleton, at 1473 K the difference is even larger.

Different morphologies of the skeletons allow only a qualitative explanation of the phenomenon. However, the differences observed in the fracture stress between WC and TiWCN skeletons show that part of the toughness of the WC-Co should also be attributed to the intrinsic toughness of the WC skeleton. A possible justification of the observed differences may come from the difference in Young's modulus between the two materials. A general rule of fracture mechanics relates the critical fracture stress σ_c to Young's modulus E and the strain energy release rate G_{1c}, which is also a material constant by

$$EG_{1c} = K_{1c}^2 = \frac{\pi a}{2}\sigma_c^2 \tag{4.4}$$

where K_{1c} is the critical stress intensity factor and a is the initial crack length [78]. The critical crack length a should be similar for both skeletons as it depends on the voids left by the cobalt. Therefore, the critical stress σ_c varies as $\sqrt{E}$. Taking $E_{WC} = 700\text{GPa}$ and $E_{TiWCN} = 400\text{GPa}$, one could justify a ratio of fracture stress of 1.3. The curves in Fig. 4.3 show a ratio of more than 2 and increasing with temperature. It may be concluded that some intrinsic superior toughness exists in the WC skeleton. Moreover, as fracture is intergranular, the toughness should derive from an energy dissipation mechanism at grain boundaries.

Chapter 5

Residual stresses measured by diffraction

Residual stresses can be very important in hardmetals, because of a substantial difference in thermal expansion coefficient of the ceramic and the metal phase. They also play an important role for the mechanical properties of these materials. The residual stresses for WC-Co and TiWCN-Co have been assessed by diffraction techniques.

Diffraction of bulk WC-Co requires high-energy neutron diffraction to achieve a sufficient penetration depth, which could not be reached by X-rays, not even by synchrotron X-rays. Residual stresses are measured as a function of temperature in order to see how stresses are relaxed. Also the build-up of stresses after sintering is measured. However, stresses can relax during plastic deformation. Load transfer between the two phases of the hardmetal might occur. The internal stresses are therefore also measured as a function of applied tensile stress.

TiWCN-Co consists of lighter and less absorbing elements. The determination of residual stresses has therefore been performed by synchrotron X-ray diffraction. The stresses in cobalt and hard phase are measured as a function of temperature.

1 Residual stresses in WC-Co

1.1 Experimental program

Different samples of the same type and dimensions (Chapter 3 §3.2.1) have been subjected to different temperature/load programs. The programs of samples 1 to 8 are shown in Table 5.1. The complete program of sample 1 is presented in Fig. 5.1 as a function of time as an example. Some test performed beforehand with different data acquisition times showed that 1 hour is sufficient for a good peak to noise ratio at least for the determination of strains in the WC phase. However, the intensities of the cobalt peaks was sometimes too low to allow for a strain analysis.

The WC powder reference data (denominated #P) was obtained in one heating-cooling cycle.

Measurements after 2 hours in-situ sintering at 1650 K are performed at 1650, 1600, 1550, 1500, 1450, 1400, 1000 and 326 K to measure the build-up of residual stresses. The sample, shown in Fig. 3.4, is referred to as #S.

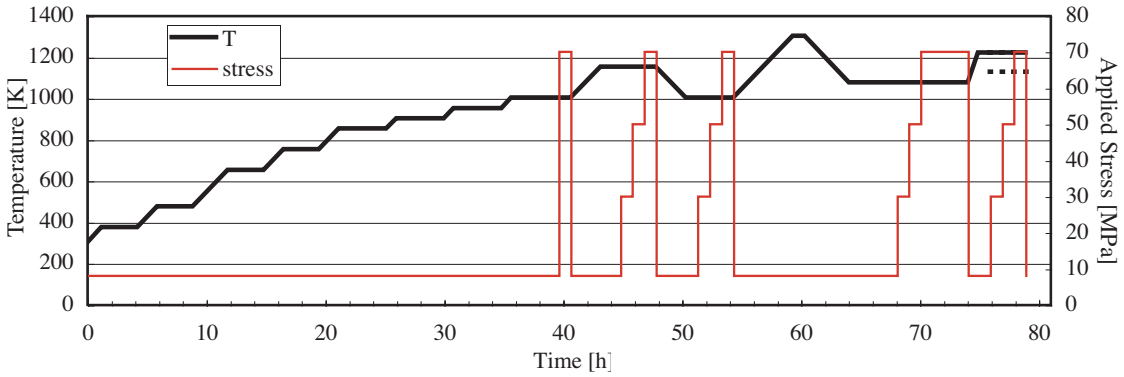

Figure 5.1: Experimental program for sample 1: temperature and load versus time

Table 5.1 : Temperature load programs for samples 1 to 8

sample no.	Temperatures [K]	load [MPa]
1	302, 373, 473, 650, 750, 850, 900, 950	8
1	1000	8, 70
1	1150	8, 30, 50, 70
1	1000	8, 30, 50, 70
1	1300	8
1	1075	8, 30, 50, 70
1	1225	8, 30, 50, 70
2	1000	8, 70
2	1300	8, 30, 50, 70
3	1375	8, 30
4	302, 374, 462, 557, 664, 773, 884, 1000	15
4	1000	15, 25, 35, 45, 55, 65, 75
5	1300	15, 25, 35, 45, 55, 65
6	1075	15, 30, 45, 60, 75, 90
6	1150	15, 30, 45, 60, 75
7	1375	15, 25, 35, 40
8	1225	15, 25, 35, 45, 55, 65, 75, 80

1.2 Data analysis

For every given combination of temperature and stress, there exist two spectra, one for the strains longitudinal to the stress axis and one for transversal strains. In principle, for isotropic samples, the results are the same in both longitudinal and transversal directions, when no stress is applied. Upon the application of a tensile stress, strains appearing longitudinally and transversely to the stress axis are measured separately on the two detector banks (Fig. 3.5a).

Strains are calculated for the two lattice parameters a and c of the hexagonal WC lattice with respect to the lattice parameters, a_0 and c_0, of a stress-free WC powder sample. The equations for the strains are:

$$\varepsilon_a = \frac{a - a_0}{a_0} \qquad \varepsilon_c = \frac{c - c_0}{c_0} \tag{5.1}$$

Stresses are determined using WC single crystal elastic constants [79] and the Reuss model as presented by Evenschor et al. [80] to calculate the homogeneous stress in the hexagonal WC phase using Eq. (5.2) [49].

$$\begin{aligned} \sigma_a &= 946\varepsilon_a + 259\varepsilon_c \\ \sigma_c &= 627\varepsilon_a + 998\varepsilon_c \end{aligned} \tag{5.2}$$

The mean or hydrostatic stress is calculated using Eq. (5.3)

$$\sigma_h = \frac{2\sigma_a + \sigma_c}{3} \tag{5.3}$$

The stresses in the cobalt cannot be calculated due to the missing reference. However, an attempt has been made to calculate the strains and stresses using the thermal expansion of pure fcc cobalt $\Delta a/a_0 = -0.343 + 1.105\times10^{-3}T + 1.93\times10^{-7}T^2 + 4.179\times10^{-11}T^3$ [81]. It is assumed that the thermal expansion of pure cobalt and that of the cobalt phase, which is alloyed with tungsten and carbon, show a similar general trend. The stresses appearing in the cobalt and in the WC phase must in any case obey the stress balance relation

$$f\sigma_{Co} + (1 - f)\sigma_{WC} = 0 \tag{5.4}$$

where f is the volume fraction of the cobalt.

1.3 The WC powder reference

The WC powder data was obtained in one heating-cooling cycle between room temperature and 1375 K. The curves shown in Fig. 5.2 show a slight deviation between heating and cooling. However, the heating curves correspond well to the thermal expansion found in [81]. The

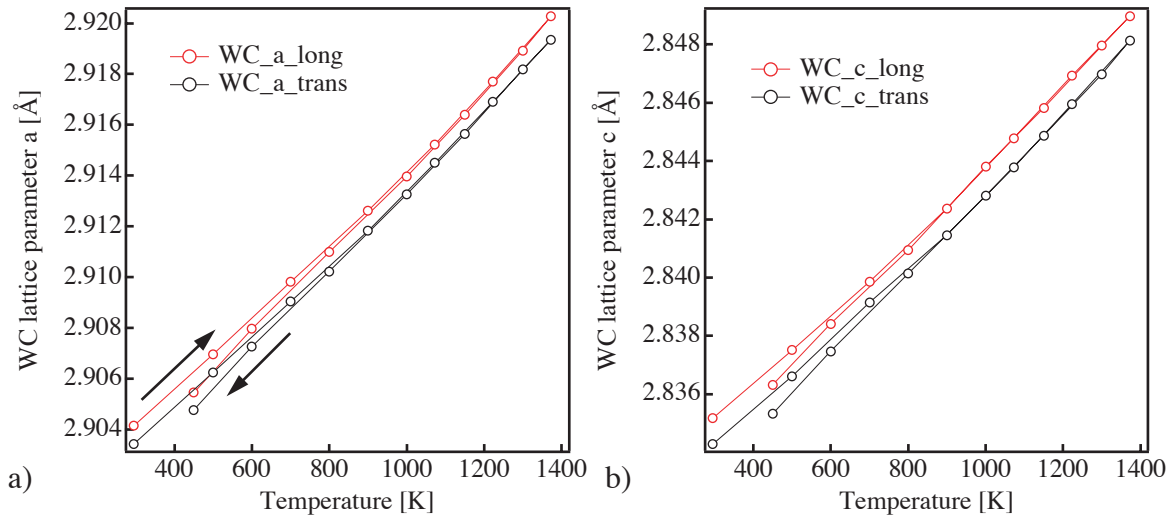

Figure 5.2: Lattice parameter a (a) and c (b) of WC reference powder for both, transversal and longitudinal, directions

heating part of the curves is fitted to be used as a reference. The fitted values are given in Table 5.2.

Table 5.2 : Polynomial coefficients for the fit of the WC powder lattice parameters as a function of temperature derived from the heating of the curves in Fig. 5.2 as $f(T) = \alpha+\beta T+\gamma T^2$

	α	β	γ
a [Å] long	2.9006±0.0002	$(1.18\pm0.05)10^{-5}$	$(1.9\pm0.3)10^{-9}$
a [Å] trans	2.8998±0.0001	$(1.20\pm0.04)10^{-5}$	$(1.6\pm0.2)10^{-9}$
c [Å] long	2.8321±0.0001	$(9.8\pm0.4)10^{-6}$	$(1.8\pm0.2)10^{-9}$
c [Å] trans	2.8313±0.0002	$(9.7\pm0.5)10^{-6}$	$(1.8\pm0.3)10^{-9}$

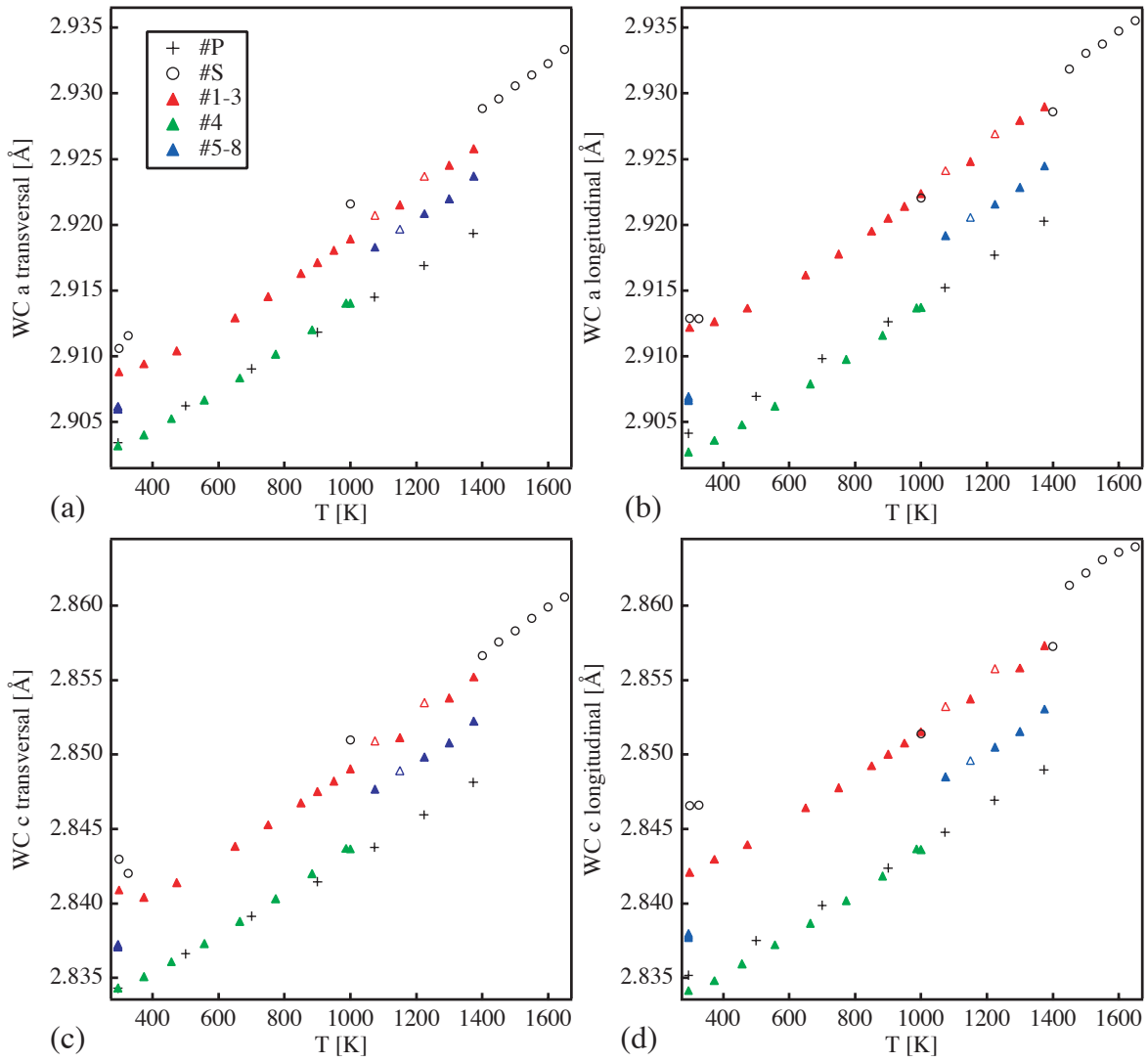

Figure 5.3: Lattice parameters *a* and *c* of hexagonal WC for the different data sets of bulk WC-Co samples 1-8 (Table 5.1), WC powder #P and the in-situ sintered WC-Co #S. The data sets present a relative offset. (a) parameter *a* measured transversely, (b) *a* longitudinally, (c) *c* transversely and (d) *c* longitudinally.

The longitudinal and transverse data should, in principle, be the same, as neither stresses nor texture are present in the powder. The difference (< 0.1 %) is likely caused by not perfect centering of the powder sample or to different detector bank calibration.

1.4 Residual stress as function of temperature (no load)

Fig. 5.3 shows the lattice parameters of WC for the two banks as function of the temperature. The data in these graphs are as determined by the Rietveld refinement [82]. A shift can be observed between the original data sets for different samples. The five different data sets (Fig. 5.3) have been measured at different times by different operators. The (non-permanent) setup being the same for all measurements had to be freshly installed each time. A small difference in alignment of sample and setup (of less than a millimeter or an angular degree) produces quite substantial differences in measured lattice spacing. Moreover, the calibration of the detectors can play a role. However, the mismatch is purely experimental and it is very difficult

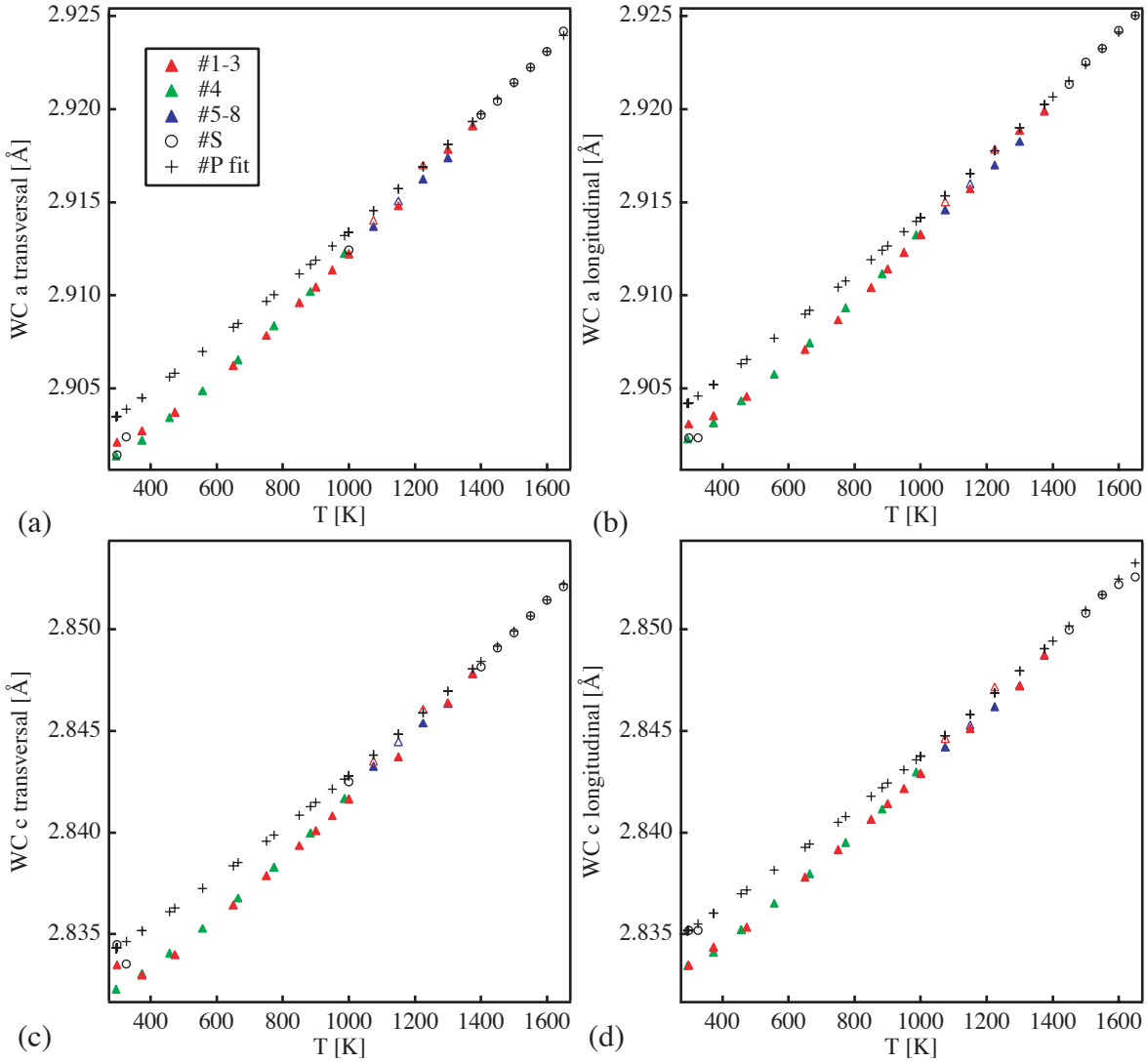

Figure 5.4: Lattice parameter *a* and *c* of hexagonal WC for the different data sets of bulk WC-Co samples 1-8, WC powder #P (fitted) and the in-situ sintered WC-Co #S after manual shift of the data. The open triangles are measured after creep. (a) parameter *a* measured transversely, (b) *a* longitudinally, (c) *c* transversely and (d) *c* longitudinally.

to avoid. It can be seen that measurements that were performed together (same markers) show a reasonable trend, whereas different runs performed at different times do not align very well. However, the offset between the curves is by no means physical. To be able to evaluate strains and stresses, the data sets are aligned. The aligned lattice parameters a and c for the two banks are presented in Fig. 5.4. The WC powder and the sintered sample are shifted so that they meet at 1550 K, where the 'zero' stress level is expected. The data sets of samples 1-3 and sample 4 are matched at 1000 K and the samples 5-8 are shifted to match with samples 1-3 at 1375 K. The combined data set (1-8) is then shifted to align with the sintered sample at 1375 K supposing that the stress built up is the same at this temperature. The maximum average error on the lattice parameters is $1 \cdot 10^{-4}$ Å. The bulk samples clearly present lower lattice parameters than the reference powder as expected from a phase under compression. The difference between bulk WC and WC powder decreases with increasing temperature.

The sintering data reported here must be taken with precaution and in particular the comparison of the data measured at room temperature before and after sintering. The data for the sin-

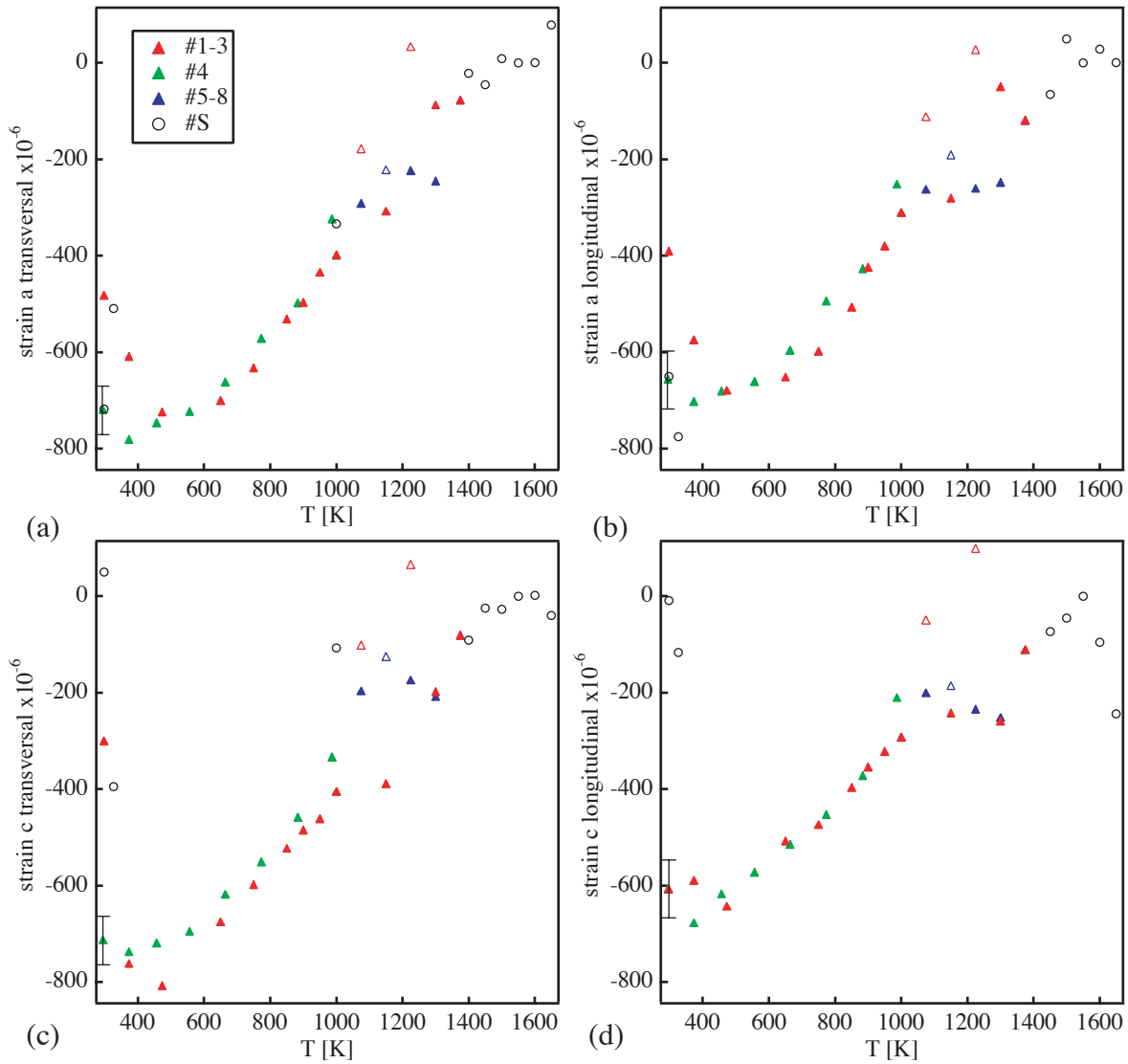

Figure 5.5: Lattice strains in the WC phase. Strains are compressive at room temperature and tend towards 'zero' with increasing temperature. The open triangles are measured after creep. (a) strain for *a* measured transversely, (b) for *a* longitudinally, (c) for *c* transversely and (d) for *c* longitudinally.

tering, especially for the longitudinal direction, is very scattered because low intensities of the WC peaks and a large influence of the graphite from the graphite container, in which the sample was kept, made the Rietveld refinement very difficult. Two points were removed for the longitudinal data of #S, i.e. 1400 and 1000 K, because clearly the low intensity made a reasonable fitting impossible.

Three points, at 1075 and 1225 K for sample 1 and at 1150 K for sample 6, are especially marked (open triangles) as these points have been obtained after the samples were subjected to creep (see also Table 5.1 for the follow-up of the measurements). It can be seen, and this becomes even more obvious in the calculated strains, that the lattice parameter (and therefore the internal stress) is somewhat higher, which means that internal stresses are relaxed during creep.

The strains for the directions *a* and *c*, calculated by Eq. (5.1), are presented in Fig. 5.5. The average error of the strains is $\pm 50 \cdot 10^{-6}$. The strains for *a* and *c* in the two directions are similar

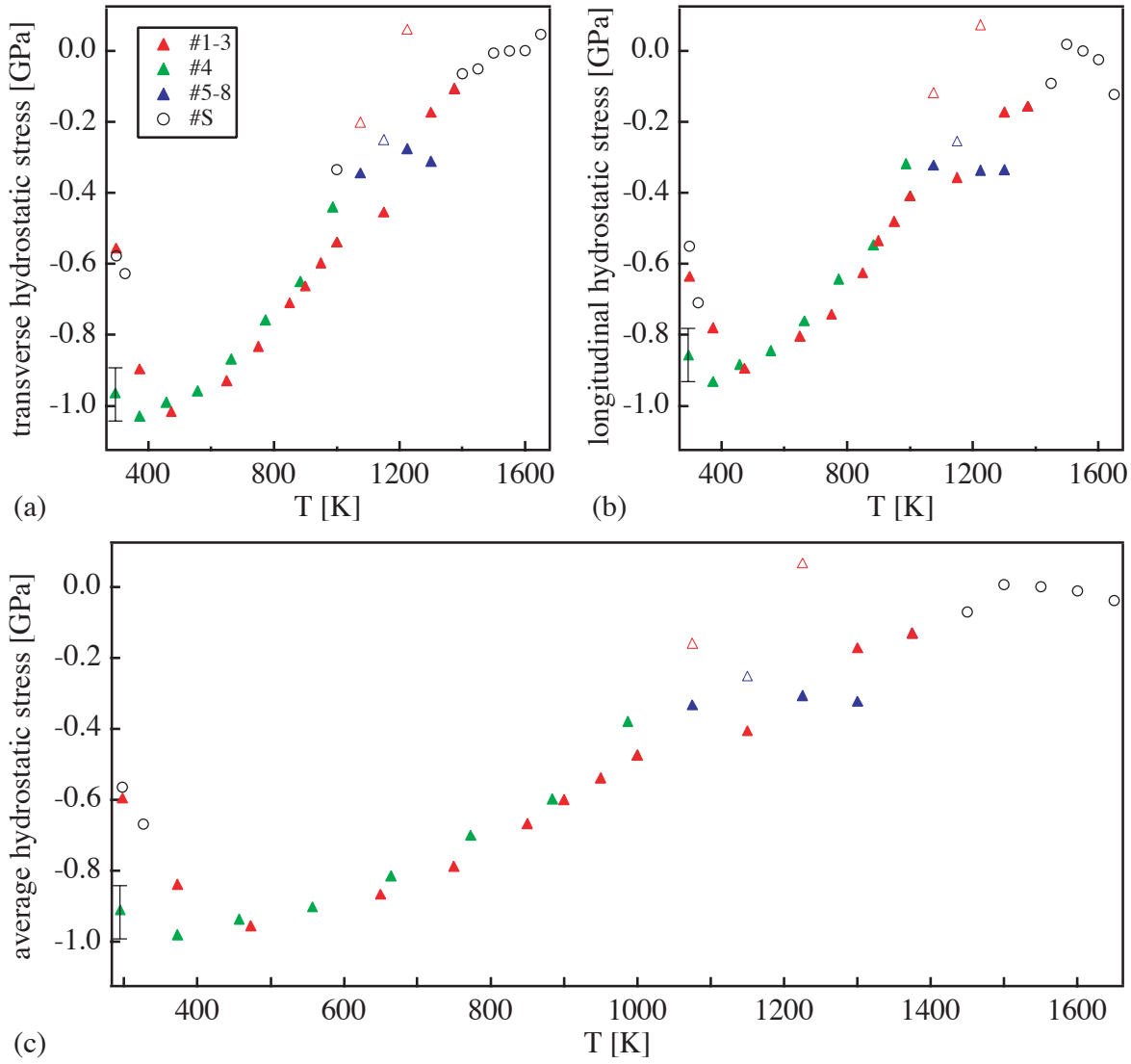

Figure 5.6: Hydrostatic stress in the WC hard phase of WC-Co bulk samples and the in-situ sintered WC-Co for the transverse direction (a), longitudinal direction (b) and the average (c) calculated from Fig. 5.5. The open triangles are measured after creep.

within this error, as expected from an isotropic material. The compressive strains are between 600 and $800 \cdot 10^{-6}$. The strains tend towards 'zero' with increasing temperature. Between 1000 and 1400 K, a small plateau is formed.

The stresses are calculated using Eq. (5.2). Supposing the thermal stress state of the material is isotropic, mean or hydrostatic stresses can be calculated by Eq. (5.3), which are presented in Fig. 5.6a and Fig. 5.6b. The hydrostatic stress is calculated as an average between the two banks (Fig. 5.6c). The residual compressive stresses, present in the WC phase, are of the order of 1 GPa at room temperature. The residual stresses tend towards 'zero' with increasing temperature.

To balance the residual stresses in the hard phase (Eq. (5.4)), the stresses in the cobalt should be about 4 GPa at room temperature.

The evolution of the cobalt lattice parameter is also determined. The data present an offset as for WC that is manually corrected for (Fig. 5.7a,b). As already justified in §1.2, the reference shown in Fig. 5.7 is pure cobalt. The absolute value of the lattice parameter of pure cobalt is expected to be lower than that of the present cobalt alloy. Therefore, the calculated strains and

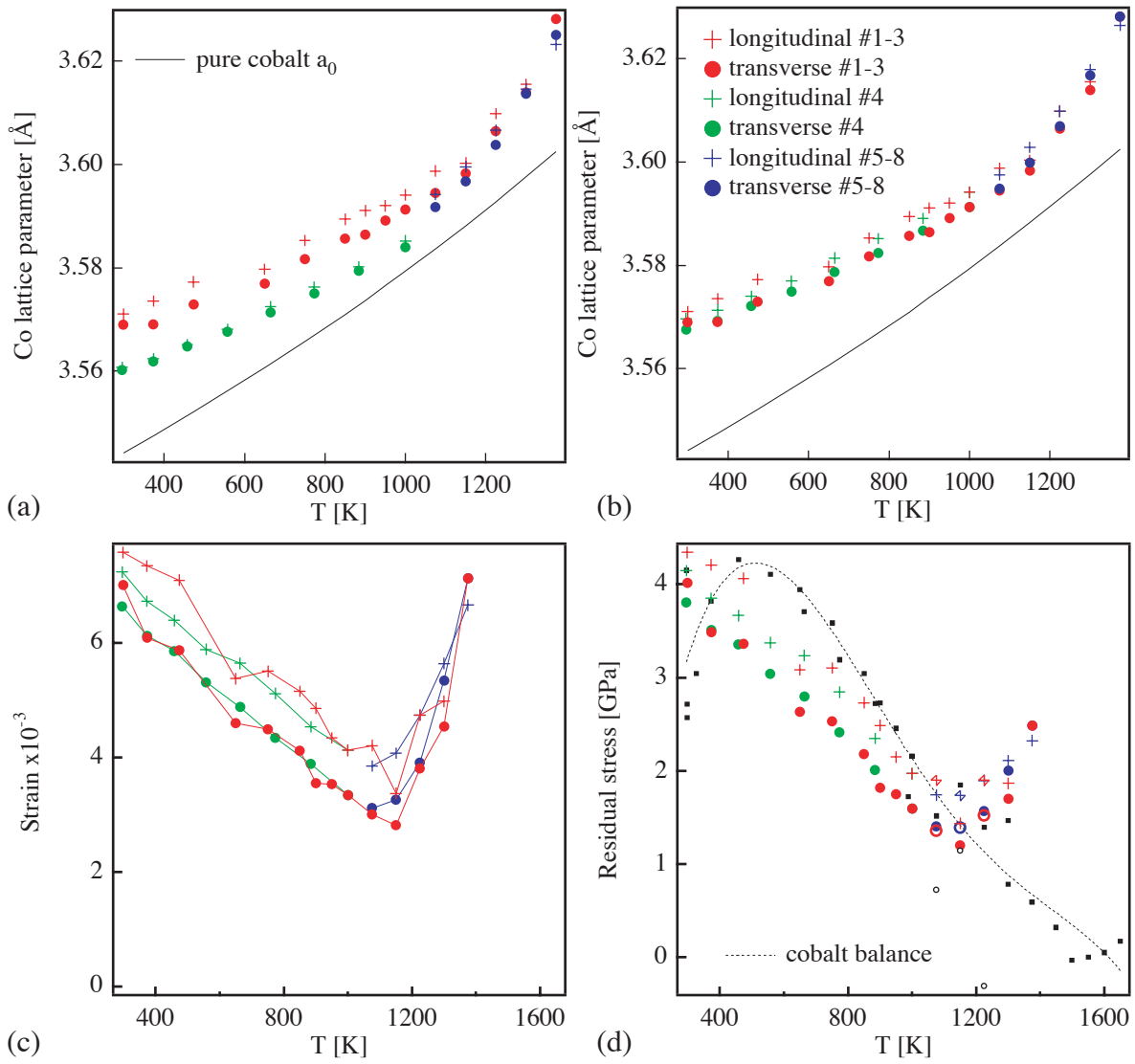

Figure 5.7: Cobalt: (a) lattice parameter as measured, (b) lattice parameter shifted, (c) strain and (d) stress

stresses are overestimated. The relative changes with temperature are, however, interesting. The strain (Fig. 5.7c) decreases with increasing temperature up to around 1100 K. From that temperature on the strain in the cobalt phase increases drastically. The decrease of strains is due to the relaxation of the huge residual stresses that are present in the cobalt at room temperature. However, the increase of strain starting at 1100 K cannot be justified mechanically. The increase of strain with increasing temperature is an effect of the change of the chemical composition of the cobalt, i.e. the solution of tungsten in the cobalt that causes an expansion of the cobalt lattice.

The cobalt stress is determined using the following equation

$$\sigma_{Co} = 3K_{Co}(T)\varepsilon_{Co} \tag{5.5}$$

where $K_{Co}(T)$ is the bulk modulus of cobalt [49]. The stress (Fig. 5.7d) shows a similar trend as the strain. As stated before, only relative changes of the cobalt stresses should be considered. However, as indicated in Fig. 5.7d, the cobalt balance stress calculated from the WC stresses by Eq. (5.4), is quite comparable to the measured cobalt stress.

1.5 Residual stress as function of load at different high temperatures

Diffraction spectra of WC-Co have been measured at different temperatures under applied tensile stress. As exemplarily shown in Fig. 5.8a, the stress is kept constant approximately 40 min, while a diffraction spectrum is acquired. At a given temperature, the lattice expansion compared to that at the minimum applied stress is determined. The measurements are performed at different temperatures (see Table 5.1). Fig. 5.8b shows the maximum attained strain during a creep test as function of the applied stress. Clearly, no or very little creep is observed at 1000 and 1150 K, while with increasing temperature the extent of creep increases. The cobalt peaks

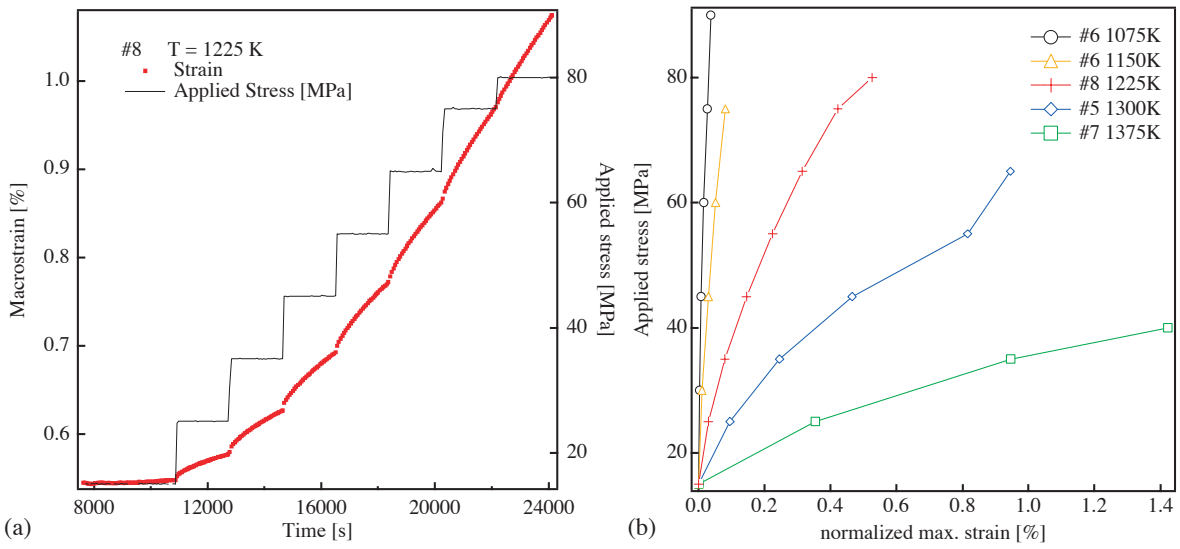

Figure 5.8: (a) Applied stress and strain measured by an additional extensometer as a function of time for the experiment on sample 8. (b) Applied stress vs. maximum strain for the stress experiments of samples 5-8.

are not resolved enough to allow for an evaluation of the stresses in the cobalt phase. The results for WC are presented as follows. The WC stresses in the samples 1-3 and 4-8 are presented in Fig. 5.9 and Fig. 5.10, respectively. For both directions, parallel (longitudinal) and

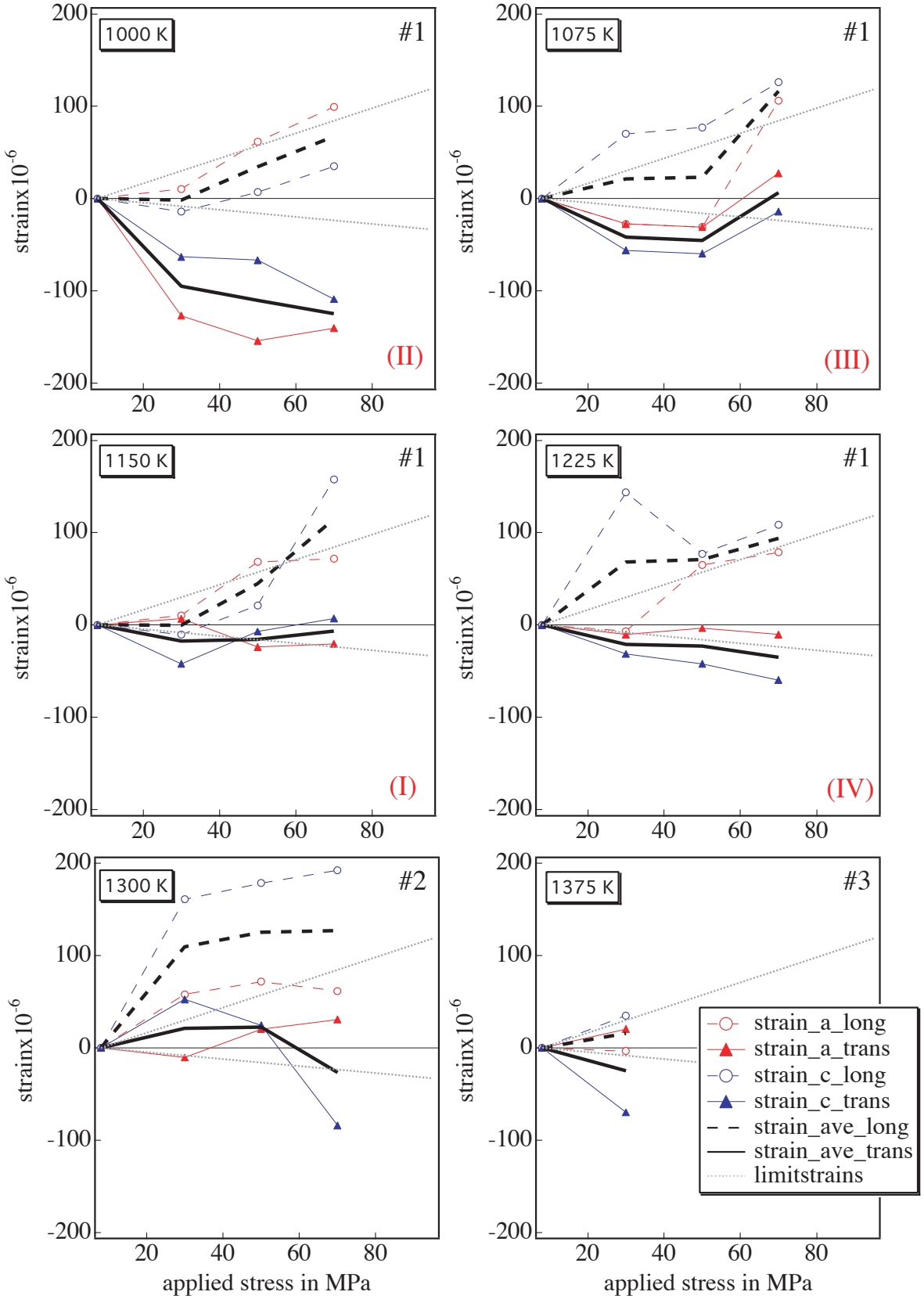

Figure 5.9: Strains measured longitudinal and transverse to the stress axis as a function of applied stress for six different temperatures. The elastic limits of WC in longitudinal and transverse directions are indicated as lines. The temperature of the measurement and the sample numbers are also indicated. Average error is about 100 microstrain.

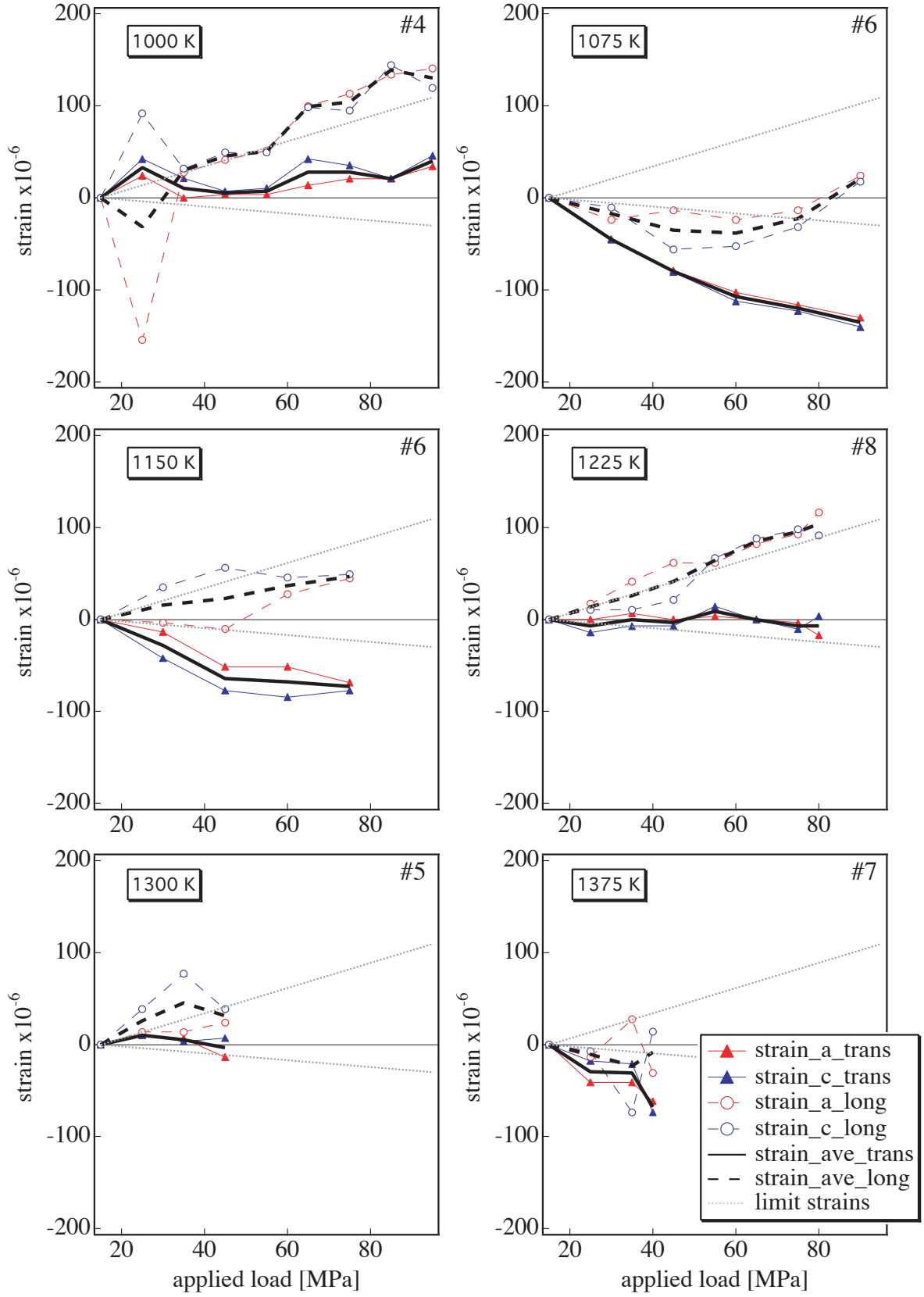

Figure 5.10: Strains measured longitudinal and transverse to the stress axis as a function of applied stress for six different temperatures. The elastic limits of WC in longitudinal and transverse directions are indicated as lines. The temperature of the measurement and the sample numbers are also indicated. Average error is about 70 microstrain.

perpendicular (transverse) to the stress axis, the strains for both lattice parameters, a and c, are presented together with an average of the two in order to minimize the scatter. On each graph, the elastic deformation limit of WC in longitudinal and transverse direction calculated according to Eshelby's model (see Appendix) are also indicated. An interpretation of these results will be given in §3.1.4.

2 Residual stresses in TiWCN-Co

2.1 TiWCN core-rim structure peaks

The hard phase of TiWCN-Co consists of three parts, i.e. core, inner rim and outer rim. The crystal structure, fcc, is the same for all three parts, which differ mainly in the amount of dissolved tungsten [16,83]. Therefore, a splitting of the diffraction peaks is expected, as the lattice spacing increases with increasing tungsten content. Effectively, it is observed that the TiCN peaks show a shoulder both at the high d-spacing and at the low d-spacing side of the peak, which correspond to the inner rim and to the core, respectively (Fig. 5.11). The main central peak is due to the outer rim phase, which constitutes with about 64 vol.% the main phase of this material. However, the splitting of the peaks is more pronounced in peaks with higher indexes, hence lower d-spacing. The most intense peaks <111> and <200> (Fig. 5.14) show only very little peak splitting. In order to have good fitting results with good statistics, the peaks <220>, <311> and <222> are chosen for the evaluation of the data. Each peak is analyzed by fitting it with three peaks of type "Pearson VII" with the *MacDiff* program (Fig. 5.11). The d-spacing is converted to the lattice parameter of the cubic lattice, which is then averaged over the three crystal planes.

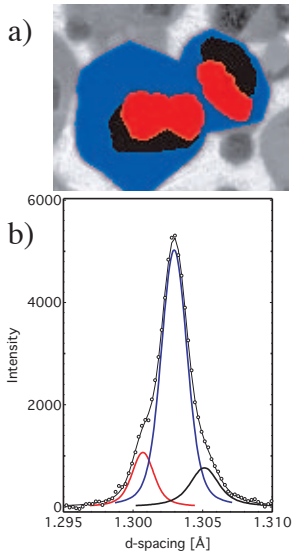

Figure 5.11: a) Core (red), inner rim (black) and outer rim (blue); b) peak splitting of <311> TiCN peak

2.2 Powder thermal expansion

A good reference is the basis of this type of residual stress measurements. In Fig. 5.12, the evolution of the lattice parameter of the insert powder as a function of temperature is shown together with the measurement of $TiC_{0.4}N_{0.6}$ raw powder. As the powder is free from internal stresses, the graph represents the thermal expansion.

The $TiC_{0.4}N_{0.6}$ powder is a single phase powder and therefore it shows a single lattice parameter. The core of the insert powder has, despite the small difference in the absolute lattice parameter due to a difference in the C/N ratio, a very similar thermal expansion as the $TiC_{0.4}N_{0.6}$ powder. The thermal expansion of the rim instead is lower in the low temperature range and seems to decrease with increasing tungsten concentration (inner rim). The difference is evidenced in Fig. 5.12 by the shifted curve of the $TiC_{0.4}N_{0.6}$ powder. The measured insert powder thermal expansion for core, inner rim and outer rim is fitted with a polynomial (Table 5.3) and will be used as reference for the strain calculation.

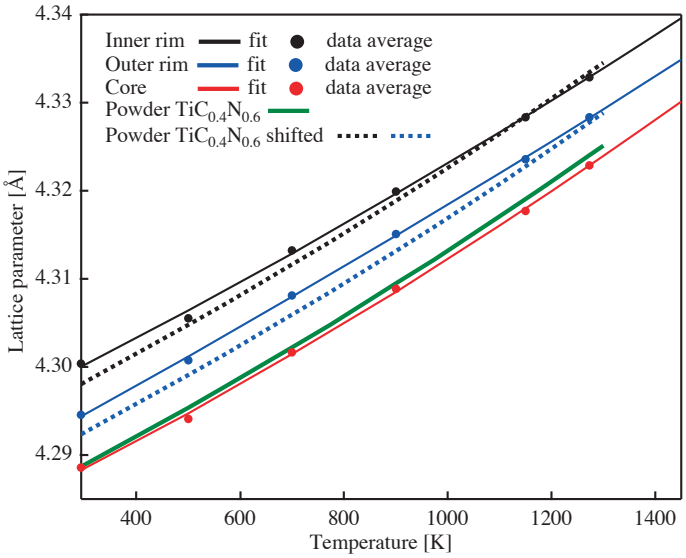

Figure 5.12: Thermal expansion of the reference powder

Table 5.3 : Polynomial coefficients for the TiWCN reference powder lattice parameters shown in Fig. 5.12 as $f(T) = \alpha+\beta T+\gamma T^2$

	α	β	γ
a (inner rim) [Å]	4.291±0.002	$(2.8\pm0.4)10^{-5}$	$(3\pm2)10^{-9}$
a (outer rim) [Å]	4.2851±0.0008	$(3.1\pm0.2)10^{-5}$	$(2\pm1)10^{-9}$
a (core) [Å]	4.280±0.001	$(2.7\pm0.3)10^{-5}$	$(5\pm2)10^{-9}$

2.3 Residual stresses in cermet

Two TiWCN-Co samples have been measured, one in two heating-cooling cycles, C1_1st and C1_2nd, and another, C2, with just one cycle. The temperature-time programs of the runs are schematically presented in Fig. 5.13. The acquisition of the X-ray spectra is performed during

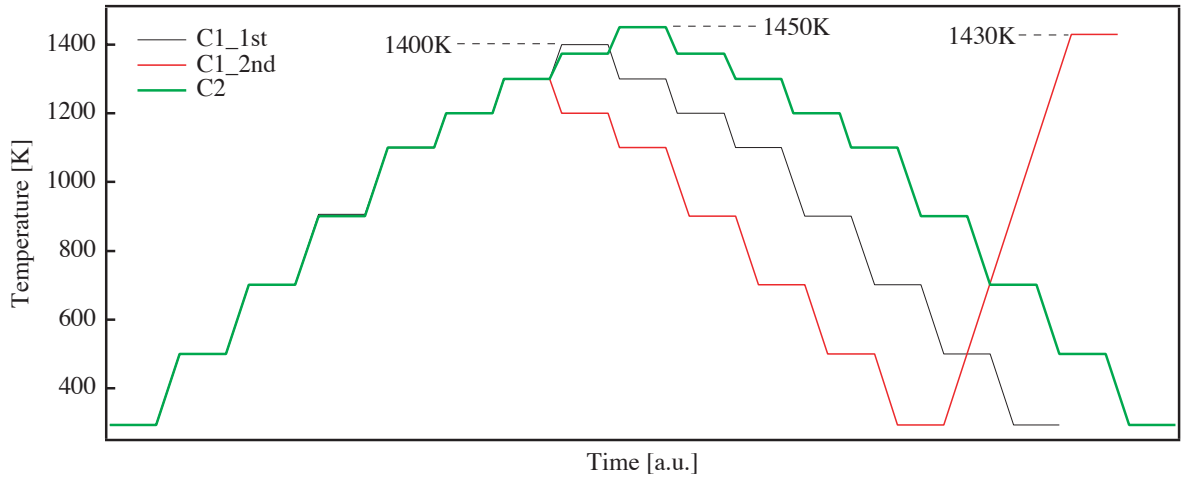

Figure 5.13: Temperature-time programs of the three runs

the dwell. Only the part of the spectrum with the five main TiCN peaks and the three main cobalt peaks (Fig. 5.14) has been measured. The evolution of the lattice parameter of the three-fold TiWCN structure as a function of temperature is presented in Fig. 5.15. All three runs show quite consistent trends. However, a difference between the two samples exists at high temperature, i.e. the inner rim of sample C1 shows an increase of lattice spacing as compared to sample C2 in both runs. This increase of lattice spacing appears at temperatures above 1200 K. During cooling below 1200 K, the general trend of all runs is again similar.

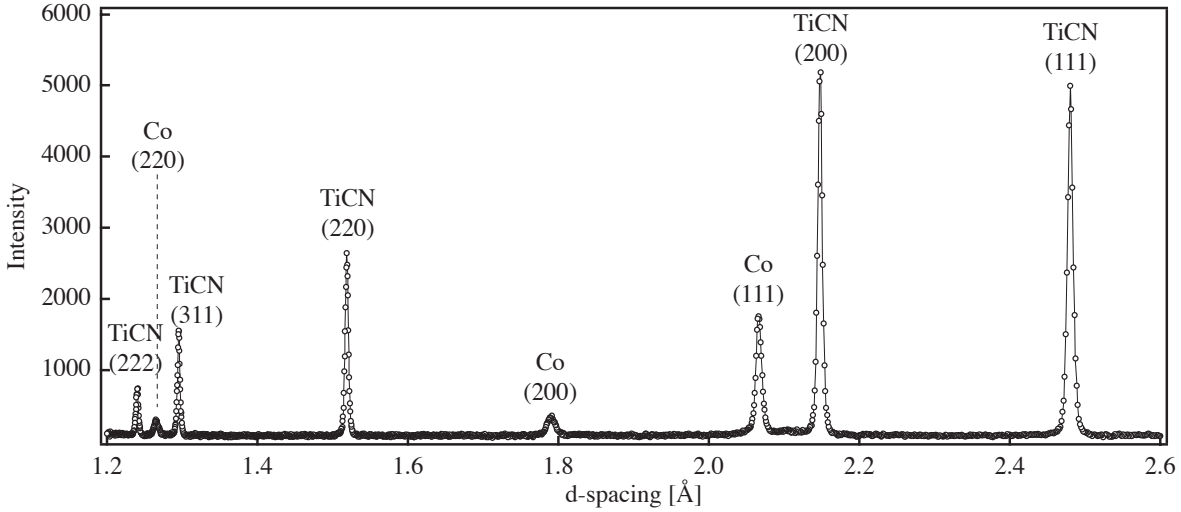

Figure 5.14: Typical X-ray spectrum of TiWCN-Co with indication of the main peaks of the two phases

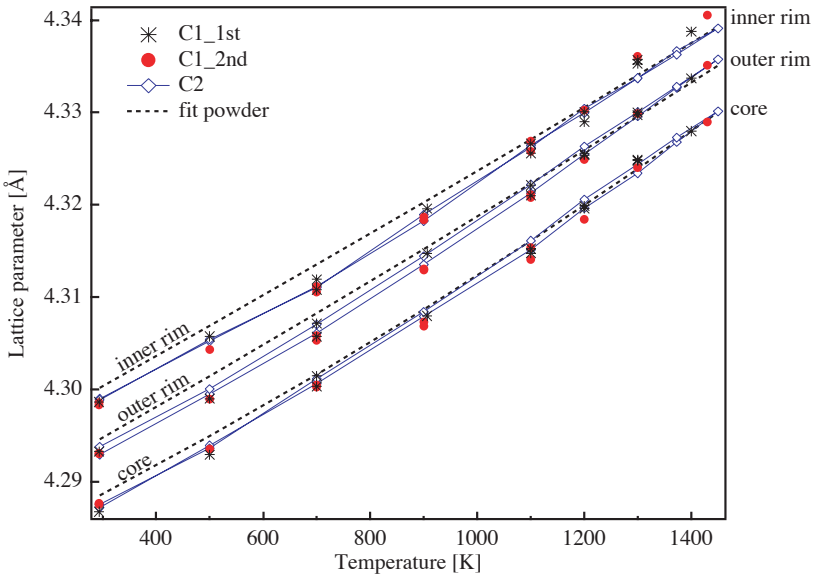

Figure 5.15: Thermal expansion of TiWCN cermet hard phase

The strain present in the hard phase can be calculated as

$$\varepsilon_i = \frac{a_i - a_{i,0}}{a_{i,0}} \tag{5.6}$$

where the index i stands for one part of the hard phase: core, inner rim or outer rim. The strains (Fig. 5.16) vary between $-6 \cdot 10^{-4}$ and 'zero' and they are lowest in the core. The stresses are calculated using $\sigma_i = 3\varepsilon_i K$, with the bulk modulus K taken as an average constant value of 314 GPa. This is a strong approximation in order to find the order of magnitude of residual stresses. The calculated stresses reach a maximum compressive stress of about 300 MPa. The stresses in the core are slightly lower. The stresses of the outer rim present a difference between heating and cooling during the first run in form of a hysteresis.

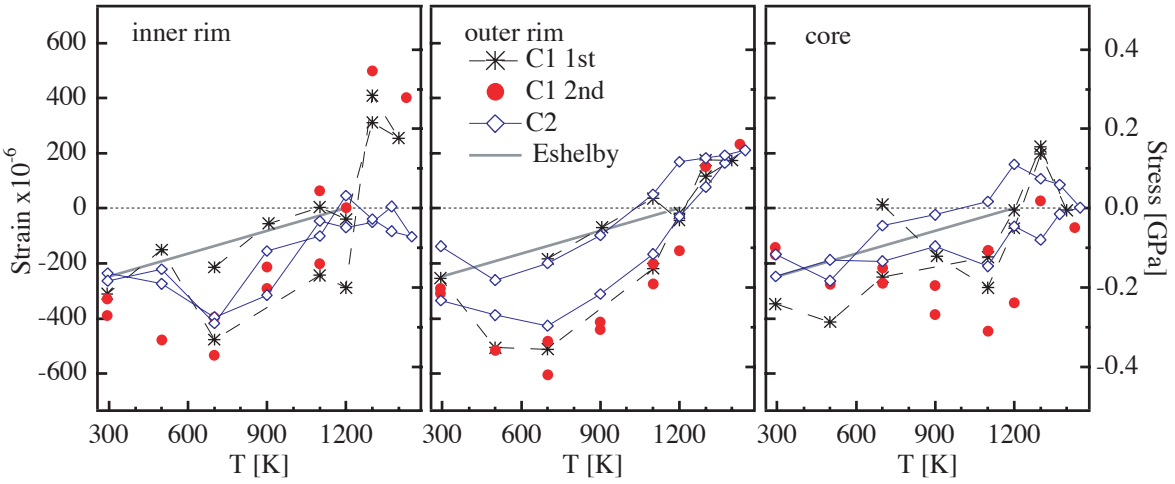

Figure 5.16: Strains and stresses (right axis) for the core-rim structured hard phase of TiWCN-Co. The expected behavior according to Eshelby is indicated by the gray lines.

The stresses in the cobalt phase are, due to the force balance equation, about 10 times higher than those in the hard phase and hence easier to assess. Fig. 5.17 shows the measured lattice parameter of the cobalt as a function of temperature. Out of lack of a good reference of the binder phase, which takes into account the alloying with tungsten, carbon and some titanium,

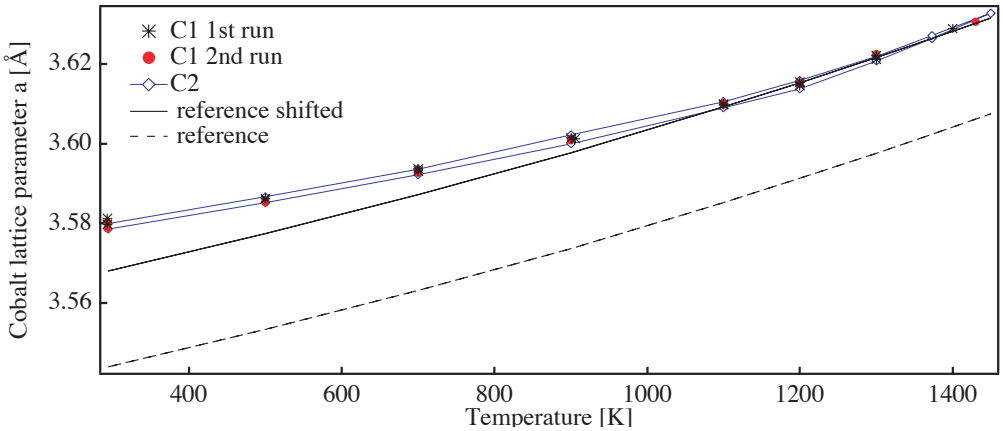

Figure 5.17: Evolution of the cobalt lattice parameter with temperature and the thermal expansion of pure, stress-free cobalt. The reference is shifted to account for the alloying effect of dissolved elements.

pure cobalt has been chosen as reference assuming that the thermal expansion is the same and that only the absolute values are shifted due to the alloying. By shifting the pure cobalt curve up to match the measured cobalt phase at high temperatures, a good agreement is found in this region. The calculated strains and stresses are presented in Fig. 5.18. The strains in cobalt reach a level of $3 \cdot 10^{-3}$ at room temperature. The cobalt stress is calculated using Hooke's law with the temperature dependent bulk modulus $K_{Co}(T)$ [49], using expression $\sigma_{Co} = 3\varepsilon_{Co} K_{Co}(T)$. The calculated stresses show that the cobalt phase is under tension at room temperature and that these stresses are relaxed during heating up. The internal stresses tend to 'zero' at ca. 1200 K.

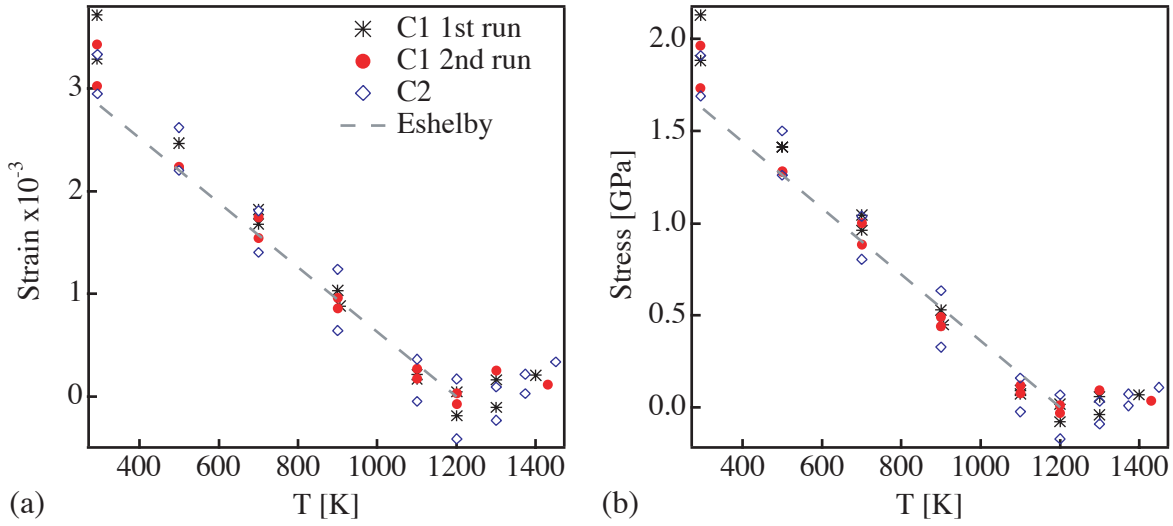

Figure 5.18: (a) Strains and (b) stresses in the cobalt phase. The behavior according to the Eshelby model is indicated as dashed lines.

2.4 Structural changes - appearance of additional phases

During the course of the experiment, additional peaks appear in the spectra. The following phases have been identified: TiO_2, WCo_3, W_6Co_6C and W_6Co_7. The TiO_2 forms at the outer surface. A thin white oxide layer was present on the surfaces of the samples after the measurements that could easily be scraped off. The WCo_3 appears during heating at 1200 K. It is not present at temperatures above 1400 K, which is in agreement with the phase diagram [84]. The WCo_3 peaks increase during cooling down, hence the amount of WCo_3 increases. A small amount of W_6Co_6C appears at temperatures above 1200 K. W_6Co_7 appears during heating at 1200 K and remains stable also during the cooling. No signs of hexagonal cobalt have been found in these experiments.

3 Discussion

3.1 WC-Co

3.1.1 WC phase

Residual thermal stresses in cobalt and WC have been measured. The stresses in the cobalt phase are tensile at room temperature, those in WC are compressive as expected. The build-up of stresses was measured during in-situ sintering. In the WC phase, the stresses reach around 1 GPa at room temperature. The thermal stresses relax with increasing temperature. However, between 1100 and 1300 K a small plateau is observed, i.e. the WC remains in an almost constant compressed state over a limited temperature range. From 1300 K on, the stress relaxation continues.

Another interesting aspect arises from the few measurements at 'zero'-stress after having crept the specimen at another temperature under applied stress (Fig. 5.19). The residual stresses measured after creep are clearly reduced, which indicates that stress relaxation occurs during creep. The extent of stress relaxation during creep increases following more severe creep conditions, which is indicated in Fig. 5.19.

The measurement of the creep relaxation justifies the alignment of the measured data with the powder at high temperature. This shift fixed the 'zero'-stress level to temperature of 1550 K. It may be argued that the stresses are 'zero' at the plateau between 1100 and 1300 K. However, this would then result in significant tensile stresses of points (1), (2) and (3) of Fig. 5.19, much higher than macroscopic yield stress at these temperatures. Such tensile stresses in WC after creep are unlikely to appear. Therefore, the chosen 'zero'-stress level seems to be appropriate. Moreover, the appearance of the cobalt peaks after the in-situ sintering showing the solidification of the binder is observed at about 1550 K.

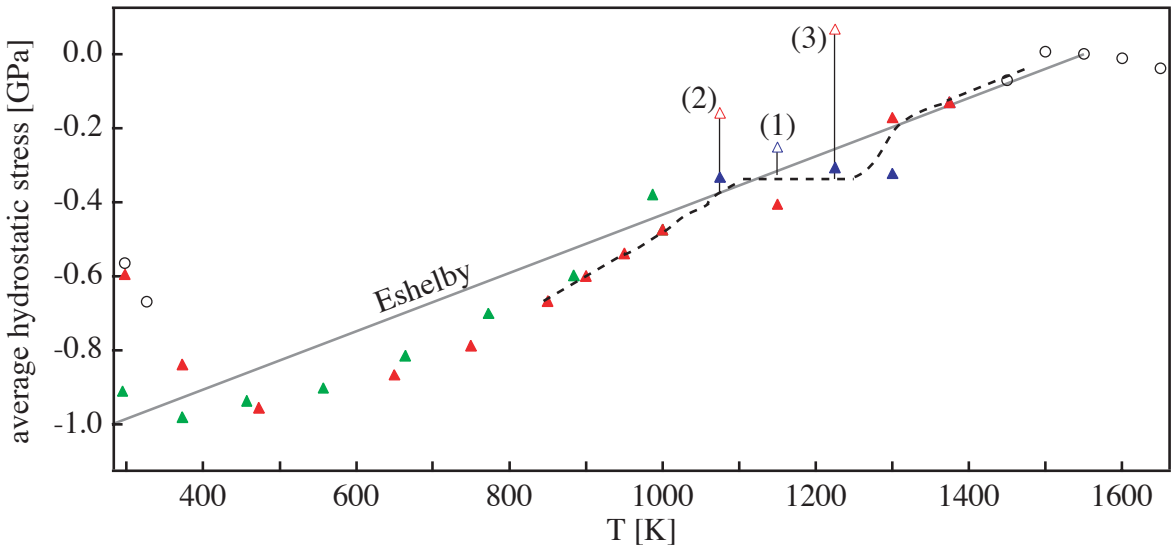

Figure 5.19: Relaxation of stresses during creep. (1) was obtained after creep at 1075 K, (2) was obtained after creep at 1150 K and (3) was obtained after creep at 1150 and 1075 K.

3.1.2 Cobalt phase

The absolute value of stresses in the cobalt cannot be derived because of lack of an appropriate reference with the same alloy composition. The trend of the evolution as a function of temperature should be however correct. The cobalt stress relaxes (quite linearly) until 1100 K, which corresponds to the expected relaxation of thermal stresses. However, above 1100 K the lattice parameter of the cobalt phase increases much more rapidly than that of the reference. Such an increase is so remarkable that it cannot be justified by a possible difference between the thermal expansion of pure cobalt and the present cobalt alloy. It is likely that the tungsten solution becomes important at these temperatures. The expansion of the cobalt lattice can therefore be explained by the increasing concentration of soluted tungsten. The increase of stress above 1100 K is therefore not mechanical or thermal, but the thermal relaxation is masked by a large chemical effect. This hypothesis is supported by the fact that this increase is not observed in the cermet, where the tungsten content in solution in the cobalt is rather decreasing (see §3.2).

A comparison of the measured cobalt stresses with the stresses expected in the cobalt due to the balance with the WC phase (Eq. (5.4)) shows that the stress level of 4 GPa at room temperature is attained in both cases (Fig. 5.7). The measured stresses, which were supposed to be overestimated, are actually at the right level. Moreover, the region where a plateau is observed in the stresses of the WC phase is the temperature region where the cobalt starts to expand because of the increasing solution of tungsten.

The creep relaxation present in WC is expected to be evident in the cobalt phase as well. However, the three points measured after creep do not present a very special behavior in the cobalt. A possible explanation is a large amount of tungsten in solution in the cobalt after the long-lasting high temperature measurements. The expansion of the cobalt due to tungsten may compensate the possible stress relaxation.

3.1.3 Model for the plateau

A peculiar stress evolution similar to the plateau in the WC phase has been observed also by Mari et al. [49], where stresses are shown to relax until 1000 K and show a small increase of compression between 1000 and 1300 K. It is also in this temperature range where the solution of tungsten in cobalt produces an expansion of the cobalt lattice. The two effects may be linked. The increase of the cobalt volume by tungsten dissolution is at least partially compensated by the increase of the available volume for the cobalt phase due to the removed WC. A mismatch between the two volume changes is present [49]. The increase of the cobalt volume due to WC dissolution is smaller than the volume freed by removed WC from the hard phase. The expected stresses due to this effect would produce compression of the WC, which could explain the plateau between 1100 and 1300 K. However, the volume changes, approximated by a simple model by Mari et al. [49] and by a thermodynamical model proposed by Uhrenius [85], are effectively too small to produce the observed effect (see Appendix). On the other hand, the models do not consider that tungsten might enter vacancy sites in the cobalt lattice. At this high temperature, a fair amount of vacancies is expected inside the cobalt. As cobalt is under tension, dislocation climb can act as additional vacancy source. The volume expansion of the cobalt due to a certain amount of dissolved WC may therefore be substantially smaller than predicted by the models. The plateau between 1100 and 1300 K may be justified in this case.

3.1.4 Effect of applied stress

The tests on samples 1-3 were preliminary ones used for a feasibility study. Therefore, the experimental schedule is somewhat uncoordinated. The results are however presented, keeping in mind the order in which the experiments were carried out, i.e. 1150 K, 1000 K, 1075 K and 1225 K (see Table 5.1). A scatter of $\pm 100 \cdot 10^{-6}$ can be assumed for the strains in Fig. 5.9. The error in Fig. 5.10 is around $\pm 50 \cdot 10^{-6}$.

The internal stresses have been assessed as a function of an applied tensile stress at temperatures between 1075 and 1375 K. Substantial creep is observed above 1150 K (Fig. 5.8). The results seem not very reliable on the first glance. A clear trend can hardly be found. But nonetheless, some curves are so neat (T=1075 K Fig. 5.10) that the results may have (within their limits) a physical basis. A few things have to be emphasized for a better understanding. First, the measurements of sample 1 have to be taken with precaution. The measurements have been performed by going up and down in temperature (Table 5.1). Therefore, an important influence on the results does not only come from residual stresses that have been relaxed during creep, but also from the thermal history of this sample. Secondly, the strains have been measured longitudinally to the stress axis (tensile, positive strains) and transversely (negative, compressive Poisson strains). As indicated with the elastic deformation limits on the graphs, the longitudinal strains are expected to be much more important. However, in the experimental setup the longitudinal and transverse diffraction paths are not equal (Fig. 3.6). This may result in the lower intensities for the longitudinal measurements and hence in an increase of the statistical error. On the other hand, surface effects could be present in the transverse direction. However, at temperatures below 1200 K, where the response is rather elastic, the measured strains are lower than the indicated limits (except 1000K sample 4 in Fig. 5.10). At 1225 K, the measured strains correspond well with the elastic strains. At 1300 K, the measured strains are higher than the limits. The behavior observed above 1225 K may be justified by the fact that creep starts at very low stress, just above 20 MPa. As the ‘zero stress’ reference is taken before creep, an apparent increase of the calculated strains may occur. This is consistent with the stress relaxation after creep observed in Fig. 5.19. Unfortunately, the cobalt peaks were too weak to obtain the corresponding strains in the cobalt, which would allow to draw conclusions about possible load transfer.

3.2 TiWCN-Co

Residual stresses have been measured in the cobalt and in the TiWCN phase. The core-rim structure is evidenced by a peak splitting in the reference powder and in the cermet. The stresses in the cobalt are tensile and the stresses in the TiWCN are compressive as expected at room temperature. As strains are much larger in the cobalt, the measure of stresses in this phase is more reliable. The value obtained at room temperature is around 2 GPa as expected from the Eshelby model (see Appendix, Table 1). The stresses are completely relaxed around 1200 K. The stresses in the TiWCN at room temperature are expected to be of the order of 200 MPa from the stress balance relation. The differences between the core and the rim are so small that they should be taken with precaution. The observed stresses are higher, but the presented stresses have average errors of about ±150 MPa. The reason for this is that the strongest peaks could not be used for the evaluation of the stresses, because the splitting of the peaks becomes more evident for higher indexes. The intensity of these peaks is lower, which leads to the increase of the error, when the position is fitted. Also the fitting of diffraction peaks with three superimposed peaks can result in some uncertainties. At high temperature, the stresses of the TiWCN hard phase go slightly towards tensile stresses. This effect may not be physical, but

rather deriving from the powder fitting. The powders have only been measured up to 1273 K and the fit of the data points had to be extrapolated to higher temperatures. However, the increase of lattice parameter in the rim above 1200 K could be related to a chemical change, i.e. either an increase of tungsten or a decrease of nitrogen in the rim lattice. In fact, an increased tungsten concentration in the rim is thermodynamically possible as shown in Fig. 5.20. This change happens in a small temperature range just before 1200 K, but it is reversed rather drastically upon the dissolution of the W_6Co_7 (see §2.4). However, kinetically, diffusion of tungsten into the rim is unlikely. A change of the stoichiometry of the rim by a decrease of the nitrogen content and an increase of the carbon content can be envisaged, which can explain the increase of the lattice parameter of TiCN. As shown by Aigner et al. [86], the lattice parameter of $Ti(C_x,N_{1-x})$ increases with increasing C/(C+N) ratio.

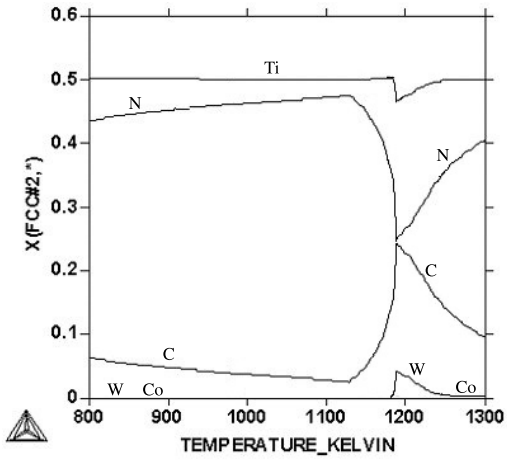

Figure 5.20: Equilibrium concentration of the TiWCN γ-phase vs. temperature. Calculated using the Thermo-Calc software [14] (courtesy of Susanne Norgren, AB Sandvik Coromant).

3.3 Comparison

The stresses in the TiWCN-Co phase are smaller than that in WC-Co. This is expected, as the thermal expansion coefficient of TiCN is closer to that of cobalt than that of WC (see Appendix Table 1). Moreover, the volume fractions are not the same. The higher volume fraction cobalt in WC-Co (18 vol.% compared to 10 vol.% in TiWCN-Co) leads to higher residual stresses in the hard phase.

Strong solution of tungsten in the cobalt phase is observed in WC-Co above 1100 K (Fig. 5.21a). This effect is not observed in the cermet (Fig. 5.21b). However, the equilibrium composition of the cermet hard phase changes as a function of temperature. In particular, the atom ratio C/N is strongly dependent on temperature.

Additional phases such as WCo_3, $W6Co_7$ and W_6Co_6C were formed in the cermet during the high temperature measurements. The tungsten concentration in the binder is unusually high for a cermet, which may explain the formation of these phases. Some traces of hexagonal cobalt were found in WC-Co upon heating from room temperature to 1000 K in measurements of sample 1, but not in those of sample 4.

In both hard phases, WC and TiWCN rim, a peculiar behavior is observed at low temperature. The stress minimum is not found, as expected, at room temperature, but at 400-600 K. A temperature artefact may arise at low temperature. Under vacuum, heating by radiation is impor-

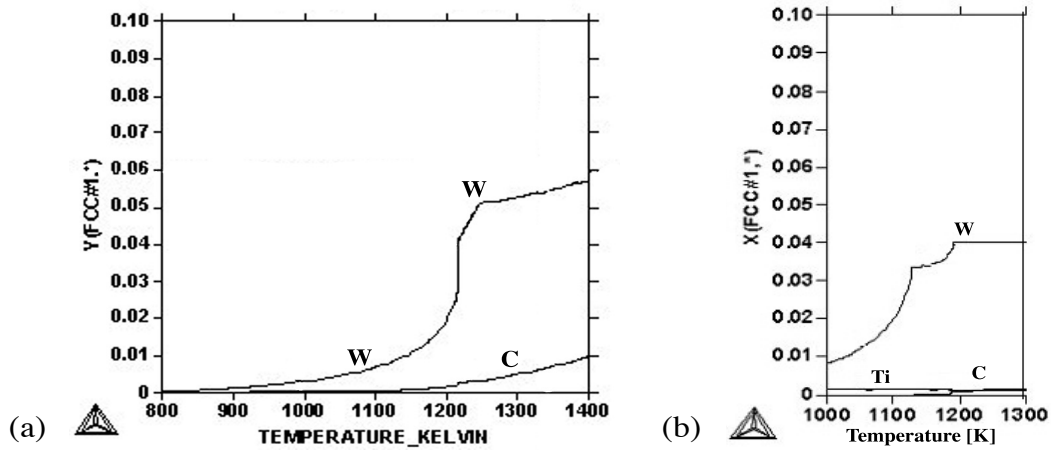

Figure 5.21: Equilibrium concentration of the binder vs. temperature for (a) WC-Co and (b) TiWCN-Co. Calculated using the Thermo-Calc software [14] (courtesy of Susanne Norgren, AB Sandvik Coromant).

tant above 700 K. Below 700 K, even a small distance between thermocouple and sample may cause an error in the temperature determination. However, the stresses in the cobalt change linearly, both in WC-Co and in the cermet, without showing a local maximum above room temperature. A temperature artefact is therefore unlikely. The observed behavior is difficult to explain. A possible error source may be that the reference powder does not correspond well to the hard phases at low temperature. This is however difficult to admit, especially in the case of WC, which is very stable, homogeneous and stoichiometric in the studied temperature range.

Chapter 6

Mechanical spectroscopy

The internal friction spectra of cemented carbides and cermets have been studied as summarized in Chapter 2. The temperature domain up to 1400 K has already been well described [10,23-26,28,32,39-43,45,51]. In this chapter, the high-temperature domain is studied more in detail. First, the results on WC-Co are presented. The cermet is studied in the second part. Finally, the common features and the differences of both hardmetals are discussed.

1 Internal friction of WC-Co

The WC-Co internal friction spectrum has been largely studied up to 1200 K [32,40-43] and 1400 K [24,25]. Up to 1200 K, the internal friction spectrum can easily be deconvoluted into one peak and a background. Measurements up to 1400 K showed that another peak is found at a temperature around 1400 K, but this peak could only be seen clearly in frequency scans. In this work, measurements have been performed up to 1480 K focussing on the high temperature domain.

1.1 Measurements as a function of temperature

Fig. 6.1 and Fig. 6.2 present the first and the second heating of WC-Co and the deconvolution of the spectra into peaks and a background. The normalized modulus is also shown. The general IF temperature spectrum can be decomposed into several peaks and a high-temperature background.

The peaks $P_{W1'}$, P_{W1} and P_{Wc}, found up to 1200 K, are consistent with earlier findings by Ammann and Bolognini [25,32]. The observations in the frame of this work confirm previous interpretations attributing these peaks to the cobalt phase (Chapter 2 §3.2).

In the high temperature domain, additional peaks are detected. In the first heating, one peak is present at around 1400 K. In the second and in the following thermal cycles, two peaks are found, P_{W2} and P_{W3}. The deconvolution (Fig. 6.2) shows these two peaks, one peak is located at 1330 K and the other at 1440 K. Many first heatings have been evaluated. All showed only one peak at 1400 K. It is difficult to determine whether the two peaks are too close to one another to be separated or only one peak exists at the first heating.

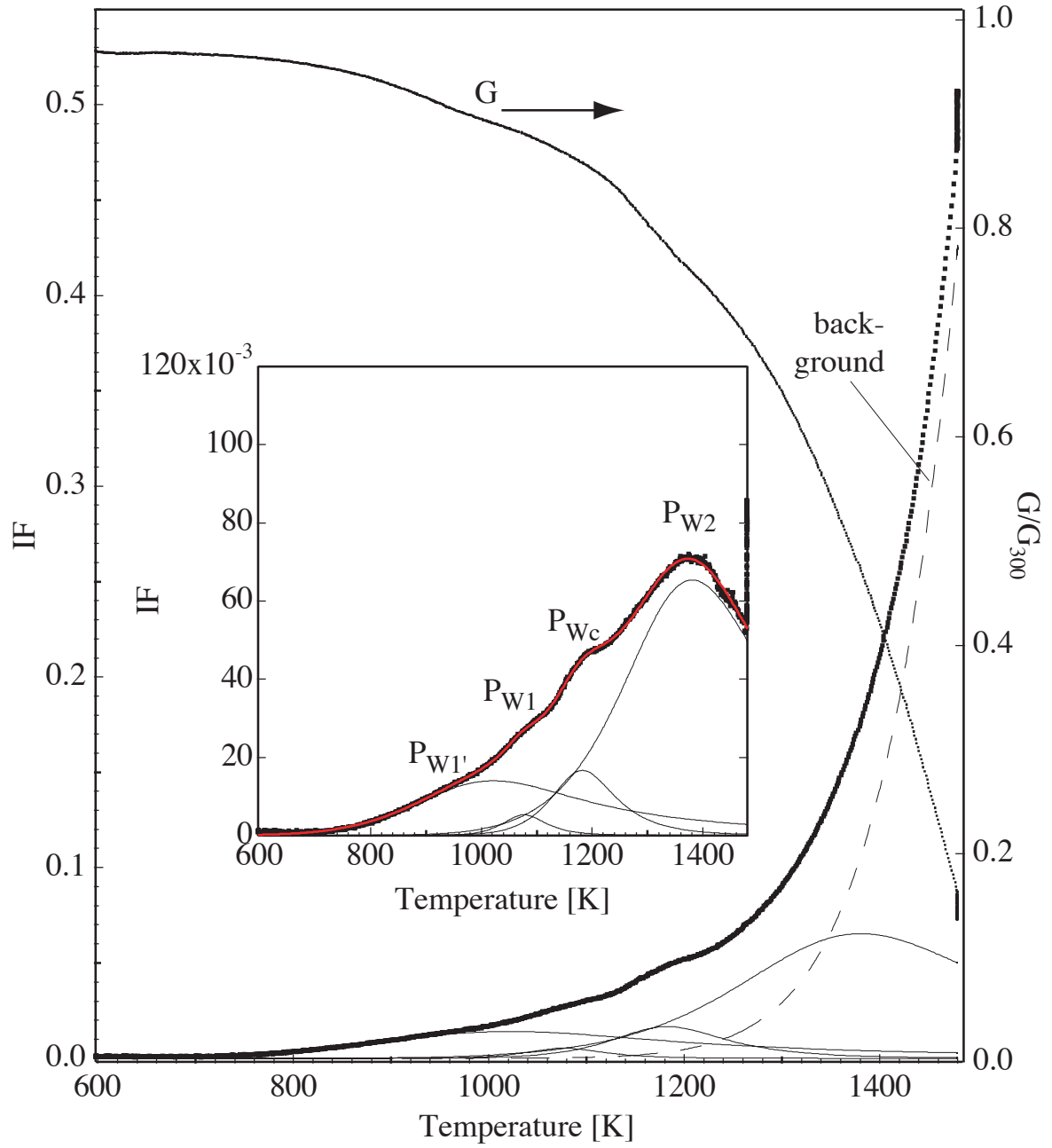

Figure 6.1: First heating of WC-6vol.%Co with deconvolution of the IF spectrum. The relative modulus G is presented on the right axis. The inset figure shows the same measurement after subtraction of the background.

The modulus drops with every peak as expected from general theory (Chapter 3 §4.2). Therefore, the modulus drop starts already at 900 K with the rise of $P_{W1'}$. In the second heating, the modulus is stable until 1000 K. The relative change from room temperature to 1480 K is about 80 %. It is generally observed, that upon cooling below 1300-1400 K, the modulus rises above the heating-modulus (Fig. 6.3).

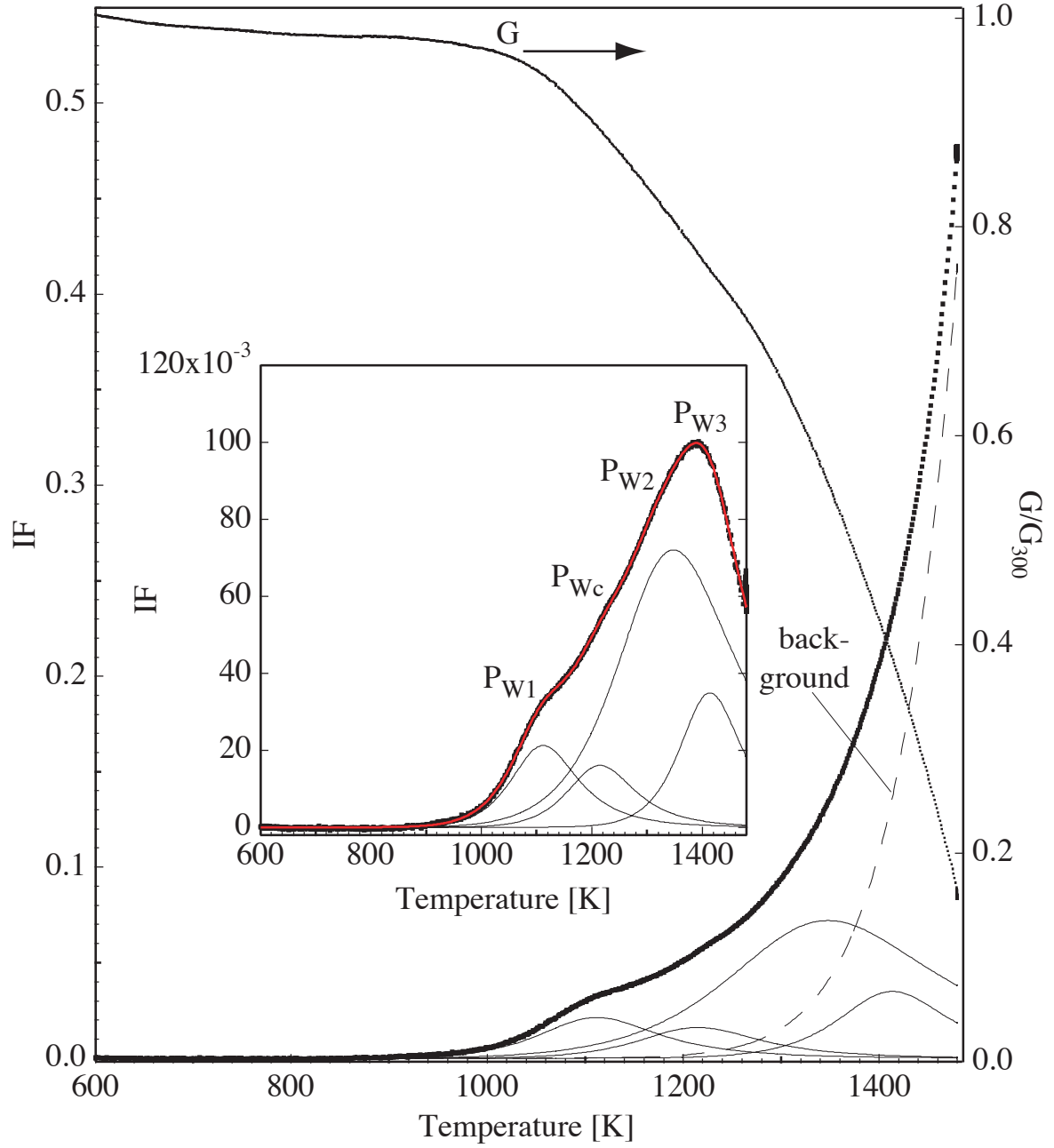

Figure 6.2: Second heating of WC-6vol.%Co with deconvolution of the IF spectrum. The relative modulus G is presented on the right axis. The inset figure shows the same measurement after subtraction of the background

The internal friction curves obtained during a heating-cooling cycle up to 1480 K with a two hours dwell at 1480 K are presented in Fig. 6.3. Only a very small difference exists between the heating and the cooling curve of a stable WC-Co spectrum. The peak P_{Wc} shifts to lower temperature in cooling.

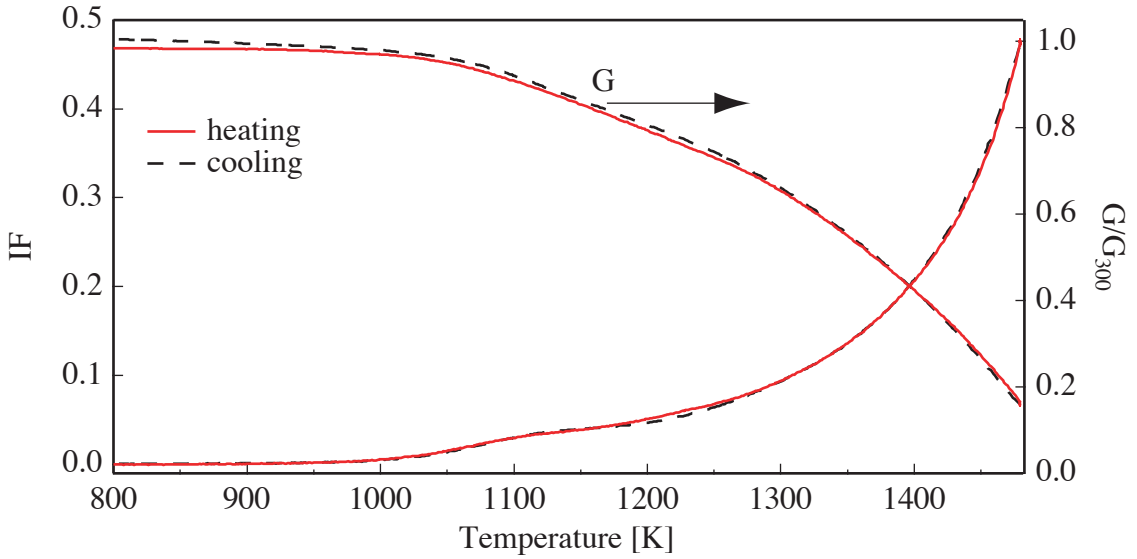

Figure 6.3: Complete heating-cooling cycle showing that heating and cooling curves of WC-Co are very similar, i.e. the IF is stable.

1.2 Measurements as a function of frequency

Frequency spectra are measured and analyzed in the temperature range from 1000 to 1480 K. Fig. 6.4 shows some of the curves at high temperature. Fig. 6.4a is a linear representation, showing the high-temperature peak P_{W4}. The peak is at the limit of visibility in the frequency range of 1 mHz to 10 Hz and moves towards lower frequencies with decreasing temperature. The relative modulus decreases by a factor 10 in agreement with the very high relaxation strength of P_{W4}. At the maximum temperature 1480 K, the peak is clearly visible at 10 mHz. The maximum of the peak seems to be well resolved. A background should, in principle, also be present and it should rise towards lower frequencies. The IF curve of the skeleton gives an

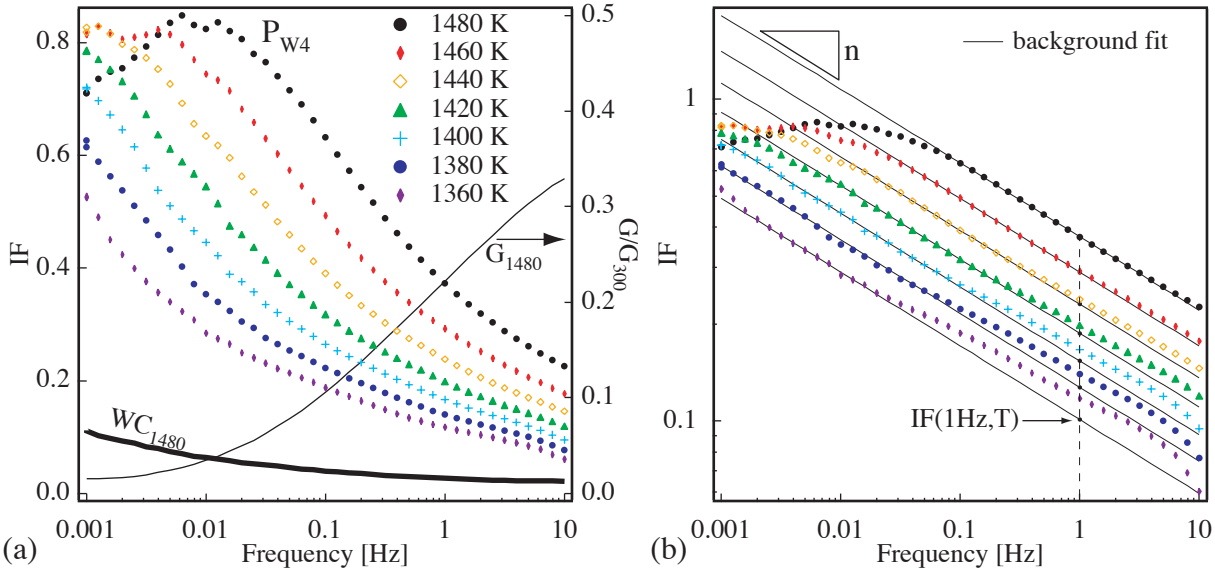

Figure 6.4: The high-temperature peak, P_{W4}, which forms the background for P_{W2} and P_{W3} (a) in linear scale together with the modulus G and the IF of the WC skeleton and (b) in log scale showing the background fitting.

idea about the height of a possible background. However, the separation of the high temperature peak and background is impossible.

The high-temperature peak P_{W4} forms the background of two other peaks, P_{W2} and P_{W3}. For the analysis of the peaks, which are small compared to P_{W4}, the high-temperature peak is treated like an exponential background, which can be subtracted from the spectra. According to Schoeck et al. [61], the high-temperature (or low-frequency) background found commonly in internal friction spectra can be identified with the left flank of a peak. Its activation energy is determined as described in Chapter 3 §4.3.1. The value for the activation energy of the background is 7.9 eV (Fig. 6.5).

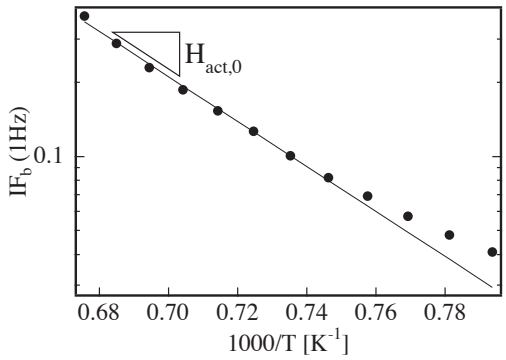

Figure 6.5: Determination of the activation energy of a background or, as in this case, of the high-frequency flank of peak P_{W4}.

After background subtraction, the peaks P_{W2} and P_{W3} are clearly revealed (Fig. 6.6). They change position to lower frequencies with decreasing temperature. This shift is presented in the Arrhenius plot (Fig. 6.7). In fact, all four peaks of WC-Co, P_{W1}, P_{W2}, P_{W3} and P_{W4}, have been found to be thermally activated. The shift of their temperature-frequency positions has been evaluated to calculate the corresponding activation energy and the attempt frequency (Fig. 6.7).

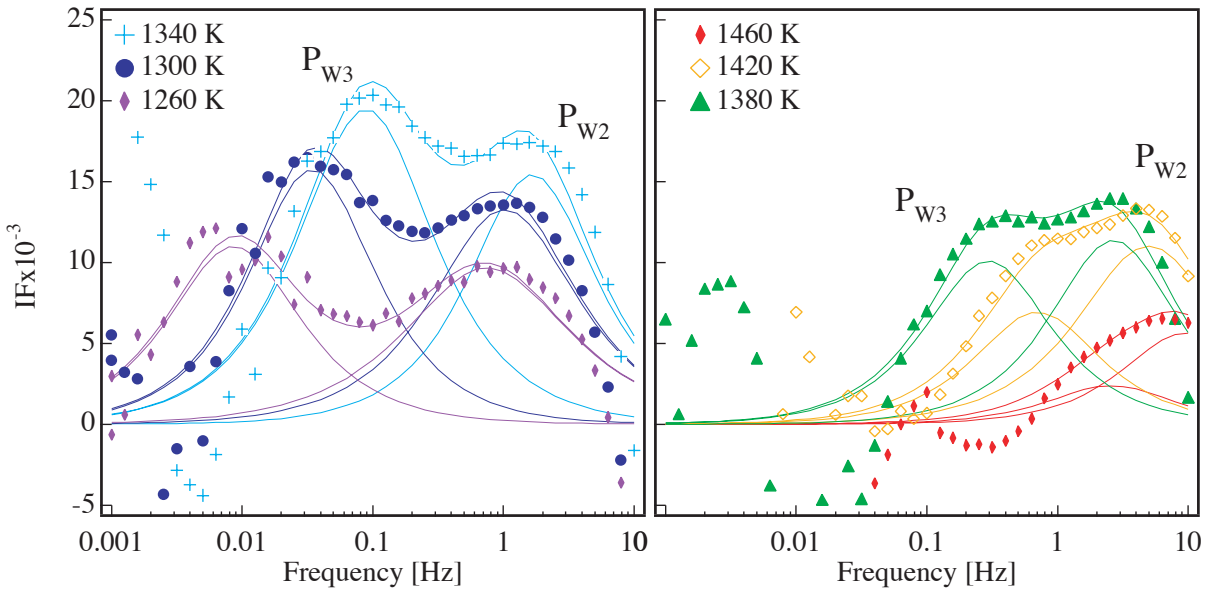

Figure 6.6: The peaks at different temperatures after subtraction of peak P_{T4}. The two peaks are very close to one another at high temperature and get apart with decreasing temperature.

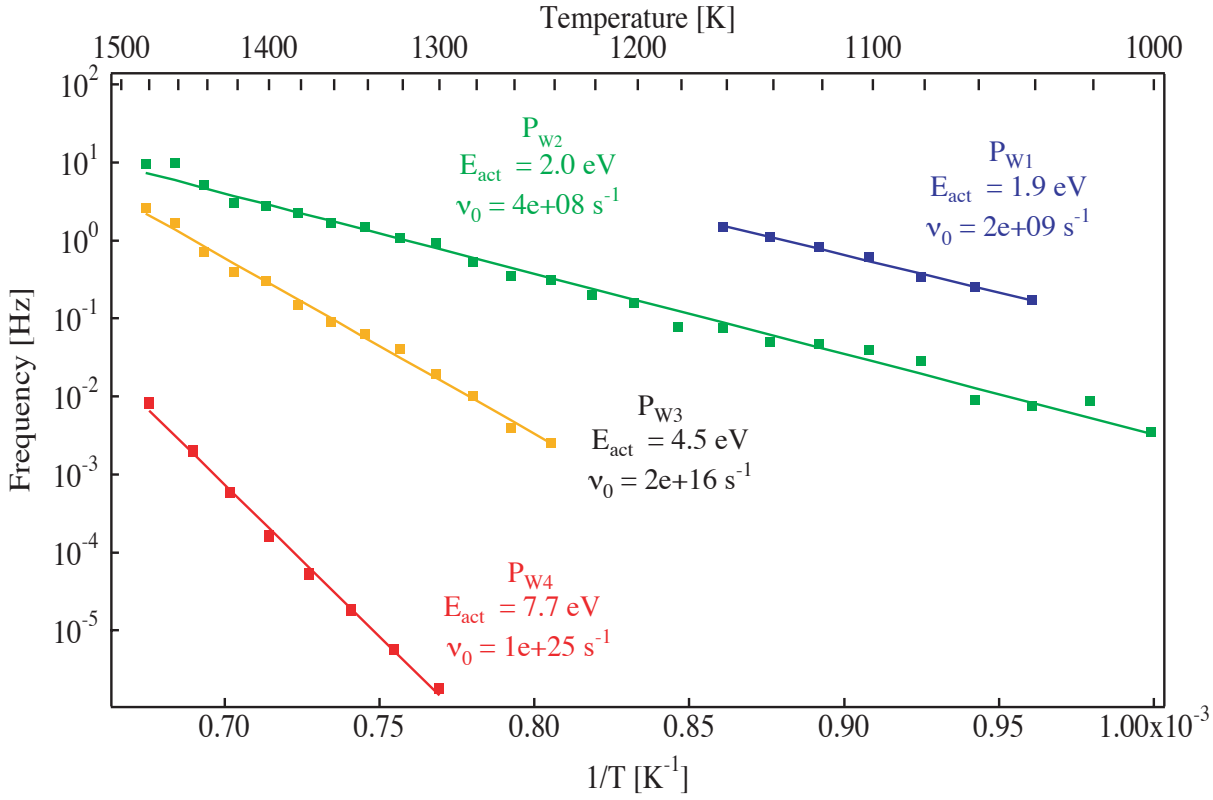

Figure 6.7: Arrhenius plot of the four peaks of WC-10vol.%Co together with their activation parameters.

The calculated activation energy of P_{W4}, 7.7 eV, agrees well with the value obtained from the background fit (7.9 eV). This confirms that generally a background corresponds to the flank of a peak. The peaks P_{W2} and P_{W3} have quite different activation energies of 2 eV and 4.5 eV in frequency spectra, respectively. At high temperature and high frequency, the peaks are very close, which is seen in temperature measurements at 1 Hz (Fig. 6.2). The cobalt peak P_{W1} shows an activation energy lower than the expected 2.5 eV for tungsten diffusion in cobalt [32].

1.3 Internal friction of the WC skeleton

The internal friction of WC skeletons is generally more than 15 times lower than the IF of the complete WC-Co. The modulus decrease between room temperature and 1480 K is only 10 % instead of 80 % for WC-Co. The importance of the presence of the cobalt binder for the dynamic modulus changes is therefore obvious.

The WC skeleton shows a very peculiar, transient behavior during the first heating, shown in Fig. 6.8. Two transition peaks are present at 1200 K and 1420 K. Both peaks are related with a drop of the modulus followed by a partial recovery. The first transition peak can be erased completely, by heating to a temperature above or annealing at a temperature close to the peak, without affecting the transient peak at 1420 K. The latter peak is erased by heating over 1450 K.

The IF is very stable after the transient peaks are annealed. This stable state is already attained by the cooling curve in Fig. 6.8 (first cooling). The stable IF spectrum can then be deconvoluted into a background and two peaks. The two peaks found in the WC skeleton compare very well with P_{W2} and P_{W3} of WC-Co regarding the temperature of the peak maximum at 1 Hz and

the activation energy, as shown in the superposition of the positions of the skeleton peaks with those from the complete WC-Co in Fig. 6.10. However, the amplitude of both peaks is strongly reduced (Table 6.1).

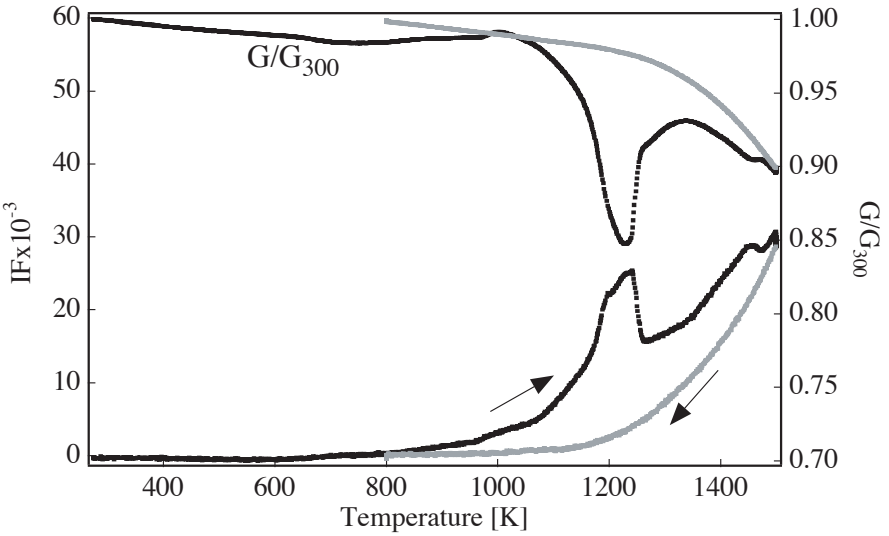

Figure 6.8: First heating-cooling cycle of a WC skeleton. Two transitions are observed, at 1200 K and at 1420 K. The first transition peak is related with a strong modulus decrease and a consecutive increase.

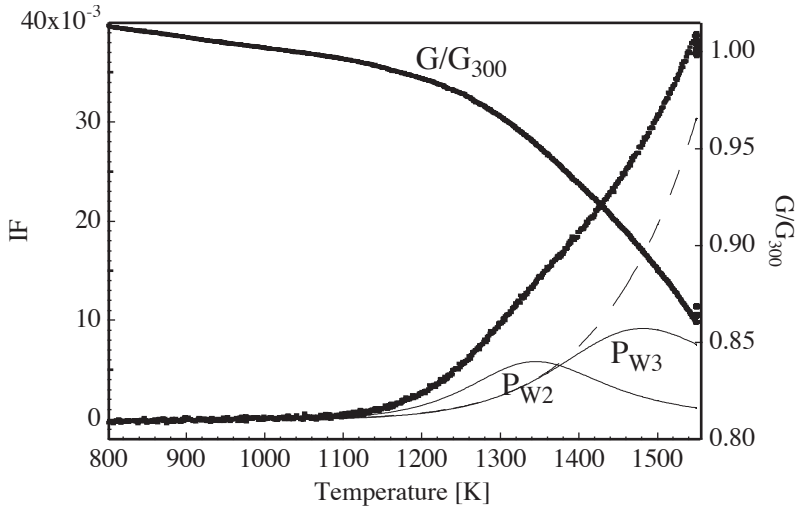

Figure 6.9: Temperature spectrum (2nd heating) of WC skeleton. Only two peaks are present after the transient peaks have been annealed.

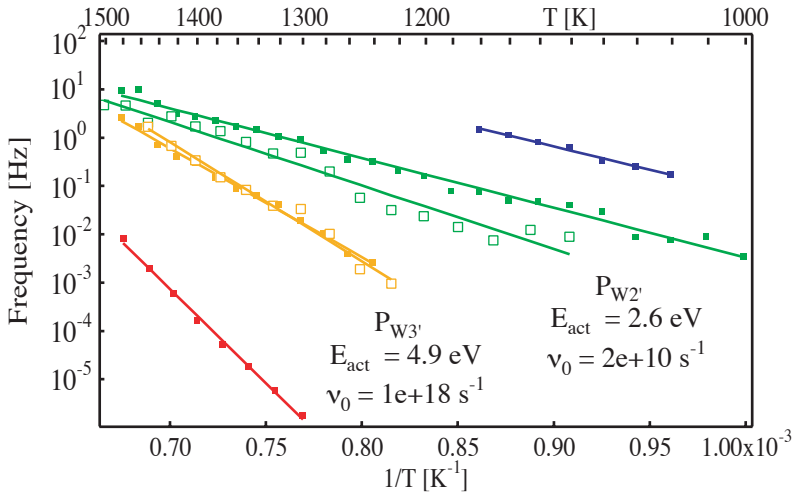

Figure 6.10: Arrhenius plot for the WC skeleton compared to the WC-Co results from Fig. 6.7.

1.4 Summary of the parameters of the peaks of WC-Co

The characteristics of all the peaks observed in WC-Co and the WC skeleton are summarized in Table 6.1.

Table 6.1 : Characteristic parameters of the peaks found in WC-Co (the peaks that appear in the skeleton are specially marked)

	T [K] at 1 Hz	**Peak height**	**Activation energy [eV]**	**Attempt frequency ν_0 [s^{-1}]**	**Broadening factor**
$P_{W1'}$ (only in first heating)	950 K	0.006	1.5 eV	10^{8}	0.6
P_{W1}	1100 K	0.02	2-3 eV	10^{9}-10^{14}	0.7-1
P_{Wc}	H: 1200 K C: 1150 K	0.008			
P_{W2} Skeleton $P_{W2'}$	1330 K 1330 K	0.03 Skel: <0.01	2 eV 2 eV	10^{9}	0.7
P_{W3} Skeleton $P_{W3'}$	1440 K 1440 K	0.02 Skel: <0.01	3-5 eV 3-5 eV	10^{17}	0.8
P_{W4}	ca. 1600 K	0.8 (without background subtraction)	> 7 eV	10^{25}	0.3

1.5 The effect of stress on the IF in WC-Co

Internal stresses as well as externally applied stresses are important for the deformation of cemented carbides. Internal stresses arise from the composite character of these materials and external stresses are always present during the usage of these materials as cutting tools. Infiltration of the grain boundaries has only been observed after stress application (Chapter 2). Different ways of measuring a possible effect of stress on IF have been explored in this work.

1.5.1 Effects of strain amplitude on IF

The strain amplitude in IF measurements is normally around $15 \cdot 10^{-6}$. In the experiments presented here, the effect of increasing the strain amplitude is measured as a function of temperature and frequency (Fig. 6.11 and Fig. 6.12, respectively). The peaks P_{W1}, P_{W2} and P_{W3} are not affected by an increase of strain. However, an effect on the background can be observed both in frequency and temperature spectra. With increasing strain amplitude, the background increases. This increase is completely reversible, as shown in Fig. 6.11, where the first and the last measurement at low strain coincide. In temperature spectra, one can observe that the peak P_{Wc} decreases (Fig. 6.11). However, this is due to an annealing effect of the Curie peak related with the increasing tungsten content in the cobalt upon subsequent thermal cycling.

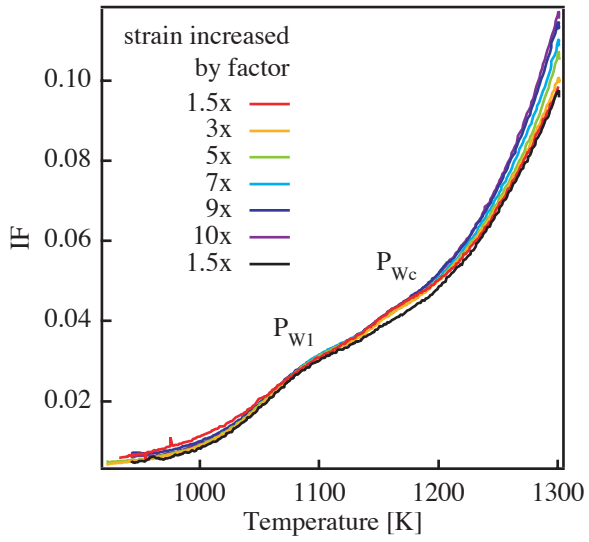

Figure 6.11: Increased strain amplitude affects mainly the high-temperature part of the spectrum. Order of measurements as indicated in the legend.

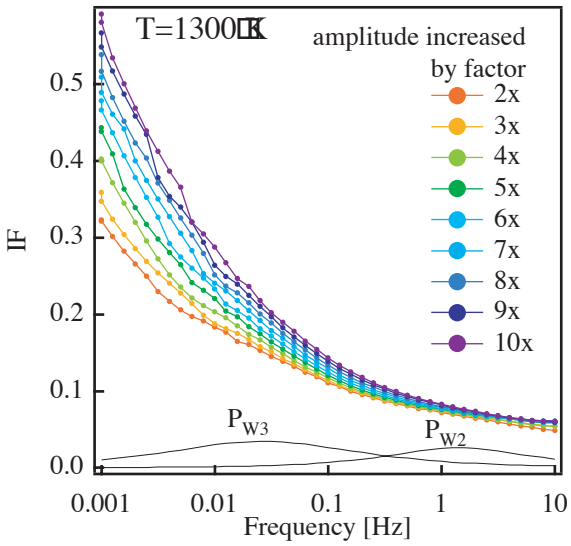

Figure 6.12: In frequency spectra, the strain amplitude influences mainly the background, P_{W2} and P_{W3} (positions indicated) are only slightly affected.

1.5.2 Tensile bias stress during IF measurements

A small tensile stress is applied on the sample during the IF measurements by adding some mass to the counterweight of the pendulum (Fig. 3.17). The stress that can be applied this way is limited by the thin wires that suspend the sample. An addition of 100 g results in a tensile stress of 0.24 MPa on the sample (cross-section 1x4 mm^2).

Fig. 6.13 shows the effect of a bias stress on WC-Co. With increasing stress, the IF at T>1100 K decreases and the modulus increases. In contrast to the usual monotone decrease of the modulus, a small plateau between 1100 and 1300 K develops under the applied stress (Fig. 6.13 inset). This plateau becomes more pronounced with increasing stress.

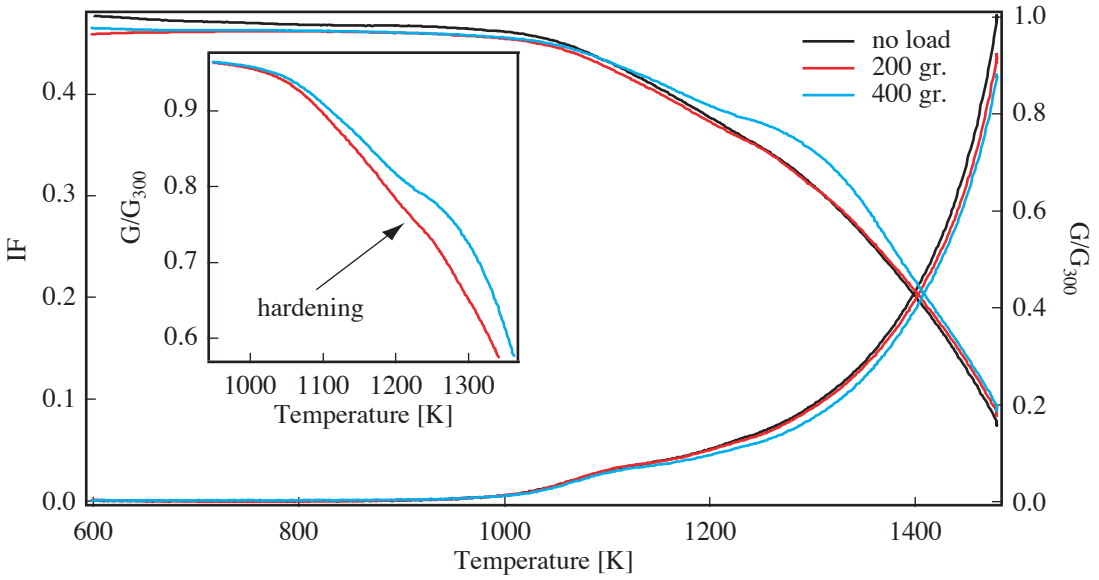

Figure 6.13: Effect of increased counterweight: IF decreases with increasing bias stress, a hardening is observed starting at 1100 K.

2 Measurements on TiWCN-Co

Cermets with cobalt binder have been widely studied, e.g. with Mo_2C addition to control the grain size [10] or with a mixed WC-TiCN hard phase [25]. In this work, a pure TiWCN-Co is chosen with some addition of carbon in order to have a cobalt binder that resembles the binder of the WC-Co, not only in volume fraction, but more importantly in composition. The tungsten does not form WC particles, it is entirely dissolved in the binder and in the hard phase rim.

2.1 Measurements as a function of temperature

A typical IF spectrum of TiWCN-Co is shown in Fig. 6.14. The spectrum is deconvoluted into several relaxation peaks and a background. Two peaks are found in the spectrum, a peak at around 1200 K and a peak at around 1500 K. Opposite to the spectra found in former works [10,25], the cobalt peak P_1 is not found in this spectrum. The peak P_{T2} corresponds to the peak pair P_2/P_3 of the studies of Feusier and Bolognini (Chapter 2 §3.3). However, its amplitude is substantially lower. A splitting into two peaks has never been observed. The peak located at 1500 K, called peak P_{T3}, is not well resolved in temperature measurements as it is located at the upper temperature limit. This peak will be studied more in detail as a function of frequency. The modulus change is also shown in Fig. 6.14. The modulus drops by 40 % between room temperature and 1480 K.

A complete heating-cooling cycle is presented in Fig. 6.15. The IF increases during the dwell of 2 hours at 1480 K. The subsequent cooling shows a higher IF than the heating. Heating and cooling form a small hysteresis above 1200 K. The modulus decreases during the dwell, but during cooling it recovers, so that after a full thermal cycle the modulus is slightly higher than before.

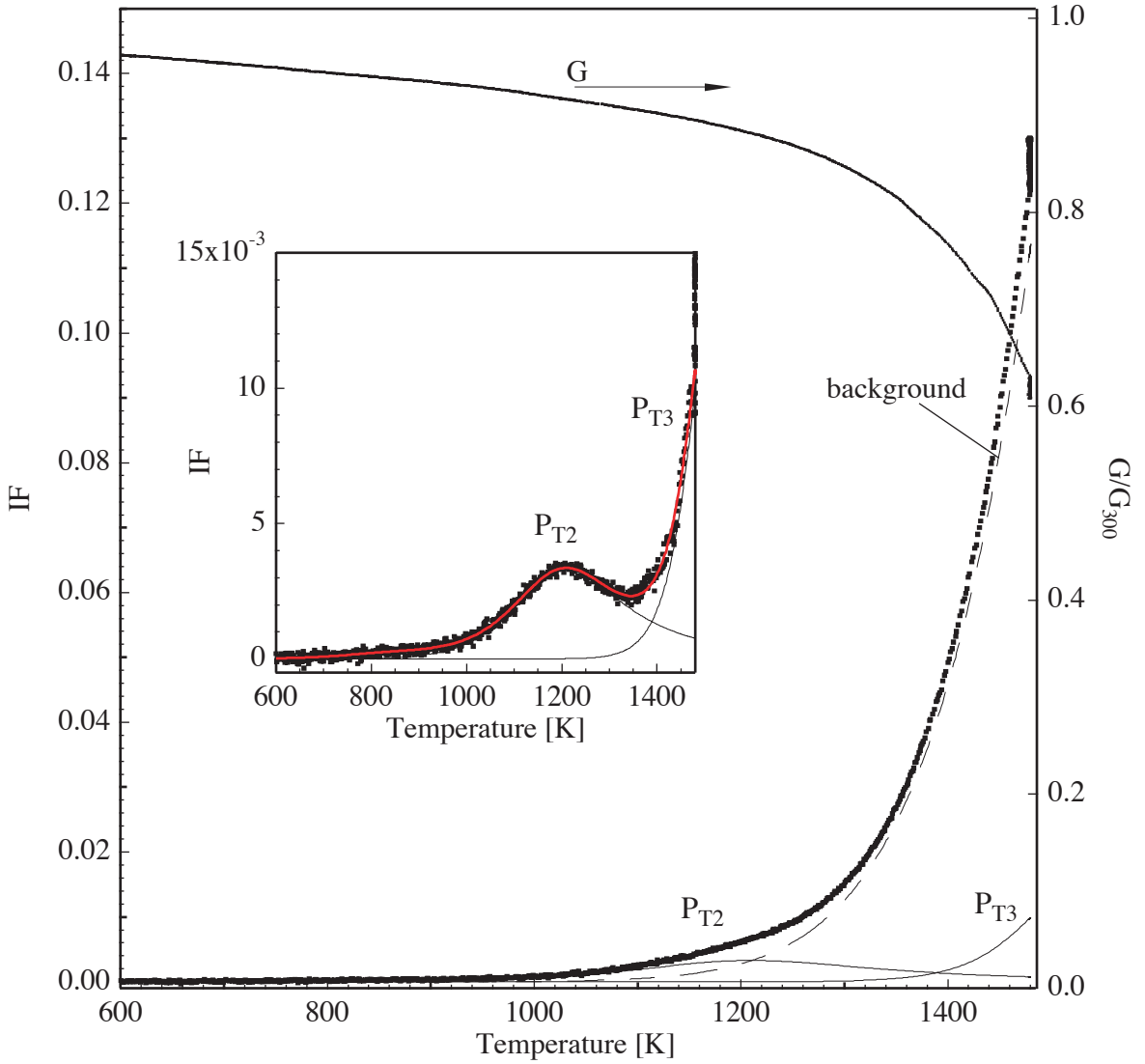

Figure 6.14: First heating of TiWCN-Co with deconvolution of the spectrum and the modulus change. No cobalt peak P_1 (around 1000 K) is found. P_{T3} is at the limit of visibility.

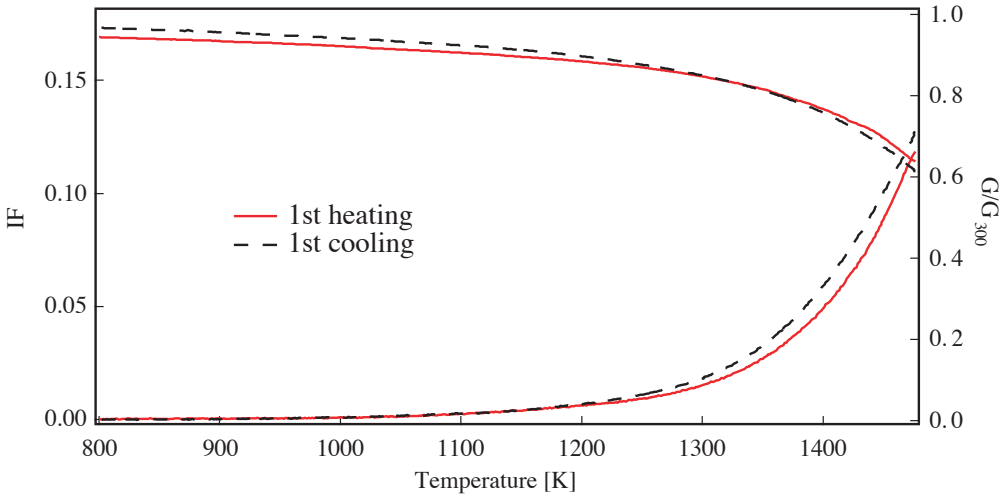

Figure 6.15: First heating-cooling cycle of TiWCN-Co.

2.2 Measurements as a function of frequency

The frequency spectra of TiWCN-Co in a temperature range of 1300 to 1500 K are presented in Fig. 6.16. The spectra have been obtained at isothermal, stabilized conditions, i.e. a dwell of 2 hours precedes every frequency scan. The measurements have been carried out upon heating starting from 1200 K to 1500 K (open circles) and back to 1200 K (+ markers). For clarity, Fig. 6.16 presents only measurements between 1300 and 1500 K. The IF increases substantially towards low frequencies, where the IF background is expected. By comparison with Fig. 6.4a, which presents the corresponding measurements in WC-Co, it may be argued that a high temperature peak comparable to P_{W4} is also present in TiWCN-Co. If such a peak was present in TiWCN-Co at a temperature 100 K higher than in WC-Co, only the high-frequency side of the peak would be visible in a frequency range from 1 mHz to 10 Hz. From present measurements it is difficult to judge, if a peak is present or not. However, the measurement at 1500 K, Fig. 6.16, shows rather well a trend towards a peak formation. Assuming that the background is the high-frequency part of a peak, it will be called P_{T4}.

Similar to WC-Co, the background, best seen in log-log scale (Fig. 6.17), is subtracted. The remaining IF (Fig. 6.18) presents one peak. At 1 Hz, it has its maximum at 1475 K, which corresponds to peak P_{T3} shown in Fig. 6.14. The peak is thermally activated, as its maximum shifts to higher frequencies with increasing temperature. Moreover, the amplitude of P_{T3} increases during heating (circles) and decreases during cooling (+ markers). The peak amplitudes measured at different temperatures upon heating agree quite well with those measured upon cooling. The amplitude of P_{T3} as a function of temperature is presented in Fig. 6.19 together with the Arrhenius plot. The calculated activation energy are 3.9 eV and 4.4 eV for heating and cooling, respectively. The corresponding attempt frequencies are of the order of 10^{-15} s^{-1}. The background (Fig. 6.20) shows a slightly higher activation energy of 4.7 and 5.1 eV, calculated according to Chapter 3 §4.3.1. The analysis of several samples yields mean

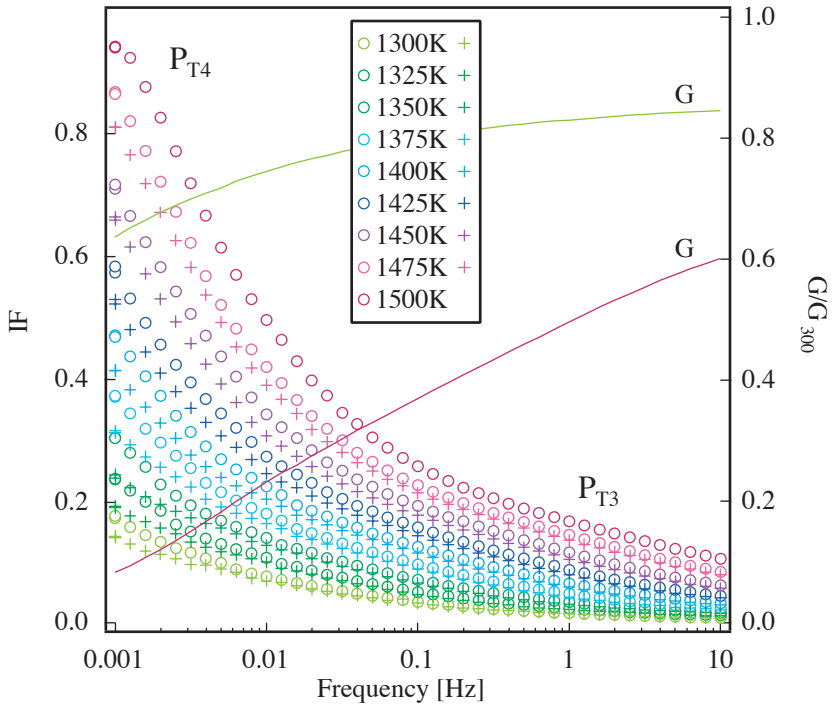

Figure 6.16: IF measurements at different temperatures, starting from 1300 K (open circles) to 1500 K and back (+ markers). The modulus is shown for 1300 and 1500 K.

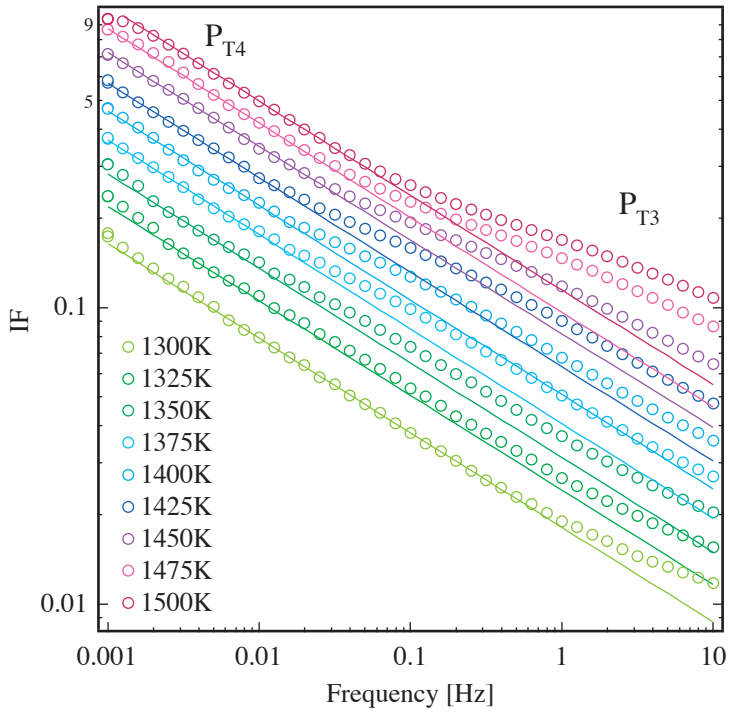

Figure 6.17: Same as Fig. 6.16, but in log-log scale, to show the background fitting.

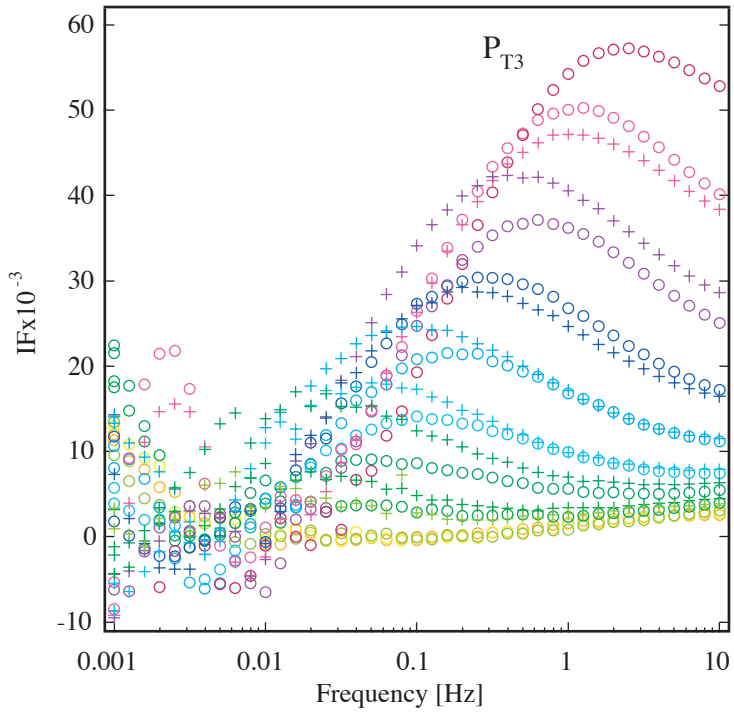

Figure 6.18: IF measurements from Fig. 6.16 and Fig. 6.17 after subtraction of the background peak. The remaining IF presents a peak, P_{T3}, with an amplitude that increases and decreases with temperature.

values for the activation energies of (4.6±0.5) eV for peak P_{T3} and (5.3±0.7) eV for the background (=P_{T4}). A significant difference between heating and cooling could not be found.

The amplitude of P_{T3}, obtained from different experiments, shows some interesting trends depending on the thermal history of the sample and on the application of stress before or during the IF measurements. All results on the amplitude of P_{T3} are summarized in Fig. 6.33 and are then discussed in §2.5.5.

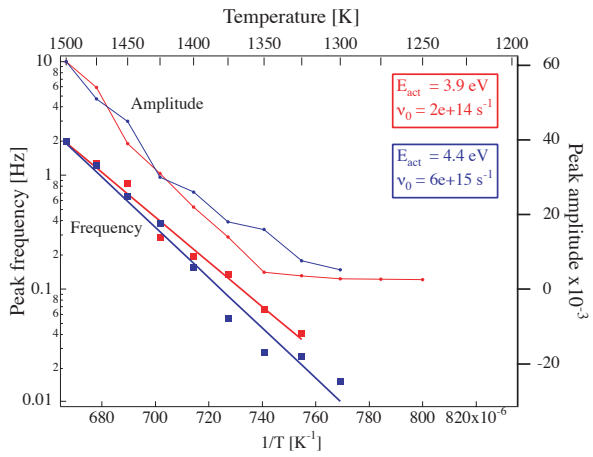

Figure 6.19: Arrhenius plot of P_{T3} for heating (red) and cooling (blue) with calculated activation energy and attempt frequency. The peak amplitude increases during heating and decreases during cooling.

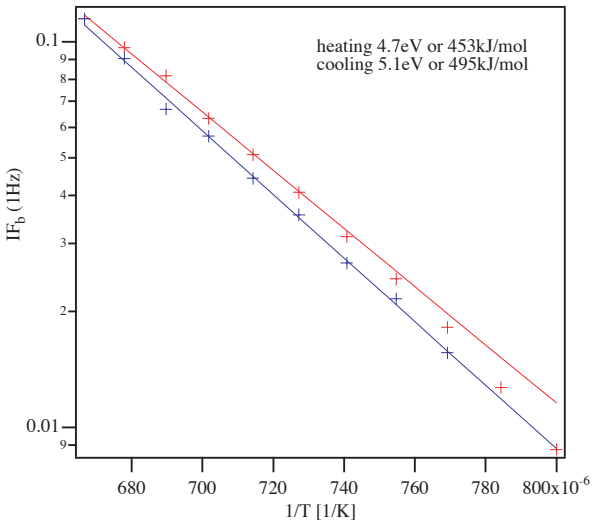

Figure 6.20: IF (value at 1 Hz) of the fitted background of the frequency spectra during heating and cooling. The activation energy of the background is calculated according to Chapter 3 §4.3.1.

2.3 Internal friction of the TiWCN skeleton

During a first heating, the IF of a TiWCN skeleton, where the cobalt has been chemically removed, is only slightly lower than the IF of an as received TiWCN-Co. However, the IF at high temperature is metastable and decreases during thermal cycling. Fig. 6.21 shows the first cycle and, for comparison, the fourth cycle. With every cycle the IF decreases, but a saturation of this decrease is observed after four cycles (Fig. 6.21), where the IF can be considered as stabilized. The deconvolution of the fourth heating is shown in the inset of Fig. 6.21. The peaks $P_{T2'}$ and $P_{T3'}$ are shifted to lower temperatures and decreased in peak height as compared to the peaks in the complete cermet.

Frequency sweeps are presented in Fig. 6.22. These measurements correspond to a well stabilized structure (compare 4th cycle in Fig. 6.21). In frequency sweeps at metastable conditions, as during a first cycle, the skeleton shows peak $P_{T3'}$ similar to that of the cermet composite (Fig. 6.17). However, the peak rapidly becomes smaller and stabilizes at a peak amplitude of about $1{\cdot}10^{-3}$. In its stable form, $P_{T3'}$ is found at 1400 K at 1 Hz and shows an activation energy of 3.4 eV with an attempt frequency of $1{\cdot}10^{13}$ s^{-1} (Fig. 6.23). The stable background ($P_{T4'}$) shows a very peculiar behavior, with a change in activation energy around 1350 K as visible from the slope in Fig. 6.22. The activation energy is 4 eV at T<1350 K and around 8 eV at T>1350 K (Fig. 6.24). This change is observed to be reversibly present during heating and cooling.

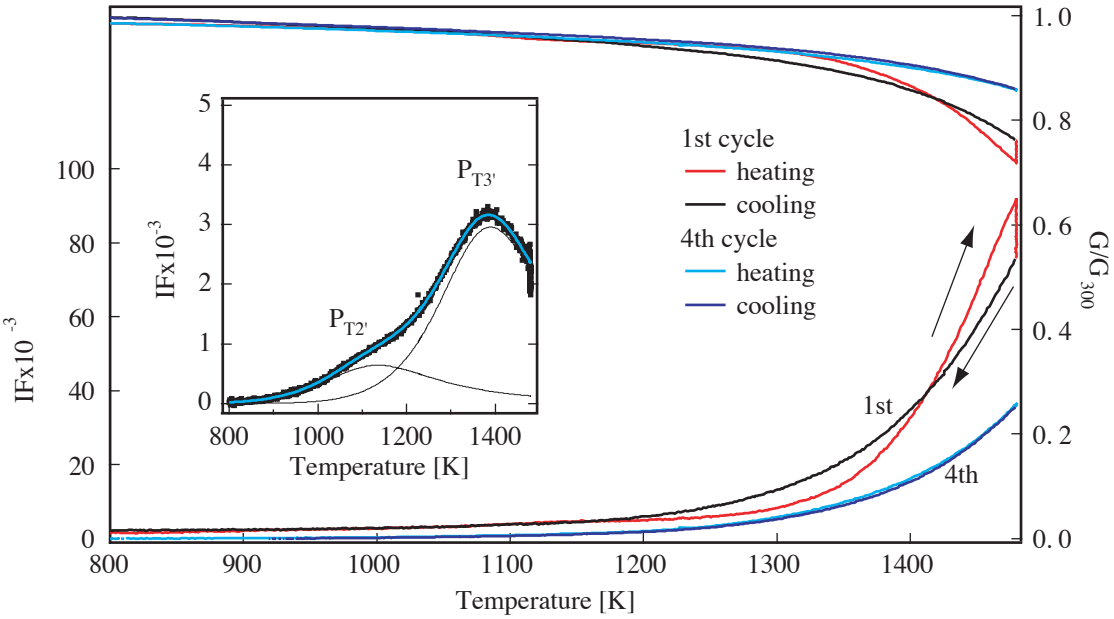

Figure 6.21: IF as function of temperature of TiWCN skeleton of the first and fourth thermal cycle. Deconvolution of 4th heating after subtraction of the background (inset) shows two peaks and a background.

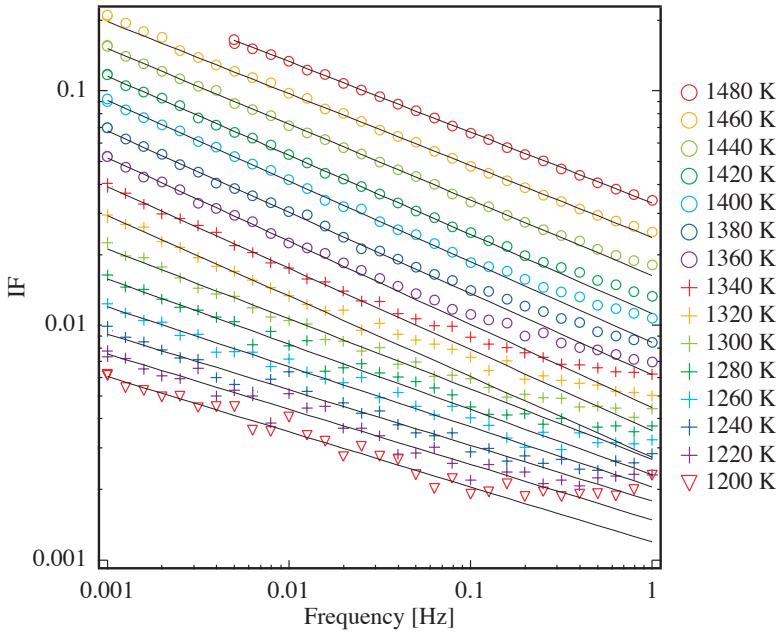

Figure 6.22: Frequency measurements of TiWCN skeleton showing a change of the background. The deflection of the curves at high frequency (Fig. 6.22) is an artefact due to the resonance of the pendulum.

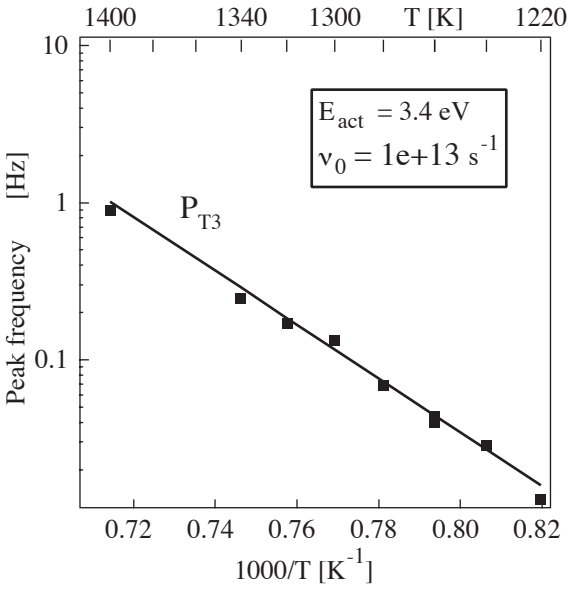

Figure 6.23: Peak P_{T3} measured at stable conditions (corresponding to the 4th cycle in Fig. 6.21)

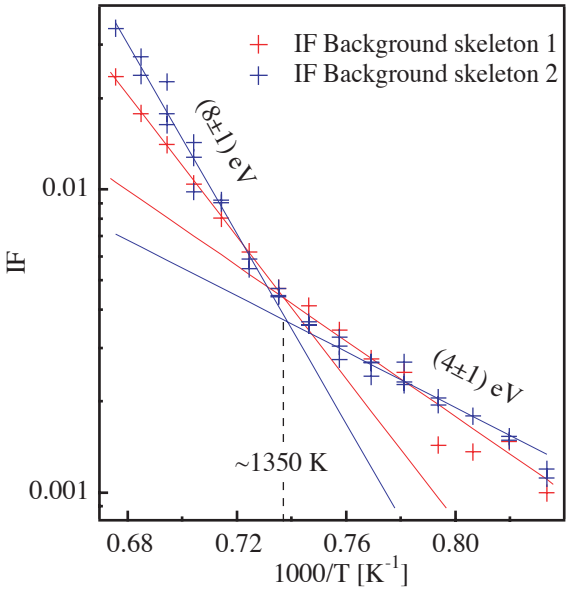

Figure 6.24: Evaluation of the activation energy of the background shows a change from 4 to 8 eV at 1350 K, measured on two different samples.

2.4 Summary of the parameters of the peaks of TiWCN-Co

The characteristics of all the peaks observed in TiWCN-Co and the TiWCN skeleton are summarized in Table 6.2. Additionally, an Arrhenius plot with the peaks P_{T2}, P_{T3} and P_{T4} from the complete cermet, and $P_{T3'}$ of the skeleton is presented in Fig. 6.25. A comparison of the IF frequency spectra of cermet and cermet skeleton at 1500 K together with the change in modulus is shown in Fig. 6.26. A comparison with Fig. 6.4a of WC-Co and its skeleton at similar temperature shows that the WC skeleton shows a much lower background compared to the cermet skeleton. The differences in IF and modulus between complete material and skeleton are larger for WC-Co than for the cermet.

Table 6.2 : Characteristic parameters of the peaks found in the cermet (the peaks that appear in the skeleton are specially marked)

	T at 1 Hz	Peak height	Activation energy	Attempt frequency ν_0	Broadening
P_{T2}	1200 K	$4 \cdot 10^{-3}$	2 - 3.5 eV	10^8 - 10^{16} s^{-1}	0.5 - 0.7
Skeleton $P_{T2'}$	1140 K	$<1 \cdot 10^{-3}$	1.5 - 2.5 eV	10^9	0.5 - 0.8
P_{T3}	(1500±50) K	see Fig. 6.33	(4.6±0.5) eV	10^{15} - 10^{18} s^{-1}	0.6 - 0.9
Skeleton $P_{T3'}$	1400 K	$\sim 1 \cdot 10^{-3}$	3.4 eV	10^{13}	~1
P_{T4}	>1700 K	(0.8)	(5.3±0.7) eV	(10^{17} s^{-1})	0.3

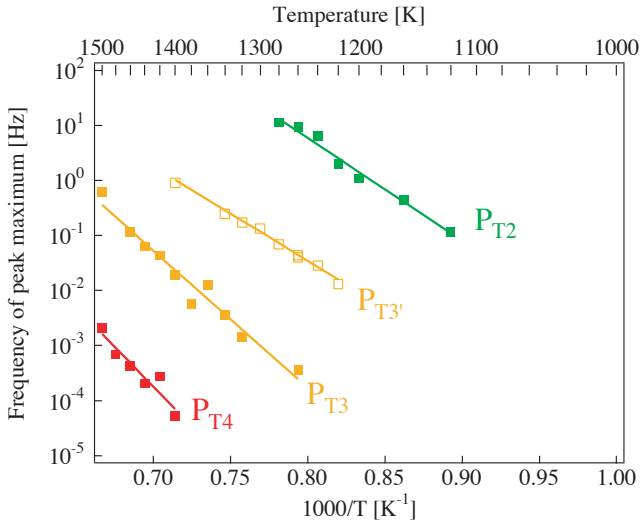

Figure 6.25: Arrhenius plot of P_{T2}, P_{T3} and P_{T4} from TiWCN-Co and $P_{T3'}$ from the skeleton. $P_{T2'}$ is present in the skeleton, but has not been analyzed further.

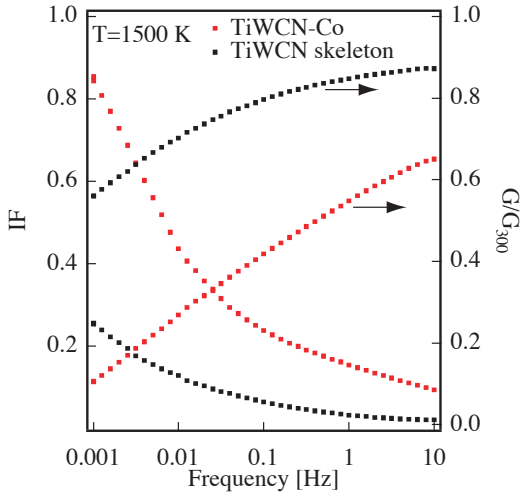

Figure 6.26: Comparison between frequency spectra of cermet and cermet skeleton at 1500 K.

2.5 The effect of stress on the IF of TiWCN-Co

The mechanical properties of cermets depend on temperature and stress. Internal stresses as well as applied stresses play an important role. Internal stresses arise from the composite nature of the material. Important external stresses act on the materials during the cutting procedure. Different possibilities to study the effect of internal and external stresses on the IF of cermets are presented.

2.5.1 IF after deformation at high temperature

A sample is deformed by three-point bending at 1473 K to a maximum strain of 2 %. The deformed sample is turned upside-down and bend-deformed at the same temperature to straighten it. The sample is then cut for IF measurements from the compression side of the bend–deformed specimen. The deformed region of the IF sample is small (Fig. 6.27). The deformed samples appear to be hardened, as the modulus does not decrease as much as that of the non-deformed reference, both in heating and cooling (Fig. 6.28). The IF is, apart from a region around 1000 K, lower in the first heating, but the cooling agrees well with the reference.

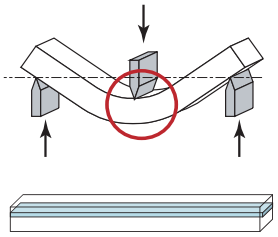

Figure 6.27: IF sample cut from a straightened bending sample after 2% deformation

However, a small, but interesting effect of the deformation is observed. The first heating IF curve of the pre-deformed sample shows an increase in a small temperature range around 1000 K (Fig. 6.28b). This rise of IF, found only in the first heating, corresponds well in temperature to the cobalt peak, P_{TI}, described in literature (Chapter 2).

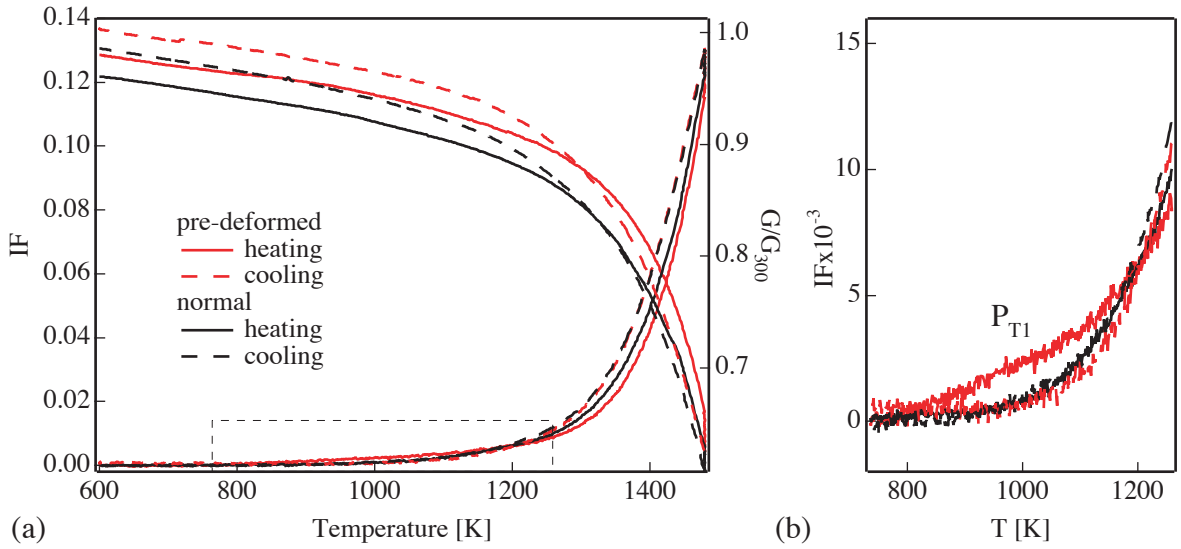

Figure 6.28: (a) First thermal cycle of the pre-deformed sample together with the first cycle of a normal sample as comparison. (b) Magnified region from (a) showing P_{T1} in the first heating of the pre-deformed sample.

2.5.2 Tensile bias stress during IF measurements

A small tensile stress is applied on the sample during the IF measurements by adding some mass to the counterweight of the pendulum (Fig. 3.17). The stress that can be applied this way is limited by the thin wires that suspend the sample. An addition of 100 g results in a tensile stress of 0.24 MPa on the sample.

As shown in Fig. 6.29, a bias stress even that small leads to an additional increase of IF (and decrease of modulus) at high temperature. The IF hysteresis is therefore increased by a bias stress. Moreover, a similar effect as described in §2.5.1 is observed. Fig. 6.29b shows that an increase of IF at the place of a possible cobalt peak during the first heating is observed. The bias stress causes internal stresses that are relaxed at high temperature.

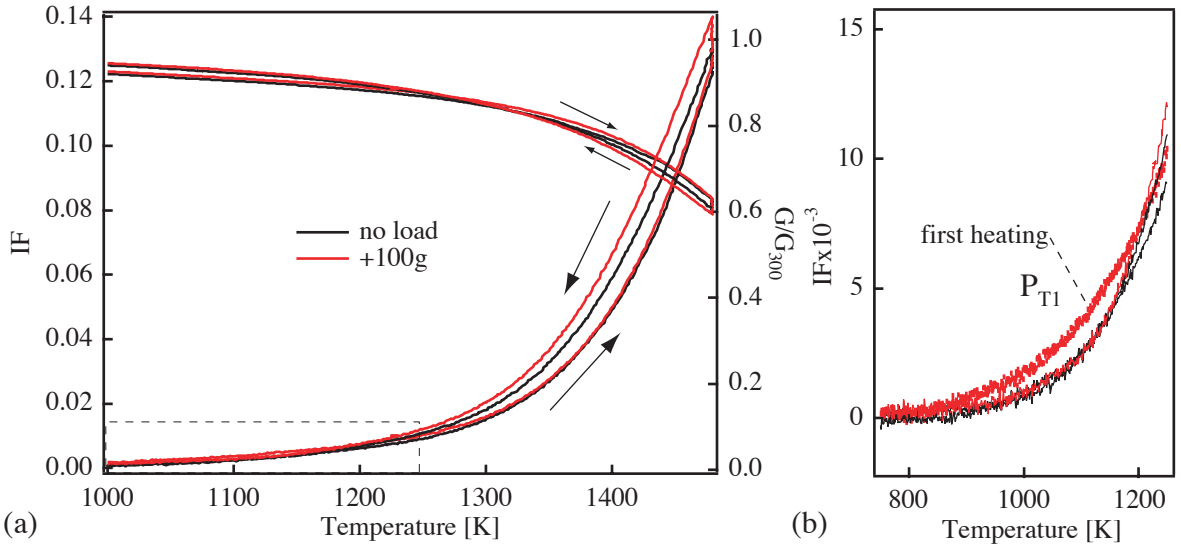

Figure 6.29: (a) A small bias stress of 0.24 MPa has an effect on IF at high temperature, where IF increases more strongly, leading to an increased hysteresis. (b) Magnified region showing the appearance of P_{T1}

2.5.3 IF after quenching

This experiment was conceived in order to preserve possible cobalt infiltrated grain boundaries, produced by tensile deformation, down to room temperature by water quenching and to measure possible changes of IF. The cermet was chosen, because clear infiltration of grain boundaries after deformation is frequently observed (Chapter 2).

TiWCN-Co is cut in shape of a dog-bone. An INCONEL steel block is prepared with a slit to hold the dog-bone. When brought to high temperature, the steel block exerts a tensile stress on the cermet dog-bone, because of the different thermal expansion (Fig. 6.30). The expected stress on the cermet sample at 1200°C is between 5 and 20 MPa. The heat-treatment is performed in a quartz tube furnace under vacuum with a heating rate of 4 K/min and a holding time at 1200°C of 1 hour. The steel block and the cermet sample are water quenched. An IF sample is cut from the dog-bone specimen.

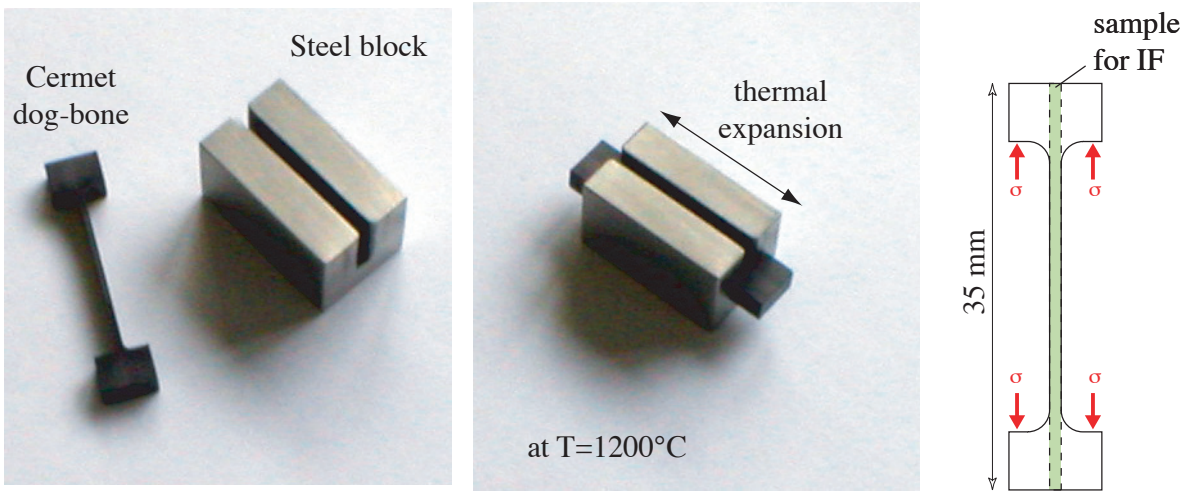

Figure 6.30: Experiment setup for quenching from a high temperature tensile stress state. An IF sample can be cut from the dog-bone specimen.

IF frequency scans are performed during the first heating from 1200 to 1480 K and during cooling at the same temperatures. Frequency scans at 1450 K are shown in Fig. 6.31a as an example. Measurements both during heating and cooling are compared to non-treated reference measurements from Fig. 6.16. The background (P_{T4}) is the same in all curves, but clearly the peak P_{T3}, positioned around 0.8 Hz, is much higher after the heat-treatment.

The IF measurements as a function of temperature between the frequency scans are shown in Fig. 6.31b. The IF at high temperature increases more rapidly than without heat-treatment. Moreover, the heating-cooling hysteresis is enlarged. The modulus decreases down to 40 % of the room temperature value, instead of 60 % in the non-heat-treated case. However, the modulus recovers completely upon cooling.

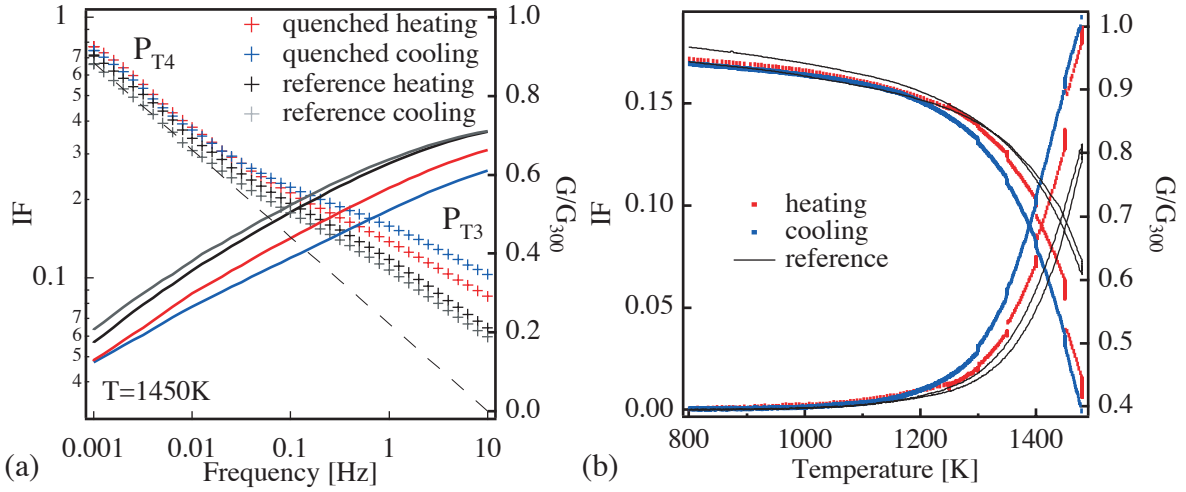

Figure 6.31: (a) Frequency scans at 1450 K showing peak P_{T3} and background (P_{T4}). The peak P_{T3} is increased after high temperature deformation. (b) Heating-cooling cycle in steps; frequency measurements have been performed during dwells every 50 K from 1200 to 1480 K.

2.5.4 Effects of strain amplitude on IF

The strain amplitude, if not specified otherwise, is around $15 \cdot 10^{-6}$. In this experiment, the effect of increasing the strain amplitude by a factor of 5 and 10 is measured. The increased strain amplitude during the heating of different thermal cycles results in a strong increase of the IF and a softening is seen in the modulus (Fig. 6.32). The IF deviates from its behavior with the usual strain amplitude at different temperatures; the higher the strain amplitude the lower the temperature, where the IF starts to increase. The subsequent cooling curves are measured with the usual strain amplitude and are completely unaffected from the strain increase beforehand. Also the following thermal cycle with the usual strain amplitude is unaffected by the strain experiment before.

2.5.5 Summary of stress effect on the height of P_{T3}

The peak P_{T3} has been analyzed under different conditions as described in the previous sections. The height of P_{T3} after subtraction of the background (P_{T4}) is derived from IF frequency scans as shown in §2.2. Fig. 6.33 shows the development of the peak height with temperature (the temperature of the frequency scan) for different samples and conditions. Obviously, the application of stress in different ways seems to influence the peak height. Different regions with different behavior are marked with A, B and C on the graph. Region B covers the 'normal' behavior with a peak amplitude at 1480 K of about $50 \cdot 10^{-3}$. After quenching as described in §2.5.3 (region C), the amplitude of the peak is almost doubled. On the other hand, the application of a bias stress, high strain amplitude and pre-deformation seems to lower the peak height (region A).

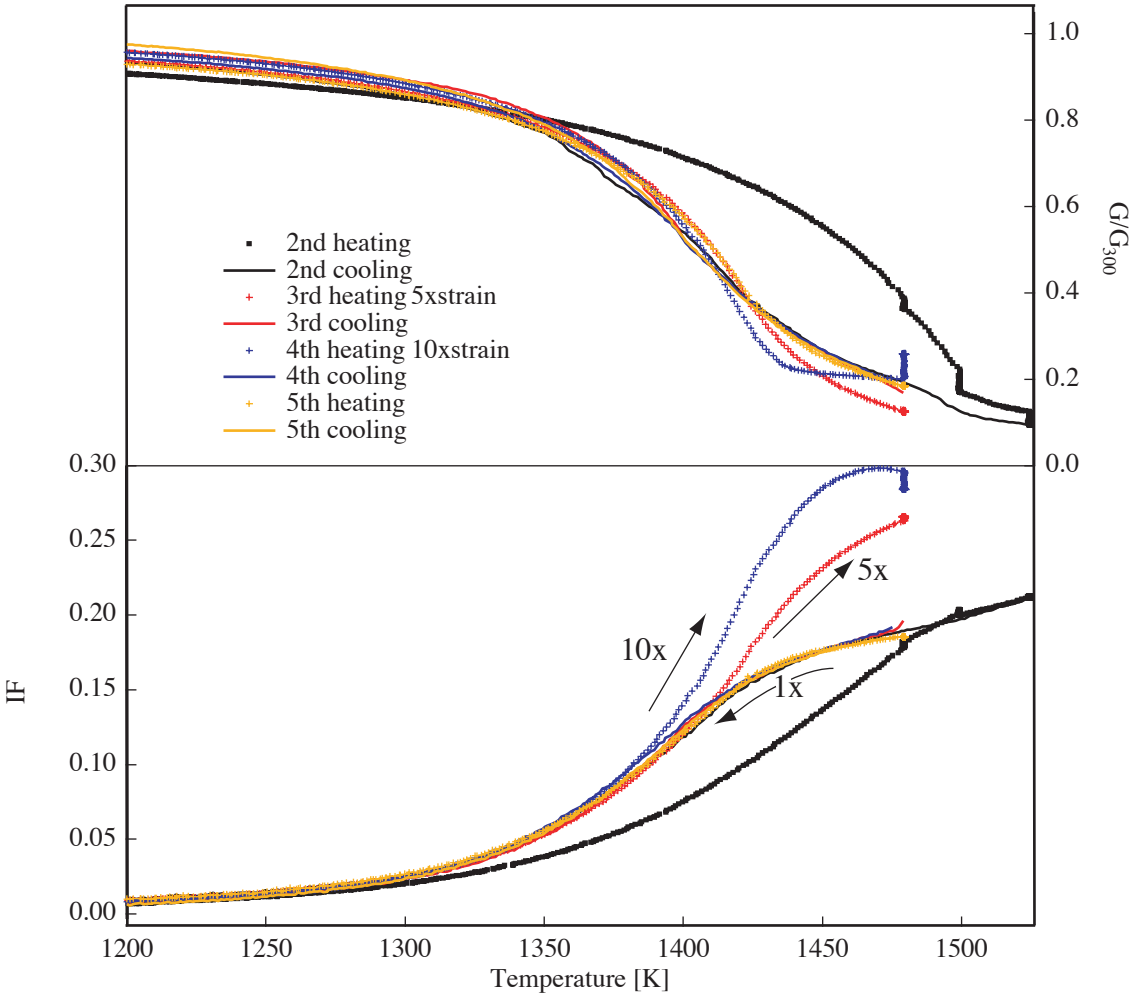

Figure 6.32: Strain amplitude effect on IF: Amplitude increase factor is marked on IF curves. During cooling, measured with normal strain amplitude, IF is reduced to standard.

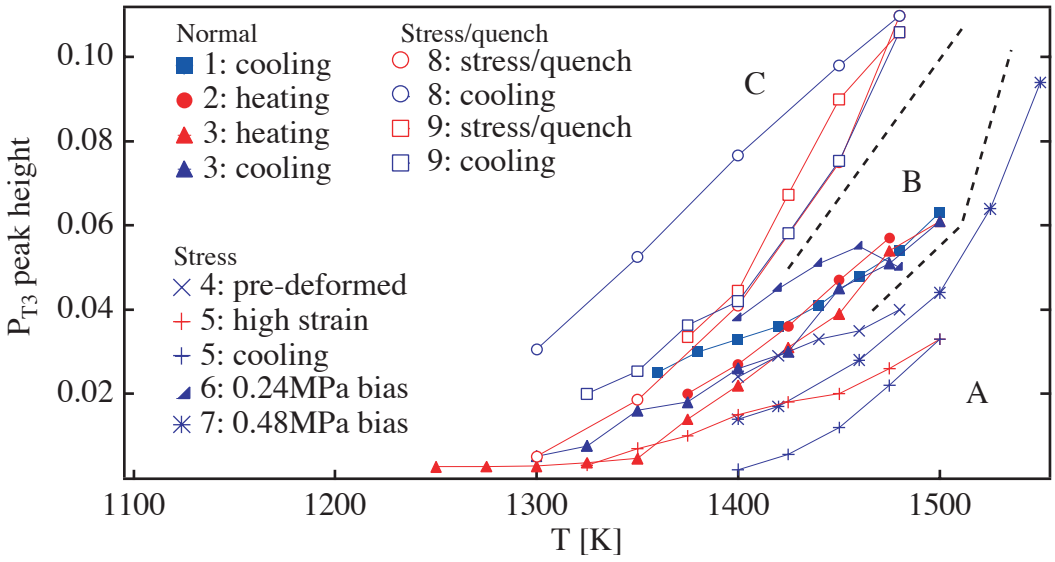

Figure 6.33: Height of peak P_{T3} from different experiments on TiWCN-Co (numbers correspond to different samples). Three different regions can be defined: *A* - low peak amplitude due to stress, *B* - normal behavior, *C* - high peak amplitude after quenching.

3 Discussion

A number of relaxation peaks are evidenced by IF measurements. The physical mechanisms underlying these relaxations are analyzed below. Their denomination and the attributed mechanisms are summarized in Appendix 3.

3.1 The cobalt peak

WC-Co spectra show the presence of a peak $P_{W1'}$ at 1000 K only in the first cycle, and a stable peak P_{W1} at 1100 K at 1 Hz. The peak P_{W1} is not observed in the skeleton and therefore it is attributed to the cobalt phase. A peak similar to P_{W1} is commonly found in WC-Co hardmetals and has been related to the movements of dislocations in the fcc cobalt phase controlled by the diffusion of tungsten [25]. This peak was shown to have a low temperature state and a high temperature state. The low temperature state, $P_{W1'}$, is only seen in as sintered materials. Upon heating, the low temperature state transforms suddenly into the high temperature state, which then becomes stable upon thermal cycling. The low temperature state was related to the movement of partial and the high temperature state to the movement of perfect dislocations in cobalt [25]. The transition to the high temperature state happens when tungsten becomes mobile and thus allows the partial dislocations to combine into perfect dislocations. The reverse transition is much slower. The dislocations dissociate again upon cooling at a lower temperature than the temperature where they recombine during heating. As the tungsten mobility is reduced at low temperature, it remains frozen in the positions, to which it was dragged at higher temperature.

The magnetic transition of the cobalt is manifested by a peak P_{Wc}. This peak is not thermally activated and therefore not visible in frequency spectra. The peak is very sharp compared to a Debye peak. Its appearance has been related to the purity of the cobalt. Upon thermal cycling, this peak gets weaker and finally vanishes.

In the cermet, none of the cobalt related peaks found in literature is observed. Interestingly, after deformation (§2.5.1) and upon application of a bias stress (§2.5.2), a peak appears during the first heating with a peak height of about $1 \cdot 10^{-3}$. The absence of this peak in the as-received cermet may be related to the low level of internal stresses at that temperature found in cermets comparatively to WC-Co (see Chapter 5). Internal stresses may be needed to overcome the stacking fault energy that fixes the distance of dissociated partial dislocations or to make dislocations break-away from pinning points. The appearance of the peak after deformation is due to increased internal stresses. These stresses are relaxed upon heating to higher temperatures and thus the peak is not observed during the cooling.

Another possible explanation of the peak amplitude increase after deformation is an increase of the density of dislocations during deformation. This may enhance the peak and as the dislocations recover at high temperature, the peak would not be present during the cooling. However, it is difficult to imagine an increase of the dislocation density due to 0.24 MPa tensile bias stress. This stress seems too small to create dislocations. Moreover, the stress was applied also during cooling, but no peak is observed there.

Another interesting point to notice is that the position of the possible P_{T1}, observed after deformation or under bias is 1000 K, is the temperature of the transient $P_{W1'}$.

3.2 Grain boundary peaks in WC-Co and Cermets

This section will be concentrated on the discussion of the peaks that are found in the hardmetals at high temperature and that might be related to the deformation in domain III, defined in Chapter 4.

The peaks P_{W2}, P_{W3} and P_{W4} of WC-Co and the peaks P_{T3} and P_{T4} of TiWCN-Co are believed to be grain boundary sliding peaks. The main arguments for this assumption are explained separately for the peaks P_{W2}, P_{W3} and P_{T3}, the peaks of relatively low amplitude, and P_{W4} and P_{T4} with huge peak amplitudes. Assuming that several GBS peaks are present in a material may be surprising at first. However, the state of the grain boundaries changes. Different mechanism are active in pure grain boundaries, in grain boundaries with cobalt segregation and with continuous cobalt layers. Moreover, the WC skeleton intrinsically bears families of grain boundaries with different characteristics. A series of relaxation peaks can therefore easily be imagined.

The peaks P_{W2}, P_{W3} and P_{T3} are present in the hardmetals with cobalt, but also in the hard phase skeletons. The activation energy of the peaks are 2 eV for P_{W2} and of the order of 4-5 eV for P_{W3} and P_{T3}. All peaks show a dependence of the peak height on temperature. Peak P_{T3} is rising from zero to ~$50 \cdot 10^{-3}$ between ca. 1350 and 1500 K (Fig. 6.33). A threshold temperature (~1350 K) for the appearance of the peak can be defined. The peaks P_{W2} and P_{W3} show a maximum of ~$20 \cdot 10^{-3}$ at around 1350 K (Fig. 6.34). However, in the skeletons, the amplitudes of these peaks are drastically decreased to $2 \cdot 10^{-3}$ for P_{T3} and around $5 \cdot 10^{-3}$ for P_{W2} and P_{W3}. In the skeletons, no amplitude change with temperature is observed. This trend has been already observed by Bolognini (Fig. 6.35), but at that time no explanation was given [25].

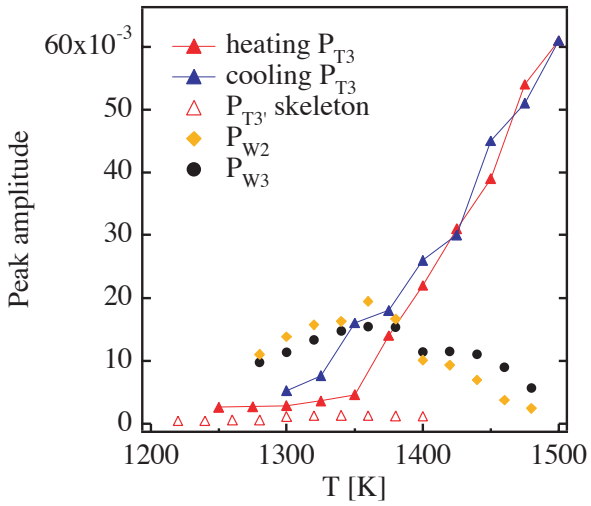

Figure 6.34: The peaks P_{W2}, P_{W3} and P_{T3} show a temperature dependent peak height, measured during isothermal frequency scans.

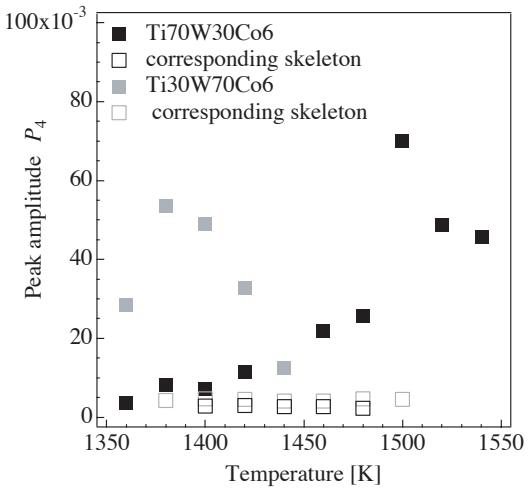

Figure 6.35: Peak height determined in mixed cermets with majority of TiCN hard phase (black) and with a majority of WC (gray) [25]

The interpretation of the peaks P_{W2}, P_{W3} and P_{T3} results mostly from two facts, i.e. the peaks show an amplitude, which depends on temperature, and the peaks exist, even if decreased, in the skeleton. A mechanism located in the cobalt is ruled out, because of the presence of the peaks in the skeletons. A dislocation mechanism of the hard phase grains could be envisaged. However, the movement of dislocations in the cermet has been shown to be related to the peak P_{T2}, which is found at 1200 K [10,25]. In the WC-Co, a deformation of the WC grains is observed only upon severe deformation conditions, as for example upon high-temperature compression of 100 % and more by Sakuma et al. [33]. The authors state that dislocations are

rarely observed with strain rates below 10^{-4} s^{-1}. The WC/WC grain boundary structure of undeformed regions of a cutting insert and of the cutting edge after turning was studied by electron backscattered diffraction [12]. The deformed region was difficult to analyze, probably because of internal stresses related with an increase of the dislocation density especially near the grain boundaries. However, an annealing of the samples did not show any improvement of the indexability [12]. It may be argued that dislocations are present at grain boundaries, but not inside the WC grains. The activation energy for dislocation movement in WC is not known. However, Sakuma et al.[33] measure a value of 5.8 eV for a dislocation related deformation mechanism and as the activation energy of tungsten diffusion in WC is 6 eV, they relate it with dislocation climb. Neither P_{W2} nor P_{W3} show such a high activation energy. The relaxation mechanisms behind the "low amplitude" peaks should be attributed to limited grain boundary sliding of the hard phase. The different dependence of the peak amplitude on temperature of the peak P_{T3} in the cermet and of the two peaks P_{W2} and P_{W3} of WC-Co leads to different relaxation mechanisms.

Grain boundary peak P_{T3} in the cermet

In cermets, the dependence of the amplitude of peak P_{T3} on temperature (Fig. 6.34) may be explained by the process of progressing segregation of cobalt in the grain boundaries. The amplitude of the peak P_{T3} is shown to increase during heating and decrease during cooling. Different equilibrium stages of cobalt segregation, maybe even in multilayer quantities, may exist at different temperatures. Multilayer segregation has been studied for example by Berthier et al. [87], who demonstrated that a series of phase transitions can occur when grain boundary segregated atoms occupy successively adjacent layers. The equilibrium state is manifested in the peak observed in isothermal frequency measurements (Fig. 6.18). At different temperatures, the peak position shift is due to the thermal activation of the GBS process and the varying peak height reflects the equilibrium amount of segregated cobalt. In temperature measurements, e.g. at 1 $Kmin^{-1}$, the equilibrium is never reached.

A strong increase of the peak height is only observed for the peak P_{T3} in the cermet (not in the skeleton). This effect should therefore be related with an evolution of the structure of the grain boundaries that is caused by the cobalt. However, the evolution starts at around 1350 K. At temperatures below 1350 K the peak is much smaller. In fact, in the cermet skeleton, the peak ($P_{T3'}$) appears with low peak height that is moreover constant with temperature (Fig. 6.34). As shown in Chapter 5, the chemical composition of the rim may change at high temperature and in particular the ratio C/N. Exchange of light elements between hard phase and binder may help the diffusion of cobalt in the boundaries and also provide vacancies for segregation. This explanation is supported by the increase of peak P_{T3} after quenching (§2.5.3), which may produce a higher vacancy density.

The background ($P_{T4'}$) measured in the skeletons shows a strange behavior with a change of activation energy from around 4 eV at temperatures below 1350 K to 8 eV at above 1350 K. The change in the background of the skeletons appears just at the temperature where the peak P_{T3} of the cermet composite starts to grow. This result shows that the structure of the grain boundaries in the skeletons may undergo a transformation at that temperature.

Grain boundary peaks P_{W2} and P_{W3} in WC-Co

In WC-Co, grain boundaries cannot be considered as general grain boundaries as in the cermets. First of all, WC grains are faceted. Secondly, substantial differences are present between the WC/WC grain boundaries. The grain boundary energy depends on its configuration, i.e. the orientation relationship (CSL), the type of facet (basal, prismatic etc.) and the termination that

can be either by tungsten or carbon atoms. The strength and stability of interfaces in WC-Co have been studied in detail by Christensen [12], showing that different types of WC/WC grain boundaries have, at equilibrium, a different attraction for cobalt. Some grain boundaries remain clean (without cobalt, e.g. Σ2 coincidence grain boundaries), some are very likely to be infiltrated by cobalt (general grain boundaries) and some allow cobalt segregation in half-monolayer quantities, which makes them more stable and resistant against further infiltration [12].

The peak P_{W3} with an activation energy of around 4 eV is attributed to more general grain boundaries that have no special orientation and that are probably weaker. Segregation of cobalt in these grain boundaries occurs easily. The activation energy of P_{W3} is apparent, i.e. it is related to a changing structure. The relaxation process, manifested by P_{W3}, is grain boundary sliding in a limited way controlled by diffusion of cobalt in the grain boundaries correlated with the movement of tungsten and carbon atoms.

The peak P_{W2} has a much lower activation energy: 2 eV. A mechanism involving the diffusion of cobalt in the WC/WC grain boundaries may be responsible for this peak. A certain number of grain boundaries with a stable half-monolayer of cobalt exists in WC-Co and, in contrast to the cermet, no further infiltration of these grain boundaries by cobalt is expected, because the presence of the segregated half-monolayer of cobalt makes these grain boundaries resistant towards further infiltration [12]. A peak related with these grain boundaries is therefore conceivable. However, it was shown that cobalt always goes into substitution. Therefore, the movement of cobalt atoms would involve the formation of vacancy sites. The movement of cobalt combined with the formation of vacancies would lead to a much higher activation energy for the peak than observed. However, if the grain boundaries were supersaturated with vacancies, which is plausible, and the cobalt could freely move, an activation energy of 2 eV seems probable. Moreover, the attempt frequency of the peak is rather low, 10^8 s^{-1}, which is typical for dislocation movement. So, in this case, the sliding of the grain boundaries may be related with the movement of dislocations controlled by the cobalt.

Both peaks, P_{W2} and P_{W3}, are present with the same activation energies, i.e. probably with the same relaxation mechanisms, in the skeletons. The peak amplitude in the skeletons is decreased compared to the peaks in the complete WC-Co. This may be due to a lower amount of vacancies present at the grain boundaries, i.e. the grain boundaries are less defective. In fact, the massive dissolution of tungsten in cobalt starting from around 1100 K might, in the complete WC-Co, lead to an increase of vacancy concentration at the grain boundaries. In the skeletons, where no solution in the binder is possible, this phenomenon is suppressed.

The sharp peak observed in the WC skeleton at about 1200 K (Fig. 6.8) has been related with the dewetting of cobalt residuals at grain boundaries [25]. However, dewetting would remove cobalt from grain boundaries suppressing both, P_{W2} and P_{W3}. It is more likely that the transient peak corresponds to a sudden recovery of vacancies. At first, a high mobility of the grain boundaries leads to a modulus drop, but then, a general rearrangement of the structure and possibly a recrystallization of the grain boundaries takes place, which explains the modulus recovery.

Concerning the peak amplitude of P_{W2} and P_{W3}, a reason for the maximum at 1350 K has not yet been found. A possible relationship with the evolution of residual stresses may serve as explanation. Another possibility is that the peaks P_{W2} and P_{W3} disappear when infiltration of grain boundaries occurs.

High temperature peaks of fully infiltrated grain boundaries

The peaks P_{W4} and P_{T4} show very similar characteristics. Both peaks show an amplitude of around 0.8. Their activation energy is high (5-7 eV), and most importantly, they are present in the as received hardmetals, but not in the hard phase skeletons. The fact that these peaks are not found in the skeletons, rules out a possible connection with the deformation of the hard phase grains and also with the clean (Co-free) grain boundaries. However, the modulus shows an important decrease at the maximum of the peak (factor 10), without going all the way down to zero, i.e. a certain mechanical resistance is still present. In view of these facts, the peaks P_{W4} and P_{T4} are interpreted as grain boundary sliding peaks of cobalt-infiltrated grain boundaries, both in WC-Co and in TiWCN-Co. The huge peak results from massive cobalt infiltration and sliding of totally lubricated grain boundaries. Supposing that cobalt and hard phase form a eutectic at the grain boundaries, the difference in eutectic melting point of the Co-TiCN and the Co-WC eutectic may well explain the different temperatures of the peak maxima.

In contrast to the grain boundary sliding model for ceramics by Lakki [67,88] (Chapter 3 §4.3.4), even with the extended grain boundary sliding marked by P_{W4} and $P_{T4,}$ peaks are always observed and not a background. Therefore, the more complex composite structure of hardmetals always maintains a restoring force and a certain stiffness of the skeleton.

The effect of stress

In WC-Co, the increase of IF strain amplitude has an effect on the high-temperature and low-frequency IF. While from Fig. 6.11, it is not possible to relate the increase of IF with increasing strain amplitude exactly to P_{W2}, P_{W3} or P_{W4}, Fig. 6.12 shows that both, P_{W2} or P_{W3}, are rather unaffected by the strain increase and that the increase is related only to P_{W4}. This observation goes in line with the given interpretation of the peaks. P_{W4}, related to sliding of fully infiltrated grain boundaries, is sensitive to the strain amplitude; higher strain produces a higher infiltration degree. Instead, the peaks P_{W2} and P_{W3}, attributed to diffusion controlled sliding are not sensitive to external stress.

The application of a tensile bias stress during IF measurements shows a change in the modulus (Fig. 6.13). This change of the modulus can be interpreted as a hardening stage, because the otherwise monotone decrease of the modulus with temperature is slowed down in a short temperature range. In the same range of temperature, a strong increase of the amount of soluted tungsten in cobalt is observed (Fig. 5.7c). The bias stress may so enhance the solution of tungsten in the binder. Thus the change of the modulus may show a solution hardening of the binder.

In the cermet, the bias stress leads to an enhanced instability of the grain boundaries, maybe caused by increased solution of hard phase from grain boundaries. The instability caused by the small stress causes an increase of the hysteresis (Fig. 6.29). Also, the IF measurement after deformation shows an increase of the hysteresis (Fig. 6.28). By changing the strain amplitude, a reversible increase of IF is achieved (Fig. 6.32). All these experiments induce an increase of P_{T4}. They show that, as in WC-Co, the infiltration of the grain boundaries by the cobalt is sensitive to the stress amplitude. They also show that when the stress is removed, the grain boundary state is restored. However, the quenching experiment (§2.5.3) clearly shows a strong effect on P_{T3} and no effect on P_{T4}. During this experiment, the grain boundaries have been modified and the modified structure was retained by the quenching. Therefore, P_{T3}, related to sliding due to cobalt segregation states is enhanced, but P_{T4}, related with sliding of fully infiltrated grain boundaries is the same.

3.3 General discussion relating IF results to results from Chapters 4 and 5

Regarding the TiWCN-Co, a remarkable parallel can be drawn between the observations in IF and the macroscopic deformation behavior studied by three-point bending. The IF background of the TiWCN skeleton changes from a low temperature/low activation energy state to a high temperature/high activation energy state at ca. 1350 K (Fig. 6.24). The appearance of the GBS peak P_{T3} of the TiWCN-Co, which then grows with increasing temperature, can be located at about 1300-1350 K (Fig. 6.34). It may be concluded that a change of the "clean" grain boundaries happens around 1350 K, which is visible in the IF background of skeletons, and that this change suddenly allows cobalt to segregate in the grain boundaries, manifested by the appearance of P_{T3}. Interestingly, the transition observed in the macroscopic deformation behavior of cermets and cermet skeletons measured by three-point bending is also located in this temperature range (Fig. 4.2b). Those observations seem to fit well into a common theory, where the macroscopic deterioration of mechanical properties can be related with the beginning segregation of cobalt in hard phase grain boundaries, due to a change of the grain boundary structure at 1350 K. After this temperature, grain boundary sliding starts either in a limited way as marked by P_{T3} or in a more extended one by cobalt infiltration induced by stress as marked by P_{T4}.

The same scheme cannot be applied directly to WC-Co. The transition in macroscopic deformation behavior between WC-Co and WC skeletons measured by three-point bending is found at 1100 K. In macroscopic deformation, this temperature is regarded as the onset of the deterioration of the mechanical properties of WC-Co. Microscopic deformation measured by mechanical spectroscopy shows that the drop of the modulus starts at exactly that temperature (Fig. 6.2). This modulus drop is related with peak P_{W1}, interpreted as a relaxation peak due to the movement of dislocations in the cobalt controlled by tungsten diffusion. In other words, it marks the beginning mobility of tungsten in the cobalt. Measurements of residual stresses have moreover shown that the amount of tungsten dissolved in the cobalt increases drastically, starting from 1100 K (Fig. 5.7c). However, this increase of tungsten concentration in the binder cannot be related directly to the deterioration of mechanical properties. An increasing solution hardening is more likely to be expected. On the other hand, the tungsten going into solution in the cobalt may partly (or even preferentially) come from WC/WC interfaces. An increase of vacancy concentration at the grain boundaries would lead to an increase of grain boundary diffusion either of tungsten and carbon (GB self-diffusion) or of segregated cobalt or both. The increased mobility of species inside the grain boundaries may result in a movement of adjacent grains under an applied stress. This may explain the comparatively high toughness of WC-Co at temperatures below 1100 K or even of the WC skeletons.

The presence of cobalt has always been the key to understand the high temperature deformation behavior. However in WC-Co, the tungsten (and carbon) may play a much more important role for the mobility of grain boundaries. When tungsten carbide goes into solution into the cobalt, assuming that dissolution takes place preferentially at grain boundaries (maybe close to triple points), vacancies are created in the same order of magnitude. The increased vacancy concentration at grain boundaries increases their mobility, no matter if the grain boundary slides because of cobalt diffusion or self-diffusion. In these early stages of GBS, the cobalt binder may act mostly as sink for tungsten carbide solution.

However, stress can play a major role by promoting more extended infiltration of the grain boundaries and therefore high creep. Depending on the stress, different GBS regimes are possible in WC-Co: at low stress, limited GBS is related to segregated cobalt depending on the grain boundary type and at high stress, extended GBS is due to cobalt infiltration that produces large

deformation. The peak P_{W4}, as well as P_{T4} of the cermet, is attributed to a cobalt infiltrated state and both are proven to be sensitive to stress. Even if the peak maximum is located at very high temperature, its amplitude is so high that the phenomenon is present already at much lower temperatures.

Chapter 7

Exploring ways to reduce hardmetals high temperature deformation: effect of tantalum

In the previous chapters, the mechanisms leading to high temperature deformation related to the wear of cutting tools were presented. It has been demonstrated that grain boundary sliding plays a major role both in cermets and cemented carbides. The purpose of this chapter is to investigate, in which way this deformation at high temperature may be reduced. In particular, the beneficial effect of a small tantalum addition to the cemented carbide and to the cermet is studied. Rolander et al. [89] investigate the effect of tantalum on structure and mechanical properties of cermets. They prove that the beneficial effect on wear resistance during metal cutting is entirely due to the addition of tantalum. Neither hard phase nor binder phase properties, such as grain size or shape, core and rim composition, core/rim ratio, solution hardening of the binder or contiguity, did show an influence that could explain the increased wear resistance. The authors suggest that tantalum influences the interfacial energies of the system, yielding a stronger hard phase skeleton.

1 Material modification

1.1 Composition, structure and properties

A WC-Co-Ta cemented carbide (labelled WTaC-Co) and a TiWCN-Co-Ta cermet (labelled TiWTaCN-Co) were developed. About 2 at.% of tantalum was added in form of TaC as replacement of tungsten in WC-Co and of tungsten and titanium in TiWCN-Co. The chemical composition of the materials is shown in Table 7.1. For a comparison with the reference material, see Table 3.1. Special care was taken in order to obtain similar binder compositions as in the reference materials, so that all investigated materials, cermets and cemented carbides, have the same binder. Therefore, the cermet studied so far contains a quite low amount of tungsten in the binder, which was achieved by an unusually high carbon content. Turning tests showed that the improvement expected with the addition of tantalum was not reached (Fig. 7.3). The carbon content obviously plays an important role. Therefore, additional cermet material with lower carbon content was produced, TiWCN-Co_{LC} and TiWTaCN-Co_{LC}. The cermets with the high carbon content will be labelled TiWCN-Co_{HC} and TiWTaCN-Co_{HC}.

The morphology of the materials is shown in Fig. 7.1. The WTaC-Co (b) is, compared to WC-Co (a), slightly more porous, the distribution of the cobalt phase is less homogeneous and

Table 7.1 : Materials compositions determined by chemical analysis after sintering

	Chemical composition in wt.%						Chemical composition in at.%					
Material	Co	W	C	Ti	N	Ta	Co	W	C	Ti	N	Ta
WTaC-Co	6.11	86.4	5.71			2.04	9.79	44.25	44.90			1.06
TiWTaCN-Co_{HC}	12.66	16.5	8.94	46.80	5.03	9.27	8.80	3.85	30.49	40.04	14.71	2.10
TiWCN-Co_{LC}	14.20	18.2	8.70	52.70	6.09		9.27	3.83	27.86	42.33	16.72	
TiWTaCN-Co_{LC}	13.20	16.3	8.26	46.60	5.55	8.86	9.23	3.93	28.35	40.13	16.34	2.02

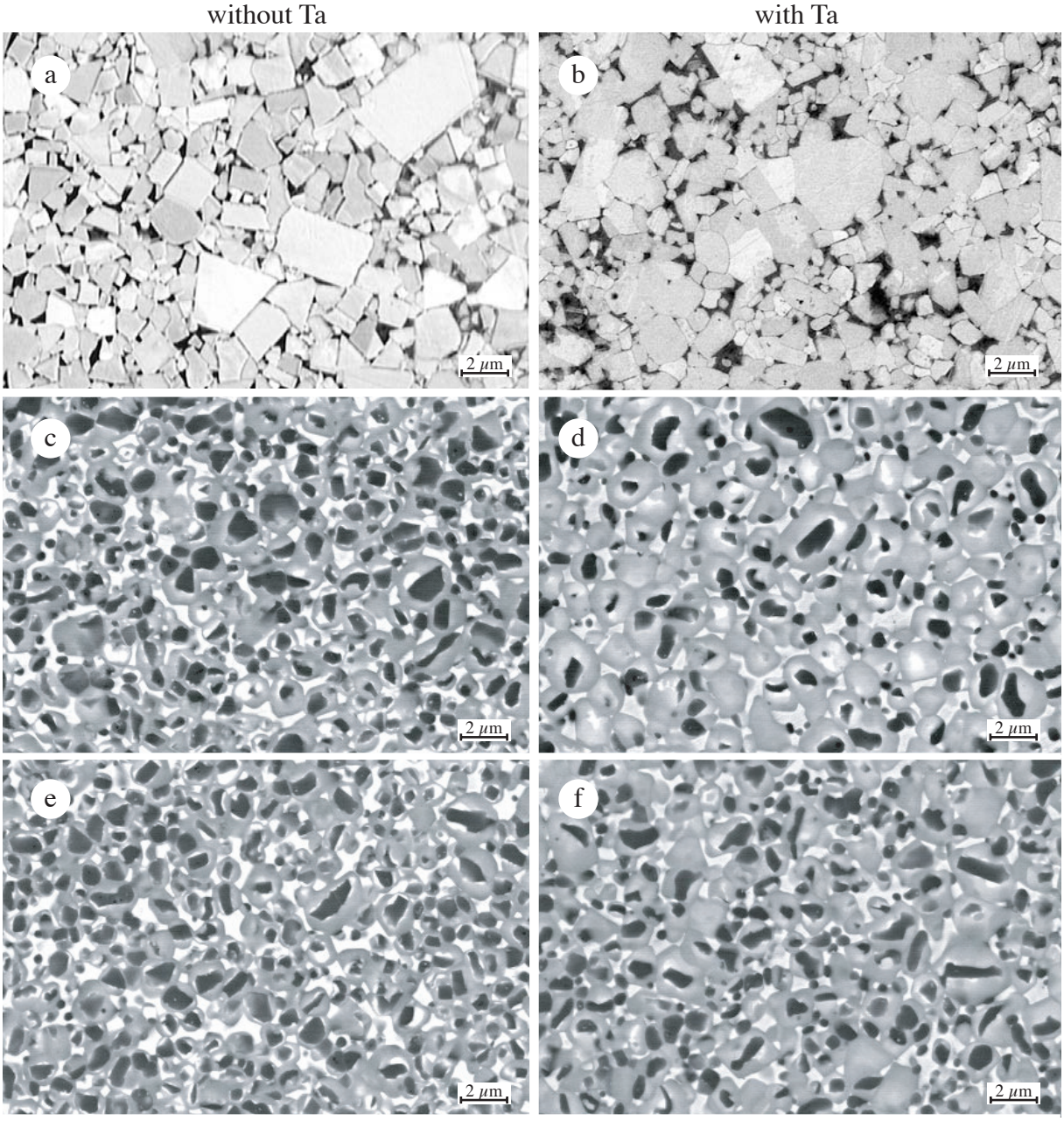

Figure 7.1: Structure of a) WC-Co, b) WTaC-Co, c) TiWCN-Co_{HC}, d) TiWTaCN-Co_{HC}, e) TiWCN-Co_{LC} and f) TiWTaCN-Co_{LC} (images supplied by S. Norgren, AB Sandvik Coromant, Stockholm, Sweden)

moreover, WTaC (a cubic carbide called γ-phase of a structure of B1 type) is finely dispersed in the structure. Larger cobalt pools are found, which is probably a first sign of a decreased wetting of cobalt on the WC surfaces due to the presence of tantalum.

The structure of the cermets (c) to (f) is quite similar, except for the high carbon cermet with tantalum, TiWTaCN-Co_{HC}. In this cermet (d), the hard phase grains appear larger and the total core volume fraction is reduced.

Table 7.2 shows some of the materials basic properties. The data for the tantalum-free materials from Table 3.2 are repeated here for a better overview. The tungsten concentration in cobalt given in the table is calculated from the cobalt magnetic saturation. The grain size, determined by the mean linear intercept (determined by G. Östberg, Chalmers University of Technology, Göteborg, Sweden), is slightly increased for the tantalum-containing materials. Important is also the lower tungsten solution in the TiWTaCN-Co_{HC}.

Table 7.2 : Basic properties of the hardmetals without and with tantalum

Material	density [g/cm^3]	grain size [μm]	HV3 hardness	magnetic saturation Co_{magn}	wt.%W in sol (calc)	at.%W in sol (calc)	coercivity H_c
WC-Co	14.97	2.10	1493	5.1	9.80	3.24	13.12
WTaC-Co	14.76	2.59	1405	5.18	9.59	3.17	13.31
TiWCN-Co_{HC}	6.34	2.05	1594	11.63	10.67	3.82	13.96
TiWTaCN-Co_{HC}	6.64	2.52	1473	11.47	5.92	2.13	12.03
TiWCN-Co_{LC}	6.3		1468	11.34	10.39	3.71	13.92
TiWTaCN-Co_{LC}	6.67		1478	9.46	21.73	7.53	13.82

1.2 Wear tests

The plastic deformation (PD) of the materials was determined during turning tests under controlled conditions. A martensitic steel tube is used as work piece. The turning is performed with a depth of cut of 1 mm and a feed rate of 0.3 mm/rev using different cutting speeds from 300 to 550 m/min until the final failure of the cutting edge. The deformation of the cutting edge is then measured as the change of the shape in mm (Fig. 7.2). The results are shown in Fig. 7.3. It can be assumed that an increase of the cutting speed is related with an increase of the temperature at the cutting edge. However, one should be careful in comparing different materials, because different thermal conductivities lead to a different heat transfer from the edge to the bulk and thus the temperature at the cutting edge can be substantially different.

A slight beneficial effect of tantalum on WC-Co may be present at lower cutting speeds. At the highest cutting speed, a sudden increase of wear beyond that of WC-Co is observed. For the cermet with high carbon content, the tantalum proves to be catastrophic. The wear is highly increased already at low cutting speeds and the cutting edge breaks easily, which shows that this cermet is very fragile. The cermet with high carbon content and without tantalum shows very good wear resistance. The low carbon cermets show the expected wear behavior. Compared to the cermet without tantalum, the cermet with tantalum is more wear resistant. However, the wear is lowest for the cermet with high carbon content and no tantalum.

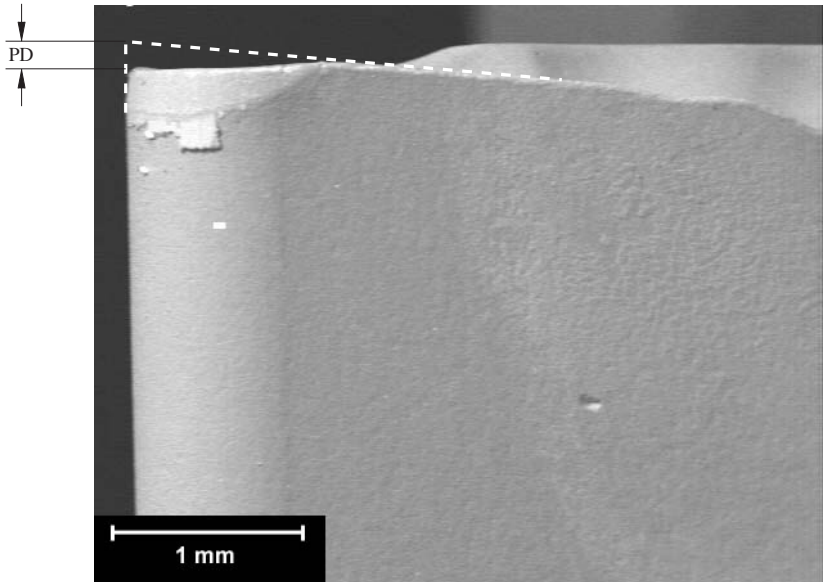

Figure 7.2: Cutting insert with worn cutting edge (PD - plastic deformation) [90]

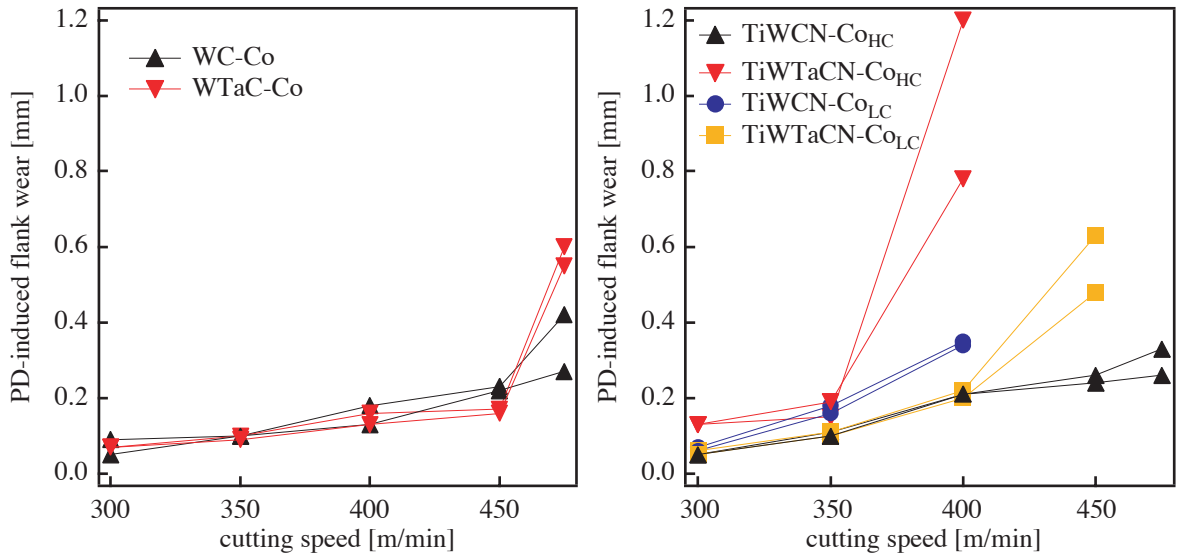

Figure 7.3: Plastic deformation of the cutting edge obtained during turning at different cutting speeds

2 Three-point bending results

2.1 Stress-strain curves

The comparison of the two base materials with their tantalum containing variant is shown in Fig. 7.4 for three different temperatures. An increase of the yield strength is observed for the WTaC-Co as compared to WC-Co at all temperatures. At the same time, the strain at fracture decreases. The material is more refractory at medium temperatures (1173 and 1273 K in Fig. 7.4a). At 1473 K, the observed flow stress is slightly higher (42 MPa instead of 31 MPa). In general, an improvement in terms of deformation strength can be attributed to the addition of tantalum.

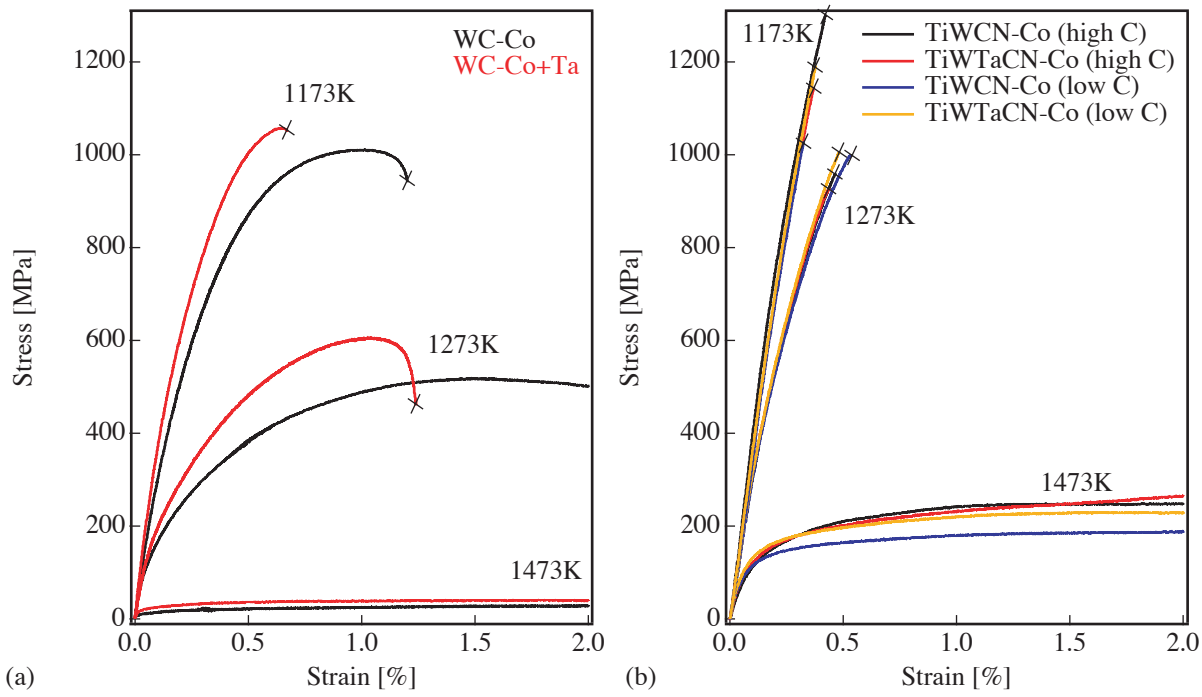

Figure 7.4: The effect of tantalum on macroscopic deformation of a) WC-Co and b) TiWCN-Co

For the cermet, no obvious change of the behavior is observed (Fig. 7.4b). Looking very closely, the tantalum addition seems to have decreased the stress and strain at fracture, but the differences are smaller than the observed scatter.

The WTaC skeletons show a lower deformation resistance, when compared with WC skeletons (Fig. 7.5a). In fact, the trend of the WTaC curves at very low strain is similar to those of WC, but the WTaC skeleton samples break much more easily. This behavior can be explained by the heterogeneous distribution of the cobalt phase (Fig. 7.1d), the larger amount of pores and also the small amount of finely dispersed γ-phase.

The TiWTaCN skeletons are also weaker than the TiWCN skeletons (Fig. 7.5b), but clear differences between samples with and without tantalum cannot be found.

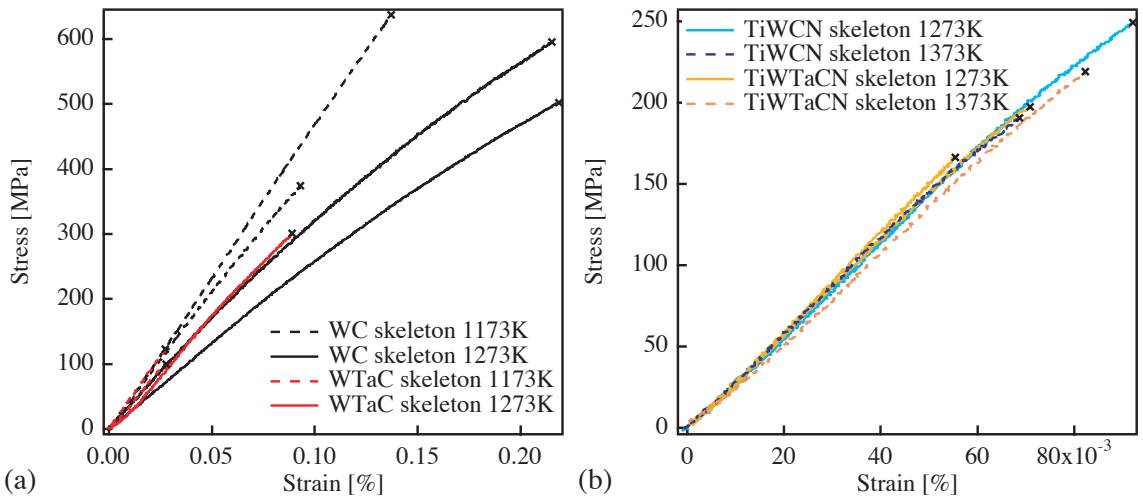

Figure 7.5: Effect of Ta on deformation of hard phase skeletons for (a) WC and (b) TiWCN

2.2 Activation energy of creep

Fig. 7.6 shows the creep activation energy. The results presented in Fig. 4.4 are shown on the same figure here for comparison. The WC-Co with tantalum (Fig. 7.6a) does not show a stable level of activation energy. The measured values are randomly distributed between 3 and 6 eV in a temperature range from 1050 to 1400 K. A dominant flow mechanism cannot be attributed.

The tantalum containing cermet with high carbon content (Fig. 7.6b) shows an activation energy level that remains at 5 - 6 eV down below 1100 K. A transition towards a low activation energy creep regime is not found. The cermet with tantalum and low carbon content has a slightly lower activation energy above 1200 K as compared to the TiWCN-Co. It also shows the transition at 1200 K.

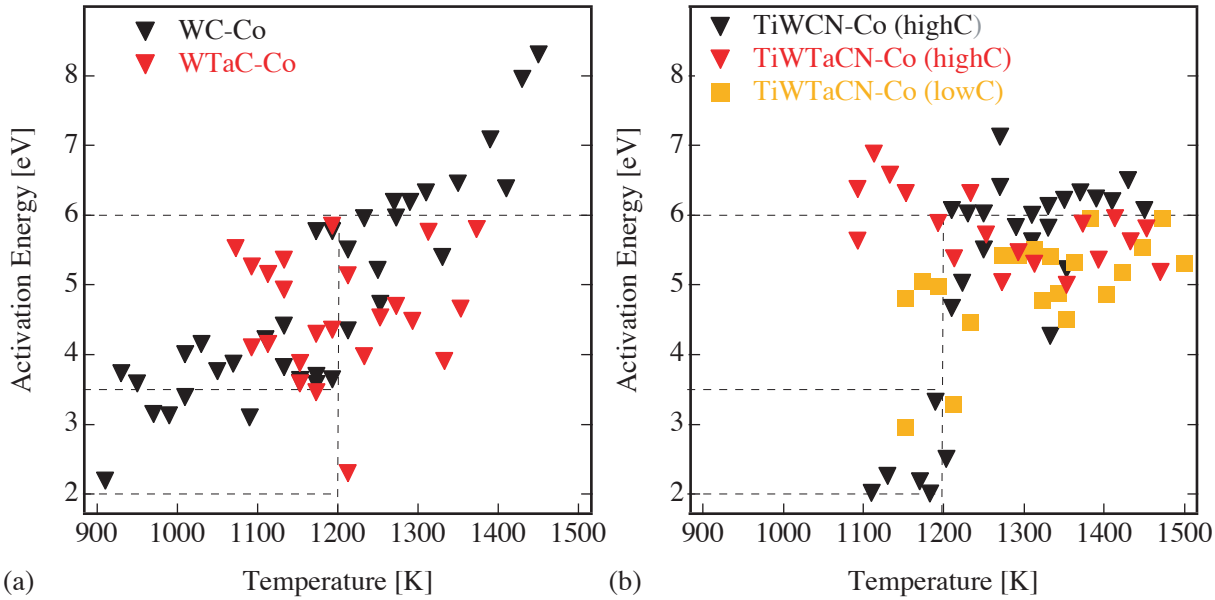

Figure 7.6: Activation energy of creep measured with the temperature jump method for (a) cemented carbides and (b) cermets

3 Internal friction results

3.1 Comparison of WC-Co with and without Ta

3.1.1 General IF spectra

The WTaC-Co shows a lower IF than WC-Co. Fig. 7.7a and Fig. 7.7b show the first and respectively second heating-cooling cycle. The IF is clearly reduced all along the temperature spectrum, but the common features, peak P_{W1} and P_{Wc}, are still present. The modulus does not decrease as fast as for WC-Co without tantalum, which goes in line with an improvement of the material by tantalum. However, at high temperature, the structure with tantalum seems more unstable. A hysteresis forms at temperatures above 1400 K. Whereas the IF in WC-Co without tantalum is very stable after the first heating (Fig. 7.7b), the WTaC-Co IF increases at high temperature. Because of the changing background, a deconvolution of the WTaC-Co spectra is extremely difficult. The peak amplitude depends very much on the background sub-

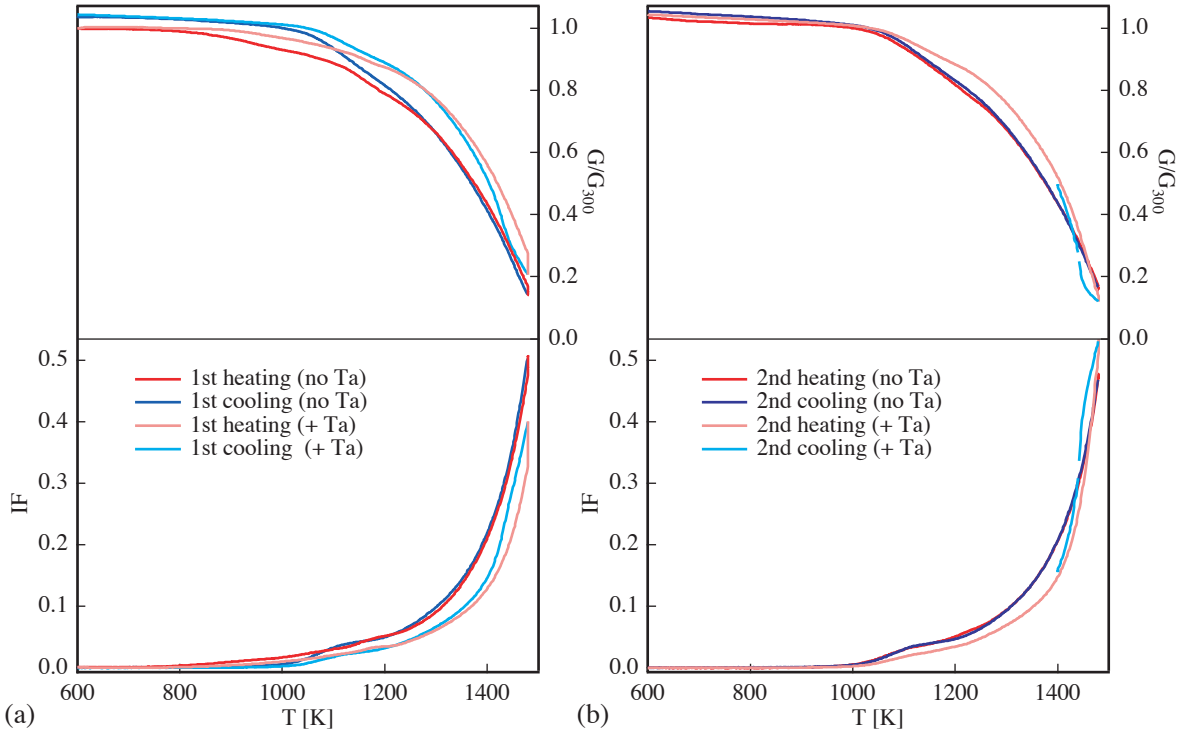

Figure 7.7: Comparison between WC-Co without and with Ta; (a) first and (b) second heating-cooling cycle

traction. A quantitative comparison between WC-Co with and without tantalum by comparing the peak parameters is therefore not given here. The high temperature IF from isothermal measurements is presented in Fig. 7.8. The high-temperature peak P_{W4} appears at the same frequency, but its amplitude is clearly increased by tantalum. However, it is clearly seen that the IF of WC-Co with tantalum at 1200 K (Fig. 7.8) is lower than the IF of Ta-free WC-Co, as in the temperature scans (Fig. 7.7b). The fitting of the peaks, called P_{W2Ta} and P_{W3Ta} is extremely difficult. Therefore, their activation parameters as well as their position should be taken with precaution.

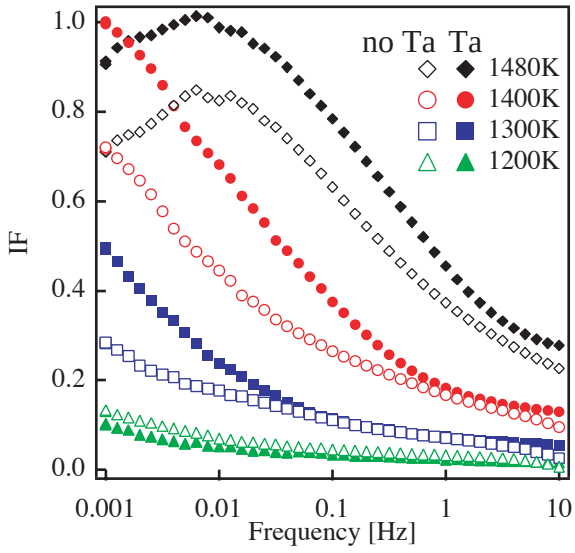

Figure 7.8: Frequency scans of WC-Co with and without Ta at different temperatures

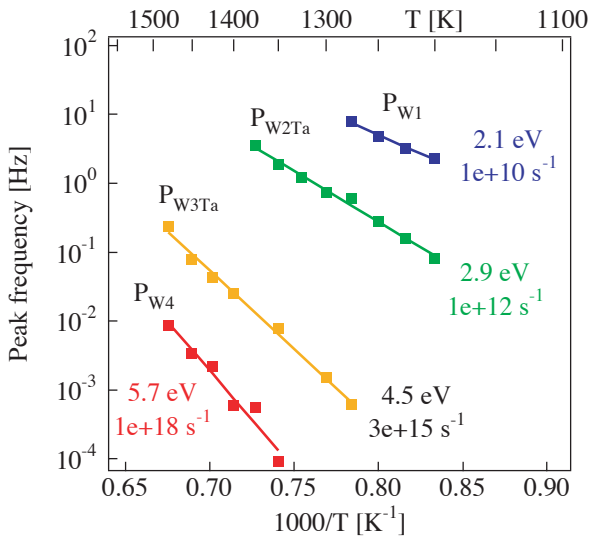

Figure 7.9: Arrhenius plot for WTaC-Co showing P_{W1}, P_{W2}, P_{W3} and P_{W4} and activation parameters

3.1.2 The hard phase skeleton

The hard phase skeleton with tantalum presents a similar transient peak as the WC skeleton (Fig. 7.10). The modulus drop, accompanying the peak is, however, much deeper. It is moreover not followed by a hardening as in the case of the WC skeleton. A small modulus recovery is observed at temperatures above 1400 K and during the dwell at 1500 K. The total modulus reduction after a full first cycle is about 15 %.

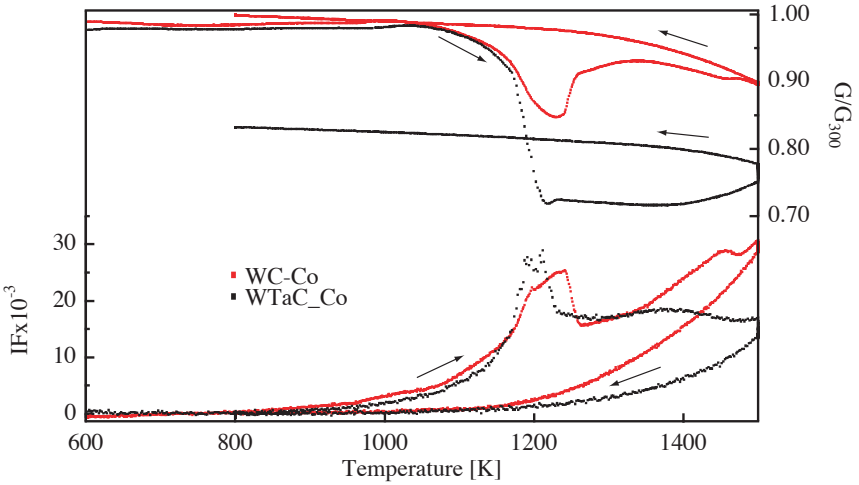

Figure 7.10: WTaC skeleton compared to WC skeleton, transition peak is accompanied by a substantial modulus drop at ca. 1200 K

Deconvolution of the IF spectra in stable conditions, i.e. after reduction of the transient peaks, shows that no peaks are present, only an IF background. The IF curves are generally lower than those from the WC skeleton at the same temperatures. The peaks P_{W2} and P_{W3} well visible in the WC-Co skeleton seem to be erased by the presence of tantalum. The activation energy of the background of about 4.5 eV corresponds to the activation energy measured for the background of WC skeletons (Chapter 6 §1.3).

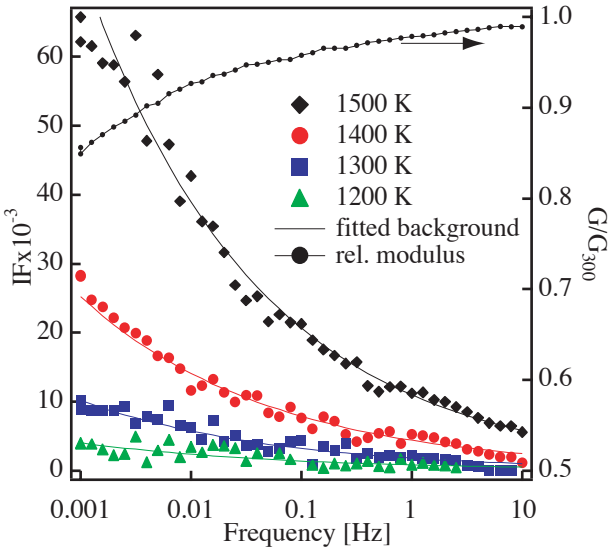

Figure 7.11: IF vs. frequency shows that the WTaC skeletons shows just a background, no peaks

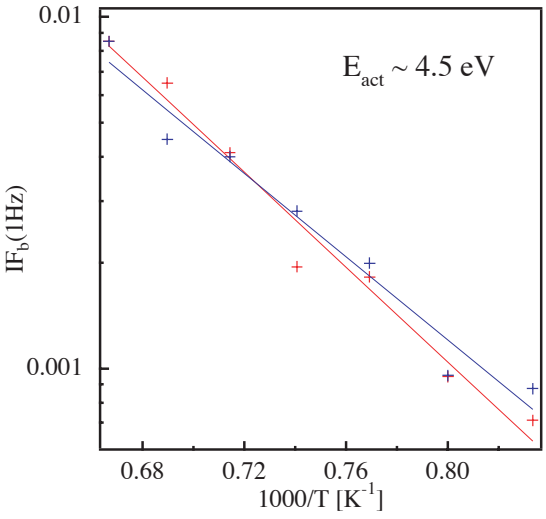

Figure 7.12: E_{act} of the WTaC IF background determined according to Chapter 3 §4.3.1

3.1.3 Sharp transition towards GBS

In some cases, probably related with the thermal history of the sample, a change of the IF at high temperatures is observed. This change involves an increase of IF and a decrease of the modulus together with the formation of a hysteresis. The hysteresis at high temperature, in fact, develops during ongoing thermal cycling into a sharp transition (Fig. 7.13). At the transition, the slope of the IF curve as well as that of the modulus changes. At high temperature, the slope is less steep than at the temperatures before the transition. The transition temperature is different in heating and cooling. In heating, the temperature is around 1405 K, and during cooling, it is around 1375 K. This behavior resembles a phase transformation. It is related with a strong decrease of the modulus, which implies a softening of the material.

An interesting detail is the disappearance of the cobalt peak P_{W1}. It may be related with a decrease of internal stresses or with a transformation of the binder.

The very low scatter of the experimental data, especially by performing frequency sweeps before and after the transition as shown in Fig. 7.14, suggests that the observed behavior is not due to an experimental artefact as for example a loosening of the grips that hold the sample.

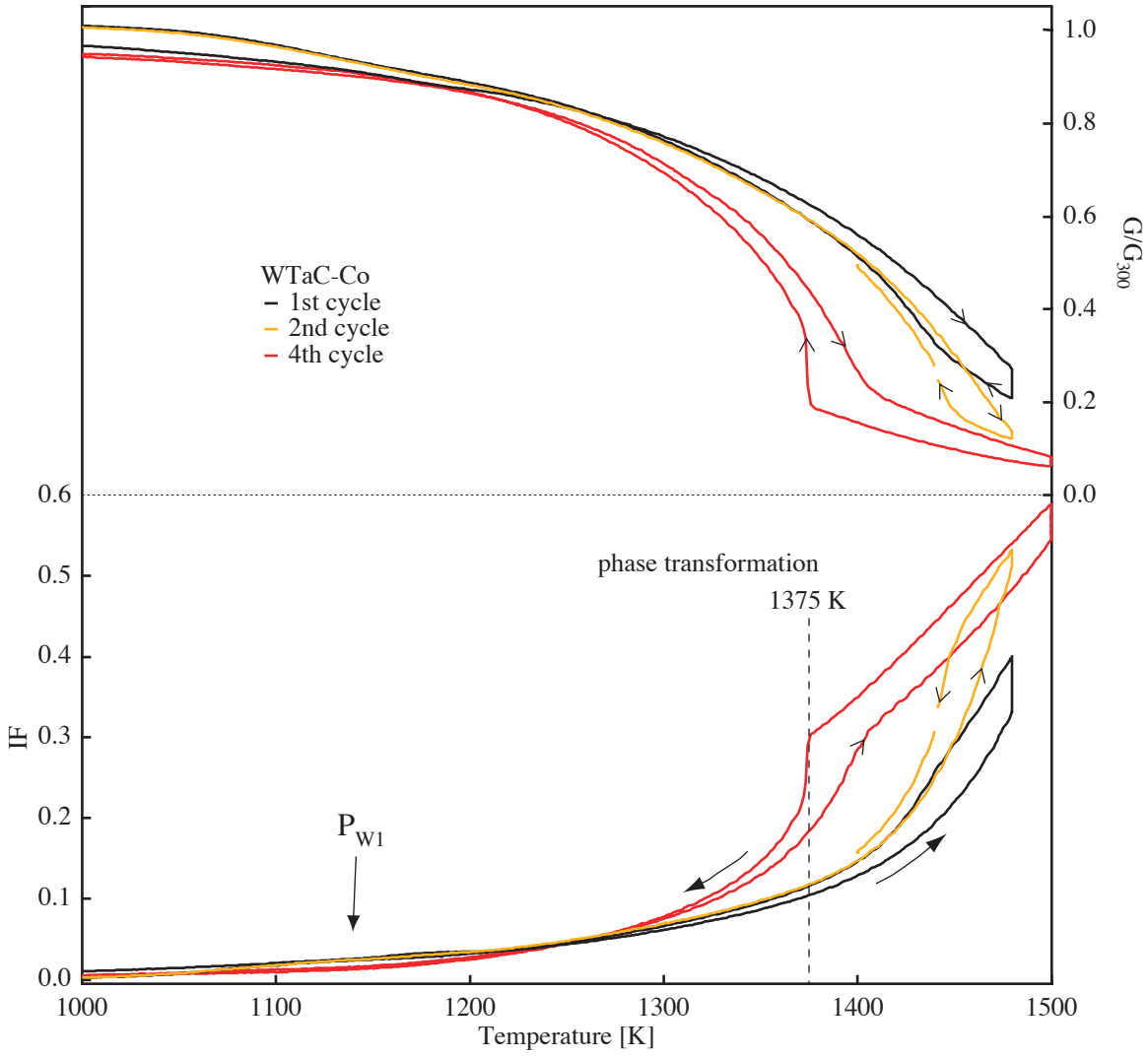

Figure 7.13: Evolution of the IF showing a transformation, probably of the cobalt

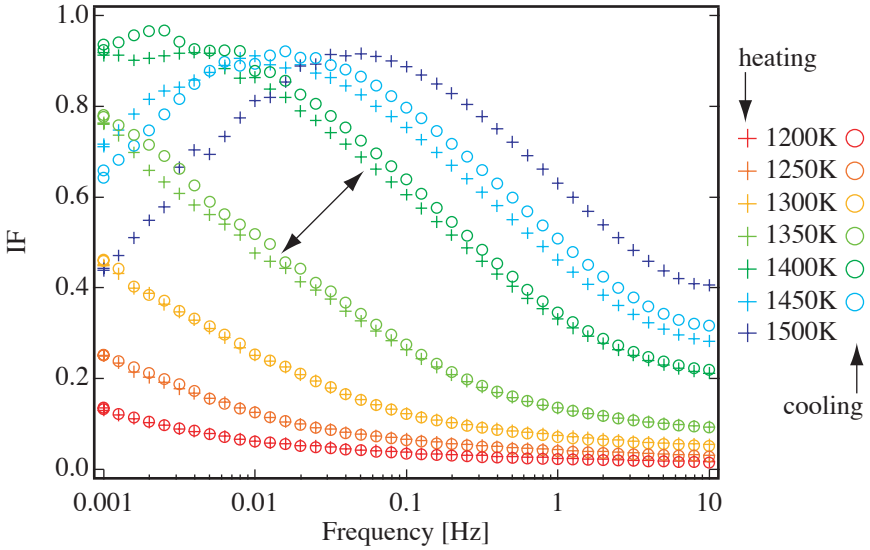

Figure 7.14: Frequency scans on WTaC-Co that shows the transformation between 1350 and 1400 K as indicated by the arrow.

Frequency scans performed on the same sample exhibiting the transition in Fig. 7.13, show that two different stages are obtained before and after the transformation at around 1375 K (Fig. 7.14). The change is completely reversible, shown by the frequency measurements that are performed isothermally at different temperatures from 1200 K up to 1500 K and back. The curves that usually shift monotonously towards high frequency with temperature, show a much larger shift between the curves below and above the transformation temperature. A comparison with measurements on a sample of the same type that does not undergo the transition shows, that below the transition, the curves are the same as obtained normally. However, above the transition, the peak shows a strong shift towards higher frequencies without, in fact, changing its height.

3.2 Comparison of TiWCN-Co with and without Ta

3.2.1 General IF results

The IF of the three additional cermet variants is measured. The general temperature spectrum for all cermets resembles the one presented in Chapter 6. No cobalt peak is observed, P_{T2} is small, compared to those known from literature (see Chapter 2) and P_{T3} shows similar characteristics, i.e. the peak grows in height with temperature. However, a deconvolution of the temperature spectra (as in Fig. 6.14) is not shown here, because the materials are very unstable at high temperature, much more than the cermet presented in Chapter 6. To illustrate this, Fig. 7.15 shows a first heating cooling cycle of all four cermets. The cermet TiWCN-Co_{HC} presented in Chapter 6 is shown in black. Clearly, the other cermets show a larger heating-cooling hysteresis. Especially the TiWTaCN-Co_{HC} shows an extremely large hysteresis, indicating that this material is the most unstable at high temperature. Parallel with the evolution of IF, the decrease of the dynamic modulus is stronger than that of TiWCN-Co_{HC}.

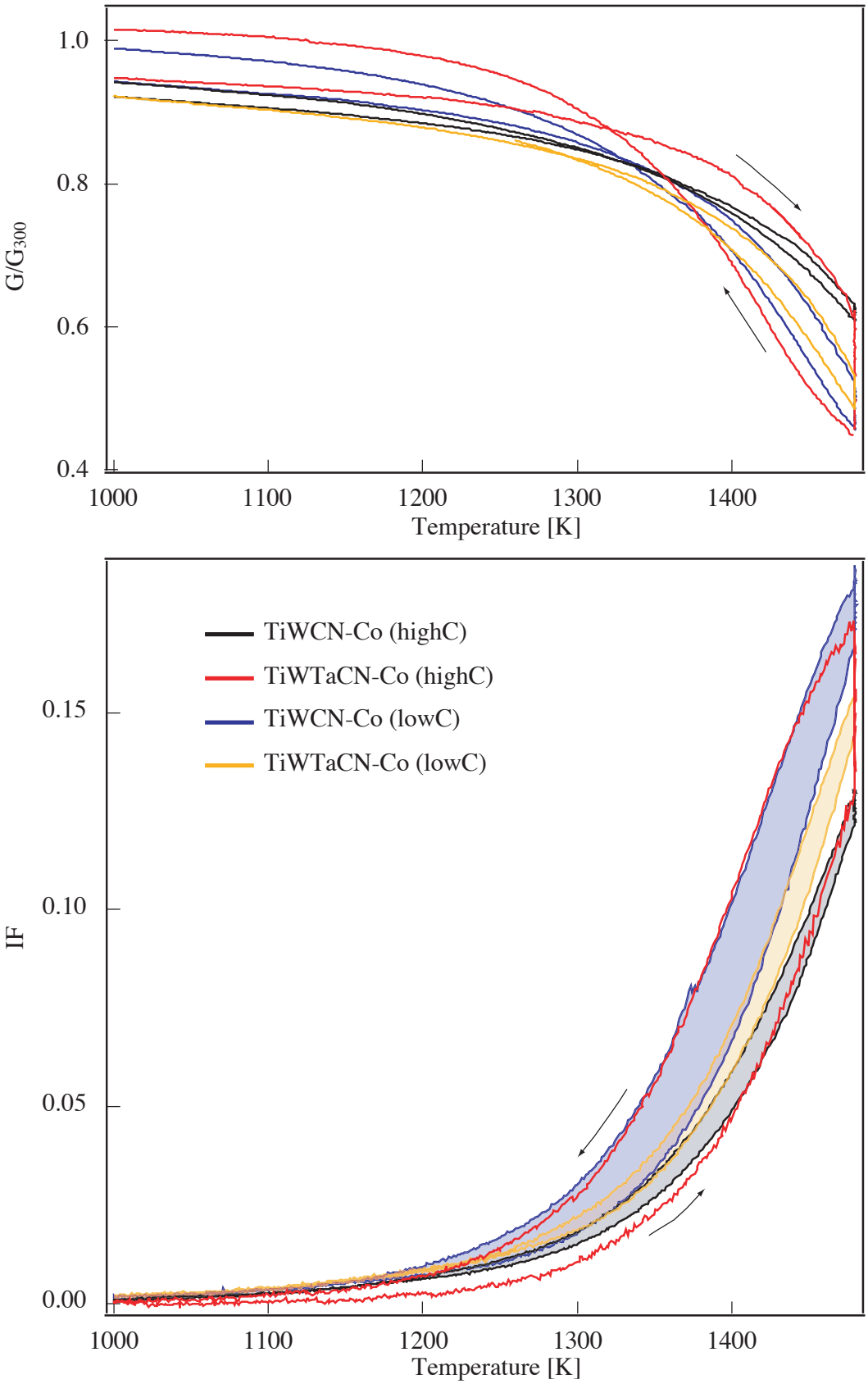

Figure 7.15: IF heating-cooling cycles and change of the dynamic modulus of all four cermet materials. The IF curves are filled to show the difference in the hysteresis.

As, during thermal cycling, the materials show a metastable character, most of the investigations are done isothermally in frequency measurements. The peak P_{T2} shows an activation energy around 2.5 eV (Fig. 7.17). The peak P_{T3} is evaluated after the subtraction of the background (P_{T4}), as presented in Fig. 7.16 for TiWTaCN-Co_{HC}. The activation energy of this peak (Fig. 7.17) corresponds to the findings in Chapter 6. The height of this peak does also correspond to the peak height of P_{T3} of TiWCN-Co_{HC}. Surprisingly, the large difference between TiWCN-Co_{HC} and TiWTaCN-Co_{HC} in temperature measurements, evidenced by the hysteresis (Fig. 7.15), does not correspond with the difference in the height of peak P_{T3}.

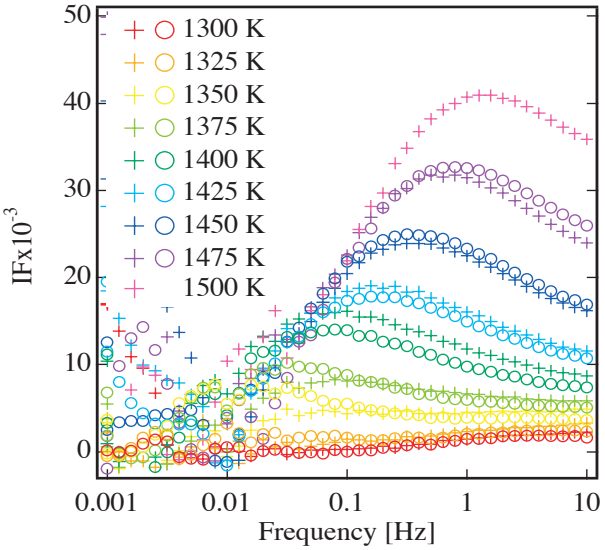

Figure 7.16: IF vs. frequency after subtraction of the background (P_{T4}) showing peak P_{T3}

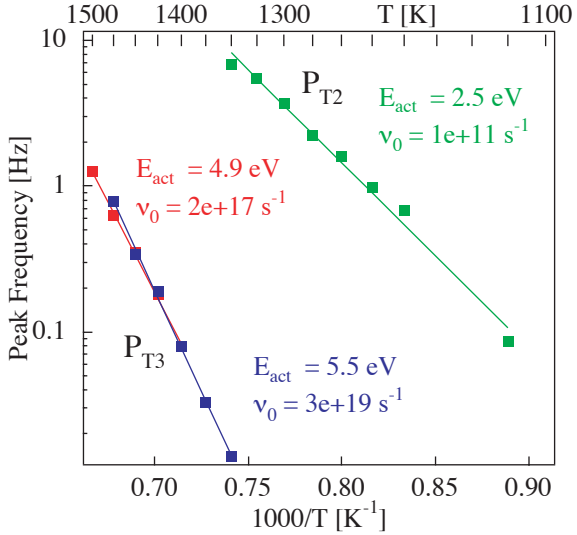

Figure 7.17: Arrhenius plot of the peaks P_{T2} and P_{T3} (in heating and cooling) of TiWTaCN-Co_{HC}

The behavior of the peak P_{T3} is shown for the three cermets in Fig. 7.18. It should be noted here that for TiWTaCN-Co_{HC} as well as for TiWCN-Co_{HC} the results have been verified by many measurements. On the contrary, only few experimental results exist for the two cermets with low carbon content, TiWCN-Co_{LC} and TiWTaCN-Co_{LC}. Therefore, these results should be taken with more precaution.

Small differences in the peak height exist, however, all results show the same trend: an increase of the peak from around $1 \cdot 10^{-3}$ at T<1300 K to 40-80$\cdot 10^{-3}$ at T_{max}=1500 K. The characteristics of P_{T3} are summarized in Table 7.3.

Notice that the amplitude increase in TiWTaCN-Co_{LC} only starts at 1400 K. Moreover, the activation energy changes from 5.8 to 8 eV and at the same temperature (Fig. 7.18b), the peak broadening goes from 1 (characteristic for a single relaxation time) to 0.5.

Table 7.3 : Characteristic parameters of the peak P_{T3} for all four cermets (* Above 1400 K)

	T [K] at 1 Hz	Peak height /10^{-3}	Activation energy [eV]	Attempt frequency ν_0 [s^{-1}]	Broadening
TiWCN-Co_{HC}	1480±40	40-60	4.7±0.5	10^{15}-10^{18}	0.6-0.9
TiWTaCN-Co_{HC}		40-60	5.5±0.8	10^{18}-10^{19}	0.5
TiWCN-Co_{LC}		80	5.5	10^{20}	0.4
TiWTaCN-Co_{LC}		30	5.8 (8)*	10^{20} (10^{28})*	1 (0.5)*

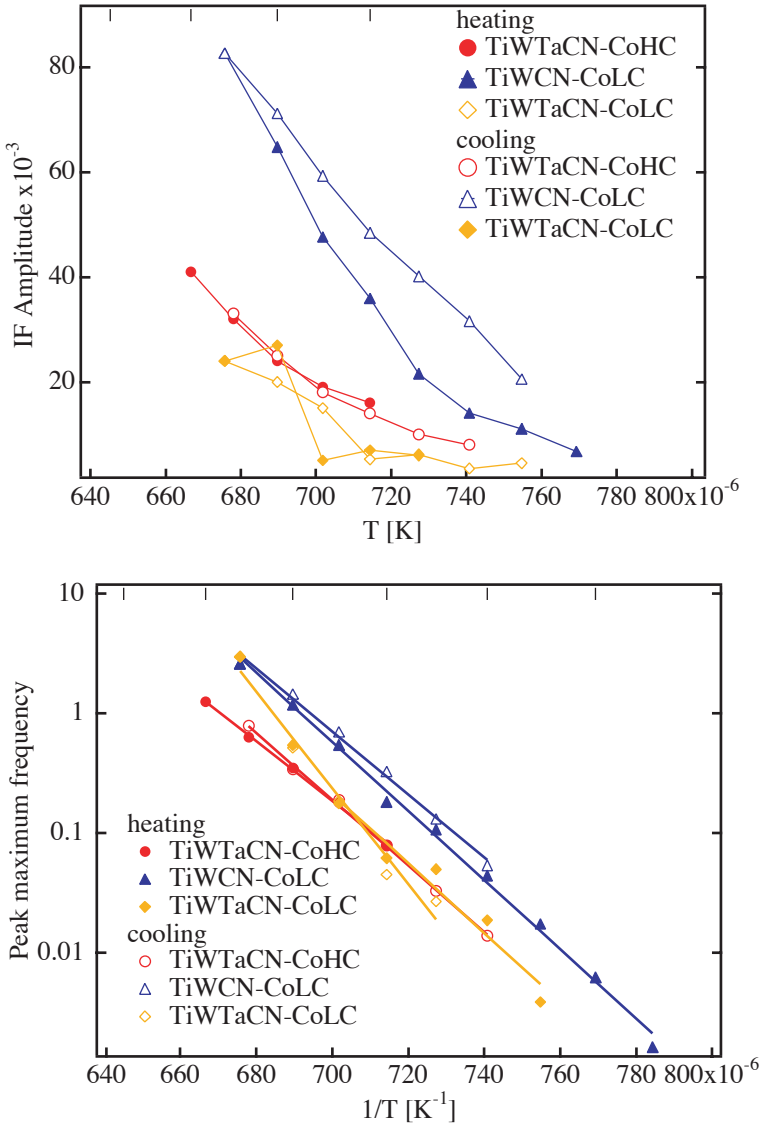

Figure 7.18: Peak P_{T3}: (a) shows the evolution of its height with temperature and (b) shows the Arrhenius plot of this peak for the evaluation of its activation energy.

Similar to the increase of the height of peak P_{T3} in frequency spectra, an increase of IF during a 2 hours dwell is observed in temperature spectra. Fig. 7.19 shows consecutive thermal cycles with a dwell at T_{max} of two hours between heating and cooling. The maximum temperature is increased in steps of 20 K. An increase of IF at T_{max} is not observed at temperatures below 1300 K. Above that temperature, the increase gets stronger with increasing temperature.

In the same experiment, the appearance of P_{T1} is observed. Fig. 7.20 shows the thermal cycles up to 1300 K. Peak P_{T1} is not present during the first heating, but it appears after annealing at 1200 K. Then the peak is stable until the annealing at 1260 K. The cooling following this annealing shows no peak and the peak is not observed upon further cycling.

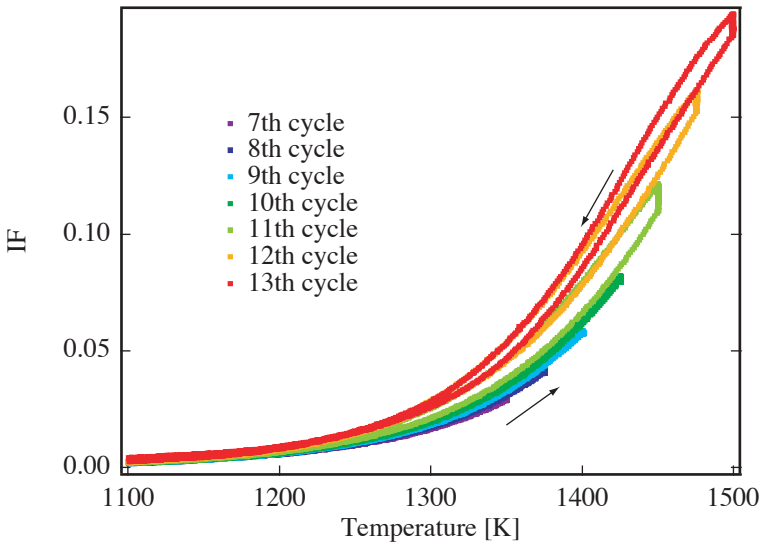

Figure 7.19: Heating-cooling cycles on TiWTaCN-Co with 2 hours annealing at T_{max}. Consecutive thermal cycles are performed by increasing T_{max}.

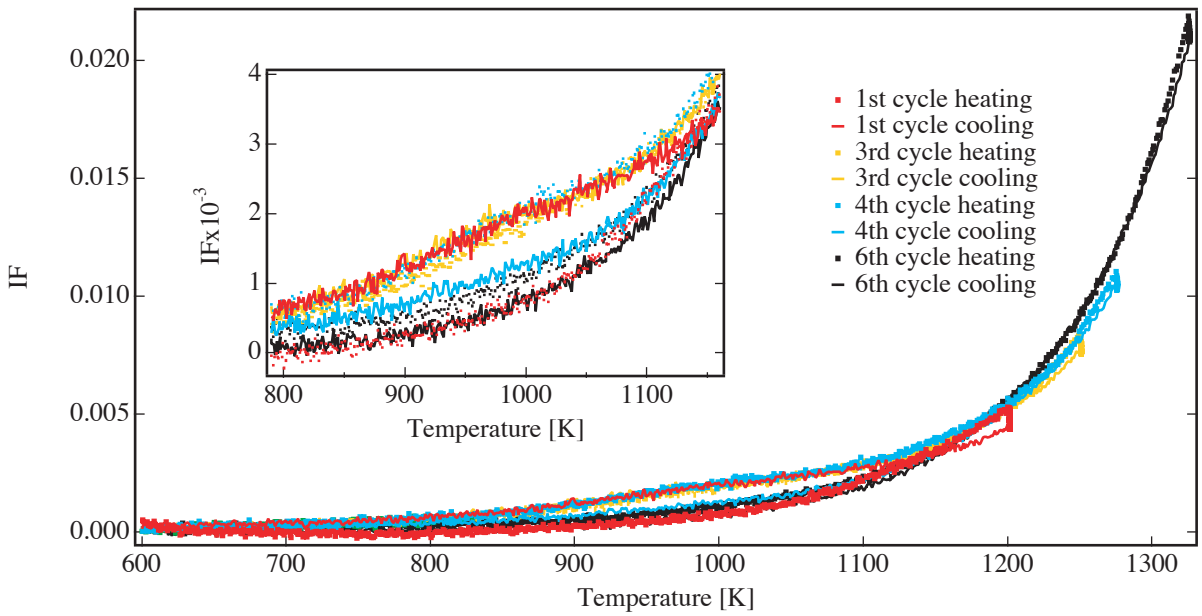

Figure 7.20: Heating-cooling cycles on TiWTaCN-Co between 600 and 1325 K with 2 hours annealing at T_{max}, showing the appearance and disappearance of P_{T1} depending on the annealing temperature.

3.2.2 TiWTaCN skeleton

The IF of a skeleton of the TiWTaCN-Co_{HC} cermet is presented in Fig. 7.21. The first heating shows a transient behavior with a strong increase starting at 1350 K and a decrease at 1500 K. During cooling and in the following cycles, the IF appears to be stable. This behavior should be compared with that shown in Fig. 6.21 where the first heating also shows an increase around 1350 K but much less steep.

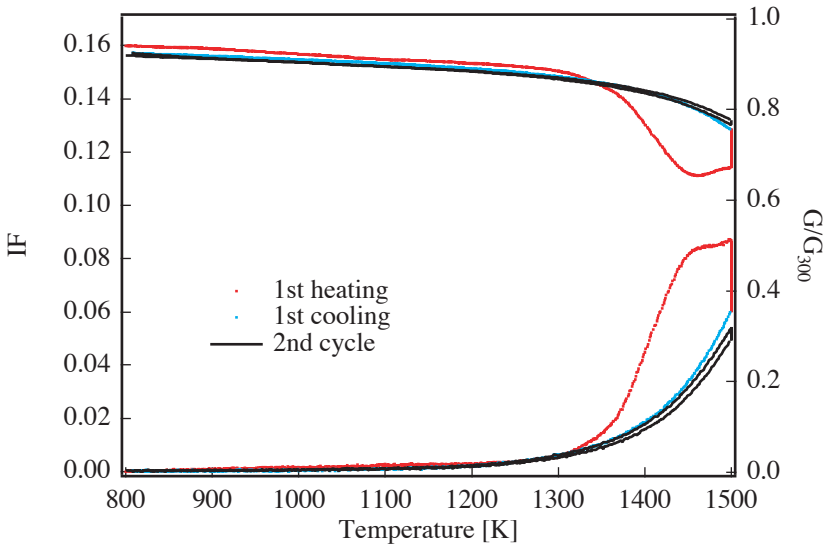

Figure 7.21: IF and modulus G of TiWTaCN-Co_{HC} skeleton

3.2.3 Transition towards GBS

Similar to the observations for the WTaC-Co in §3.1.3, a trend towards a transformation is observed for the cermet TiWTaCN-Co_{HC}. This transition is seen after 2 hours annealing at 800 K (Fig. 7.23) and by heating with 0.25 K/min (Fig. 7.22), which is 4 times slower than normally. The IF increases drastically and it is accompanied by a strong softening (G changes from 0.8 to 0.1). The following measurement, performed at a normal heating rate of 1 K/min, cannot restore the behavior, the IF remains high and the modulus low.

To investigate if these observations are caused by the annealing at 800 K or by the slow heating/cooling rate, an annealing of 12 hours has been performed at 800 K, followed by measurements at normal 1 K/min. The measurements are presented in Fig. 7.23. An even stronger effect with a sharp transformation is observed.

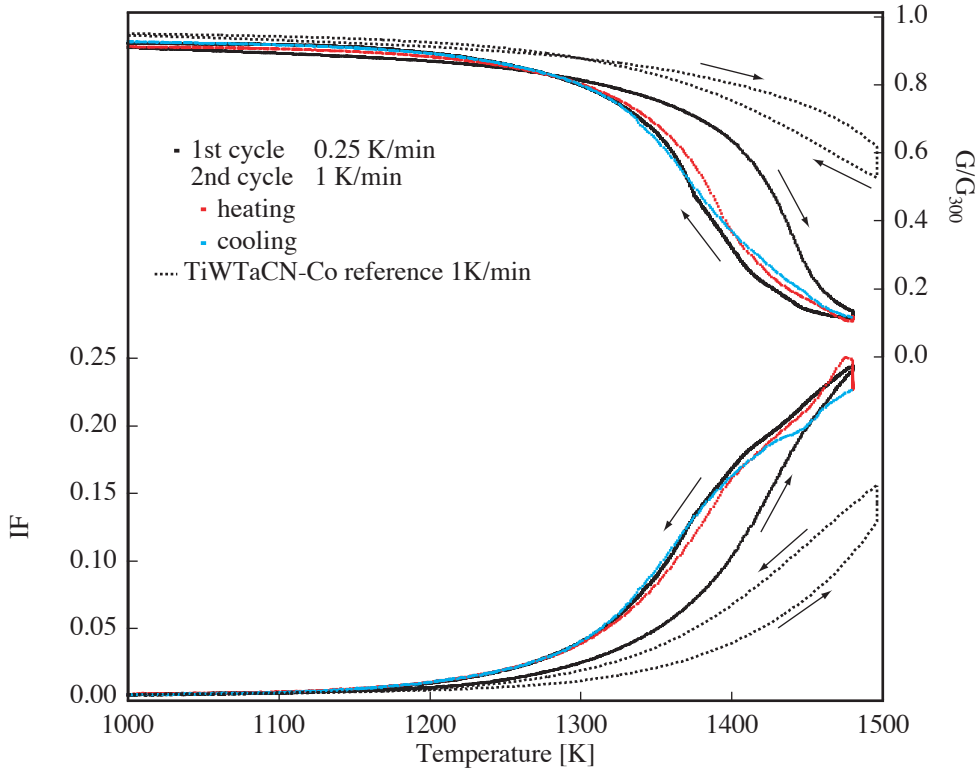

Figure 7.22: IF and modulus G upon heating with 0.25 K/min. 2nd cycle performed at normal speed

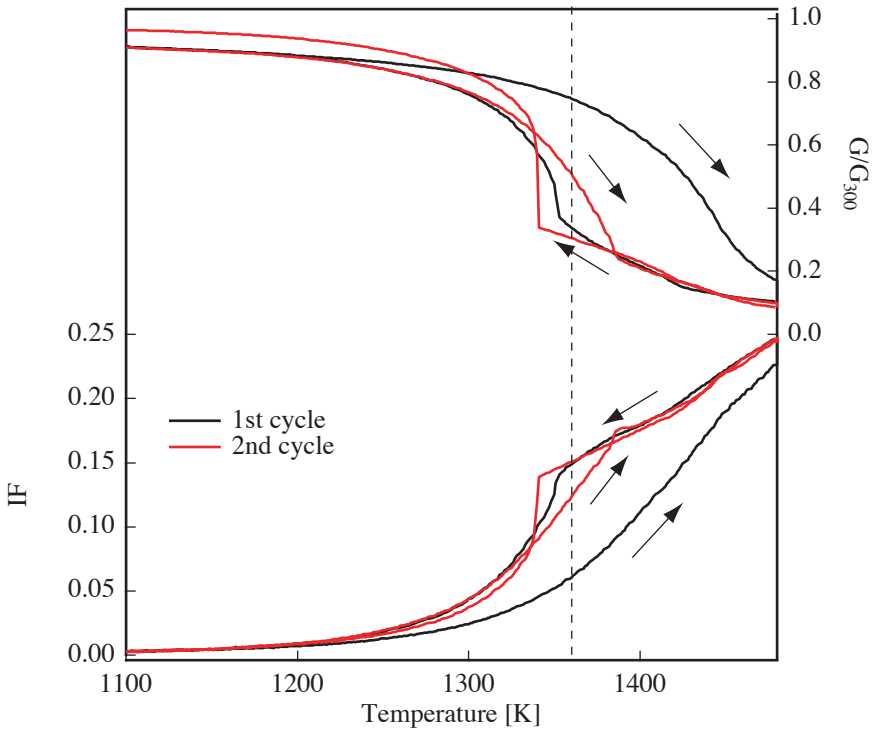

Figure 7.23: IF and modulus G after 12 hours in-situ annealing at 800 K

4 Discussion

4.1 Macroscopic deformation behavior

The deformation behavior of WC-Co and TiWCN-Co both with addition of tantalum has been first investigated by three-point bending. Macroscopic mechanical tests show that a beneficial effect on WC-Co can be attributed to the tantalum addition, at least up to a temperature of 1273 K (Fig. 7.3). However, at 1473 K, the WTaC-Co shows a flow stress that is as low as in WC-Co. For the cermet, no striking difference between the four grades, two with tantalum and two without, is observed.

The wear behavior (Fig. 7.3) measured by turning tests shows that indeed a small beneficial effect of tantalum on WC-Co is observed, but that, on the other hand, an important increase of wear is observed at very high cutting speeds. As the cutting speed can, even if qualitatively, be related to the temperature at the cutting edge, a more detrimental effect at high temperature can be expected.

A clear difference of the wear behavior of the four cermet grades is observed, which allows a well defined classification of the materials. From excellent to bad wear behavior, the four cermets should be ordered as follows: 1) TiWCN-Co_{HC}, 2) TiWTaCN-Co_{LC}, 3) TiWCN-Co_{LC} and 4) TiWTaCN-Co_{HC}. However, the deformation measured by three-point bending tests do not correlate with the differences in the wear properties of cermet cutting tools.

4.2 Mechanical spectroscopy

The mechanical spectroscopy gives a better insight of the mechanisms underlying macroscopic deformation. The investigation of remarkable tantalum effects allows a better understanding of the fundamental mechanisms already studied in Chapter 6. The denomination of relaxation peaks and the mechanisms attributed to them are summarized in Appendix 3.

4.2.1 Tantalum effect on WC-Co

Tantalum seems to have different effects at low temperature and at high temperature. A critical temperature may be defined that marks the change from beneficial to detrimental effects.

At lower temperatures, T<1400 K, the tantalum has a positive effect on the deformation behavior of WC-Co. It seems to prevent sliding of the grain boundaries, because the two peaks P_{W2} and P_{W3}, which are attributed to limited sliding of grain boundaries with segregated cobalt, are suppressed in the WTaC skeleton. A relationship of the peaks P_{W2} and P_{W3} to WC bulk dislocations can be excluded, as such realxation process would not be affected by the addition of Ta, which is not dissolved in the WC grains. In the complete WTaC-Co, these peaks can be traced, but they cannot surely be related to the ones found in WC-Co. The tantalum probably creates an unstable situation at the grain boundaries. In the skeleton, the cobalt atoms may be rejected from the grain boundaries during the rearrangement of the structure, which is seen in the first heating (Fig. 7.10). A strong modulus drop marks this transient behavior. In the WTaC skeleton, this decrease is much stronger than in the WC skeleton and the modulus does not fully recover upon cooling. This effect might be explained by the rejection of the cobalt that substantially changes the structure of the hard phase grain boundaries. It is also possible that the grain boundaries are already much cleaner in WTaC-Co after sintering. In this case, the presence of P_{W2} and P_{W3} might be explained by the fact that, at high temperature, the rejection of

cobalt by tantalum may be counteracted by a driving force leading cobalt into the grain boundaries. In fact, the peak P_{W4}, attributed to the infiltration of cobalt, is even enhanced in WTaC-Co. Possibly, the stress applied during IF measurements may be the source of this driving force. The peaks P_{W2Ta} and P_{W3Ta} so obtained show slightly different activation energies with respect to P_{W2} and P_{W3}. Different relaxation phenomena involving tantalum may be possible.

At temperatures higher than 1273 K, in stress-strain experiments, the tantalum addition does not show an improvement. In creep tests, the material seems to be changing between different creep regimes, a high activation energy regime and a low activation energy regime, all along the temperature range (Fig. 7.6). This type of behavior may result, for example, from small obstacles that block the grain boundaries, when the applied stress is small, but when the stress is sufficient, the obstacles can be overcome. This pinning-depinning is probably highly dependent on temperature and stress, which justifies the fact that no unique activation energy is observed [6]. In IF measurements, a strong increase of IF and a decrease of the modulus is observed at temperatures above 1400 K. Clearly, the amplitude of peak P_{W4} is increased in WTaC-Co (Fig. 7.8), which means that at high temperature, tantalum enhances grain boundary sliding. However, after the first heating, i.e. after rearrangement of the structure, the WTaC skeleton shows a much lower IF than the WC skeleton. This shows that the tantalum cleans the grain boundaries from cobalt, which is effective to reduce sliding at lower temperatures.

Finely dispersed WTaC precipitates are found in the structure and these may also contribute to the mechanical properties. However, these precipitates should not be found at grain boundaries. If they were present at grain boundaries, they would not suppress the peaks P_{W2} and P_{W3} in the skeleton, because we suppose that peaks are due to point defect relaxations involving diffusion. They would rather shift the peaks by changing the relaxation time τ.

Thermal cycling and dwelling at high temperature, causes a new effect. The high-temperature IF (Fig. 7.13), shows an abrupt transition between 1350 and 1400 K. This effect will be further discussed in §4.2.3.

4.2.2 Tantalum effect on cermets

At low temperature, neither three-point bending nor IF shows a difference between the four investigated cermet grades. However, a difference is found in the structural stability at high temperature, evidenced by an IF hysteresis that forms between a low heating curve and a higher cooling curve (Fig. 7.15). A strong correlation is observed between the hysteresis, or more quantitatively, the area of the hysteresis, and the wear of the cermets (Fig. 7.3b): the larger the area of the hysteresis, the higher the wear. The wear behavior is therefore not correlated with macroscopic mechanical properties measured by bending, but rather with the micromechanical stability of the hard phase grain boundaries. The observed hysteresis is related with the peak P_{T4} and thus with an enhanced sliding of the material. In fact, it was shown in Chapter 6 that a metastable increase of the IF at high temperature very similar to that in TiWTaCN-Co is related to P_{T4} and not to P_{T3}.

The carbon content plays an important role for the stability of the hard phase. In particular, an appropriate carbon content is essential, to obtain a beneficial effect of tantalum. It was shown that tantalum in combination with a too high carbon content, results in highly unstable structures producing a larger hysteresis.

The IF measurements of the skeletons show a strong increase during the first heating at around 1350 K, which is also the temperature of transition in the skeleton background (Fig. 6.23). This

temperature marks the onset of grain boundary sliding. An increase of IF is also observed in TiWCN skeleton (Fig. 6.21), but it seems stronger in the tantalum-containing cermet. This effect should be related to an increased instability of the interfaces.

4.2.3 Grain boundary phase transition and grain boundary sliding

The increase of the IF at high temperature and the hysteresis are signs of microcreep of the hardmetals. These phenomena seem to be related with the very high and broad peaks, P_{W4} and P_{T4}. The activation energies of these peaks are apparent, showing that the appearance of the peaks is related to a change of the structure with temperature. Moreover, in WTaC-Co, a shift of P_{W4} towards higher frequencies is observed in connection with a sharp transition of IF and modulus at $1350<T_c<1400$ K (Fig. 7.13, Fig. 7.14). At temperatures above the transition, the material softens, i.e. the modulus is drastically decreased. These observations are possibly related to a phase transformation at the grain boundaries that promotes the sliding. Another possible explanation may be a phase transformation in the binder. The magnetic transition of pure cobalt is located at 1394 K. The dissolution of WCo_3 is expected at 1366 K. However, a trend towards the formation of the high temperature phase is observed in the second cycle (Fig. 7.13) at temperatures much higher. Most importantly, the transformation involves a drastic change of the global mechanical properties of the composite, i.e. internal friction and modulus that are maintained at higher temperature. In particular, the modulus drop implies a global softening of the material. This effect cannot occur if the skeleton cohesion is not modified. It is therefore assumed that the transformation is located at grain boundaries.

Given the abrupt modulus change it is suggested that below the transition, the grain boundaries are of a crystalline structure with segregated cobalt, which is changing with temperature. Above the transition, a layer of an amorphous cobalt alloy is found in the grain boundaries and promotes the sliding.

The peak P_{W4} shows a change of activation energy. Fig. 7.24a shows the fit of the left flank of P_{W4}, which shows a change of the slope at $T>T_c$. The slope below T_c is constant, but above T_c, it becomes smaller with increasing temperature. Below the transition, the activation energy is 6.4 eV, and above the transition it is somewhat lower. The value of 4.2 should be taken with

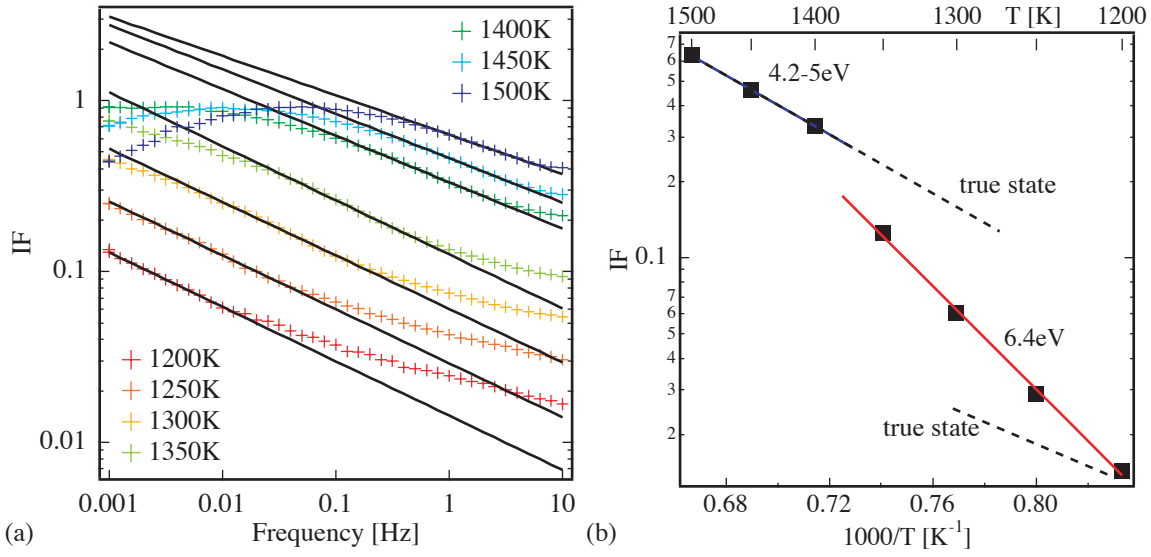

Figure 7.24: (a) Same as Fig. 7.14 in log-log scale showing the fitting of the flank of P_{T4} for an evaluation of its activation energy, shown in (b)

precaution as the number of points fitted is very limited. Moreover, with decreasing slope the activation energy rises. One should notice that the high activation energy below the transition is apparent, because an attempt frequency of about $\nu_0=10^{25}$ s^{-1} is measured. Instead, an energy of 4.2 eV is physically plausible, with an attempt frequency around $\nu_0=10^{15}$ s^{-1}, and could be related to a diffusion process in the amorphous layer.

One may find in this effect a justification for the apparent activation energies found for P_{W4} and P_{T4}. Apparent activation energies, represented by steep lines in the Arrhenius plot, result, in fact, from a transition between two physical states with true activation energies, presented in Fig. 7.24b by dashed lines. Often, the range of frequency and temperature is too small, to observe the true states. The 6.4 eV slope in the Arrhenius plot in Fig. 7.24b represents a changing trend towards a physical activation energy due to a structure that is also continuously changing. The phase transformation stops this change abruptly and allows to visualize the true activation energy. As activation energies found for grain boundary peaks are always apparent [91] this may be the first parallel observation of the apparent and the physical activation energy in grain boundary relaxations.

Chapter 8

Conclusions

This work is motivated by the need of the cutting tool industry to improve the product performance in order to support harder and harder working conditions, namely increasing cutting speed and working on stronger modern materials. It is observed that with increasing speed a limiting factor of tool life is the plastic deformation. This phenomenon occurs essentially because of the high temperature attained by the cutting tool coupled with the stress on the tool tip. Tool materials are mostly coming from two families of hardmetals: cemented carbides of type WC-Co and cermets of type TiCN-Co. The aim of this work was then to study the mechanical properties of these tool materials at relatively high temperature i.e. as high and over 1000°C. In this temperature range, the observation of the morphology of the deformed cutting tool materials show that grain boundary sliding of the ceramic phase is likely to occur. Moreover, in many cases the infiltration of grain boundaries by the metal binder is observed. We have therefore focused our attention to the investigation of these mechanisms and their relation to the mechanical properties. Two model materials were chosen, a WC-10vol.%Co and a TiWCN-10vol.%Co processed to have the same binder content and composition. On the basis of recent studies the materials were modified by the addition of tantalum. The influence of this element on the mechanical properties and on interface stability is investigated.

1 Summary of results

Macroscopic deformation

Deformation tests by three-point bending show a transition, located at 1100 K for WC-Co and at 1325 K for the cermet, between two mechanical behavior domains. Below this transition (domain II), high yield stresses are observed. Creep activation energies of 2 eV for the cermet and 3.5 eV the cemented carbide respectively, are measured. Above the transition temperature (domain III), the yield stress decreases rapidly. This decrease is associated with the presence of the binder. In fact, removing the cobalt by chemical etching produces a hard phase skeleton with a yield stress higher than that measured in the complete hardmetal. The activation energy of creep measured in this domain is 6 eV for both hardmetals. Generally, in all domains, the cermet is more refractory than the cemented carbide despite the presence of the same amount of binder.

The tantalum leads to an improvement of the mechanical properties of WC-Co at temperatures up to 1273 K evidenced by an increased yield stress. However, at 1473 K, no difference between WC-Co with and without tantalum is noticed. Concerning the creep behavior, tantalum leads to an increased instability, i.e. the material jumps between high and low activation energy states all through the temperature range depending on strain rate. The cermets, with and without tantalum, do not show any differences in the stress-strain curves. The creep experiments indicate a dependence on the carbon content. A transition between the high activation energy and low activation energy state is present for the cermet with tantalum in combination with a low carbon content. The cermet with tantalum and a high carbon content shows a high activation energy regime (domain III) prolonged down to low temperatures.

Residual stresses

Measurements of residual stresses performed by X-ray diffraction in the cermet and by neutron diffraction in WC-Co show that the residual stresses in WC-Co are much larger. Compressive stresses up to 800 MPa at room temperature are found in the WC phase, while the stresses in the cermet are of the order of 200 MPa. The corresponding tensile stress in the cobalt phase is around 4 GPa in WC-Co and 1.8 GPa in the cermet. Residual thermal stresses are completely relaxed in the cermet above 1200 K. In WC-Co, residual stresses are present until 1500 K. Another important difference is a strong solution of tungsten in the binder of WC-Co above 1100 K, while, in the cermet, the tungsten content in the binder remains rather stable. However, a change of the hard phase composition at high temperature and in particular of the nitrogen/carbon ratio is likely.

Anelastic relaxations

While deformation tests do not allow a precise definition of the mechanisms by which deformation occurs, mechanical spectroscopy allows a separation of ongoing phenomena by showing very distinctly relaxation peaks that appear as a function of temperature and frequency. In the studied materials, mechanical spectroscopy has evidenced different relaxation phenomena in the hardmetals, in particular, a series of high temperature relaxations located in the grain boundaries.

In domain II, relaxation phenomena intrinsic to the binder and the hard phase are observed. A relaxation peak P_{W1} is observed in WC-Co, which is attributed to the movement of dislocations in cobalt controlled by the diffusion of tungsten. In fact, this peak is found at the temperature of transition between the domains II and III. Both, the peak P_{W1} and the transition to domain III are strongly related to the increasing mobility of tungsten. In the cermets (in contrast to cermets of other studies [10,25]), the peak P_{T1}, related to the same mechanism as P_{W1}, is not observed, due to the low level of internal stresses, maybe in combination with the rather low tungsten content in the cermet binder. However, this peak could be found after deformation and after annealing between 1200 and 1240 K. Another relaxation process is observed in the cermet, related to the movement of dislocations in TiCN, evidenced by a relaxation peak P_{T2}, around 1200 K. A corresponding peak related to the movement of dislocations in WC is not observed. None of the peaks in domain II is affected by the addition of tantalum.

In domain III, several peaks that can be attributed to grain boundary relaxations are observed, both in cermets and cemented carbides. Two base mechanisms are related to these relaxations: limited grain boundary sliding, i.e. small range movements of adjacent grains due to diffusion and dislocation climb at the grain boundaries and grain boundary sliding promoted by cobalt infiltration.

Limited grain boundary sliding

Two relaxation peaks are present in WC-Co, one at lower temperature, P_{W2} at 1330 K (at 1 Hz), and another at higher temperature, P_{W3} at 1440 K (at 1 Hz), with activation energies of 2 and 4 - 5 eV, respectively. Both peaks are also present in the ceramic WC skeleton with the same activation energy and at the same temperatures but with lower amplitudes. When tantalum is added, the peaks are observed in the complete material, but both peaks are suppressed in the skeleton. Therefore, both peaks are attributed to limited sliding at grain boundaries, related with segregated cobalt. The difference between the two peaks is related to the presence of families of grain boundaries with different structures. The peak P_{W2} is associated with more stable grain boundaries with half a monolayer of cobalt. With an activation energy of 2 eV and an attempt frequency of 10^8 s^{-1}, this peak is likely attributed to diffusion of cobalt in the grain boundaries. The sliding of the grain boundaries is attributed to misfit dislocation movement controlled by cobalt diffusion. On the other hand, the peak P_{W3} is associated with all the grain boundaries that do not have a special orientation and that are less strong and less resistant to infiltration of cobalt. The activation energy is apparent with an attempt frequency of 10^{18} s^{-1}, which is a sign for relaxation in a changing structure. P_{W3} is also related to the presence of cobalt at grain boundaries, but it may involve a correlated movement of cobalt with tungsten and carbon atoms.

Concerning the presence of the peaks in the skeleton, it can be admitted that, even after removal of the cobalt binder, segregated cobalt still resides at the grain boundaries. In fact, the peaks P_{W2} and P_{W3} in the complete WC-Co are enhanced by the presence of vacancies at the grain boundaries, which facilitate the diffusion of cobalt, tungsten and carbon. These vacancies are produced during the dissolution of WC in the binder at temperatures above 1100 K. Upon removal of the cobalt, during the first heating of the skeleton, vacancies are recovered and a general rearrangement of the grain boundary structure takes place, which afterwards is more stable. This is evidenced by a transient peak accompanied with a strong modulus decrease, followed by a complete recovery of the modulus. In contrast, the presence of tantalum really drives out most of the cobalt from the grain boundaries, which explains why the modulus is not fully restored upon cooling, as is the case for the WC skeleton.

In the cermet, a relaxation peak, P_{T3}, related to cobalt segregation is observed. This peak appears suddenly, related with a structural transition inside the cermet grain boundaries. This transition is observed in the skeleton, by a change of the activation energy of the IF background from 4 eV below 1350 K to 8 eV above 1350 K. This temperature is also the transition temperature between domain II and III shown by bending tests. Above this temperature, the peak P_{T3} grows continuously, but reversibly, as a function of temperature. In isothermal conditions, each temperature is related with a certain, stable peak height. The peak is therefore attributed to the movement of cobalt atoms, which are segregated in the grain boundaries and which progressively occupy several layers. The activation energy of around 4.6 eV is apparent, because of the continuous change of the grain boundary state where the relaxation takes place. In the skeleton, a very small peak is observed with a stable peak height and a true activation energy of 3.4 eV. This energy is probably related with small amounts of segregated cobalt in the as received cermet material, the content of which remains stable.

Grain boundary sliding by cobalt infiltration

In both materials, a peak with similar characteristics is observed, P_{W4} and P_{T4}. These peaks are very high, with relaxation strengths up to almost 1. They are also very broad, which means that not a single relaxation process is active, with a single relaxation time, but that multiple relaxation processes take place. The measured activation energies are apparent, over 7 eV (attempt

frequency 10^{25} s^{-1}) and around 5 eV (attempt frequency 10^{17} s^{-1}) in cemented carbides and cermets, respectively. These peaks, that are not present in the skeletons, are also very sensitive to stress. These peaks are attributed to sliding of the grain boundaries infiltrated by cobalt.

Upon tantalum addition, the high temperature IF increases more drastically, both in cermets and cemented carbides. In WTaC-Co, the peak height of P_{W4} is clearly increased. Moreover, thermal cycling at high temperature produces a special state of the grain boundaries. The IF temperature spectrum presents a sharp transition, found both in WTaC-Co and TiWTaCN-Co between 1350 and 1400 K. This transition is correlated with a strong modulus decrease, which can only be interpreted as sliding of the grain boundaries on an amorphous if not even liquid phase. However, a sharp reverse-transition is observed in the same temperature range and the modulus is fully restored during cooling. Therefore, in this special case, a phase transformation is taking place at the grain boundaries from a crystalline structure at temperatures below the transformation temperature to an amorphous phase. Interestingly, the activation energy of P_{W4}, which shows an apparent high value before the transition, becomes smaller, 4.2 eV, above the transition with an attempt frequency of 10^{15} s^{-1}, which could be the true activation energy for the grain boundary sliding process. The apparent activation energy is representative of a structure continuously changing at interfaces.

2 General conclusions

Cemented carbides and cermets, used for the production of cutting tools, are composite materials with a majority of ceramic phase forming a continuous skeleton structure. Plastic deformation of hardmetals must involve either the deformation of the hard phase or the deformation of the skeleton. In fact, bulk deformation of the hard phase is observed in cermets, but this deformation is very limited and cannot account for the plastic deformation that is observed by mechanical testing. Bulk deformation in the WC skeleton is rarely observed. However, at high temperature and under application of stress, the hard phase skeletons of both, cemented carbides and cermets, can deform by grain boundary sliding. This deformation mechanism can lead to a substantial deformation by local rearrangements of neighboring grains. The deformation of the skeleton is the main deformation mechanism and the presence of cobalt as binding metal is crucial for this mechanism to take place. The transition temperature where, macroscopically, grain boundary sliding becomes the dominant deformation mechanism is 1100 K for the cemented carbide and 1325 K for the cermet.

Grain boundary sliding of hardmetals

Depending on external conditions, such as temperature and stress, different stages of grain boundary sliding are observed, limited grain boundary sliding related to cobalt segregation and extensive grain boundary sliding related to cobalt infiltration.

In the cemented carbide, the mechanism for limited grain boundary sliding depends strongly on the grain boundary type. Two different processes are found: the first in special low coincidence grain boundaries that are stable and the second in general grain boundaries that change their structure with temperature. In both cases, an excess of vacancies at the grain boundaries due to the dissolution of tungsten and carbon into the binder at high temperature, may enhance the sliding mechanism.

In the cermet, a continuous change of the amount of segregated cobalt, in submonolayer quantities, is observed. The cobalt segregation is strongly related to the change of the chemical

equilibrium of the hard phase. Moreover, a structural change of the boundary at 1350 K, which defines the onset of grain boundary sliding, can be envisaged.

The extensive grain boundary sliding mechanism is very similar in cemented carbides and cermets. It is due to the sliding of fully infiltrated grain boundaries possibly in monolayer quantities. However, this infiltrated state is metastable. It is favoured, in a reversible manner, by the application of stress.

The effect of tantalum

The effect of tantalum on the deformation behavior of these material has been studied. Wear test show that, in WC-Co, a beneficial effect is observed until a certain cutting speed, i.e. until a certain temperature. Concerning the cermets, the wear depends strongly on the carbon content. Without tantalum, a high carbon content leads to an improvement of the wear behavior; with tantalum, a high carbon content has negative effects.

The beneficial effect of tantalum on WC-Co is proven by mechanical testing and by mechanical spectroscopy. The positive effect is related with the presence of tantalum, which rejects cobalt from WC/WC grain boundaries and thus blocks the limited grain boundary sliding, defined above. However, at temperatures above 1400 K, the tantalum perturbs the otherwise stable WC-Co structure, favoring the cobalt infiltration and therefore extended sliding.

Mechanical bending tests do not show any difference between cermets, which show considerable differences in their wear behavior. In contrast, mechanical spectroscopy shows that the performance of the tools is correlated with the stability of the structure of the grain boundaries at high temperatures. The impact of tantalum on the deformation behavior depends strongly on the carbon content.

Finally, it was shown that grain boundaries, both in cemented carbide with tantalum and cermet with tantalum, may transform after thermo-mechanical treatment consisting in slow thermal cycling up to temperatures around 1500 K under a cyclic stress. A phase transformation of the grain boundaries from a crystalline to an amorphous state can be produced.

Appendix

1 Residual stresses in composites

1.1 The Eshelby Model

The Eshelby model [92] allows to calculate stresses due to the difference of thermal expansion coefficients of a material inclusion inside the matrix of another material. This difference leads to a misfit $\varepsilon^{T}*$ between the inclusion and the cavity that it contains. In this paragraph, the formulation by Clyne and Withers [93] have been used. The model assumes an ellipsoidal inclusion with different elastic constants than the surrounding matrix *m*. To arrive to an analytical solution, the real inclusion is replaced by an imaginary inclusion *i* with the same elastic constants as the matrix that leads to the same final stress state. The stress state of matrix and inclusion can then be determined by the equivalent deformation ε^{T} of the imaginary inclusion.

The tensor of the equivalent deformation ε^{T} of the imaginary inclusion is given as a function of the misfit $\varepsilon^{T}*$:

$$\varepsilon^{T} = -\{(C_m - C_i)\cdot[S - f(S-I)] - C_m\}^{-1} C_i \varepsilon^{T}* \tag{A.1}$$

where *f* is the volume fraction of the inclusions, *I* the identity matrix, *C* the rigidity tensor (Eq. (10)) and *S* the Eshelby tensor (Eq. (9)).

From Eq. (A.1), the average stress tensor of the hardphase matrix $<\sigma>_m$ and the metallic inclusion $<\sigma>_i$ can be calculated:

$$<\sigma>_m = -f C_m (S-I)\varepsilon^{T} \tag{A.2}$$

$$<\sigma>_i = (1-f) C_m (S-I)\varepsilon^{T} \tag{A.3}$$

In the case, where the misfit is due to the differences in thermal expansion between matrix *m* and inclusion *i*, it can be expressed in terms of $\varepsilon^{T}*$:

$$(\varepsilon^{T*})_j = (\alpha_i \cdot \Delta T - \alpha_m \Delta T) g_j \tag{A.4}$$

where α is the thermal expansion coefficient and $g_j = 1$ for $j = 1$ to 3 and $g_j = 0$ for $j = 4$ to 6 if there is no shear.

For the calculation of elastic strains of the components of a composite resulting from an applied stress, the equivalent deformation ε^{T} changes to:

$$\varepsilon^{T} = -\{(C_m - C_i)\cdot[S - f(S-I)] - C_m\}^{-1}(C_m - C_i)\varepsilon_A \tag{A.5}$$

where ε_A is the overall strain arising from the applied stress (Eq. (A.6)).

$$\varepsilon_A = C_m^{-1} \cdot \sigma_A \tag{A.6}$$

The average stress tensor for the hardphase matrix $<\sigma>_m$ and the metallic inclusion $<\sigma>_i$ is then derived as follows:

$$<\sigma>_m = -fC_m S - I\varepsilon^T + \sigma_A \tag{A.7}$$

$$<\sigma>_i = (1-f)C_m(S-I)\varepsilon^T + \sigma_A \tag{A.8}$$

Finally, in the elastic regime, the equivalent transformation strains ε^T from different origins (thermal, applied stress) can be added together.

In the present study, it is supposed that the matrix is the ceramic phase, which has the larger volume fraction and the inclusion is the cobalt.

1.2 The Eshelby tensor

The Eshelby tensor for a spherical inclusion [93] :

$$S = 15(1-\nu)\begin{bmatrix} 7-5\nu & 5\nu-1 & 5\nu-1 & 0 & 0 & 0 \\ 5\nu-1 & 7-5\nu & 5\nu-1 & 0 & 0 & 0 \\ 5\nu-1 & 5\nu-1 & 7-5\nu & 0 & 0 & 0 \\ 0 & 0 & 0 & 4-5\nu & 0 & 0 \\ 0 & 0 & 0 & 0 & 4-5\nu & 0 \\ 0 & 0 & 0 & 0 & 0 & 4-5\nu \end{bmatrix} \tag{A.9}$$

where ν is the Poisson ratio. This tensor depends on the geometry of the particle.

1.3 The rigidity tensor for WC, TiCN and Co

The rigidity tensor or compliance tensor of the matrix m or the inclusion i :

$$C_{m,i} = \begin{bmatrix} C^{11}_{m,i} & C^{12}_{m,i} & C^{13}_{m,i} & 0 & 0 & 0 \\ C^{12}_{m,i} & C^{11}_{m,i} & C^{13}_{m,i} & 0 & 0 & 0 \\ C^{13}_{m,i} & C^{13}_{m,i} & C^{33}_{m,i} & 0 & 0 & 0 \\ 0 & 0 & 0 & C^{44}_{m,i} & 0 & 0 \\ 0 & 0 & 0 & 0 & C^{44}_{m,i} & 0 \\ 0 & 0 & 0 & 0 & 0 & C^{44}_{m,i} \end{bmatrix} \tag{A.10}$$

For the WC matrix the elastic constants from Lee and Gilmore [79] where used:

$C^{11}_m = 720\cdot10^9$ $\quad C^{12}_m = 254\cdot10^9$ $\quad C^{13}_m = 267\cdot10^9$

$C^{33}_m = 972\cdot10^9$ $\quad C^{44}_m = 328\cdot10^9$

For the TiCN matrix the following elastic constants where used [94]:

$C^{11}_m = C^{33}_m = 514.5\cdot10^9$ $\quad C^{12}_m = C^{13}_m = 106.0\cdot10^9$ $\quad C^{44}_m = 178.8\cdot10^9$

For the cobalt inclusion the elastic constants where derived as follows:

$$C_i^{11} = C_i^{33} = \frac{E \cdot \nu}{(1+\nu)\cdot(1-2\nu)} + \frac{E}{1+\nu} \qquad C_i^{12} = C_i^{13} = \frac{E \cdot \nu}{(1+\nu)\cdot(1-2\nu)}$$

$$C_i^{44} = \frac{C_i^{11} - C_i^{12}}{2}$$

where E=206 MPa is the elastic modulus and ν the Poisson ratio.

1.4 Numerical data used in this work

The following table summarizes used constants and calculated values from the Eshelby model. Three materials have been considered, the TiWCN-10vol%Co and the WC-10vol%Co as mainly used in this work and WC-18vol%Co as used for the neutron diffraction experiments. The parameters introduced in the calculation are the volume fraction f, the Poisson ratio ν, the thermal expansion α, the temperature difference between the stress-free state and the final state ΔT. The calculated values are thermal strain and stress inside the composite due to an externally applied stress.

Table A.1 : Constants and calculated values

Phase	f	ν	$\alpha/10^{-6}$ [K^{-1}]	ΔT [K]	thermal strain $\varepsilon/10^{-6}$	thermal stress σ [MPa]	σ [MPa] upon 100 MPa applied (no thermal stress)
TiWCN-10vol%Co							
TiCN	0.9	0.191	8.9	1200-300	-248	-180	
Co	0.1	0.32	15	1200-300	2834	1622	
WC-10vol%Co							
WC	0.9	0.23	4.4* 3.7*	1550-300	-449* -332*	-526* -563*	106
Co	0.1	0.32	15	1200-300	7755	4732	44
WC-18vol%Co (as used for diffraction experiments)							
WC	0.82	0.23	4.4* 3.7*	1550-300	-830* -625*	-975* -1050*	112
Co	0.18	0.32	15	1200-300	7231	4442	47

*) The two values in one table cell correspond to the direction normal to prismatic planes (a-direction) and normal to basal planes (c-direction) of the hexagonal WC, respectively.

2 Internal stress from solution of WC in cobalt

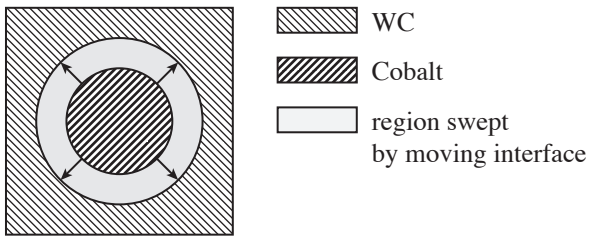

Figure A.1: Illustration of the volume changes of a cobalt inclusion inside a WC cavity due to dissolution of WC in the cobalt.

2.1 Cavity increase

Volume increase of the cavity inside the WC matrix that contains the cobalt by solution of 1 at.% W [49] :

$$\frac{\Delta V_{WC}}{V_0} = 0.01 \cdot \frac{V_{WC}}{V_{Co}} = 0.01 \cdot \frac{20.79}{11.1} = 1.87 \cdot 10^{-2}/\text{at.\% W} \qquad \text{(A.11)}$$

2.2 Cobalt volume increase from thermodynamical model by Uhrenius [85]

In this model, pure cobalt is supposed to consist of cobalt atoms and vacancies. If tungsten and carbide is dissolved in the cobalt, tungsten atoms are assumed to replace cobalt atoms and carbon atoms are supposed to go to vacancy sites. The increased cobalt volume due to 1 at.% WC yields:

$$V_m = V_{CoC} + y_W(V_{WC} - V_{CoC}) + y_v(V_{Cov} - V_{CoC}) + y_W y_v(V_{CoC} - V_{Cov} + V_{Wv} - V_{WC})$$

$$V_m = 7.05 \cdot 10^{-6}\,\text{m}^3/\text{mol} \qquad \text{(A.12)}$$

where V_{Cov} is the volume of pure cobalt containing vacancies, which depends on temperature. For 1000 K, the cobalt volume is V_{Cov}=6.99·10^{-6} m^3/mol, and thus the volume change is:

$$\frac{V_m}{V_{Cov}} - 1 = 0.8637 \cdot 10^{-2}/\text{at.\% W} \qquad \text{(A.13)}$$

1 at.% cobalt atoms are substituted by tungsten, but they remain in the cavity and thus add another 1% volume increase. The total volume increase of the cobalt is therefore 1.86·10^{-2} /at.% W. The cavitation volume increase and the volume of expanded cobalt are almost identical.

2.3 Vacancy concentration in cobalt

The energy of vacancy formation in cobalt was not found in literature. In metals, typical energies of formation are of the order of 1 eV.

The concentration of thermal vacancies can be approximated by

$$C = 11.2e^{-\frac{Q}{kT}}. \quad \text{(A.14)}$$

At T=1273 K, the vacancy concentration is $1.2 \cdot 10^{-3}$, which is not sufficient to accommodate the dissolving tungsten atoms and thus produce the described stresses.

3 Peak denomination in IF measurements

Table A.2 : IF peak denomination

WC-Co	TiWCN-Co	remarks
P_{W1},	P_{T1},	transitory stage of P_{W1}
P_{W1}	P_{T1}	dislocation movement in Co controlled by W diffusion
	P_{T2} skeleton: P_{T2},	dislocation movement in TiCN by Peierls mechanism
P_{W2} skeleton: P_{W2},		limited GBS of special grain boundaries with half a monolayer of Co
P_{W3} skeleton: P_{W3},		limited GBS of general WC/WC grain boundaries with segregated Co
	P_{T3} skeleton: P_{T3},	GBS enhanced by continuous segregation of Co
P_{W4}	P_{T4}	GBS due to fully infiltrated grain boundaries

Bibliography

[1] D. Mari, *Cermets and Hardmetals* in *Encyclopedia of Materials* (Elsevier Science Publisher Pergamon Press, Amsterdam, 2001).

[2] P. Schwarzkopf and R. Kieffer, *Refractory Hard Metals* (The MacMillan Company, New York, 1953).

[3] H. E. Exner, *Physical and Chemical Nature of Cemented Carbides*, International Metals Reviews 4, 149 (1979).

[4] H.-O. Andrén, *Microstructures of cemented carbides*, Materials & Design 22, 491 (2001).

[5] R. M. German, *Sintering Theory and Practice* (John Wiley & Sons, New York, 1996).

[6] D. Mari, *Déformation à Haute Température des Composites WC-Co*, Thesis EPFL N°938, 1991.

[7] T. W. Penrice, *Alternative binders for hard metals*, The carbide and tool journal 20, 12 (1988).

[8] V. A. Tracey, *Nickel in Hardmetal*, International Journal of Refractory Metals & Hard Materials 11, 137 (1992).

[9] H. E. Exner, *Qualitative and Quantitative Interpretation of Microstructures in Cemented Carbides* in proceedings of Int. Conf. Sci. Hard Mater. (eds. R. K. Viswanadham, D. J. Rowcliffe and J. Gurland, Plenum Press, New York, Jackson, Wyoming, 1981).

[10] G. Feusier, *Etude des propriétés mécaniques à haute température des cermets Ti(C,N)-Mo-Co par mesures de frottement intérieur et par essais de flexion trois points*, Thesis EPFL N°1659, 1997.

[11] S. Kim, S.-H. Han, J.-K. Park and H.-E. Kim, *Variation of WC grain shape with carbon content in the WC-Co alloys during liquid-phase sintering*, Scripta Materialia 48, 635 (2004).

[12] M. Christensen, *Strength and Stability of Interfaces in Cemented Carbides*, Thesis N°2133 (ISBN 91-7291-451-3), Chalmers University of Technology, Gothemburg, Sweden, 2004.

[13] P. Gustafson, *Thermodynamic Evaluation of C-W System*, Materials Science and Technology 2, 653 (1986).

[14] B. Sundman, B. Jansson and J.-O. Andersson, *THERMO-CALC DATABANK SYSTEM*, Calphad: Computer Coupling of Phase Diagrams and Thermochemistry 9, 153 (1985).

[15] A. Markström, B. Sundman and K. Frisk, *A revised thermodynamic description of the Co-W-C system*, IM-2003-143, Swedish Institute for Metals Research, Stockholm.

[16] J. Zackrisson, U. Rolander, B. Jansson and H. O. Andren, *Microstructure and performance of a cermet material heat-treated in nitrogen*, Acta Materialia 48, 4281 (2000).

[17] S. V. Dudiy and B. I. Lundqvist, *First-principles density-functional study of metal-carbonitride interface adhesion: Co/TiC(001) and Co/TiN(001)*, Physical Review B - Condensed Matter and Materials Physics 64, 454031 (2001).

[18] M. Christensen, S. Dudiy and G. Wahnström, *First-principles simulations of metal-ceramic interface adhesion: Co/WC versus Co/TiC*, Physical Review B 65 (2002).

[19] G. Östberg, H.-O. Andrén, M. Christensen, G. Wahnström, M. U. Farooq, U. Klement and I. Reineck, in proceedings of *EuroPM2002 Hard Materials* (Lausanne, 2002).

[20] M. Christensen and G. Wahnström, *Effects of Co intergranular segregation on interface energetics in WC-Co*, Acta Materialia 52, 2199 (2004).

[21] C.-S. Kim and G. S. Rohrer, *Geometric and Crystallographic Characterization of WC Surfaces and Grain Boundaries in WC-Co Composites*, Interface Science 12, 19 (2004).

[22] F. Ueda, H. Doi, F. Fujiwara and H. Masatomi, *Bend Deformation and Fracture of WC-Co Alloys at Elevated Temperatures*, Transactions of the Japan Institute of Metals 18, 247 (1977).

[23] S. Bolognini, G. Feusier, D. Mari, T. Viatte and W. Benoit, *High Temperature Mechanical Behaviour of Ti(C,N)-Mo-Co Cermets*, International Journal of Refractory Metals & Hard Materials 16, 257 (1998).

[24] D. Mari, S. Bolognini, G. Feusier, T. Viatte and W. Benoit, *Experimental strategy to study the mechanical behaviour of hardmetals for cutting tools*, International Journal of Refractory Metals & Hard Materials 17, 209 (1999).

[25] S. Bolognini, *Propriétés mécaniques à haute température de cermets Ti(C,N)-WC-Mo-Co à gradient de composition pour outils de coupe*, Thesis EPFL N° 2161, 2000.

[26] D. Mari, S. Bolognini, T. Viatte and W. Benoit, *Study of the mechanical properties of TiCN-WC-CO hardmetals by the interpretation of internal friction spectra*, International Journal of Refractory Metals & Hard Materials 19, 257 (2001).

[27] Y. V. Milman, S. Luyckx, V. A. Goncharuck and J. T. Northrop, *Results from bending tests on submicron and micron WC-Co grades at elevated temperatures*, International Journal of Refractory Metals and Hard Materials 20, 71 (2002).

[28] S. Bolognini, G. Feusier, D. Mari, T. Viatte and W. Benoit, *TiMoCN-based cermets: high-temperature deformation*, International Journal of Refractory Metals & Hard Materials 21, 19 (2003).

[29] L. S. Sigl, H. E. Exner and H. F. Fischmeister, *Characterization of fracture processes and facture relevant parameters in WC-Co hardmetals*, in proceedings of 2nd Int. Conf. Science Hard Mater. (eds. E. A. Almond, C. A. Brookes and R. Warren, Inst. Phys. Conf. Ser. N.75, Adam Hilger Ltd, Rhodes, 1984).

[30] L. S. Sigl and H. E. Exner, *Experimental Study of the Mechanics of Fracture in WC-Co Alloys*, Metallurgical Transactions A 18, 1299 (1987).

[31] L. S. Sigl and H. F. Fischmeister, *On the Fracture Toughness of Cemented Carbides*, Acta Metallurgica 36, 887 (1988).

[32] J.-J. Ammann, *Etude des Propriétés Mécaniques du Matériau WC-Co par Frottement Intérieur*, Thesis EPFL N°861, 1990.

[33] T. Sakuma and H. Hondo, *Plastic flow in WC-13wt.%Co at high temperatures*, Materials Science and Engineering A156, 125 (1992).

[34] T. Viatte, S. Bolognini, T. Cutard, G. Feusier, D. Mari and W. Benoit, *Investigation into the potential of a composite combining toughness and plastic deformation resistance*, International Journal of Refractory Metals & Hard Materials 17, 79 (1999).

[35] D. Mari, J. J. Ammann, W. Benoit and C. Bonjour, *High temperature deformation of WC-Co hardmetal*, in proceedings of 9th Risø International Symposium on Metallurgy and Materials Science (eds. S. I. Andersen, H. Lilholt and O. B. Pedersen, Risø National Laboratory, Roskilde, Denmark, 1988).

[36] S. Lay, J. Vicens and F. Osterstock, *High temperature creep of WC-Co alloys*, Journal of Materials Science 22, 1310 (1987).

[37] G. Wirmark, C. Chatfield and G. L. Dunlop, in *Institute of Physics Conference Series* 669 (1986).

[38] D. Mari, U. Marti and P. C. Silva, *A New Photolithographic Technique to Detect the Local Deformation of Materials: Application to WC-Co Composites*, Materials Science and Engineering A158, 203 (1992).

[39] M. Gardon, *Etude par Spectrométrie Mécanique de l'Evolution Structurale à Haute Température du Composite WC-Co*, Thesis INSA, Lyon, France (1993).

[40] R. Schaller, J. J. Ammann, D. Mari and M. Maamouri, in *ASTM Special Technical Publication* 510 (1992).

[41] R. Schaller, J. J. Ammann and C. Bonjour, *Internal friction in WC-Co hard metals*, Materials Science and Engineering A105-6, 313 (1988).

[42] J. J. Ammann, D. Mari, R. Schaller and C. Bonjour, *Mechanical properties of WC-11Co studied by internal friction*, in Proceedings of the Risø International Symposium on Metallurgy and Materials Science 257 (ASTM Special Technical Publication) (1988).

[43] J.-J. Ammann and R. Schaller, *Influence of a Changing Microstructure on High Temperature Relaxation Peaks, an Example: WC-11wt.%Co*, Journal of Alloys and Compounds 211/212, 397 (1994).

[44] D. Mari and D. R. Gonseth, *A New Look at Carbide Tool Life*, Wear 165, 9 (1993).

[45] S. Bolognini, D. Mari, T. Viatte and W. Benoit, *High Temperature Mechanical Behaviour of Ti(C,N)-WC-Co Hardmetals* in *Advances in Mechanical Behaviour, Plasticity and Damage* (Elsevier Science, Oxford, 2000).

[46] J. T. Smith and J. D. Wood, *Elevated Temperature Compressive Creep Behavior of Tungsten Carbide-Cobalt Alloys*, Acta Metallurgica 16, 1219 (1968).

[47] A. D. Krawitz, M. L. Crapenhoft, D. G. Reichel and R. Warren, *Residual Stress Distribution in Cermets*, Materials Science and Engineering A105/106, 275 (1988).

[48] A. D. Krawitz, D. G. Reichel and R. L. Hitterman, *Residual Stress and Stress Distribution in a WC-Ni Composite*, Materials Science and Engineering A119, 127 (1989).

[49] D. Mari, A. D. Krawitz, J. W. Richardson and W. Benoit, *Residual Stress in WC-Co Measured by Neutron Diffraction*, Materials Science and Engineering A209, 197 (1996).

[50] J. P. Poirier, *Creep of Crystals* (Cambridge University Press, Cambridge, 1985).

[51] T. Viatte, *Propriétés Mécaniques à Haute Température des Cermets Ti(C,N)-Mo_2C-Ni Étudiés par Mesures de Frottement Intérieur et de Fluage*, EPFL, 1995.

[52] *LANSCE Activity Report 2001*, LA-13943-PR, Los Alamos Neutron Science Center, Los Alamos, NM, USA.

[53] A. C. Larson and R. B. V. Dreele, *General structure analysis system (GSAS)*, LAUR 86-748, Los Alamos National Laboratory, Los Alamos.

[54] http://www.esrf.fr/exp_facilities/BM1A/index.htm (Olga Bandilet, 2004).

[55] G. Fantozzi, *Phenomenology and definitions* in *Mechanical Spectroscopy Q-1 2001* 3 (TRANS TECH PUBLICATIONS LTD, Zurich-Uetikon, Switzerland, 2001).

[56] R. M. Fuoss and J. G. Kirkwood, *Electrical Properties of Solids. VIII. Dipole Moments in Polyvinyl Chloride-Diphenyl Systems*, Journal of the American Chemical Society 63, 385 (1941).

[57] F. R. N. Nabarro, *Deformation of Crystals by the Motion of Single Ions (Report of a Conf. on Strength of Solids)*, Physical Society of London 60, 75 (1948).

[58] D. Herring, *Diffusional Viscosity of Polycrystalline Solid*, Journal of Applied Physics 21, 437 (1950).

[59] R. L. Coble, *A Model for Boundary Diffusion Controlled Creep in Polycrystaline Materials*, Journal of Applied Physics 34, 1679 (1963).

[60] W. Benoit, *Grain boundary: Description and dynamics* in *Mechanical Spectroscopy Q-1 2001* 291 (TRANS TECH PUBLICATIONS LTD, Zurich-Uetikon, Switzerland, 2001).

[61] G. Schoeck, J. Shyne and E. Bisogni, *Activation Energy of High Temperature Internal Friction*, Acta Metallurgica 12, 1466 (1964).

[62] A. P. Sutton and R. W. Balluffi, *Interfaces in crystalline materials* (Oxford University Press, Oxford, 1996).

[63] R. Raj and M. F. Ashby, *On grain boundary sliding and diffusional creep*, Metallurgical Transactions 2, 1113 (1971).

[64] M. F. Ashby, *Boundary Defects, and Atomistic Aspects of Boundary Sliding and Diffusional Creep*, Surface Science 31, 498 (1972).

[65] A. S. Nowick and B. S. Berry, *Anelastic Relaxation in Crystalline Solids* (Academic Press, New York, 1972).

[66] C. Zener, Physical Review 60, 906 (1941).

[67] A. Lakki, *Mechanical Spectroscopy of Fine-Grained Zirconia, Alumina and Silicon Nitride*, Thesis EPFL N°1266, 1994.

[68] T. S. Ke, *Fifty-year study of grain-boundary relaxation*, Metallurgical and Materials Transactions A - Physical Metallurgy and Materials Science 30, 2267 (1999).

[69] W. Benoit, *Grain boundary relaxation in metals* in *Mechanical Spectroscopy Q-1 2001* 306 (TRANS TECH PUBLICATIONS LTD, Zurich-Uetikon, Switzerland, 2001).

[70] B. Cao, R. Schaller, W. Benoit and F. Cosandey, *Internal friction associated with grain boundaries in Ni-Cr alloys*, Journal of Alloys and Compounds 211-1, 118 (1994).

[71] R. Schaller and A. Lakki, *Grain boundary relaxations in ceramics* in *Mechanical Spectroscopy Q-1 2001* 315 (TRANS TECH PUBLICATIONS LTD, Zurich-Uetikon, Switzerland, 2001).

[72] R. Schaller, G. Fantozzi and G. Gremaud (eds.) *Mechanical Spectroscopy Q-1 2001: with applications to Materials Science* (Trans Tech Publications, Uetikon-Zuerich, Switzerland, 2001).

[73] G. Dixon and N. Wright, *Creep deformation of WC-Co alloys*, International Journal of Refractory Metals & Hard Materials, 55 (1989).

[74] B. Roebuck and E. A. Almond, *Equivalence of indentation and compressive creep tests on a WC/Co hardmetal*, Journal of Materials Science Letters 1, 519 (1982).

[75] F. Osterstock, *High temperature creep of some WC-Co alloys*, in proceedings of Int. Conf. Sci. Hard Mater. 1 671 (Wyoming, 1981).

[76] B. Roebuck and E. A. Almond, *Deformation, fracture processes and the physical metallurgy of WC-Co hardmetals*, International Materials Reviews 33, 90 (1988).

[77] B. Roebuck and E. A. Almond, *Compressive creep tests on WC cemented carbides with different binder-phase compositions*, in proceedings of 11th Plansee Seminar (1985).

[78] W. D. Callister, *Materials Science and Engineering: An Introduction* (John Wiley & Sons, Inc., 1997).

[79] M. Lee and R. S. Gilmore, *Single crystal elastic constants of tungsten monocarbide*, Journal of Materials Science 17, 2657 (1982).

[80] P. D. Evenschor, W. Fröhlich and V. Hauk, *Calculation of X-Ray Elastic Constants from Single Crystal Coefficients of Hexagonally Crystallizing Metals*, Zeitschrift für Metallkunde 62, 38 (1971).

[81] Y. S. Touloukian, R. K. Kirby, R. E. Taylor and I. R. Lee, *Thermal expansion, nonmetallic solids, thermophysical properties of matter* (IFI/Plenum, New York, 1977).

[82] R. B. Von Dreele, J. D. Jorgensen and C. G. Windsor, *Rietveld Refinement with Spallation Neutron Powder Diffraction Data*, Journal of Applied Crystallography 15, 581 (1982).

[83] E. Conforto, D. Mari and T. Cutard, *The role of molybdenum in the hard-phase grains of (Ti, Mo)(C, N)-Co cermets*, Philosophical Magazine 84, 1717 (2004).

[84] T. B. Massalsky, *Binary alloy phase diagrams* (ed. H. Okamoto et al.) (ASM International, Materials Park, Ohio, 2001).

[85] B. Uhrenius, *Evaluation of molar volumes in the Co-W-C system and calculation of volume fractions of phases in cemented carbides*, International Journal of Refractory Metals and Hard Materials 12, 121 (1993).

[86] K. Aigner, W. Lengauer, D. Rafaga and P. Ettmayer, *Lattice parameters and thermal expansion of Ti(CxN1-x), Zr(CxN1-x), Hf(CxN1-x) and TiN1-x from 298 to 1473 K as investigated by high temperature X-ray diffraction*, Journal of Alloys and Compounds 215, 121 (1994).

[87] F. Berthier, J. Creuze, R. Tétot and B. Legrand, *Multilayer properties of superficial and intergranular segregation isotherms: A mean-field approach*, Physical Review B 65, 195413 (2002).

[88] A. Lakki, R. Schaller, M. Nauer and C. Carry, *High temperature superplastic creep and internal friction of yttria doped zirconia polycrystals*, Acta Metallurgica et Materialia 41, 2845 (1993).

[89] U. Rolander, G. Weinl and M. Zwinkels, *Effect of Ta on structure and mechanical properties of (Ti,Ta,W)(C,N)-Co cermets*, International Journal of Refractory Metals & Hard Materials 19, 325 (2001).

[90] G. Östberg, SEM observations, Chalmers University of technology, Gothemburg, Sweden (2003).

[91] W. Benoit, *High-temperature relaxations*, Materials Science and Engineering A 370, 12 (2004).

[92] J. D. Eshelby, *The determination of the elastic field of an ellipsoidal inclusion, and related problems*, Proc. R. Soc. 241A, 376 (1957).

[93] T. W. Clyne and P. J. Withers, *An Introduction to Metal Matrix Composites* (eds. E. A. Davis and I. M. Ward) (Cambridge University Press, Cambridge, 1993).

[94] L. E. Toth, *Transition Metal Carbides and Nitrides* (ed. J. L. Margrave) (Academic Press, New York and London, 1971).

Acknowledgements

I wholeheartedly thank my thesis director Professor Willy Benoit for accepting me into his laboratory and supporting me throughout this work even after his retirement. I am most grateful for his scientific advice, but even more for his kindness, his generosity and the family atmosphere that he creates all around him.

Great thanks goes also to my supervisor Daniele Mari, for sharing with me his enormous knowledge in the hardmetal field and beyond. He was always available for discussions and very supportive with a great deal of enthusiasm and an inexhaustible optimism. His far-reaching connections made this work possible and thus allowed me to gain experience even outside the laboratory at AB Sandvik Coromant in Stockholm, Sweden, at the Los Alamos Neutron Science Center, New Mexico, USA and also at the ESRF Synchrotron in Grenoble, France.

This work would not have been possible without the continuous help of the technicians, who do an invaluable job. Thanks to Bernard Guisolan for his help with the mechanical equipment, to Gerald Beney for the sample preparation and various heat-treatments, to Alessandro Ichino for the help in electric and electronic matters, to Antonio Gentile and Guillaume Camarda for the sample cutting and to Philippe Bugnon for his help in the chemistry lab and with the X-ray diffraction. Enfin, un grand merci à tous les techniciens de m'avoir donné la possibilité de pratiquer le français!

I would also like to express my gratitude towards the members of the project "Fundamental mechanisms for plastic deformation of cemented carbides and cermets". I am happy for having been part of this collaboration, which always gave me additional motivation during the three and a half years of research and opened my eyes towards different views and new ideas. Thanks to my fellow-PhD students Mikael Christensen and Gustaf Östberg, and to their thesis directors Prof. Göran Wahnström and Prof. Hans-Olof Andrén, from Chalmers University of Technology in Gothemburg, Sweden. Special thanks to Gustaf for providing microscopic images, partially used in this work but also in presentations and posters for conferences. I thank AB Sandvik Coromant, Stockholm, Sweden, for providing all the materials used in this work. My thanks go to Ingrid Reineck and Susanne Norgren, who put all their expertise into the making of the materials. I would like to thank Susanne especially for the very kind and easy communication throughout the years of this work, for her patience in teaching me some hardmetal thermodynamics, for the

microscopical and chemical analysis of the materials and for providing the equilibrium diagrams presented in this work.

My gratitude also goes to those that have helped me, practically day and night, during my diffraction experiments. I thank Mark Bourke and Bjørn Clausen and also Geoff Swift, Sven Vogel and Tom Sisneros from the Los Alamos Neutron Science Center, NM, USA, and Prof. David Dunand from Northwestern University, IL, USA, for their help with the neutron diffraction experiments and the data analysis. For the support with the X-ray diffraction experiments, I thank Hermann Emerich and Wouter van Beek at the Swiss Norwegian Beamline at ESRF, Grenoble, France.

I thank everyone (inside and outside the institute) that made me have a good time in Lausanne; thanks for movie nights, parties, hiking, swimming, talking etc. I am especially happy to have found great friends in my office colleagues and fellow doctorants Iva Tkalcec and Patrick Mayor. Apart from being good friends they've also had a big part in the success of my PhD; Pat by teaching me physics and math and by successfully pushing me through Quantum Mechanics, and Iva by her great inventiveness in solving technical problems (sometimes simply by pulling and re-plugging cables) and discussing all kinds of scientific, technical or not at all work-related matters.

Last but not least, I thank Jens for his love and support.

Curriculum vitae

Katharina Buß

born on November 20th, 1975 in Röbel, Germany

nationality: German

Education:

2001-2004:	*Ph.D. student at EPF Lausanne, Faculty of Basic Sciences, Institute of Physics of Complex Matter under supervision of Dr. D. Mari and thesis director Prof. W. Benoit*
2000:	*Diploma work "Electrochemical impedance spectroscopy measurements on stainless steels with different surface treatments", performed at SANDVIK STEEL, Sandviken, Sweden*
1996-2000:	*Materials Engineering at FH Jena, Germany*
1996:	*Abitur at the Elly-Heuss-Knapp-Gymnasium in Heilbronn, Germany*

Teaching:

2002-2004:	*Assistant for "Practical training" for 2nd year physics students, with Dr. G. Gremaud (taught in French)*
2001-2002:	*Assistant for exercises of "Physics I and II: Mechanics and Thermodynamics" for 1st year engineering students, with Prof. R. Gotthardt (taught in German)*

Conferences:

2004:	*G. Östberg, K. Buss, M. Christensen, S. Norgren, H.-O. Andrén, D. Mari, G. Wahnström, I. Reineck: "Mechanisms of plastic deforma-*

tion of WC-Co and Ti(C,N)-WC-Co", 8th International Conference on the Science of Hard Materials 2004, San Juan, Puerto Rico (oral presentation)

2003: *K. Buss, D.C. Dunand, M.A.M. Bourke, H. Emerich, D. Mari: "Residual stresses measured by diffraction techniques", EUROMAT 2003, Lausanne, Switzerland (Poster)*

K. Buss, D. Mari: "Grain boundary sliding in cermets", Annual meeting of the Swiss Physical Society (SPS), Basel, Switzerland (oral presentation)

2002: *K. Buss, D. Mari: "High temperature deformation of cermets and cemented carbides with same amount of binder phase", PM 2002, Lausanne, Switzerland (oral presentation)*

K. Buss, D. Mari: "High temperature deformation mechanisms in cemented carbides and cermets studied by mechanical spectroscopy", ICIFUAS 13, Bilbao, Spain (Poster)

K. Buss, D. Mari: "A neutron diffraction study of internal stresses in WC-Co at different loads and temperatures", Plasticité, Lyon, France (oral presentation)

Publications:

K. Buss, D. Mari, M.A.M. Bourke, B. Clausen, D.C. Dunand: "A neutron diffraction study of internal stresses in WC-Co at different loads and temperatures", to be published in International Journal of Refractory Metals and Hard Materials

G. Östberg, K. Buss, M. Christensen, S. Norgren, H.-O. Andrén, D. Mari, G. Wahnström, I. Reineck: "Mechanisms of plastic deformation of WC-Co and Ti(C,N)-WC-Co", to be published in International Journal of Refractory Metals and Hard Materials

G. Östberg, K. Buss, M. Christensen, S. Norgren, H.-O. Andrén, D. Mari, G. Wahnström, I. Reineck: "Effect of TaC on plastic deformation of WC-Co and Ti(C,N)-WC-Co", to be published in International Journal of Refractory Metals and Hard Materials

K. Buss, D. Mari: "High temperature deformation mechanisms in cemented carbides and cermets studied by mechanical spectroscopy", Materials Science and Engineering 370A (2004) 163-167

K. Buss, D. Mari: "High temperature deformation of cermets and cemented carbides with same amount of binder phase", Conference proceedings PM 2002, Lausanne, Switzerland